Laura Badano

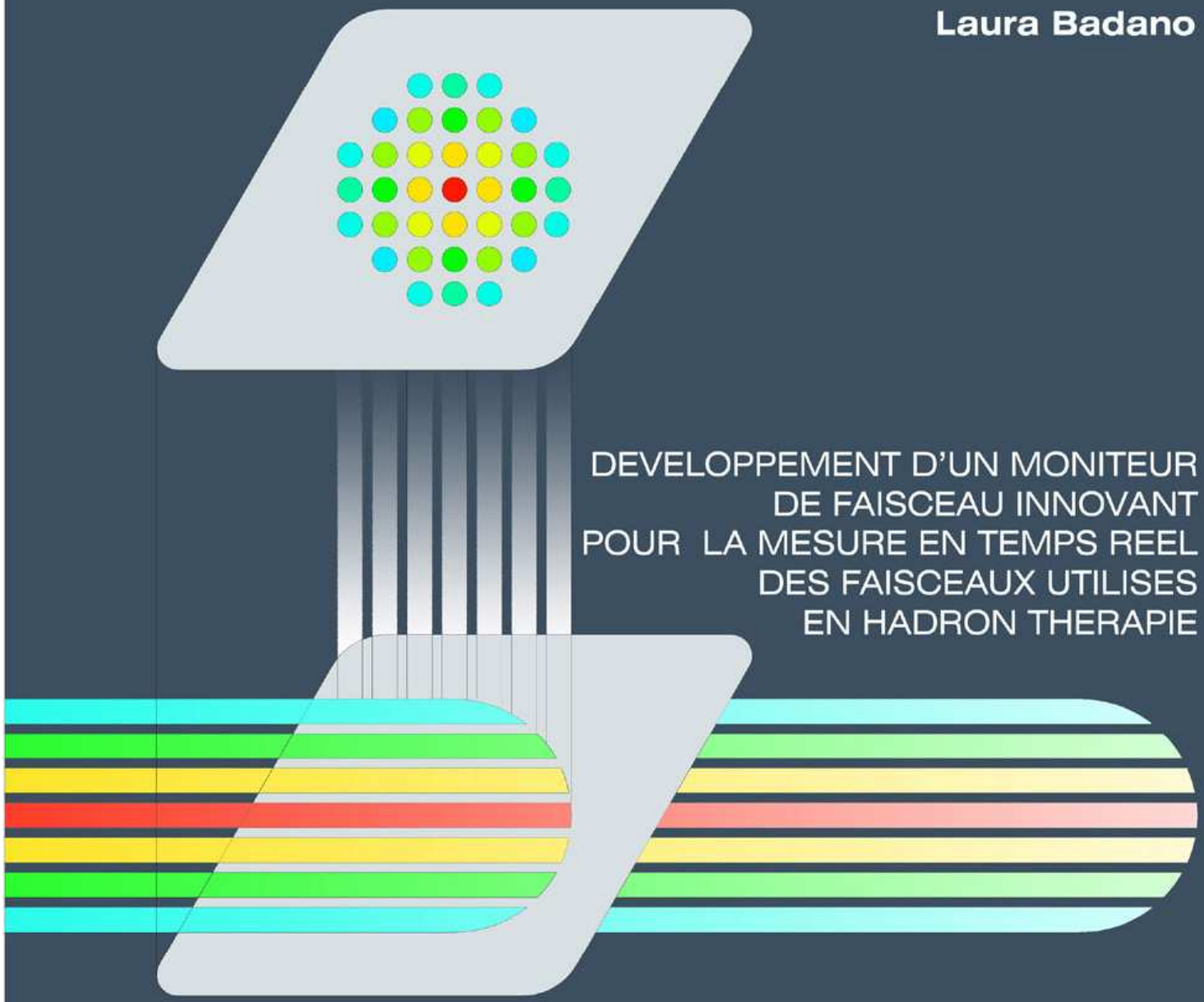

DEVELOPPEMENT D'UN MONITEUR DE FAISCEAU INNOVANT POUR LA MESURE EN TEMPS REEL DES FAISCEAUX UTILISES EN HADRON THERAPIE

Laura Badano

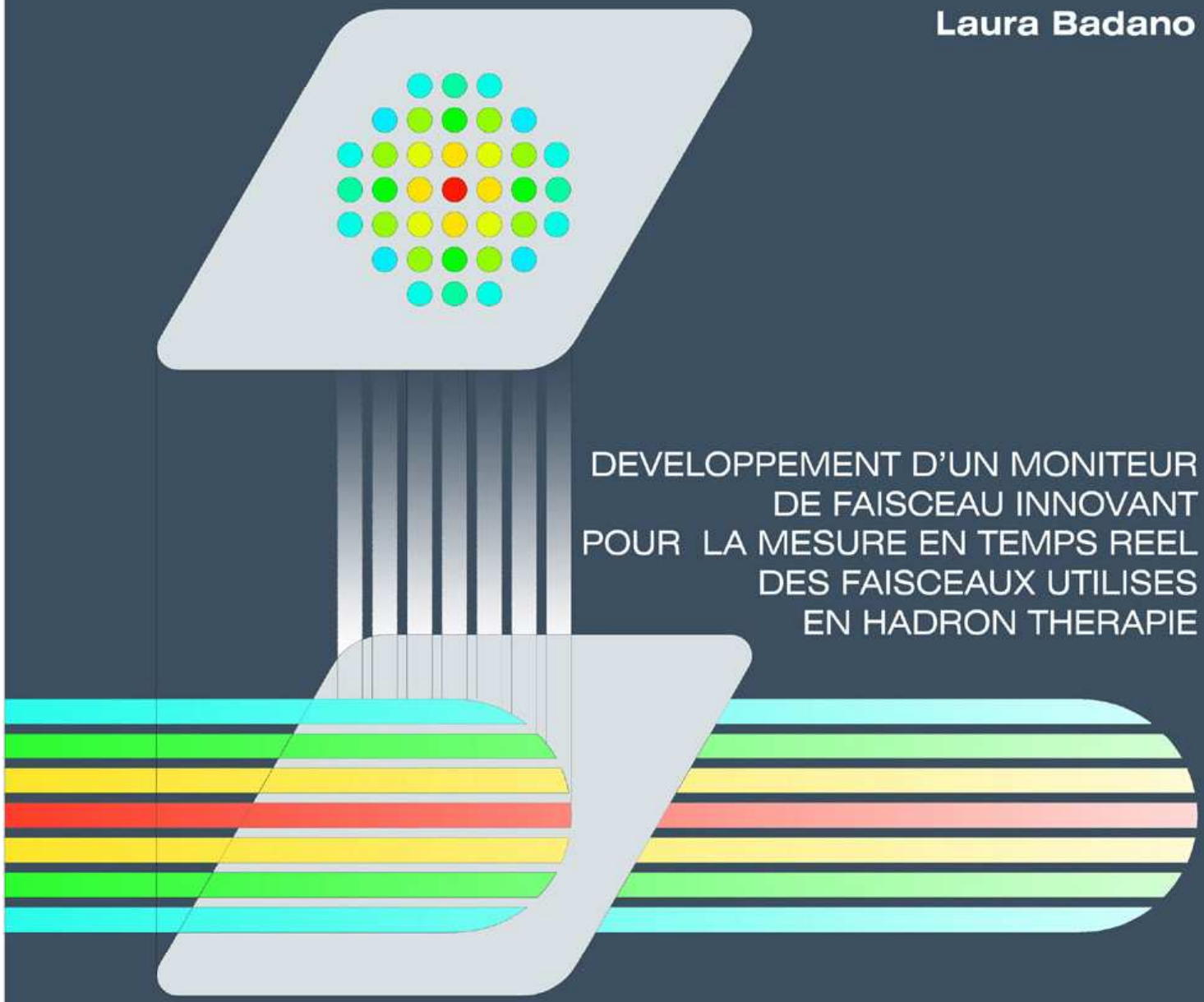

DEVELOPPEMENT D'UN MONITEUR DE FAISCEAU INNOVANT POUR LA MESURE EN TEMPS REEL DES FAISCEAUX UTILISES EN HADRON THERAPIE

Thèse présentée pour obtenir le grade de
Docteur de L'Université Louis Pasteur
Strasbourg I

Discipline: **PHYSIQUE**
par: **Laura BADANO**

Titre

Développement d'un moniteur de faisceau innovant pour la mesure en temps réel des faisceaux utilisés en hadronthérapie

Soutenue publiquement le 29 septembre 2005

Membres du Jury

Directeur de Thèse: Professeur Jean-Louis RIESTER
Rapporteur Interne: Professeur Abdelmjid NOURREDDINE
Rapporteur Externe: Docteur Walter SCANDALE
Rapporteur Externe: Professeur Peter WEILHAMMER
Examinateur: Professeur Massimo CACCIA

to the SUCIMA collaboration,
for three exciting and enriching years

Acknowledgments

Professor Ugo Amaldi, the president of TERA Foundation, gave me the chance to become a beam diagnostics expert by working in international environments of excellence such as CERN, the SUCIMA collaboration and the Cyclotron Laboratory of the Joint Research Centre for nearly a decade. He has guided and inspired me over the years.

My warmest thanks go to the entire SUCIMA collaboration for three enriching years and in particular: to Massimo Caccia, the enthusiast and restless project coordinator and to the indefatigable optimist Wojtek Kucewicz, with whom the SUCIMA adventure started. I am indebted to them for teaching me how to become the scientific responsible of a research project. Thanks to Agnieszka Zalewska for her constant support, for many precious suggestions and discussions and for showing me that a pragmatic approach is often *the solution*. I thank Jacek Marczewski for his enthusiastic support, especially in the critical phases, Eugene Grigoriev for carefully reading and correcting all the SLIM papers and notes, and Adam Czermak for many useful discussions on the Data Acquisition System architecture. Wojtek Dulinski and Grzegorz Deptuch answered my naïf questions on the MIMOTERA sensor. Professeur Riester gave me the chance to write this doctoral thesis at the Univeristé Louis Pasteur and supported me as a true mentor. Genuine thanks to Hermann Schweickert for suggesting to use the SLIM beam monitor for the real time control of radioisotope production at cyclotron facilities and many fruitful discussion on the subject. Thanks to my PhD candidate comrades Antonio Bulgheroni and Chiara Cappellini for answering many questions, from science to LaTEX, and for helping with the data taking and analysis with unequalled patience; and to Mario Alemi for several stimulating discussions on the electro-optics for the focusing system. I thank Barbara Spanò and Lorenza Paolucci for their professional and efficient support for all the issues concerning EC project administration which otherwise would have been chaotic at best.

I extend my heartfelt gratitude to the CERN experts who made the SLIM project possible. Gianni Molinari, the SLIM guardian angel, gave me the idea of using the thin aluminum foils for hadrontherapy beams in real-time diagnostics. He taught me the subtle tricks of the thin foils production and of beam instrumentation physics, always answering my questions with competence and a smile on the face. Remo Maccaferri, Gianfranco Ferioli and Enrico Chesi taught me with patience and willingness the secrets of their trade they do with so much talent and passion for years. Enrico Bravin for giving many precious suggestions on several electronics aspects and for lending the frame grabber and software used for the CERN laboratory test. Christian Joram for several useful advices on the electro-optics for the focusing system. Very special thanks also go to Alfredo Placci, Michel Delattre and Andre Domeniconi for the focusing system engineering design and construction and, together with Andre Braem and Serge Mathot, for many crucial discussions and suggestions on me-

chanical, electrical and material aspects; Christian Lacroix and Sophie Meunier for valuable and repeated support on the vacuum system. I warmly thank Peter Weilhammer for the pad sensor used for the first in-beam tests with a silicon sensor and for his thoughtful commentary and practical advice; and Walter Scandale for careful reading of this thesis and his help and criticism along the years.

I thank several TERA/CNAO colleagues: Marco Pullia for his continuous support and many stimulating discussions on beam monitor features over the years; Saverio Braccini for his help in the beam monitor installation in the JRC cyclotron and many discussions on the experimental setup; Maria Di Rosa for helping with the administrative issues at CERN with admirable patience; Mirco Nodari for the vacuum chamber technical drawings and the beautiful SLIM animation; Giacomo Primadei for his contribution to the realization of the slow control electrical system; and Ivan Ferrari for calmly and efficiently solving the notebook problems when I was panicking.

Thanks to the JRC colleagues Hermann Stamm, Neil Gibson, Uwe Holzwarth, Kamel Abbas, Hans Hofman, Wijbe Horstmann, Fernando Arroja for giving us the chance to test the SLIM on a proton beam and sharing with us the first beam image record. Their support and dedication during the monitor installation at the JRC cyclotron, and the in-beam measurements were crucial for success at the first try.

I give warmest thanks to the wonderful SLIM/TERA team who made this project a success beyond what was imagined possible. I especially acknowledge Ornella Ferrando for her qualified, enthusiastic and dedicated work. She is the author of the SIMION simulations for the focusing system described in the third chapter of this thesis. We shared our joys and sorrows since the SLIM project beginning and without her support, none of this would be possible. I thank Marco Pezzetta for many fruitful suggestions and discussions in the first year of the project; and Tomasz Klatka and Michal Koziel for their professional, passionate and successful work on the slow control system despite the time pressures.

Finally, I would like to acknowledge the support of the TERA Foundation, of the European Commission and of the Monzino Foundation.

Last but not least, my deepest gratitude goes to my family and friends for believing in me and offering their constant and precious support over the years. I thank you all.

Contents

Introduction

Hadrontherapy is a radiotherapy technique using light ion beams (usually protons or carbon) to irradiate tumours. The intense end-of-track Bragg ionization peak and a small lateral beam diffusion are employed to deliver optimized dose to the tumour thereby minimizing the damage to neighboring healthy tissues.

Normally the main beam parameters are measured at the start up phase. Patient safety, accelerator operation, and optimum dose delivery would all benefit from continuous beam intensity and profile monitoring during treatment. An effective device for on-line beam monitoring must produce negligible effects on the few nA clinical beam, featuring a granularity not exceeding 1 mm, a beam current measurement resolution of few percent and a frame rate of the order of 10 kHz.

Up to present this has not been possible. Existing interceptive monitors interfere with the beam and cause a non-negligible beam blow up or a beam disruption for therapeutic kinetic energies (60 to 250 MeV for protons and 120 to 400 MeV/nucleon for carbon ions). Non-interceptive instrumentation on the other hand is not sensitive enough to detect beam intensities from few pA to few nA, with $\approx$ 1 s spill duration.

To overcome this limitation a novel non-disruptive monitor, **S**econdary emission monitor for **L**ow **I**nterception **M**onitoring (SLIM), capable of providing beam intensity and profile during the treatment without degrading the hadron beam, has been proposed. The design, development and testing of the SLIM beam monitor are the subject of this doctoral thesis.

The work has been carried out in the framework of the **S**ilicon **U**ltra fast **C**ameras for electrons and gamma sources **I**n **M**edical **A**pplication (SUCIMA) project funded by the European Commission[1] with the primary goal of developing a novel silicon real-time, high granularity, monolithic, pixel sensor for medical applications.

SLIM is based on the secondary emission of electrons from a sub-micron thick aluminium foil intercepting the beam at 45-degrees. Ionization of the Al atoms by the hadron beam can result in electrons receiving energy and momentum sufficiently large to escape from the foil surface. The secondary electrons are emitted with a flux proportional to the primary particle beam intensity and accelerated up to 10 - 30 keV by an electrostatic focusing system onto an imaging device. The imaging system makes the beam intensity and its position with the required 1 mm precision at a 10 kHz frame rate possible.

1 European Commission contract: G1RD-CT2001-00561.

The first part of the thesis, after the rationale for a new beam monitor and the definition of the performance requirements, focuses on the beam monitor conceptual design, the engineering study optimized for hadrontherapy and the beam monitor construction and integration. While the second part is dedicated to the results of the laboratory tests for the characterization of the focusing system with thermionic electrons emitted from a hot tungsten wire and to the in-beam tests performed on a low intensity hadron beam at the Cyclotron Laboratory of the Joint Research Centre in Ispra.

After an historical review, the advantages of hadron beams compared to electron and photon beams due to their higher ballistic selectivity and biological properties are described in Chapter 1. An accurate three dimensions description of a tumour in relation to the critical organs of the patient combined with accurate dose delivery techniques are crucial to fully exploit the hadron beams physical and radio-biological superiority. To assure the best available techniques to a large number of patients hospital-based hadrontherapy facilities have been funded in Germany, Italy, Austria and France and are at present (September 2005) being built in Germany and Italy.

The critical issues in the design of new hadrontherapy facilities are the optimization of the accelerator extraction scheme for the smoothest extracted beam, speed and accuracy of the dose delivery system and real-time beam monitoring during therapy.

The design of an accelerator complex optimized for hadrontherapy is presented in Chapter 2 together with the rationale for the novel beam monitor and its working principle with specifications. The commercial system and the two solid-state detectors, used as imaging devices of the SLIM secondary electrons, are analyzed in detail in Section 2.4. The hybrid solution based on a pad silicon sensor read-out by low noise current integrating front-end chips has been engineered in the framework of the SUCIMA project. MIMOTERA, the monolithic active pixel detector based on the SLIM beam monitor specifications and the dedicated data acquisition system have both been designed and developed within SUCIMA.

The beam monitor conceptual design is described in Chapter 3 and covers the secondary emission efficiency and focusing system studies. The secondary electrons angular and energy distribution and yields provided the input conditions for the design of a stigmatic electro-optics for the electrons transport. SLIM imaging depends crucially on the focusing system performances. The common guidelines for the design of the different prototypes are examined in Chapter 3. A detailed analysis of the final prototype, inspired by the cross-focusing optical scheme of an image intensifier tube, is discussed in Section 3.2.2.

The construction of the electrostatic focusing system for the final prototype with high vacuum materials is described in Chapter 4. The procedure to manufacture sub-micron thick secondary emission foils starting from 0.1 mm thick 99% purity aluminium sheets is also presented there. The vacuum chamber design allows for the in/out positioning of the focusing system with respect to the hadron beam path and host all the necessary flanges and bellows to insert the system in the beam pipeline. It also features simple connection to vacuum system, to the actuator for the focusing system rotation and to high voltage feedthroughs for the detector bias and the focusing system polarization.

A dedicated control system ensures the maximum users safety. The highest security on vacuum, motion and high voltage equipment is guaranteed trough process automation. These issues are addressed in Section 4.4.

Laboratory tests of the focusing lenses have been performed using thermionic emission from a hot tungsten wire as a source of electrons, and the results of the measurements analysis are described in Chapter 5. A commercial system consisting of a micro channel plate coupled to a phosphor screen imaged on a standard charge-coupled device was used to assess the beam monitor specifications in terms of optical system linearity, demagnification factor and spatial resolution. The experimental results are discussed in details in Section 5.3. The effect of an external magnetic field was also investigated to explain the observed image shift with respect to the detector centre. Finally, the experimentally observed fluctuations of the wire intensity were verified with SIMION 3D simulations.

The complete system qualification with hadron beams is ongoing at the Cyclotron Laboratory of the Joint Research Centre. The Scanditronix MC40 cyclotron is capable of accelerating various light ions up to an energy of 39 MeV (protons) with a maximum beam intensity of 50 μA and a minimum beam controllable intensity of $\approx$ 5 nA. The SLIM beam monitor was installed in one of the extraction lines (Section 6.1).

As a proof of principle the same commercial system used to measure the optical properties of the electrostatic focusing system has been initially integrated, despite lower than required frame rate. The results of the measurements and the related data analysis are explained in Section 6.2.

The moderate granularity, high dynamic range hybrid solution with a shallow back-plane silicon pad sensors has been integrated in the SLIM to assess the sensitivity to beam current variations and the system dynamic range. Four 128-channel low noise VASCM2 ASICs chips read out the sensor via the dedicated data acquisition system. The ASICs amplify and store the charge deposited on each pad over a pre-set integration time and four different gains. The results of the pad measurement are covered in Section 6.3.

As a follow up study, before the final measurements with the dedicated sensor MIMOTERA, profiling capability and sensitivity to low energy electrons were studied integrating a back-thinned monolithic sensor of the MIMOSA family (MIMOSA V), featuring a high granularity but limited dynamic range. The results of the in-beam measurements together with the analysis of the high background signal recorded are described in Section 6.4.

The final full qualification of the SLIM beam monitor with MIMOTERA, designed in the framework of the SUCIMA collaboration on the base of the SLIM specifications, will be scheduled in the nearest future.

The direct contribution of the candidate is in the original idea, in the assessment of the electron detection and data acquisition systems specifications, in the novel beam monitor conceptual and engineering design, in the organization and technical performance of the laboratory and in-beam measurements and the related data analyses. The candidate was also the scientific responsible of the SUCIMA project for the TERA Foundation and led the team in charge of the beam monitor development.

Chapter 1

Hadrontherapy

Within a few months of Röntgen discovery of x-rays in 1895, investigators realized that x-rays could be used for both diagnostics and therapy purposes. These soft x-rays were far from optimal for radiation therapy, but new and better x-ray machines continually become available for clinical work as medicine took advantage of the improved technology developed for basic science research.

Today many hospital use electron linear accelerators (linacs) with modern radiofrequency and control systems to deliver 4 to 25 MeV electron beams which can be used directly for therapy or targeted on tungsten to produce photons for therapy. Because of low penetrating ability of electrons, electrons therapy is used primarily to treat superficial diseases such as skin and lymph node tumours, whereas photon therapy has become the *workhorse* of radiation therapy as discussed in Section 1.2.1.

Despite the advantages of modern electron linacs, extensive clinical experience with photon therapy has shown that some tumours, called radioresistant tumours, respond poorly to photon therapy, and that sometimes even non-radioresistant tumour cannot be given a tumouricidal dose[1] because of the unavoidable associated dose to neighboring healthy tissue. Hadronic radiotherapy (or hadrontherapy) uses particles such as protons, neutrons and light ions such as carbon to treat radioresistant tumours and tumours located near critical body structures.

After the historical outlook of Section 1.1, the therapeutical advantages of hadron beams when compared with electron and photon beams due to a higher ballistic selectivity are detailed in Section 1.2.1, while those due to the biological properties of hadrons are described in Section 1.2.2. An accurate three dimensions description of the tumour in relation to critical organs of the patient combined with accurate dose delivery techniques are crucial to fully exploit the hadron beams superior selectivity and radio-biological effectiveness and are described in Section 1.3. Section 1.4 lists the numbers of patients treated with hadrons and justifies the construction of new hospital-based centres where relatively large number of

1 By definition the absorbed dose (symbol D), sometimes called dose, is the ratio between the energy E_d imparted by the radiation to a small volume of material (tissue) and the mass m of this volume of material. The ratio $D = E_d/m$ is measured in Gray. 1 Gy equals 1 Joule per kg.

patients can be irradiated with the best available techniques. Hadrontherapy projects have been funded in Germany, Italy, France, Austria to respond to the European need of new hospital-based facilities. The status of the construction of the Italian Centro Nazionale di Adroterapia Oncologica is detailed in Section 1.5.

1.1 Historical background

The underlying concept for using protons for therapy originated in physics laboratories, beginning with Wilson's seminal insight in 1946 [1]. Wilson anticipated that the physical characteristics of a proton beam would provide the clinician with superior controllability of dose distribution when compared to photons or electrons. He foresaw that radiotherapeutic prescriptions could be so written that the physician could deliver a high dose to a designated cancer-containing volume while delivering a significantly lower dose, or no dose at all, to tissues outside that volume, and that as a result, the opportunity for disease control would increase while the incidence of normal-tissue morbidity would be reduced[2].

In the early 1950s, Tobias and his colleagues at the University of California Radiation Laboratory (UCRL) performed pioneering studies in animals that led to the use of protons and helium ions in treating human diseases [2, 3]. Those investigations established that beams of protons and other heavy charged particles penetrated tissues with little scatter, produced well-circumscribed radiolesions and spared more of the adjacent normal tissues. Larsson, beginning his work in the mid-1950s, acknowledged the inspiration provided by Tobias's work (1962) and expanded on it, establishing the first comprehensive series of investigations devoted to protons [4–6].

Some patients were treated as early as 1954, yet proton therapy did not become feasible clinically until the 1980s. There were mainly three reasons for this:

- until the target could be defined with an accuracy equal to that of the irradiation itself, physicians could not exploit the precision of protons;
- proton accelerators were larger, more complex, and had been designed initially for physics research, not clinical work, requiring in turn greater numbers of highly technical people to manage them and deliver treatments, so the cost was much greater;
- the technology to exploit protons and develop cost effective machines, with reasonable cost, did not evolve until the 1980s.

2 Wilson, with many of his colleagues who had done their graduate work in physics under Ernest O. Lawrence at Berkeley in the 1930s, was aware of the medical implications of particle radiation. In [1] he elucidated all of the qualities that made protons potentially attractive and have, indeed, proved to be so:"*... the specific ionization or dose is many times less where the proton enters the tissue at high energy than it is in the last centimeter of the path where the ion is brought to rest; ... these properties make it possible to irradiate intensely a strictly localized region within the body, with but little skin dose; ... since the range of the beam is easily controllable, precision exposure of well defined small volumes within the body will soon be feasible; ...the biological damage depends not only on the number of ions produced in a cell, but also upon the density of ionization. The biological effects near the end of the range will be considerably enhanced due to greater specific ionization, the degree of enhancement depending critically upon the type of cell irradiated.*"

Things are different now. It has been almost 60 years Wilson suggested the use of fast protons for therapy, and almost 50 years since a proton beam from a high-energy physics research accelerator was first used to treat a human being. The exceptional improvements in the last two decades of the conventional imaging modalities from Computer Tomography (CT) to Magnetic Resonance Imaging (MR) and Position Emission Tomography (PET) and of the technology to develop hadrontherapy accelerators with reasonable cost since the 1980s, have given a substantial boost to the diffusion of hadrontherapy.

Proton radiation therapy has a history [7] and clinically dedicated accelerators and facilities now exist. Around the world, thousands of people have been treated with protons, as detailed in Section 1.4, the majority at physics research facilities, but an increasing number at clinically dedicated facilities [8]. Proton-beam treatment is now an accepted radiotherapeutic modality and more facilities dedicated to hadrons are on the way.

1.2 Rationale for hadrontherapy

At the beginning of the third millennium one European citizen out of three will have to deal with a cancer episode in the course of his/her life. The word *cancer* indicates more than one hundred different tumours arising in different tissues diagnosed at various stages of development. Tumour cells are biologically similar to normal cells and at present the therapeutical approaches are strictly limited by this lack of specificity. Most scientists are confident that in the long run significant improvements in cancer cure will come from immunotherapy and/or gene therapy and drug targetting; research toward such systemic treatments is and will be of the utmost importance.

However, progress is slow and for the next decades great revolutions valid for most types of cancers are unlikely, but rather specific improvements on some forms of tumours and, at the same time, on steady improvements in the screening, diagnosing and treatments which make use of techniques currently known.

Radiation therapy is the use of directly or indirectly ionizing radiation to damage the DNA in cancerous cells so that, having lost the ability to replicate, they ultimately die. The body then rids itself of dead cancer cells in the same manner that it removes any other unwanted tissue. The main objective of radiotherapy is the local control of the tumour and, in some situations, of the surrounding diffusion paths (loco-regional radiotherapy).

In order to reach this objective, a sufficiently high dose must be delivered to the tumour nidus, which may be considered in physical terms as the *target*, so as to destroy it, at the same time maintaining the dose to the surrounding healthy tissues within the tolerance limit. On the basis of this consideration it is clear that the probability of destroying the tumour increases in line with the *ballistic selectivity* or *conformity* of the irradiation delivered, i.e. the gradient between the dose to the target and the dose to the surrounding healthy tissue.

The superior ballistic selectivity attainable with protons and light ions, as compared to photons, electrons and neutrons is due to the following reasons [9]:

- a well defined range in tissue; this property allows one to avoid irradiation of the

healthy tissue located beyond the tumour, by shaping the distal dose fall-off to the distal (deepest) edge of the tumour volume;

- depth dose curve characterized by a low value at the entrance (plateau) and a sharp maximum (Bragg peak) at the end of range, as detailed in Section 1.2.1; this feature allows one to selectively irradiate deep seated targets while keeping the dose delivered to the healthy tissue upstream of the tumour within the tolerance limit;

- limited lateral scattering, which translates into a better definition of the edges of the radiation field at the treatment depth. The scattering increases with decreasing ion mass, but also with proton beams it is always much less than with conventional radiotherapy electron beams.

Dose conformation is the crucial parameter in the choice of the ion to be used in hadrontherapy. Range straggling decreases with increasing ion mass but, on the other hand, heavier projectiles undergo fragmentation in traversing a medium before reaching the target. The secondary particles produced in the fragmentation process have a lower ionization density and, therefore, a longer range than the primaries; they are responsible for the energy deposition in the tail beyond the Bragg peak and for a complication in the dose deposition pattern. For this reason, together with radiobiological considerations, ions heavier than argon have no radiotherapeutical indications; in fact physical and radiobiological information point to ^{12}C and ^{16}0 as the best candidates for ion therapy, as detailed in Sections 1.2.1 and 1.2.2.

The above characteristics of proton and light ions translate into a better conformation of the dose to the tumour volume. A homogeneous transverse distribution of the dose over a given area is obtained by spreading the beam by a combination of absorbers and scatterers or by magnetic scanning of a pencil beam, as explained in Section 1.3.

In addition to their ballistic selectivity, light ions show a higher radiobiological effectiveness as compared to protons (see Section 1.2.2) [9], providing the following further advantages:

- a higher effectiveness on hypoxic cells [3], which are usually dominant in the central part of a tumour;

- a reduction in the intrinsic radiosensitivity among the various cell populations (desirable in the treatment of well differentiated tumours) and in the dependence of the biological response on the position of the cells in the mitotic cycle[4] (desirable for slowly growing tumours);

- less repair of sub-lethal damage by the irradiated cells, with subsequent reduced dependence of the biological response on the dose fractionation scheme.

3 Cells deprived of adequate oxygen concentration because of an insufficient blood supply to the tumour.
4 During development from stem to fully differentiated, cells in the body alternately divide (mitosis) and 'appear' to be resting (interphase). This sequence of activities exhibited by cells is called the cell cycle. Interphase is actually a period of diverse activities indispensable in making the next mitosis possible.

1.2.1 Physical properties

In order to reach depths of more than 25 cm in the human body, necessary to treat deep-seated tumours, proton and carbon beams must have an initial energy not lower than 200 MeV and 400 MeV/u, respectively. For eye melanomas, as for the treatment of macular degenerations, protons of energies in the range 60 - 70 MeV are sufficient, whilst all the clinical needs with carbon ions in terms of penetration in tissue, field, size and dose rate, can be satisfied by energies in the 120 - 400 MeV/u range. This is represented in Figure 1.1 that shows the range-energy curves in tissues for protons and various ion species [10]. With regard to proton beams, all the clinical needs can be satisfied by energies between 60 - 70 MeV and 200 - 250 MeV[5] corresponding to ranges in tissues which go from 2.5 - 3 g/cm^2 to 25 - 38 g/cm^2.

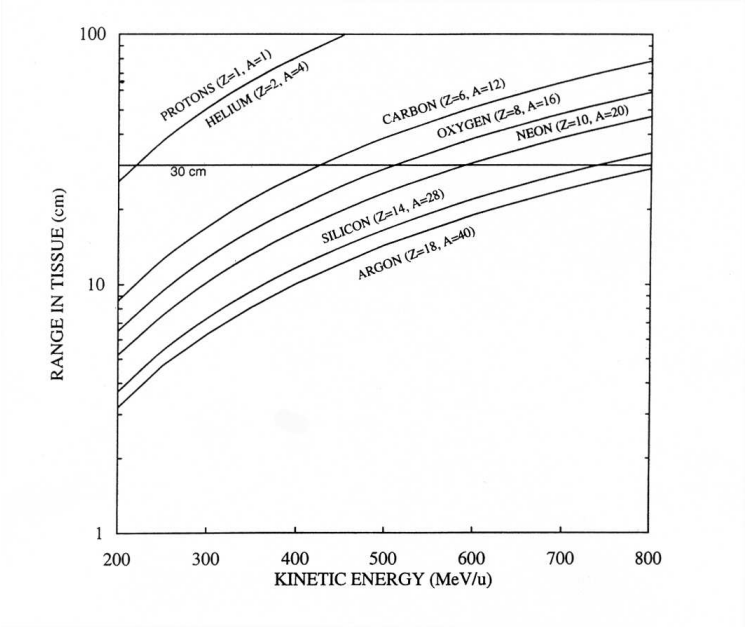

Figure 1.1: *Range-energy curves (in cm) for protons and various types of ions.*

In the therapeutic energy range charged particles lose energy primarily by ionizing and exciting electrons as they penetrate a medium. Because the energy deposited at a given depth is inversely proportional to the square of the particle's velocity, depth dose curves for protons and heavier ions exhibit a sharp peak, called Bragg peak, followed by a rapid decline in dose at the end of the particle range as shown in Figure 1.2.

Figure 1.2 shows the percentage of the absorbed dose in water at typical treatment energies, 20 MeV electron beams and photon beams produced by 8 MeV electrons, together

5 The higher 250 MeV proton beams are needed for medical imaging with proton-radiography. Proton radiography will provide an interesting alternative to conventional radiography for checking the position of the patient with better density resolution at a much lower dose.

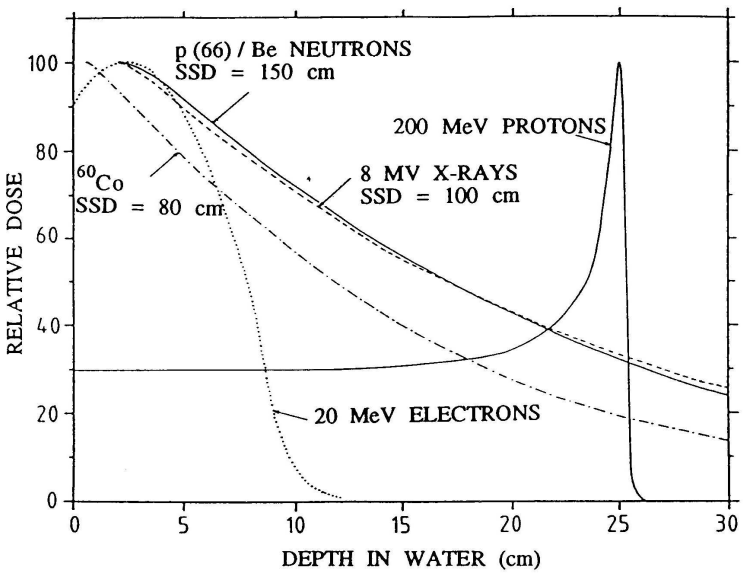

Figure 1.2: *Depth-dose curve for photons for a Co source and a 8 MV electron linear accelerator, neutrons (produced by a 66 MeV proton beam on beryllium target), 20 MeV electrons and 200 MeV protons. SSD is the source-to-skin-distance.*

with the curves representing the energy depositions in matter due to the hadron beams. Electrons and bremsstrahlung photons have the same biological effects on the irradiated cells, but the delivered doses have very different spatial distributions as shown in Figure 1.2, where electron beams are characterized by a maximum range in the tissue (depending on their initial energy) beyond which there is a low intensity tail due to bremsstrahlung photons. For this reason electron beams are suitable for the treatment of superficial or semi-deep tumours and are used in about 10% of all conventional treatments.

On the other hand, photon beams are characterized by an absorption of an exponential type, after a maximum at 2 cm for beams of 8 MeV maximum energy. This depth corresponds to the maximum range of the secondary electrons produced by the primary photons in the more superficial layers of the irradiated tissue. As a consequence of this *build-up effect*, in a high-energy x-ray irradiation the skin dose is relatively low. In spite of the roughly exponential decrease of the dose with depth, x-ray beams from a linear accelerator are suitable for an efficient treatment of even deep-seated tumour targets.

In order to irradiate selectively such targets, radiotherapists use multiple beam entry ports onto a point usually coinciding with the geometrical centre of the target. To this end, it is necessary for the whole accelerating structure of the electron linear accelerator to rotate around a horizontal axis.

Proton and light ion beams proceed through the tissue in nearly a straight line, and the tissue is ionized at the expense of the energy of the proton until the proton is stopped. The dosage is proportional to the ionization per centimeter of path, or specific ionization, and

this varies almost inversely with the energy of the proton. Thus the specific ionization or dose is many times less where the proton enters the tissue at high energy than it is in the last centimeter of the path where the ion is brought to rest.

Clinically, the most important physical property of charged hadron beams is the sharp fall-off in dose at the end of the particle range. This sharp decrease is in direct contrast to the approximately exponential decrease in dose exhibited by photon beams and allows a higher tumour dose to be delivered without exceeding the tolerance dose of the surrounding healthy tissues. The depth at which the hadron Bragg peak occurs depends on the initial energy of the projectile and its width on the energy spread of the beam.

Considering secondary effects, first, the energy loss of the proton is a statistical effect due essentially to the production of ions along its path; hence, not all protons of the same energy will stop at the same distance beneath the skin. The range straggling results in a longitudinal width in which most protons come to rest of about 1% of the initial range [1]. A second effect is due to the many small angle scatterings of the proton as it passes the nuclei of the atoms of the tissue. Multiple scattering spreads out the end of the beam transversely causing an infinitely narrow starting beam to have at the end of its range a transverse width of about 5 per cent of the initial range [1].

The beam lateral spread is reduced as the projectile mass increases. This property is well demonstrated by the spots of protons and carbon beams obtained with Polaroid photos taken at various positions in the Bragg curves [11], showing that in the Bragg peak the carbon beam is much better defined than the proton beam. From proton to helium ions, as shown in Figure 1.3, the lateral scattering is reduced by a factor of two and a further decrease is observed with carbon ions [11].

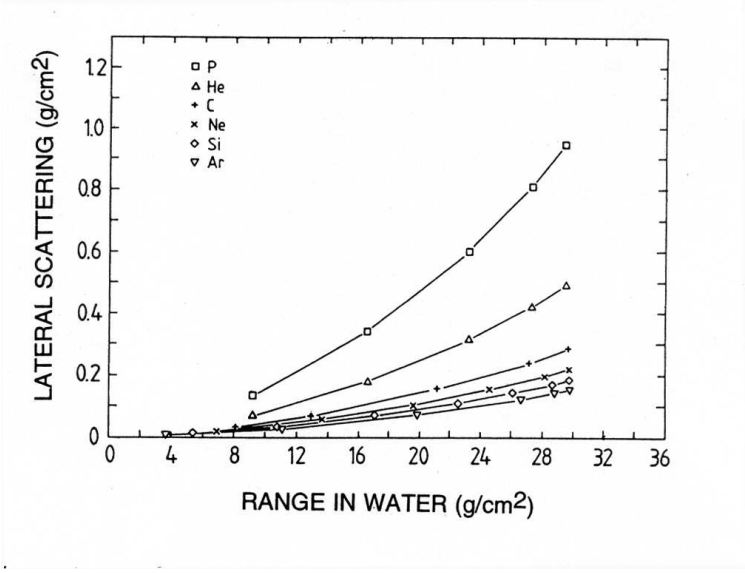

Figure 1.3: *Lateral scattering as a function of the range in water for different ions.*

By varying the energy during the irradiation in a well controlled manner it is possible superimpose many narrow Bragg peaks and obtain a so called *spread out Bragg peak*, necessary to deliver a uniform dose to an extended tumour volume, even if at the expense of an increased dose to the entrance as shown in Figure 1.4 [11].

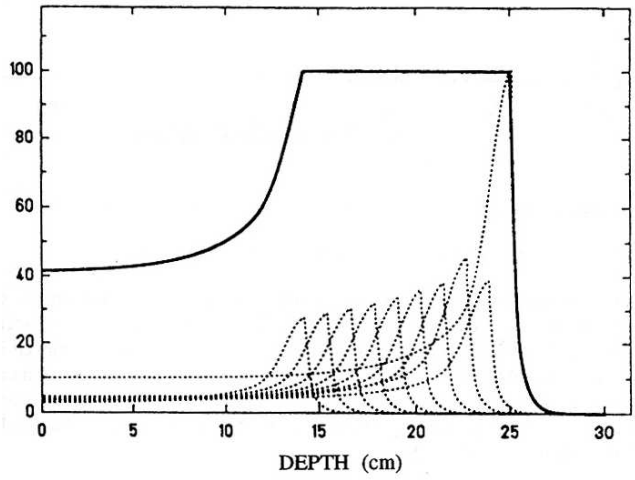

Figure 1.4: *A Spread Out Bragg Peak (SOBP) is obtained as a superposition of many peaks by varying the ion energy.*

For protons (light ions) the surface dose in practice never exceeds about 70% (50%) of the dose in the SOBP when the SOBP is 8 cm wide. This is a fundamental difference with respect to the dose distribution due to photon beams, which has its maximum at only 2-3 cm from the surface, as shown in Figure 1.2.

In Figure 1.5, that illustrates the SOBP for different ion species, the tail of the curve for light ions after the Bragg peak is due to the fragmentation of the impinging nuclei. The lighter fragments have a longer range in matter than the parent ions and give rise to an increase of the absorbed dose beyond the peak. The percentage increase of the dose in this region strongly depends on the mass of the ion: it is of the order of 15% of the dose in the SOBP for ions like carbon and oxygen, whilst it can reach 30% in the case of neon ions. This is the reason why it is not justified, as mentioned above, to use ions heavier than oxygen for a really conformal therapy.

The dose distributions in depth for protons and ions reproduced in Figure 1.5 justify the statement that, by choosing appropriate treatment techniques, both protons and ions can be used to realize very accurate conformal therapies. To this end not only the energy but also the lateral distribution of the beam has to be carefully controlled. The best way of delivering a conformal dose to a tumour is thus to change, during the treatment, at the same time the energy of the beam and, with magnets placed upstream, its direction. These sophisticated active spreading systems, discussed in Section 1.3, are at present coming into function in the main centres.

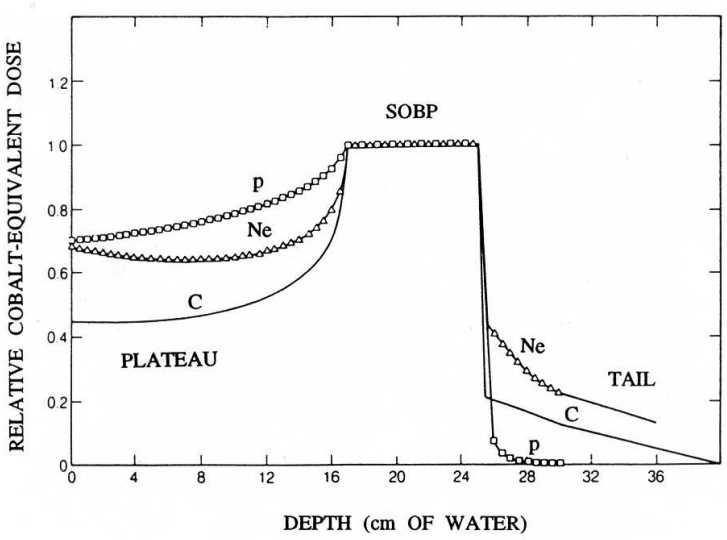

Figure 1.5: *SOBP for ion beams.*

Simpler methods of spreading the beam laterally have been common until now (Section 1.3). They make use of a scattering material placed upstream - which diffuses the protons - and of a collimator placed close to the part to be irradiated. These passive spreading systems are very effective and have been employed for most of the patients treated until now with hadrons, but in the longer term they will be substituted by active systems.

In conclusion, the use of charged hadrons combined with the modern diagnostic and dose measurement and delivery techniques allows conformal treatments both of tumours located near the skin and of deep-seated tumours. In this way it is possible, in comparison to conventional radiotherapy, either to increase the dose to the tumour for an equal dose to the surrounding healthy tissues, or to reduce the dose to the healthy tissues, while keeping the same dose to the tumour.

1.2.2 Biological properties

In radiobiology, particle beams are often characterized by the linear energy transfer (LET) distribution. The LET[6] of a particle is the average energy locally imparted to a medium by a charged particle of specified energy, per unit distance traversed. LET is an important quantity because the amount of radiation damage incurred by a cell depends on the number of ionizing events produced by the radiation in vicinity of the cell DNA.

6 The Linear Energy Transfer is defined as the ratio between the energy ΔE deposited by a charged particle in a very short track element, and its length Δx. In formula $L_\infty = \Delta E/\Delta x$, where the index ∞ indicates that there is no limitation on the amount of energy ΔE released in any single collision of the particle with an atom or a molecule of the treated medium. Physicists call L_∞ the *unrestricted energy loss* or the *unrestricted stopping power*.

Radiation damage along a particle track is caused by direct mechanism in which DNA molecules are ionized by the particle and by indirect mechanism in which free radicals produced by the ionizing particle react with the DNA. Because cells contain more than 70% water, most of the energy transferred by an ionizing particle goes into producing free radicals. The oxygen content is generally low in the scarcely vascularized tumorous tissues (which are often found at the centre of a slowly growing tumour) and the biological effects-mediated by the OH^- and H^+ highly reactive free radicals usually decrease when the oxygen content reduces.

Particles with LET values smaller than 30 - 50 $keV/\mu m$ are called low LET particles whereas those with larger LET values are categorized as high LET particles [12]. High LET particles are more biologically damaging because they cause more directly and indirectly ionizing events per unit track length. When a beam of high-LET particles traverses a cell, it leaves a very dense pathway of ionization; that dense pathway causes much disruption in both normal cells and tumor cells, and overwhelms the cells' natural capability to repair the damage.

Low-LET particles, on the other hand, leave a sparsely ionizing pathway, which results in sparse ionization; the cell is left sufficiently intact to repair itself. As the damage to cells increases, the cells' repair ability decreases. The high local deposition of energy at the microscopic level with consequent more frequent double strand break of the DNA of the hit cell is represented in Figure 1.6.

Figure 1.6 shows qualitatively how the detailed spatial structure of energy deposition calculated for various particles compares with the structure of biological relevant targets, such as chromatin, nucleosomes and DNA. It appears that ions have a much larger probability of producing clusters of breaks in both strands of the cellular DNA, while such a phenomenon is negligible in the case of low LET radiations. Moreover DNA, the biologically meaningful target for radiations, has nanometre dimensions. Thus nanodosimetry will be needed to understand the effect of the energy depositions due to ionizing radiation and their fluctuations.

The radiobiological rationale for high-LET radiotherapy is threefold [13]:

- cells cannot repair the more extensive damage incurred by high-LET radiation as easily as they can low-LET radiation damage;
- tumour cells are often hypoxic. Such cells are more responsive to high-LET than to low-LET radiation. This difference in response is due in part to the reduced production of oxidizing radicals under hypoxic condition for low-LET radiation;
- for low-LET radiation, cells exhibit varying degrees of radio-responsiveness depending on whether they are actively dividing. High-LET particles may be advantageous in treating slowly growing tumour with a significant fraction of cells in the resting phase [14].

Radiobiologist use various quantities to describe the radio-responsiveness of cells. The oxygen-enhancement-ratio (OER) is the ratio of the dose required to achieve a given bio-

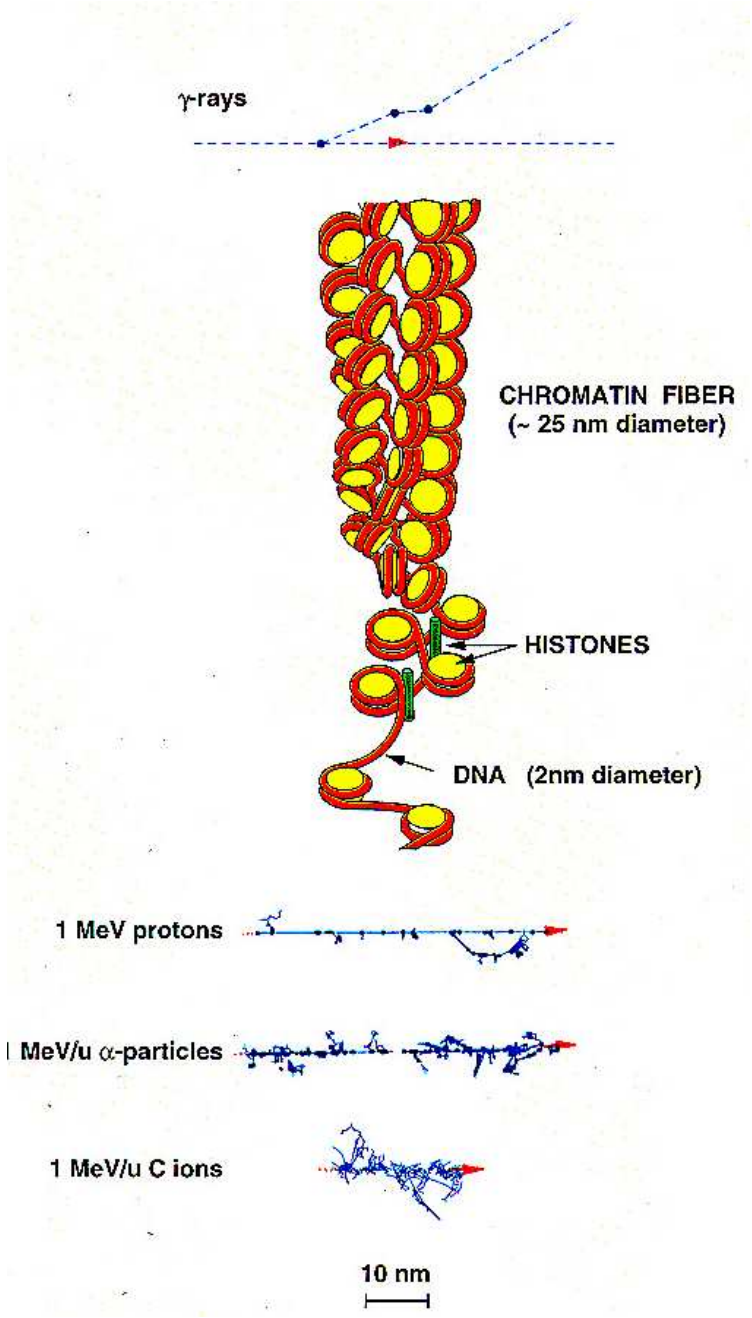

Figure 1.6: *Schematic representation of tracks of sparsely and densely ionizing radiation compared with the relevant biological targets.*

logical effect under hypoxic conditions to the dose required to achieve the same effect under oxygenated conditions[7]. The OER for high-LET radiation is typically between 1 and 2 and for low-LET radiation is between 2 and 3.

Another way to characterize a given type of radiation is the relative biological effectiveness (RBE) that represents the ratio of the dose required to achieve a defined biological result using some radiation standard to the dose required to achieve the same result using test radiation, typically x-rays. Since the first studies, it has become clear that the RBE depends on the LET value and on the effect under study. RBE for tumour cell inactivation is the most important parameter in view of the use of charged hadrons for tumour sterilization. There is now experimental evidence that the enhancement of the RBE of densely ionizing radiation is related to energy depositions at the nanometer scale, i.e. at the sub-cellular level.

The RBE is highest at the distal end of the spread-out Bragg peak, where the LET is the largest. To deliver an uniform effective dose to the tumour volume with light ion beams, the treatment plan must compensate for the variation in RBE across the spread-out Bragg peak to keep the effective dose constant. The ratio between RBE around the Bragg peak and that in the entrance plateau region (or, equivalently, the corresponding cell killing ratio at the same dose) is a significant factor determining how much the traversed tissue could be spared.

The RBE dependency on LET is shown in Figure 1.7. Data are collected *in vitro* with many cell lines globally summarized as a band based on the results from nine cellular systems [15–17]. The LET ranges available with protons, carbon and neon ions at energies of interest in radiobiology and radiotherapy are indicated in the figure.

The horizontal bars in Figure 1.7 give the LET range of three nuclei stopping in water. The left end corresponds to particles which stop after 25 cm. The right end corresponds to particles almost at rest. It is clear that high-LET radiations are more effective than electrons and photons in damaging the hit cell, by a factor that can be as large as three at the 10% survival level, but is even lower than one at extremely high values of the LET. These in vitro studies indicate that carbon is close to the optimum: it has RBE next to 1 in the entrance channel and large RBE at the end of its range, i.e. at the target.

Due to the much larger proportion of direct effects, charged ions are suited for clinical situations where the radio resistance linked to hypoxemia represents a problem difficult to overcome both by conventional radiations and by protons. Although these properties of ions were already known qualitatively in the fifties, the first clinical study on neon beams was undertaken only in 1975 at the San Francisco Medical Center and the Lawrence Berkeley Laboratory (LBL) in California [18]. This work was seminal but, a posteriori, was done with a non-optimal ion.

Only in the nineties, radiobiologists and radiotherapists reached the conclusion that the optimum has to be found around Z = 6, which defined the carbon ion. There are two reasons

7 In formula the definition is OER = D/D_0, where D is the dose needed to produce the effect in the actual tissue and D_0 is the dose which would be needed if the tissue were fully oxygenized in an air atmosphere under normal pressure.

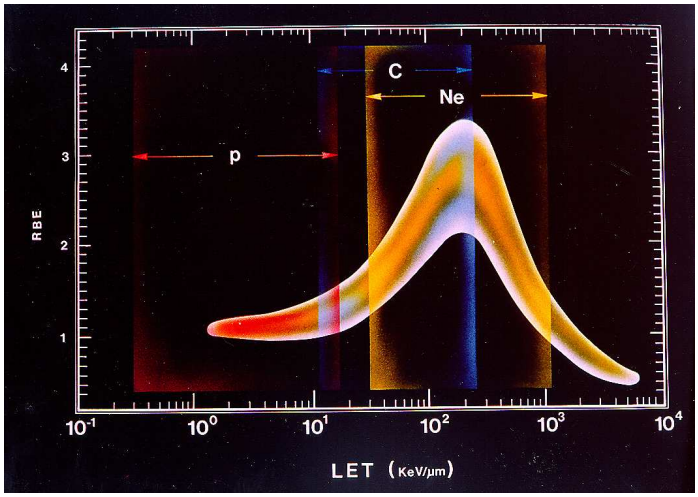

Figure 1.7: *Summary of the experimental data on the LET-dependence of the Relative Biological Effectiveness at 10% survival levels. The LET ranges available with protons, carbon and neon ions at energies of interest in radiobiology and radiotherapy are indicated in the figure.*

for this. First, because for neon ($Z^2 = 100$), already in the first layers of tissue the LET value is more than 20 keV/μm, and is therefore too high and can produce dangerous retarded effects. The second reason is that, when traversing matter, ions fragment into smaller ions which, because they have a longer range, go beyond the Bragg peak of the parent ions and produce a *tail*, as shown in Figure 1.5. This effect makes the Bragg peak far less pronounced in comparison to that due to protons, thus deteriorating the conformal properties of the irradiation and carbon ions are preferred to heavier ions because they fragment less than heavier nuclei.

In conventional radiotherapy, the total dose is usually delivered over the course of several weeks. The amount of dose delivered in each treatment is called fraction size. In a typical proton treatment each session delivers 2 - 2.5 Gy to the tumour, while giving less than 1 - 1.2 Gy to any of the organ at risk. The treatment lasts about 30 session, usually spread over 6 weeks, with a total dose to the target of 60 - 75 Gy.

Successful implementation of high-LET radiotherapy requires an understanding of the complicated dependency of RBE on fraction size, total treatment time and absolute dose, as well on the type of tissue irradiated and on the position on the depth-dose curve at which the RBE is evaluated.

For high-LET particles, due to the inability of cells to repair high-LET radiation damage, a smaller dose per fraction does not help protect healthy normal tissues as is the case for proton therapy. By increasing the dose delivered per fraction with high-LET radiotherapy, the overall treatment time can be shortened to two or three weeks, minimizing the probability of tumour proliferation during the course of the treatment [14].

1.3 Dose delivery and treatment quality

To fully exploit the sharp fall-off in dose of the Bragg peak, an accurate three dimensions description of the tumour in relation to critical organs of the patient is needed. Computer axial tomography (CT) provides the detailed anatomical information together with tissue density data. Magnetic resonance imaging (MRI) is also frequently used to identify the tumour volume. Positron Emission Tomography (PET) scans are used to help identify tumor tissue by the behavior of its cells, sometimes in cases where the tumor tissue is not visible on CT scans or MRI. Conventional radiation sources usually irradiate deep tumors with energy that is being deposited after the point of their peak energy deposition; this deposition falls off exponentially as the beam continues through the patient, as shown in Figure 1.2.

Multiple portals are used to add up the various lesser, post-peak doses so that in the treatment volume the additive dose is higher than that received by normal tissue at any one point. Photon treatment plans are designed to build up the dose within the target while still keeping the normal-tissue dose low enough to minimize damage.

Radiotherapists using rotating linacs to treat patients with electron and photon beams (see Figure 1.8) would like to have the same possibility when using hadron beams. This is accomplished with a mechanical/magnetic structure, named gantry, that moves the terminal part of a beam transfer line to vary the incidence direction of the beam on the patient, as in conventional radiotherapy. In this way the conformation of the dose distribution to the tumour volume (especially for tumours having a complex shape) can be optimized and, consequently, the dose delivered to the surrounding healthy tissues reduced.

Figure 1.9 represents the eccentric gantry implemented at PSI (Paul Scherrer Institut, Villigen), where also the patient bed is moved during the treatment. An isocentric gantry (see Figure 1.10 for that implemented at the NPCT, Northeast Proton Therapy Center, Boston) is a large rotating mechanical structure which rotates around a horizontal axis and rigidly supports the needed bending magnets and quadrupoles without the need of moving the patient bed.

The magnetic rigidity of 200 MeV protons is such, that the magnetic channel capable of doing so has a typical radius of 5 m. For this reason fixed (mainly horizontal) proton beams have been used worldwide till 1992, when the first hospital-based center became operational at the Loma Linda Medical Centre (Los Angeles). Since then the new facilities have usually one or more gantries.

Protons and light ions deposit most of their energy in the Bragg peak, that is in volumes of the order of a cubic centimetre or smaller; therefore it is necessary to spread the beam over the entire target volume and produce a homogeneous dose distribution. The more usual technique to exploit the Bragg-peak behavior is the passive spreading, which uses a specially designed double scatterer to spread the beam by multiple Coulomb scattering uniformly over a large area that is sufficient to treat the whole tumour, or a large part of it [19]. In this approach proton beams are treated similarly to photon beams in conventional radiotherapy. By treating the tumor in layers, defined by the depth of the Bragg peak, and applying

Figure 1.8: *Modern linear accelerators for photon and electron treatments rotate around the patient to directed the beam to the target from any direction.*

Figure 1.9: *The PSI eccentric rotating gantry.*

Figure 1.10: *The NPCT isocentric rotating gantry: mechanical support (a) and treatment room equipment (b).*

collimators and shaped absorbers, as schematically illustrated in Figure 1.11, a high degree of conformal treatment can be achieved.

Moreover a spread-out beam is well-suited to large tumours in parts of the body that are difficult to immobilize. For example, the treatment can be synchronized with patient breathing and, since always the whole tumour volume is covered, there is no problem of dose uniformity within a moving tumour.

With a passive dose delivery system, the beam intensity is essentially not determined by the target volume but by the field size. The highest intensity is required when treating the distal layer of the tumour volume, and rapidly decreases when *pulling back* the Bragg peak to treat the other layers, because these have already received part of the dose during the irradiation of the deepest layers. However, scatterers, ridge filters, range modulators, collimators, compensating *boli*[8] and multileaf collimators have the disadvantage of reducing the duty factor and the quality of the beam because of nuclear interactions between the proton beam and the beam shaping devices with consequent material activation. This results not only in a deterioration of the dose profile and in a change in the biological response, but in the drawback of manufacturing patient-specific hardware and its activation during the irradiation raising radioprotection issues.

8 In a passive beam spreading system a bolus is a custom-made block positioned on the extracted beam path just before the patient. The contours and thickness of the block conform the beam to the shape of the far edge of the target (Figure 1.11).

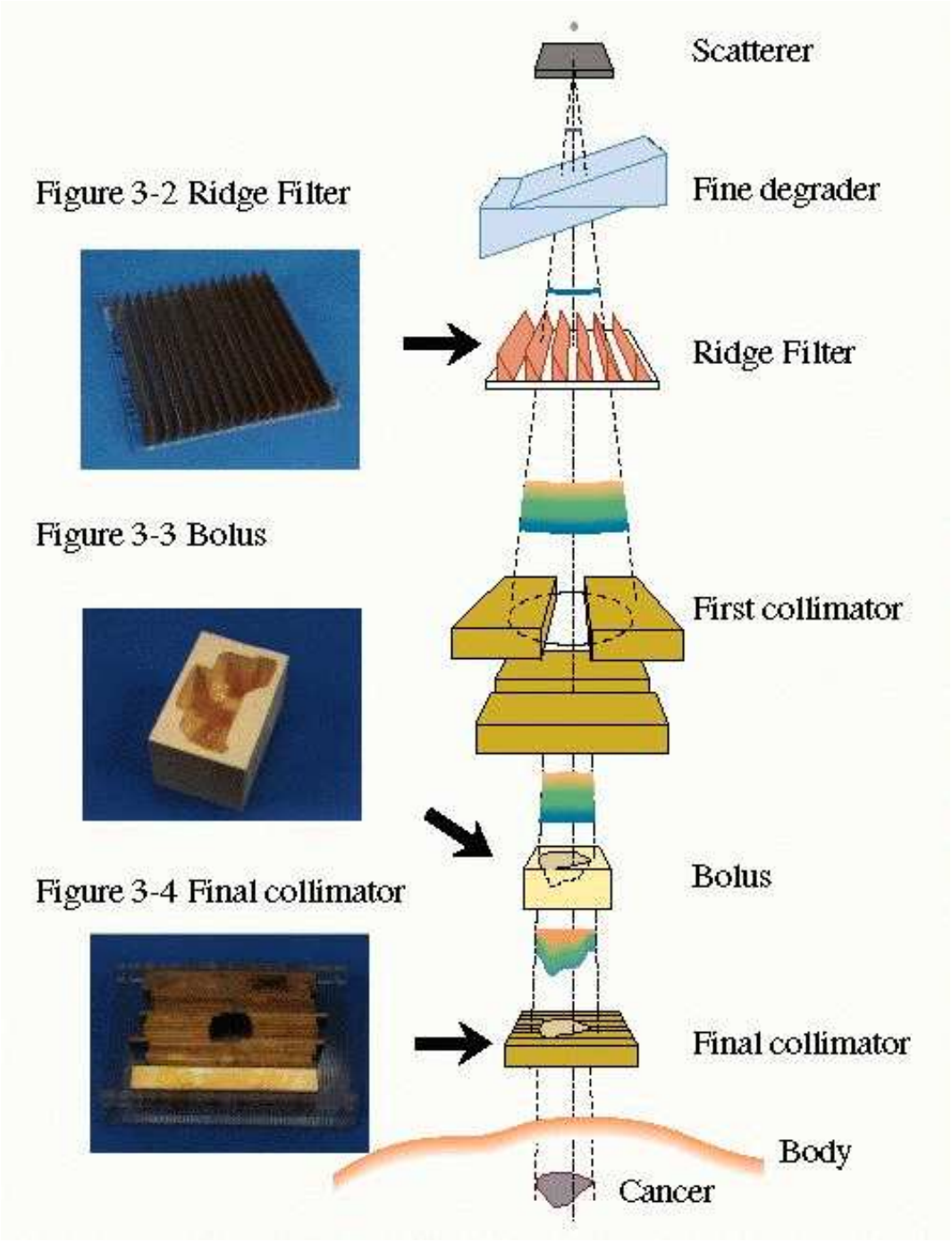

Figure 1.11: *Dose conformation with a passive beam spreading device.*

The second technique, which is of primary interest in the new hadrontherapy centres, is active scanning which uses a *pencil* beam to *paint* the tumour in three-dimensional space with sub-millimeter accuracy as represented in Figures 1.12 and 1.13. When scanning, the tumour is treated in a series of slices at decreasing ranges. Once a slice has been *painted* by the magnetically steered *pencil* beam, the energy is lowered to reduce the depth of the Bragg peak and *painting* is repeated on the next slice. While treating the distal slice (deepest) part of the dose is delivered to the proximal slice (closer to the surface) and the beam intensity should be reduced consequently.

A magnetic scanning system consists essentially of two dipoles producing two magnetic fields perpendicular to the trajectory of the charged particles: by changing these two fields and the energy of the beam it is possible to achieve an accurate distribution of the particles within the target boundaries and a full 3-D conformal therapy. Active beam delivery was developed and first used at PSI in 1997 in the form of *voxel scanning* [19, 20], commonly referred to as 'volume pixels' and at GSI(Darmstadt) [21] in the form of *raster scanning*.

In the case of *voxel scanning* the dose is delivered to volume elements, voxels, with the beam turned off after the irradiation of each voxel. In the case of *raster scanning* the beam is scanned continuously across a slice at a given depth and the dose delivery is controlled by the scanning speed and/or by the intensity of the extracted beam (i.e. the higher the speed and/or the lower the intensity, the lower the dose).

With both passive and active beam spreading systems Bragg peak modulation is achieved by varying the extraction energy from the synchrotron in discrete steps, but the latter technique is mandatory with light ions in order to avoid the fragmentation processes.

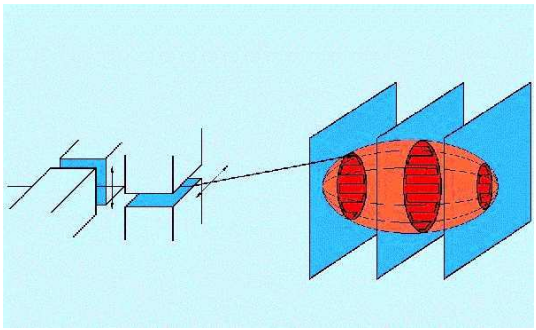

Figure 1.12: *Sketch of the active scanning system with on the left the vertical and horizontal scanning magnets and, on the right, the tumour volume (in red) divided in slices at different depths in the patient (in blue).*

To benefit fully from the active scanning techniques, it is necessary to achieve smooth extracted beams (spills) through slow extraction scheme and to design precise optics for beam delivery system [22].

To this aim a crucial role is that played by beam instrumentation that provides all the necessary information on the extracted beam characteristics and the signals to correct and/or

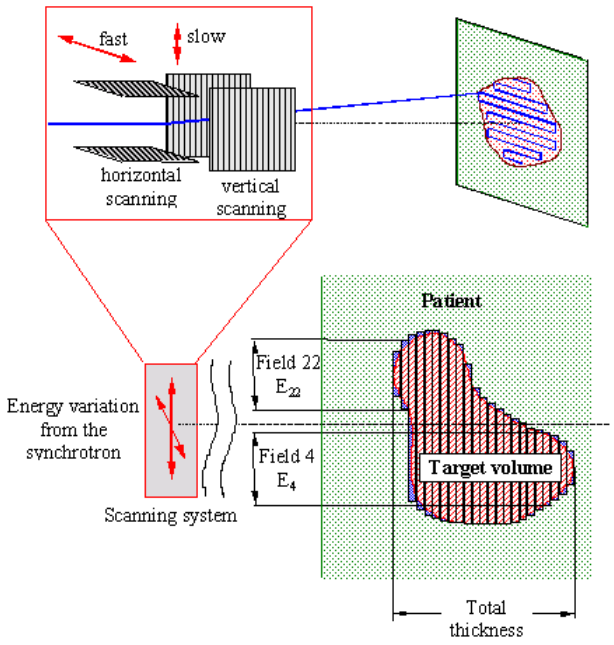

Figure 1.13: *Sketch of the active scanning system assuming that the tumour is treated in 22 longitudinal slices at decreasing beam ranges.*

abort the beam in case of problems, as discussed in details in Section 2.2. The development of a novel, non-disruptive beam monitor for the real-time measurement of the profile and intensity of the beam for therapy is the object of this doctoral thesis.

1.4 Clinical results and perspectives

In the developed countries about half of all cancer patients are irradiated in conventional radiotherapy facilities either with x-rays or, ten times less frequently, with electrons [23, 24]. Every 10 million people there are about 20 000 new patients/year. In the most advanced centres new conformal and intensity modulated techniques allow the delivery of larger doses to most tumour targets without undue increase of the doses absorbed by the adjacent organs at risk.

Hadrontherapy with proton and carbon ion beams is rapidly developing since the beginning of the nineties. For protontherapy cyclotrons are widely used together with synchrotrons, which are the only practical accelerators for bringing carbon ions to the 400 MeV/u needed for the therapy of deep-seated tumours, as detailed in Section 2.1. This development is due to cost reductions and to the increased reliability of the facilities, but also to the fact that the expense and the technological effort needed to build a medically-dedicated proton and ion accelerator were not justified when doctors could not localize the target tissues with

an accuracy equal to that of the irradiation itself.

In fact, the potential advantage offered by the superior physical selectivity intrinsic in a heavy-charged particle beam can be translated into a real improvement of the clinical results only if combined with a suitable physical extrinsic selectivity, achievable by means of accurate techniques of tumour definition and irradiation modalities of high level. The exceptional improvement, in the last fifteen years, of the conventional imaging modalities (in particular CT, MRI and PET) and of all the devices aiming at a conformal irradiation justifies the recent developments in conformal x-ray radiotherapy and has given a substantial boost to the diffusion of hadrontherapy.

Since Wilson first proposed using charged hadrons for tumour radiotherapy, more than 46 412 patients have been treated worldwide, 40 801 with protons and 4 511 with ions (numbers taken from the January 2005 Particles issue[9] [25]).

Hadrons have biological and/or physical characteristics that enable them to be used to treat malignant tumours and other lesion that either do not respond well to conventional photon radiotherapy or are located close to critical structures, which limit the dose that may be delivered safely. The high LET and limited lateral scattering of light ions provide a biological advantage, whereas Bragg peak of protons and light ions allows the dose distribution to be conformed closely to the tumour volume. Protons have been proven effective in treating early stage (rapidly growing and oxygenated) tumours close to critical structures. Light ions has proven effective for slow growing, hypoxic tumour close to critical structures.

The number of potential patients for protontherapy have been determined in many studies with quite different results. At the European level Gademan concludes that the percentage of all patients at present treated with conventional radiations who would profit from protontherapy is in the range of 30-40% [26]. Italian radiotherapists have published a general review of all the results obtained worldwide with protontherapy [27] and conclude that about 10% of the persons treated with x-rays have a tumour or a lesion which could benefit from a treatment with a proton beam [28]. For 1% of these patients the treatment with protons is the elective cure. American studies give a percentage which exceeds the Italian figures and is close to the 30-40% estimated by Gademan.

These figures indicate that different medical doctors have different opinions on the number of potential patients. Taking into account the present trend in the development of new protocols and being at the same time very conservative, protontherapy is a cure to be preferred to photons in at least 3% of the present radiotherapy patients, corresponding to about 600 patients per 10 million inhabitants.

Since a hospital based centre with three treatment rooms can irradiate about 1000-1200 patients/year, it can be safely concluded that there is the need for a centre every about 20 millions inhabitants. As far as the number of potential patients of carbon ion therapy is concerned, deep-seated tumours have to be considered, which are radioresistant both to

9 PTCOG, established in 1985, is an informal but dedicated international group of physicists, physicians and other scientists, who work together to realize delivery systems and facilities for charged-particle radiation therapy. Particles, PTCOG's newsletter (see http://ptcog.mgh.harvard.edu/), contains information about the current activities of the organization, summarizes the total numbers of patients treated by protons and ion beams at facilities around the world, and lists facilities that are being built or planned.

photons and to protons. These are at least 10% of all the tumours treated with photons [29], corresponding to 2000 patients/year per 10 millions inhabitants. The indications partially overlap with the ones of protontherapy and not all radioresistant tumour can be irradiated. The study performed for the GSI proposal concludes with an overall fraction of about 5% [30]. According to this figure, Europe should certainly have more than one carbon ion centre, even if the development of clinical protocols is in its infancy since only 2000 patients have been irradiated up to present in Japan and Germany.

In conclusion, great hopes are placed in the unique properties of hadrons to control radioresistant tumours through the microscopic distribution of the delivered dose. This justifies the construction of new hospital-based centres where relatively large number of patients can be irradiated with the best available techniques, in particular with the active spreading systems, described in Section 1.3.

1.5 Status of the Centro Nazionale di Adroterapia Oncologica

The Centro Nazionale di Adroterapia Oncologica (CNAO) will be the first Italian centre for treatment of deep seated tumours with hadron beams. CNAO is at present under construction in the north of Italy (Pavia) and is scheduled to treat the first patient at the end of 2007.

The origin of the Italian hadrontherapy centre dates back to 1991, when the first proposal was made [31]. CNAO is based on an evolution of the PIMMS project described in details in Section 2.1 and consists of a synchrotron capable of accelerating carbon ions up to kinetic energies of 400 MeV/u and protons up to 250 MeV [32].

Figure 1.14 shows the layout of the CNAO lattice with the injection chain, the synchrotron, the transfer lines and fixed beam delivery stations (3 horizontal, 1 vertical). Patients will initially be treated with protons and carbon ions (in the figure separate ion sources indicates different type of particle beam), but the possibility to add other species is left open.

Hadrons are injected in the synchrotron from the inside, to better exploit the space and the two non-dispersive synchrotron regions, at kinetic energies of 7 MeV/u. Multi-turn injection is foreseen to relax the requirements on the source intensity. After injection, the beam is scraped to the nominal emittance and then accelerated in the synchrotron to the required extraction energy in less than one second.

The CNAO synchrotron is made by two symmetric achromatic arcs joined by two dispersion free straight sections. The dispersion free sections host the injection/extraction region, the resonance driving sextupole and the accelerating RF cavity. The total bending of 360° has been divided in 16 identical dipoles powered in series. The focusing action is provided by 24 quadrupoles grouped in three families, while the chromaticities are controlled by four sextupoles grouped in two families. A fifth sextupole is used for resonance excitation. The total length of the synchrotron ring is approximately 78 m.

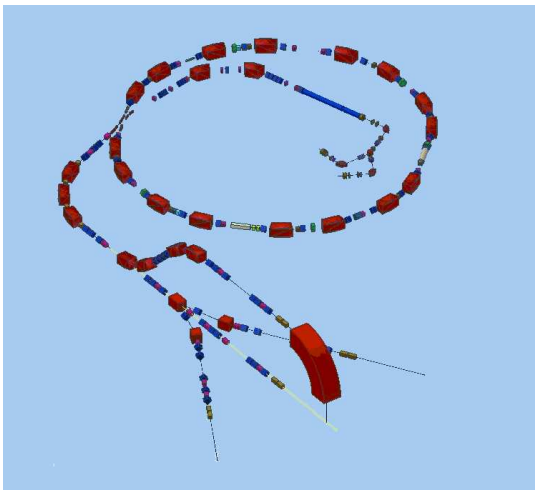

Figure 1.14: *CNAO accelerator complex layout.*

The beam is slowly extracted via a betatron core magnet that smoothly drives the particles into the extraction resonance. The extracted beam is then delivered to the tumour via a totally active beam spreading system. As a future upgrade the centre will be expanded with two additional rooms equipped with isocentric gantries to assure the best available techniques to the patients.

The CNAO will be built in a 37000 m^2 area donated by the Town of Pavia. The site is next to the highway, to the university and to three hospitals. The contract for the construction of the buildings has been signed at the beginning of 2005. At present (September 2005) the foundations have been digged and geological and ground consolidation tests are being made. Figure 1.15 shows the status of the site at the end of August 2005.

Figure 1.15: *The CNAO site at the end of August 2005. Jet-grouting techniques are adopted to realize the foundations of the building.*

Chapter 2

Beam instrumentation for the extraction lines of a hadrontherapy complex

An accelerator designed for hospital use must meet a number of requirements substantially different from those of a machine for the research environment. Energy span, beam intensity and all other beam parameters must be optimized for clinical use. Reliability, flexibility, safety and simplicity of operation from the user's point of view represent the basic aspects against which the choice of the accelerator system should be balanced, along with the investment and running costs.

The clinical specifications and the consequent physical specifications for the beam are similar in all the existing and planned facilities. Therapeutic beams can be produced with linacs, cyclotrons and synchrotrons, but when carbon ions are also to be accelerated, the synchrotron is the only practical choice. To reach a depth of 27 cm, carbon ions have to be accelerated to a total energy of 4800 MeV (400 MeV/u) that makes cyclotrons and linacs unsuitable.

The first design of a dedicated carbon ion synchrotron was the European Light Ion Medical Accelerator (EULIMA) study [33, 34], a cooperative European effort to compare a cyclotron solution with a synchrotron choice.

The accelerator design and beam parameters used for the development of the innovative beam monitor described in this thesis are those of the Proton-Ion Medical Machine Study (PIMMS) [22]. The PIMMS was set up at the PS-Division in CERN in 1996 following an agreement between TERA, MED-AUSTRON, CERN and GSI. The aim of the study was to investigate and design a synchrotron-based medical facility that would allow the direct clinical comparison of protons and ions for cancer treatment. The study lasted four years and resulted in a green-field conceptual design, with a particular attention to the theoretical aspects.

The machine was designed primarily for high-precision active beam scanning for both protons and carbon ions, capable of delivering proton beams by passive scattering. The main beam specifications agreed for PIMMS are resumed in Section 2.1. One of the clinical specifications most crucial for the accelerator design is the uniformity of dose that has to be distributed over the treatment volume with a maximum tolerable error of $\pm 2.5\%$.

This implies that the dose has to be carefully measured during irradiation and that the flux of particles at the patient has to be low enough to allow such an accurate measurement. This calls for a slow extraction and for a very constant spill to avoid overdose due to fluctuations.

Passive beam delivery systems are less prone to fluctuations but, on the other hand, as discussed in Section 1.3, require patient-specific hardware and the dose conformation is less accurate. With active scanning, the large number of voxels needed to cover the whole tumour means a short time per voxel and imposes very tight limits on the spill uniformity. In this respect, besides the beam dosimetry, the beam diagnostics system plays a major role, as detailed in Section 2.2, and has to be fully integrated with the control and safety systems of the entire facility[1].

This role is particularly crucial for the instrumentation in the extraction lines where the beam measured is the same of therapy. Patient safety, accelerator operation, and optimum dose delivery would all benefit if the extracted beam intensity and profile could be continuously monitored during treatment, rather than just during the set-up.

This has not been previously possible, since existing interceptive monitors interfere with the beam, causing a non-negligible beam scattering or a beam disruption for the therapeutic kinetic beam energies. However, available non-interceptive instrumentation is not sensitive enough to detect average beam intensities from few pA to few nA (see Section 2.1).

To overcome this limitation a novel non-interceptive monitor, named **S**econdary emission monitor for **L**ow **I**nterception **M**onitoring (SLIM) [35–38], capable of providing beam intensity and profile measurement during the treatment without degrading the hadron beam, has been proposed and is described in Section 2.3. It is based on the detection of secondary electrons emitted from a submicron thick Al_2O_3/Al foil intercepting the beam at 45° degrees.

The device has been developed and tested in the framework of the **S**ilicon **U**ltra fast **C**ameras for electrons and gamma sources **I**n **M**edical **A**pplication (SUCIMA) project [39] funded by the European Commission under the contract G1RD-CT-2001-00561 with the primary goal of developing a real-time dosimeter based on direct detection of secondary electrons in a silicon substrate.

A commercial system and two solid-state detectors (named pad or pixel detector, according to the cells/sensor size) have been used as imaging devices of the SLIM secondary electrons accelerated to a final electron energy in the 10 - 30 keV range by an electrostatic

1 With beam dosimetry system it is meant the set of interceptive monitors, as ionization chambers and multi-wire chambers, that measure according to international standards the beam dose, position and profile in air, just before the patient. Their effect on the beam for therapy is well quantified and considered in the treatment plan simulations. The beam diagnostics system is the set of monitors along the beamline (inside or just outside) to measure the beam main parameters for the most efficient and safest operation of the accelerator complex.

focusing system and are described in Section 2.4. Section 2.4.1 summarizes the main feature of the commercial system consisting of a MCP (microchannel plate) coupled to a phosphor screen viewed with a CCD camera (charged coupled device).

The hybrid solution, based on a pad silicon sensor read-out by low noise charge integrating ASICs (Application Specific Integrated Circuits), has been engineered in the framework of the SUCIMA project and is described in Section 2.4.2. While the CMOS dedicated monolithic active pixel detector, called MIMOTERA, has been designed and developed in the framework of the SUCIMA project and is described in Section 2.4.3.

An overview of the dedicated data acquisition system, also developed in the SUCIMA framework and used for the tests with both the pad and CMOS sensors, is illustrated in Section 2.5.

2.1 Accelerator complex for hadrontherapy

The exploitation of the Bragg-peak behavior can take many forms, relying on different types of accelerators, different modes of operation and different particles. In all cases, it is necessary to measure and to control the dose delivered to the patient. The measurement and the control of the beam require time in which to operate and this imposes the need for a quasi-continuous beam with, what is in accelerator terms, a low intensity. Quasi-continuous, low intensity hadron beams in the hadrontherapy energy ranges can be provided by synchrotrons using a slow-extraction scheme, cyclotrons and linacs. The latter is included for completeness, but in comparison with synchrotrons and cyclotrons, are too expensive for this application.

Cyclotrons can produce high-intensity, large-emittance beams, whereas synchrotrons tend to produce lower intensities in smaller emittances. When using only protons, the cyclotron has a clear advantage in size, cost, commercial availability and simplicity of operation. However, for ions and dual species machines, cyclotron would become very heavy and probably more expensive than a synchrotron.

Although a synchrotron is larger the empty space inside the magnet ring can be used for power supplies. In addition, the size of the accelerator becomes relative when compared to the space needed for the therapy rooms. The use of superconducting cyclotrons has also been discussed, especially in the EULIMA project, but was given up because of the extended repair times of several days in case of an accelerator failure. It must be kept in mind that patients have to be treated daily for 20 to 30 fractions (single treatments), as detailed in Section 1.2.2. The closing of an accelerator for many days would be intolerable.

Moreover, in general it is difficult to change the energy of a cyclotron whereas a synchrotron can change the energy on a pulse to pulse basis. Thus the cyclotron is well suited to passive proton beam delivery systems in which the energy is adjusted to the required depth by absorbers and the beam is spread over the irradiation field by scatterers also considering that these techniques entail large beam losses (approximately 70%) cyclotron can easily accept.

The synchrotron is better suited to active beam delivery systems in which the energy is

adjusted by the accelerator and a small pencil beam is scanned conformally over the tumour. This method is capable of a sub-millimetre precision in three-dimensional space, for complex tumour shapes. The patient specific aspects are entirely contained within the software of the treatment plan. However, the above implies that there should be little or no tumour movement during the treatment since different parts of the tumour are irradiated at different times.

Active scanning also requires a continuous on-line measurement of the dose, delivered to each elementary volume (voxel) of the tumour. The time needed to measure and control the beam is the reason for using a resonant slow extraction scheme from the synchrotron. The third-integer resonance extends the beam extraction time sufficiently to perform on-line dosimetry at the patient and to switch the beam on and off according to the dose required. The uniformity of the extracted beam intensity (spill uniformity), and the achieved dose distribution, depend critically on the method of extraction, on the lattice design and the stability of the power converters.

The performance parameters are defined by the clinical needs and are similar in all the existing and planned synchrotron-based facilities. In the case of the PIMMS study the maximum energy of the machine is set to 400 MeV/nucleon for carbon ions with a synchrotron circumference of 75 m and 250 MeV for protons. The beam intensities and repetition rates have been adjusted so as to deliver a single treatment, or fraction, in about two minutes. For active scanning, it is assumed that a nominal fraction corresponds to 2 Gray in 2 litres (or equivalent combination) delivered by 60 extractions in 2 minutes. For passive scanning, it is assumed that a nominal fraction corresponds to 2 Gray in 7.5 litres (or equivalent combination) delivered by 120 extractions in 2.5 minutes.

Ideally, machine operation would be *ramp and hold* with a minimum cycle rate of about 0.5 Hz. This allows synchronization with breathing if required. Some 60 spills of maximum $4 \cdot 10^8$ carbon ions each, or 60 spills of maximum 10^{10} protons each would comprise a single treatment (known as a *fraction*) with a minimum treatment time of 2 min.

While with passive spreading the beam intensity is almost constant during the patient treatment, all the instrumentation should cope with the intensity variation required by the active scanning techniques [22]. When scanning, the tumour is treated in a series of slices at decreasing ranges as explained in Section 1.3. Once a slice has been *painted* by the magnetically steered *pencil* beam, the energy is lowered to reduce the depth of the Bragg peak and *painting* is repeated on the next slice. As part of the dose is delivered to the proximal slices while treating the distal slice, the beam intensity should be reducible up to a factor 100.

This results in a extracted particle beam intensity ranging from $\approx 5 \cdot 10^{-12}$ (carbon beams) to $\approx 15 \cdot 10^{-9}$ A (proton beams for passive techniques) with the constraint on beam instrumentation and dosimetry to work in the whole intensity range. The beam spot should be variable between 4 and 10 mm full-width at half-height and have a positional stability and precision of a few tenths of a millimetre.

The main beam specifications agreed for PIMMS based on the clinical need are summa-

rized in Table 2.1.

Table 2.1: *PIMMS main performance parameters.*

	Active scanning	**Passive Scanning**
Extraction energies for carbon ions	120 - 400 MeV/u	-
Extraction energies for protons	60 - 220 MeV/u	60 - 250 MeV/u
Nominal treatments	2 min[a]	2.5 min[b]
Nominal dose delivered	2 Gray in 2 litre	2 Gray in 7.5 litre
Max n.° of p/spill at patient	10^{10}	$2 \cdot 10^{10}$
Max n.° of C-ions/spill at patient	$4 \cdot 10^{8}$	
Spot sizes (all energies)[c]	4 - 10 mm	4 - 10 mm

[a] 60 spills of 1 s + 1 s to ramp up and down
[b] 120 spills of 0.25 s + 1 s to ramp up and down
[c] full width half-height

2.1.1 Extracted beam specification

The dose has to be distributed over the treatment volume with a maximum tolerable error of $\pm 2.5\%$, as required by the clinicians. A detailed knowledge of the extracted beam (spill) is essential in order to obtain the quality that is required for high-precision active scanning. The momentum spread and emittance of the spill must be well understood to ensure a reproducible spot size and to correctly adapt the focusing and apertures in the transfer lines and gantries under all conditions. The transverse distribution of particles within the spill affects the dose calculations and the way in which the beam spot is scanned. The uniformity of the spill is the most important aspect of all as the better the spill quality, the faster and more accurate the scan becomes.

Fortunately, the scanning system itself is tolerant to high-frequency fluctuations and can be made to correct on-line for low-frequency fluctuations. Should the spill irregularities overwhelm the capabilities of the system for compensation, then an alarm message must be issued and the beam be switched off. This implies that the dose has to be carefully measured during irradiation and that the flux of particles at the patient has to be low enough to allow such an accurate measurement.

This can be understood looking at Figures 2.1 and 2.2 that represent the GSI extracted beam measured with the dosimetry ionization chamber in 30 μs bins and a record of a treatment, respectively. In the background of Figure 2.2 are shown the slices in which the tumour is longitudinally divided (in green the slices already *painted*) and in the foreground the slice under treatment with the distinct positions of the beam centre over the tumour slice under treatment.

As clearly visible in Figure 2.1, the spill is strongly modulated and without a fast measurement and control systems this would result in locally over- or under-dosing of the tumour

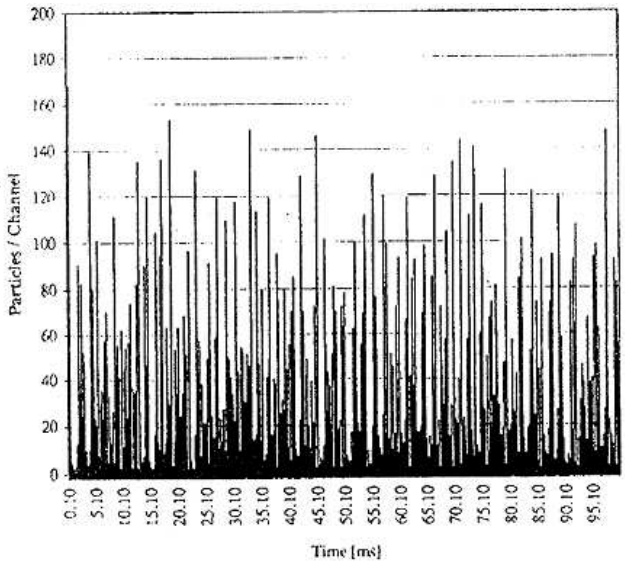

Figure 2.1: *Slow extracted spill measured with a 30 μs bins ionization chamber (courtesy of GSI).*

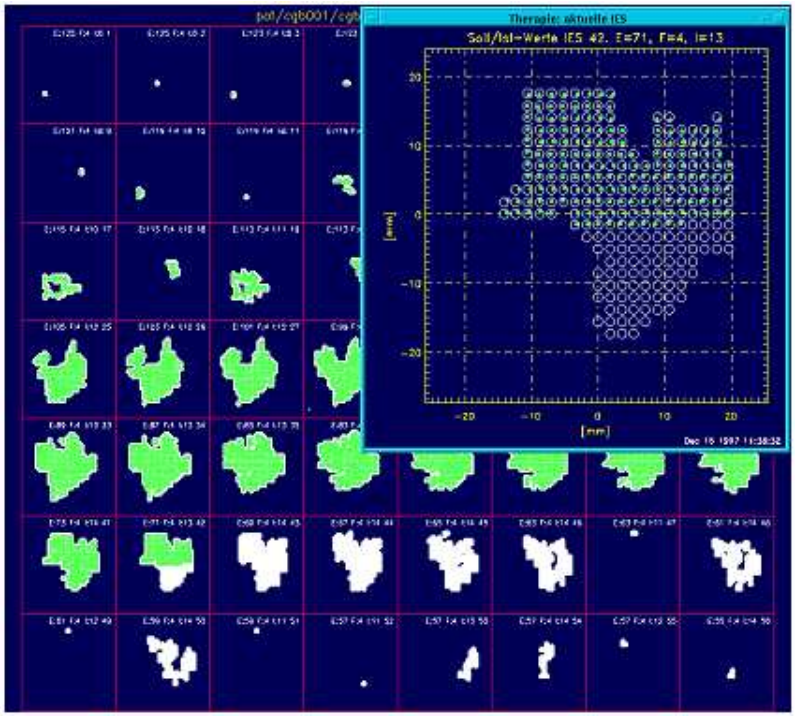

Figure 2.2: *Tumour treatment record with the tumor slices already* painted *in green and the positions of the centre of the beam in the enlarged picture of the slice under treatment (courtesy of GSI).*

(the so-called *hot and cold spots* in correspondence of the different beam positions shown in Figure 2.2).

The requirement on overall uniformity (precision) of the treatment plan of $\pm$ 2.5% in the PIMMS study is implemented by tailoring the spill intensity and the dwell time for each voxel so that with nominal parameters the slightly better target precision of $\pm$ 2% is obtained. The spill intensity is varied by injecting more or less current in the machine and a finer adjustment is obtained by varying the extracted beam intensity [40]. However, the ultimate adjustment must be made by the scanning system itself that relies on the beam information provided by the dosimetry system, as described in Section 2.2.

2.2 Extraction lines beam instrumentation

The beam dosimetry and diagnostic systems of a hospital based hadrontherapy complex have a crucial role in the efficient and correct operation of the beam lines and to guarantee the maximum safety to the patient. With dosimetry system it is meant the set of beam monitors in air, just before the patient, that provide the information (dose, beam intensity, profile, position) to start, control and stop the treatment [41]. With active scanning of the tumour the dosimetry system provides the information to control the speed of the bending magnets and to act in case of problems with either a feedback system or a fast beam abort.

The PIMMS on-line dosimetry is based on a certain number of measurement bins of the extracted beam in a nominal *dwell* time over any given point in the tumour. For voxel scanning the nominal time to fill a voxel is 5 ms, which is consistent with 50 bins at a sampling frequency of 10 kHz. An error of one bin then corresponds to the nominal 2% specification for precision in dose uniformity with the maximum variation in the beam charge to be expected in one bin from 0 to 200% of the nominal value (i.e. 100% spill modulation). The order to switch-off the beam is given once the dose exceeds 98% of the desired dose with a delay time assumed assumed to be 1 measurement bin of 100 μs. In this way the final integrated dose can then rise to a maximum of 102% or, alternatively, be just 98%, i.e within the precision required by the clinicians.

Requirements on the instrumentation for beam dosimetry, calibrated according to international standards, are more stringent than those of extraction lines beam monitors. Nevertheless it is fundamental to have a performant beamline instrumentation to counter check the beam dosimetry measurements and to understand the causes of eventual problems in the acceleration chain that prevent the treatment and act quickly to solve them.

The basic guideline behind the choice of the diagnostic system for a hospital-based accelerator complex is to be reliable and easy to manufacture and operate. While the beam parameters in the injection line and in the synchrotron are similar to those of many existing accelerators and make possible the use of standard instrumentation, the situation is more delicate for the extraction lines monitors. Due to the very low beam intensities, the instrumentation used in the extraction lines of the existing facilities is interceptive. As any *standard* monitor (thickness exceeding a few μm) put on the path of the beam is strongly

perturbative at the kinetic energies of Table 2.1 [42], the instrumentation in the extraction lines is used to set the lines and then removed while treating the patient.

During irradiation, beam intensity, position and shape at the end of the extraction lines are nowadays determined only via the dosimetry system and the treatment control and the safety procedures rely exclusively on these measurements.

The standard instrumentation normally used in the extraction lines of existing hadrontherapy centers includes the following monitor [42]:

- Scintillation screens imaged with CCD cameras [43] (see Figure 2.3). CsI(Tl) is the most convenient material for the screens in the extraction lines, as its measured sensitivity for minimum ionizing protons is of the order of 10^5 protons/mm^2·s corresponding to the minimum estimated beam density in the extraction lines at the monitor position. This number can be improved using image intensifiers as reported for profile measurements in the LEAR transfer lines [44]. CsI(Tl) screens can cope with a 10^4 range in beam flux density (a factor 10^3 due to different beam fluctuations, and a factor 10 for differences in the same Gaussian beam from the central peak to the two edges). Scintillation screens are easy to build and their spatial resolution can reach 0.05 mm [45]. They are rather fast (decay time $\lesssim 1\mu$ s) and can therefore be used for time structure analysis. Moreover, applications at SLAC (Stanford Linear Accelerator Center) showed that they can survive proton fluxes of more than 10^{18} protons/mm^2 [46]. The main drawback of screens is that, due to their thickness ($\approx$ 1 mm), they cause a significant beam blow-up and, depending on the beam energy, only a limited number of screens can be used simultaneously.

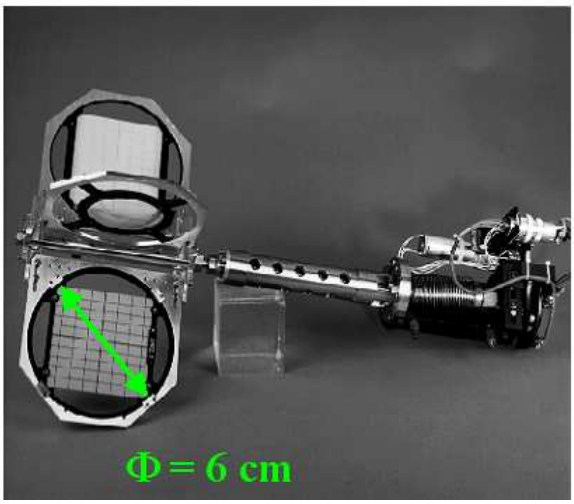

Figure 2.3: *Examples of scintillation screens mounted on an actuator for in-beam positioning.*

- Multi-Wire Proportional Chambers (MWPC) [47] are the most popular solution in the extraction lines of medical complexes as Loma Linda [48] and HIMAC, Heavy Ion

Medical Accelerator in Chiba (Japan) [49, 50]. This is mainly due to the fact that these monitors have been widely used in particle physics since more than 30 years and work properly in the intensity range of interest. At HIMAC, for example, MWPCs were tested with a 70 to 800 MeV proton beam and worked well in the intensity range 10^6 - 10^{11} pps (protons per second) [51]. Their major drawback is that they are complicated to be manufactured and to be operated (gas filling, high voltages), they are also beam disruptive and they do not reach the scintillation screens spatial resolution (their limit is of the order of 0.5 mm). A typical MWPC is shown in Figure 2.4.

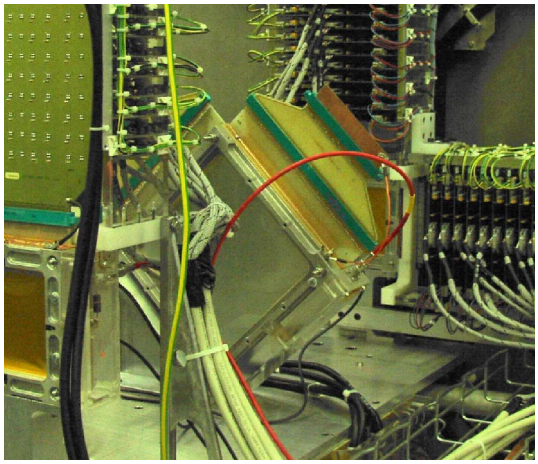

Figure 2.4: *A typical MWPC.*

- SEM (Secondary Emission Monitor) Grids [52] (see Figure 2.5). When a beam crosses a foil or a wire, a few percent of low energy electrons, with respect to the incoming particles, are emitted from the surface layers. This charge depletion is proportional to the local density of the beam and can be used to measure a beam density profile. The main limitations of these monitors are their resolution, limited by the finite number and dimension of the strips, and the overall gain spread from channel to channel. Moreover the small signal (DC) generated under a very high source impedance, and the collection of unwanted parasitic charges are making their use difficult. At GSI (Darmstadt, Germany) it was estimated that a minimum charge of 0.1 nA in 5 ms is required per wire with a typical low-noise grid electronics [52]. Considering an optimistic secondary emission efficiency of 10% and a factor 10 between the beam peak and edge intensities, this integration time would be prohibitively long with the lower intensities of the PIMMS extracted beams.

By the time of the PIMMS design, a conservative choice for the position and profile measurement with interceptive, disruptive monitors in the extraction lines was made. Considered the positive experience at CERN [43], the monitors chosen for the position and profile measurement in the extraction lines of PIMMS were the scintillation screens with completely

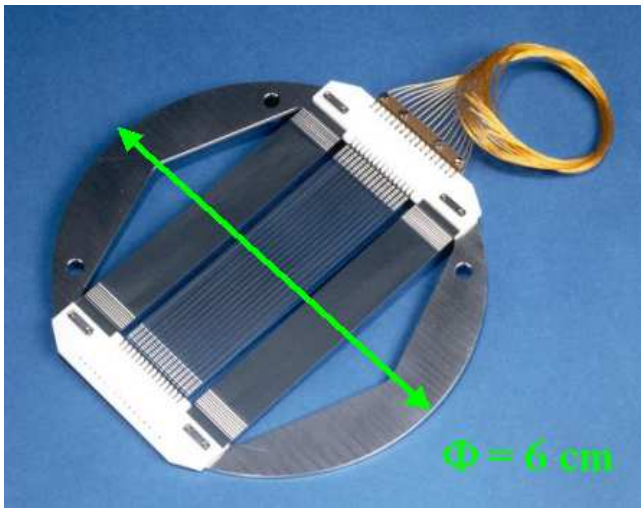

Figure 2.5: *A typical SEM.*

destructive Faraday cups for the beam intensity measurement. To guarantee the maximum safety level during the treatment, the veto-counter (or *watchdogs*) monitors were included in the extraction lines diagnostic system.

Watchdogs have been tested in the GSI medical line [53] as a nearly non-destructive method to determine the beam centre of mass, width and intensity. They consist of four stepping motor driven scintillator paddles (two horizontal and two vertical) that detect 0.1 - 1 % of the particles from the beam halo. These devices are located where the beam should not be and alert the control system every time the beam moves beyond a fixed region. In this way they make possible the control of the beam during the treatment of the patient, even if the absence of signals from a watchdog does not necessarily mean that everything is working as it should.

It is clear, then, that the possibility of monitoring the beam during the treatment (on-line), independently from the dosimetry system, is strongly envisageable, as it makes possible an efficient operation of the accelerator complex and guarantees the maximum safety to the patient. The alternative to the existing extraction lines devices is the innovative non-disruptive real-time beam monitor, object of this doctoral thesis, described in Section 2.3.

2.3 SLIM, a novel extraction lines beam monitor for hadrontherapy

A novel real-time monitor, named **S**econdary emission monitor for **L**ow **I**nterception **M**onitoring (SLIM), for the extraction lines of a hadrontherapy centre was developed in the framework of the SUCIMA project. SLIM is based on the detection of the secondary electrons emerging from a thin aluminium foil crossed by the primary beam for the treatment.

Such a system admits multiple measurements on the same beam, providing the maximum information on the beam for therapy for the correction of its parameters or a fast dump if serious problems are detected. Moreover, it crosschecks the dosimetry system, maximizing the safety conditions.

2.3.1 SLIM working principle

The operation of the beam monitor is based on secondary electron emission. A thin metallic foil set at an angle to the beam serves both as a source of secondary electrons (SE) and as an electrode of an electrostatic focusing system (FS) with electric field lines from the foil surface that guide the emitted electrons to a position sensitive detector beyond the beam volume. A schematic layout of the beam monitor is shown in Figure 2.6, that also illustrates the working principle.

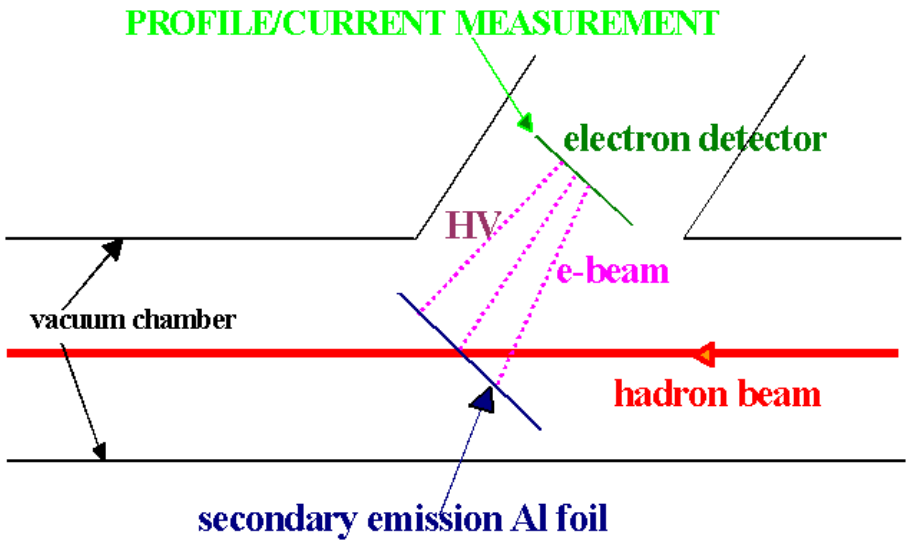

Figure 2.6: *Schematics of the SLIM (Secondary electron emission for Low Interception Monitoring) beam monitor working principle (HV = high voltage).*

The thin foils are produced following a technique consolidated at CERN [54] and consist of a support of 0.1 - 0.3 μm of Al_2O_3 coated on each side with 0.01 - 0.05 μm of Al for a maximum diameter of about 65 - 70 mm (see Section 4.3). As secondary emission is a surface phenomenon, it concerns just the most superficial aluminium layers. The energy lost by the hadrons in the foil is transferred to the electrons of the medium. Those that receive a sufficient impulse to escape from the foil surface can be classified into high energy electrons (δ-rays) and electrons with a kinetic energy below 50 eV, conventionally called secondary electrons (SE). The last are the predominant component in the spectrum of the escaping

electrons (see Section 3.1) and are, therefore, the most important for this application.

The field of the electrostatic lenses accelerates the secondary electrons and focuses them on the detector with the final electron energy in the range 10 to 30 keV, as described in details in Section 3.2. The optics for the collection of the SE, the type, size and pitch of the electron detector, the front-end electronics an the read-out system have been designed on the base of the key requirements on the performances of the SLIM beam monitor summarized in Section 2.3.2.

The secondary electrons final energy of about 20 keV requires no dead layer in the sensor volume. This is actually one of the most stringent requirements on the dedicated CMOS monolithic detector development since a *back-thinning* of the devices down to the ≈ 10 μm level has to be foreseen. On the other hand, such low energy electrons are completely stopped in the silicon first micrometers (20 keV electrons' range in silicon is ≈ 2 μm) and, in a back-illuminated sensor, the front-end circuitry is not expected to be affected by the high flux of ionizing radiation, thus loosening the radiation hardness requirements.

Previous attempts to use the secondary emission from thin foils as a mean to measure the main extracted beam parameters can be found in [55–58]. The devices illustrated in [55] and [56] concern only beam intensity measurements (no information on beam profile), while the detectors illustrated in [57] and [58] do not fulfill the hadrontherapy requirements either in terms of beam acceptance (70 mm), or in terms of spatial (1 mm) and time resolution (100 μs).

2.3.2 SLIM beam monitor requirements

As explained in Section 2.2, the requirements on the extraction lines beam monitors, as the SLIM, are less stringent than those on the dosimetry system. Nevertheless, beam monitor with comparable speed and precision in the measurement of beam parameters, allow the most efficient and secure operation of the accelerator for therapy.

It was, therefore, decided to require a sampling of the beam position at a few kHz with a precision of 1 mm; while the beam intensity is measured with a 10 kHz frame rate and a 10% accuracy (to be compared with the more stringent requirements of dose accuracy measurement better than 2% for the monitors of the dosimetry system).

Taking into account the main accelerator and beam parameters, the SLIM beam monitor must meet the following requirements:

- real-time monitor (to be used during the treatment of the patient);
- stigmatic optics (demagnifying or proximity) for the secondary collection to preserve the information on the beam profile;
- thin foil diameter $\Phi = 70$ mm (with beam on 10 x 10 mm^2);
- beam profile granularity not exceeding 1 mm;
- vacuum compliant ($10^{-6} \div 10^{-7}$ Torr).

The secondary electron detector should have a 2D active surface subdivided in cells providing picture elements (hence the name of pixel detector) and should be optimized for low energy (20 keV) β particles. The readout speed of 10 kHz and the dynamic range (up to 10^8 β particles/s·mm^2) are defined by the hadrotherapic beam intensity fluctuations, together with the requirement on the absence of any dead time. The constraints on the SE detector and related electronics can be summarized as follows:

- active surface subdivided in cells (pads or pixels);
- 5000 cells or more;
- sensitive to low-energy ($\approx$ 20 keV) electrons;
- large dynamic range ($3 \div 9{\cdot}10^3$ e^-/pixel·100 μs);
- 10 kHz frame rate to guarantee 2% dose uniformity on the tumour;
- no dead time.

Last but not least, the monitor will be installed in a hospital-based facility: it should, therefore, be easy to operate and maintain, reliable and have a limited cost.

2.4 SLIM secondary electron detectors

The SLIM beam monitor and dedicated secondary electrons imagers were developed in the SUCIMA framework. The SUCIMA project primary goal is the development of an advanced imaging technique of extended radioactive sources, based on the direct detection of the ionizing particles in a real time, monolithic silicon sensor [39]. Besides real-time, non-destructive monitoring of hadrontherapy beams, the other major applications foreseen by the SUCIMA consortium is imaging of radioactive β source for intra-vascular brachytherapy.

Brachytherapy derives from the Greek word *brachy* that means 'close, short distance' and defines a radiotherapic procedure in which the delivery of a radiation dose to a well defined target volume is obtained by the use of radioactive sources directly placed inside or in the vicinity of the region of interest [59]. Intravascular Brachytherapy for Coronary Artery Diseases is the local radiotherapy of arteries with an abnormally narrow cross section (stenosis) [60, 61]. It is usually connected to post-angioplasty stenosis [62] and it relies on high doses (8-30 Gy) and high dose rates ($\approx$ 5 Gy/minute), delivered by extended β sources emitting about one billion particles per second. The sensor developed by the SUCIMA consortium are intended to maximize the safety conditions before and during the intervention, improving quality control, both at production sites and in hospitals, and therapy itself, by the definition of a customized treatment plan.

The major SUCIMA detector characteristics as defined by the foreseen applications are summarized in Table 2.2.

Two are the main techniques that could be used for the development of this pixel sensor:

Table 2.2: *Specific requirements for the detector for brachytherapy and real time beam monitor applications. A demagnification factor 5 has been assumed for real time beam imaging.*

Requirement	**Hadrontherapy**	**Brachytherapy**
Sensitive Area	15×15 mm^2	70 ×30 mm^2
Granularity	≈ 0.200 mm	≈ 0.050 mm
Readout speed	10 000 frames/s	no special request
Dynamic range	$3 \div 9 \cdot 10^3$ e^-(20 keV)/$pixel \cdot 100$ μs	1 MIP/pixel/100 μs

- the 'hybrid pixel technique' in which the sensor and the FE (Front-End) ASICs are separate parts of the detector module and are connected by small conducting bumps applied using the *bump-bonding* technology [63] or, in the case of strip and pad sensors, by wire-bonding;
- the 'monolithic pixel technique' in which the amplifying and logic circuitry as well as the radiation detecting sensor are integrated in the same chip.

Both hybrid and monolithic approaches suffer from the complexity of the technology used. In the case of the monolithic approach, both detectors and VLSI (Very Large Scale Integration) technologies are combined in a single process, which consistently has a low processing yield. In the hybrid approach, the detector and VLSI electronics are fabricated on two different substrates and it is, in this case, the bonding procedure to be complicated and expensive [64].

The monolithic technique has been chosen by the consortium for the development of the final device (Section 2.4.3) [65], but in order to provide an early feedback from the hadrontherapy end-users, intermediate solutions have been used for the assessment tests. The optical properties of the beam monitor electrostatic lenses have been initially measured (Section 5.3) with a commercial system consisting of an image intensifier microchannel plate, coupled to a phosphor screen viewed with a standard CCD camera (Section 2.4.1) that does, nevertheless, not feature the required frame rate.

A moderate granularity, large dynamic range hybrid solution with a shallow back-plane silicon pad sensors (Section 2.4.2) read out by low noise charge integrating front-end electronics (Section 2.4.2.1) has been integrated to assess the low energy electron detection proof of principle in terms of sensitivity to beam current variations (Section 6.3).

As a successive stage before the final measurements with the dedicated MIMOTERA CMOS sensor (Section 2.4.3), profiling capability and sensitivity to low energy electrons were studied (Section 6.4) integrating a back-thinned monolithic CMOS sensor of the MIMOSA[2] family [66–68], named MIMOSA V, featuring a high granularity but limited dynamic range.

While in the case of brachytherapy, a hybrid detector based on silicon micro-strip sensors and the same integrating FE electronics used for the pad sensor has been assembled for

2 The acronym MIMOSA stands for **M**inimum **I**onizing particle **MOS** **A**ctive pixel sensor.

the feasibility study and a monolithic high granularity, radiation-tolerant detector, named SUCCESSOR5, has been developed for the final measurements.

2.4.1 The SLIM commercial detector

The commercial imager consists of a MCP (microchannel plate) to amplify the electron signal according to the primary beam intensity, coupled to a 32 mm diameter phosphor screen that convert the amplified electrons into visible light. The phosphor screen is observed with a CCD camera (charged coupled device).

The secondary electrons are accelerated onto the 32 mm sensitive diameter, single stage MCP with 12 μm channel diameter. According to the primary beam intensity they are amplified varying the MCP bias voltage, as schematically shown in Figure 2.7 (maximum gain $\approx 10^4$ for polarization voltage $V_D \approx 1000$ V) and converted into visible photons in the phosphor screen.

The chosen phosphor is a P47 for its conversion efficiency (10^{16} photons/Joule deposited) and its fast decay time (persistence decay time to 10%: 80 ns) with 410 nm peak emission.

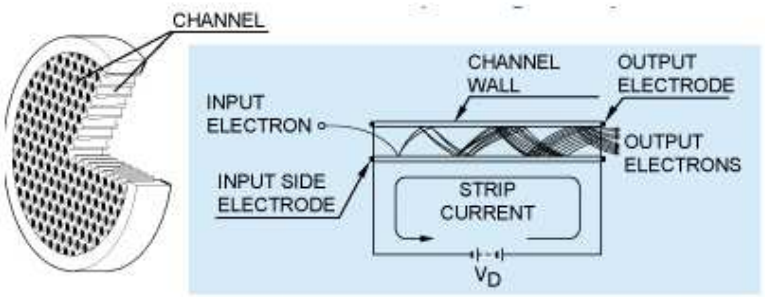

Figure 2.7: *Schematic construction and operating principle of MCP.*

The phosphor screen is observed through a glass view-port with a CCD camera mounted outside the vacuum chamber, as detailed in Chapter 4. The CCD is a black & white camera with a sensor of 752 x 582 pixels and 20 ms frame rate. The camera maximum spectral response is at 550 nm and the sensor saturates for uniform illumination of 2 lux. Due to the vacuum chamber/focusing system geometry the CCD was used with a lens of 25 mm length, as detailed in Chapter 5. The camera video signal is either directly displayed on a video monitor or digitized with a frame grabber (Section 4.5). Commercial equipment technical

details on the are described in Appendix C.

2.4.2 The pad sensor

The pad silicon sensor [69, 70] has been developed for the detection of single photons in a Hybrid Photo Diode (HPD). A HPD consists of a vacuum tube, capped with a transparent front window and a photocathode deposited by vacuum evaporation on the window inner side as shown in Figures 2.8 and 2.9.

Photoelectrons emitted from the photocathode are accelerated toward the silicon sensor by a fountain shaped electric field as shown in Figure 2.9 to $\approx$ 20 keV final energy in analogy with the electrostatic focusing system of the SLIM beam monitor. In the HPD design, the field configuration is such that a 2.3 fold demagnified image of the photocathode is produced on the silicon sensor.

The pad sensor used for the SLIM beam monitor tests has been produced with standard planar technology. It has 484 pads of 1.4 x 1.4 mm^2 for a total sensitive area of 30.8 x 30.8 mm^2. Each pad is routed to external bonding pads for connection with front-end chips on top of 5 μm thick polymide; each row of double bonds on the four sides of the sensor has 128 bonding pads with 50 μm pitch. Pads are p^+ implants DC-coupled to metal 1 connected to metal 2 routing lines through 40 x 40 μm^2 vias. Routing lines are 20 μm wide and 3 μm thick to minimize capacitance. The total load capacitance per pad is 4 pF with a very low leakage current of 10 pA per pad and a guard ring current of about 30 nA.

In a Hybrid Photo Diode (HPD) the low noise analog electronics is integrated inside the vacuum envelope and the multiplexed signals are readout through 40 vacuum feedthroughs on the baseplate. In the case of the SLIM beam monitor the sensor and the ASICs (Section 2.4.2.1) are mounted on a ceramic fixed at the final electrode of the focusing system and the signal readout through a 50-pin vacuum feedtrough.

As the pad detector was primarily developed for low energy electron detector in a Hybrid Photodiode, it was expected to be sensitive to the secondary electrons emitted by the target of the beam monitor and accelerated to 20 keV for a practical range in Si of $\approx$ 2 μm. But it had not been previously tested with integrating front-end chips that are expected to cover the dynamic range of interest, roughly corresponding to a maximum value of 10^4 fC mm^{-2} in a 100 μs integration time window.

2.4.2.1 The readout ASICs for the pad sensor

The only chip on the market having a dynamic range suitable for the beam monitor application, being essentially dead-timeless due to an architecture with twin alternating sample and hold circuits, featuring 128 channels/chip at proper pitch and the required dynamic range, is the VASCM2 ASICs [71] produced by IDEas[3] in AMS 0.8 μm CMOS, double metal technology.

3 Veritasevien 9, Box 315, N-1323, Hovik, Norway. http://www.ideas.no

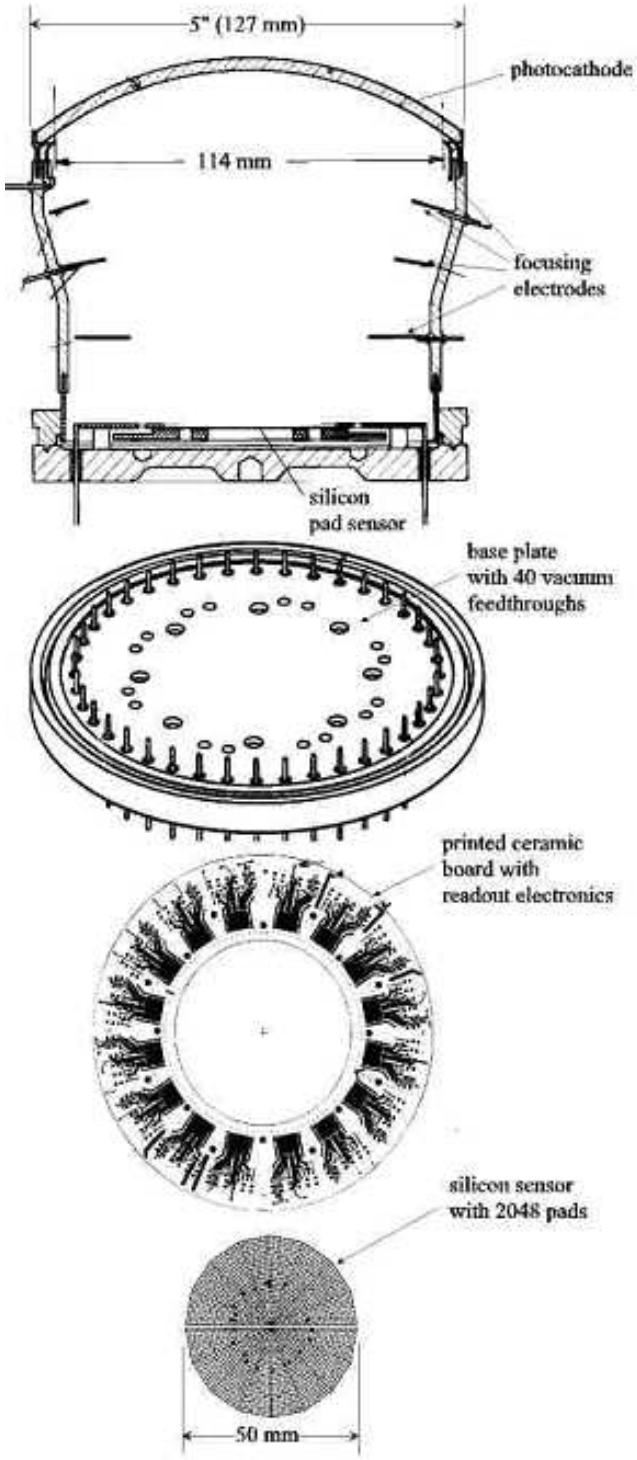

Figure 2.8: *Exploded view of the pad HPD.*

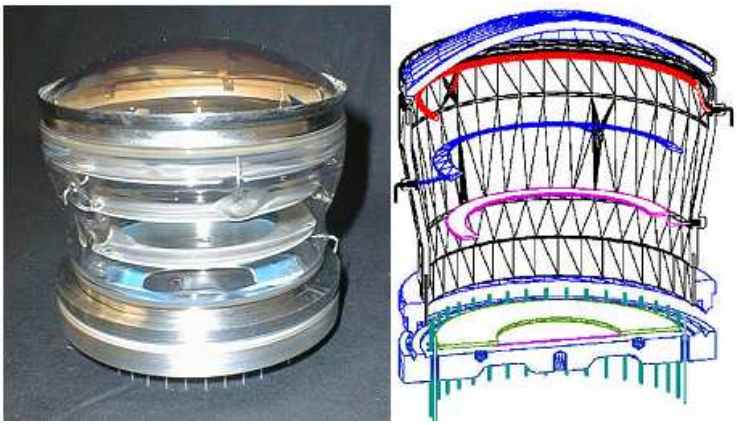

Figure 2.9: *A sealed HPD with full readout electronics and bialkali photocathode (left) and a schematic representation of the vacuum envelope with the electrodes for electrons focusing on the silicon sensor on the lower end of the tube (right).*

Two evaluation boards, integrating a single bare chip and a single chip connected to a baby silicon detector were used to perform the first qualification, assessing the basic functionalities, measuring the gains against the nominal values and defining the protocol for the tests during the assembly. The ASICs were fully qualified after the system integration.

Each pad sensor is readout by four ASIC, each consisting of 128 low noise[4], current integrating, channels that work in parallel. The power dissipation is of the order of 100 mW in operating conditions and $\leq$ 5 mW when the ASIC is in standby mode. The schematic of the VASCM2 single channel is represented in Figure 2.10.

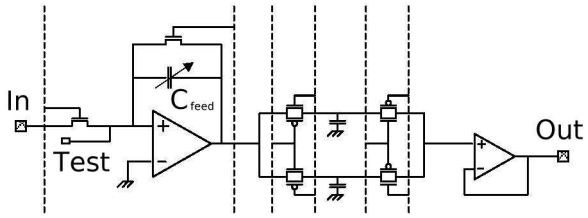

Figure 2.10: *Schematic model of one channel of the current integrating VASCM2. The main elements are the charge sensitive preamplifier with a tunable feedback capacitor (corresponding to different gain values) and the twin S&H addressed alternatively by a digital signal to the output stage.*

The current flowing into each amplifier is integrated during an adjustable integration time and the voltage output, without any shaping, is directly sensed by one of the two parallel Sample & Hold circuits, storing the signal while the twin memory is being readout.

4 The noise is equal to 2 bits on a 14 bit digitalization scale, with ≈10 pF load capacitance.

The VASCM2 architecture reduces the dead time to the amplifier reset width and allows a continuous signal tracking. Moreover, it implements four different gains that are listed in Table 2.3 together with the corresponding dynamic ranges and feedback capacitor values.

Table 2.3: *Values of the four different gains available with the VASCM2. For each gain the dynamic range and the value of the feedback capacitor are also listed.*

Gain value [μV/fC]	**Dynamic Range [fC]**	**Feedback Capacitor [pF]**
36	$\pm\ 4.2 \cdot 10^4$	28
125	$\pm\ 1.2 \cdot 10^4$	8
$1.25 \cdot 10^3$	$\pm\ 1.2 \cdot 10^3$	0.8
$3.7 \cdot 10^3$	$\pm\ 4.1 \cdot 10^2$	0.27

The ASIC can be calibrated using an external pulse. An enable gate can be switched to disconnect the preamplifier input from the sensor and to allow a specific calibration pulse to enter the preamplifier via the Test input line (see Figure 2.10).

2.4.3 The CMOS imager

CMOS technology [72] is nowadays leading the way in microprocessors, memories and ASICs development. In this technology, both n-type and p-type transistors are used to implement logic functions and the main advantage is the much smaller power dissipation allowing a larger integration scale [72].

In CMOS monolithic pixel sensors the detector part is integrated on the low-resistivity silicon epitaxial layer that is the standard substrate for the technology [73]. They have been proposed and used as an attractive alternative to CCDs in visible imaging since the early '90s, but their practical implementation has been made possible by the continuous development of microelectronics, where the minimum size feature over the past decade shrunk from 5 to 0.25 μm and below.

Their use for charged particle detection has been recently demonstrated [67]. Two main types of CMOS sensors exist: the PPS (Passive Pixel Sensor) and the APS (Active Pixel Sensor) [74]. In the former, a photodiode is integrated within the pixel together with the selection switches for the direct connection to the readout line. In the latter, the signal charge is directly buffered by an amplifier integrated in each pixel.

Today most CMOS imagers have an APS structure because of its better performances; the baseline architecture for each pixel is made of one photodiode and three transistors: a reset switch, the input for a source follower and a selection switch. The sensor and the readout electronics are both integrated on the same, low-resistivity silicon wafer. The working principle of a typical MAPS (Monolithic Active Pixel Sensor) is explained in detail in [75], while the main characteristics making it a better alternative to CCDs, both for visible light imaging and particle detection, are listed here:

- low cost, since they are fabricated in standard technology;
- low power, since the circuitry in each pixel is active only during the readout and no clock signal, requiring large capacitances, is foreseen;
- random access, since each pixel can be directly addressed for the readout;
- spatial resolution: better than 3 μm with a binary readout and less than 1 μm, taking advantage from the analogue readout and the charge spread between neighbouring pixels;
- versatility, since the control logic, the analogue-to-digital converter or any other signal processing element can be integrated in the same substrate as the sensor matrix.

The straightforward application of a CMOS sensor as a charge particle detector is nevertheless not an easy task, especially because the thickness of the active layer is not exceeding 15 μm.

In order to overcome these limitations, a novel structure has been proposed [76, 77] and is presented in Figure 2.11. While the three transistors are built within a p-well, the charge collection is accomplished using the junction between the n-well and the p-type epitaxial layer. Since the epi-layer doping is a few orders of magnitude smaller than the one of the p-well and the p^{++} substrate, potential barriers exist at its boundaries. The barriers act like mirrors for the excess electrons (minority charge carriers) produced by the radiation that, since there is no externally applied electric field, are bounced back both from the p-well and from the p^{++}-substrate and *focalized* toward the n-well diode contacts. Because of the reflective potential barriers, the sensor is fully sensitive over the whole pixel surface.

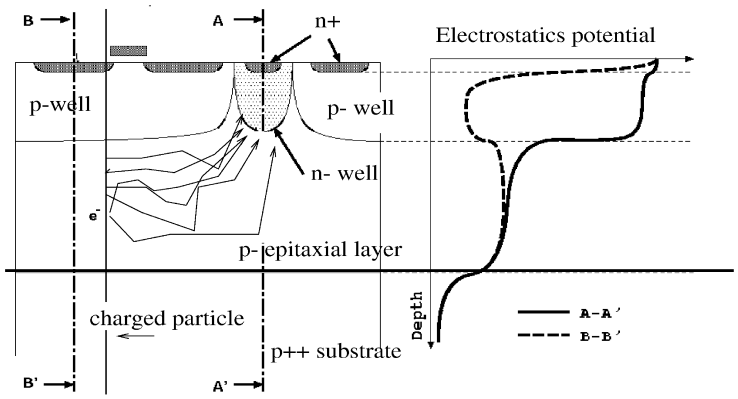

Figure 2.11: *Schematic of a CMOS detector [78].*

The SUCIMA CMOS sensor development focuses on the improvement of this structure in terms of back-thinning, with the aim to guarantee a sensitivity to 20 keV electrons and on the design of a fast, dead-time free, large dynamic range readout architecture. The

back-thinning development was mandatory in order to provide the device sensitivity to low energy electrons. Whether thinning of ICs is pursued for mobile and smart card applications down to 50 μm, the hadontherapy beam monitor application requires the reduction of the original silicon wafer to the thickness of the epitaxial layer, namely ≈ 15 μm for the chosen technology.

The step from 50 to 15 μm is highly non trivial and requires leading edge know-how. The process was performed in collaboration with an industrial partner[5], identified on the market as one of the few companies interested in the development of an extreme thinning procedure.

The test vehicle was a MAPS, MIMOSA V, developed by the ULP team for high energy physics applications [79] and made available to the SUCIMA collaboration. The MIMOSA V technical details are listed in Table 2.4.

Table 2.4: *MIMOSA V sensor main characteristics*

MIMOSA V	
Size	1020 × 1024 pixel
Pixel pitch	$17 \times 17\,\mu\text{m}^2$
Readout frequency	up to 40 MHz
Parallel analog output	4 channels
Frame readout time (normal mode) @ 10 MHz	26 ms
Frame readout time (fast and coarse mode) @ 20 MHz	$160\,\mu$s
Dynamic range	~ 10 (20-keV e^-)
Technological process	$0.6\,\mu$m AMS
Epitaxial (sensitive) layer before thinning	$\sim 14\,\mu$m
Epitaxial (sensitive) layer after thinning	$\sim 10.3\,\mu$m

The new back-thinning technology allowed to completely remove from the sensor backside with both mechanical and chemical etching all the passive $p^{++}-$substrate and to protect the epitaxial layer with only a 100 nm thick passivation layer, as schematically represented in Figure 2.12. Before all the thinning procedures, the mechanical structure of the chip is reinforced by attaching a several hundreds μm thick support, as schematically represented in Figure 2.12, to the entire front surface.

Dies were bonded to the dedicated hybrids using a fine-pitch wedge-bonding tool and a 17 μm diameter aluminium wire. Hybridization and bonding was highly not trivial by itself, requiring the capability of stitching a bond wire through 15 μm deep trenches, etched through the surrounding epitaxial layer to the metal pad (Figure 2.12).

This solution allowed the successful assembling of 15 printed circuit boards[6] (PCB) shown in Figure 2.13.

5 The SUCIMA consortium signed a non-disclosure agreement with the sub-contractor such that also its name cannot be revealed.

6 The chip mounting to the test Printed Circuit Board and following bonding service was provided by S. A. Microbonding (http://www.microbonding.com/).

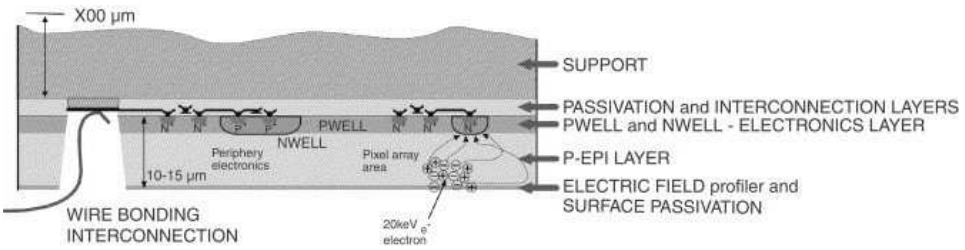

Figure 2.12: *Cross-section view of the back-thinned MAPS device.*

The basic parameters, like charge-to-voltage conversion factor, noise, leakage current, of the thinned devices were estimated and compared to those characterizing non-thinned detectors. A standard procedure with a ^{55}Fe source proved that the chip performances were not altered by the thinning procedure. In order to assess the sensitivity of the thinned devices for low energy electrons detection, tests with both a 3H (Tritium) radioisotope source and with monoenergetic electrons produced using an Hybrid Photo-Diode (HPD) structure were proposed and performed.

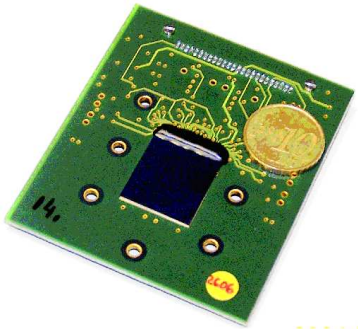

Figure 2.13: *Back-thinned MIMOSA V mounted on a test PCB.*

Sensitivity to low energy electrons has been demonstrated well below 10 keV, the charge-to-voltage conversion gain was preserved, while the charge collection efficiency was measured to be reduced by $\sim$ 40% for 20 keV electrons and to $\sim$ 50% for 10 keV electrons [80–82]. The MIMOSA V sensor used for the experiments described in Chapter 6 is one of the first prototype of extremely thinned sensors.

The technical details of the dedicated CMOS monolithic sensor of the MIMOSA family, named MIMOTERA, designed and developed on the basis of hadrontherapy beam monitor specifications, are summarized in Table 2.5. A serious flaw in the MIMOTERA functionality was detected, identified and fixed but the chip had to be re-submitted for fabrication at the end of 2004. The functionality has been assessed and, by the time of writing, the final devices are being thinned. The full integration in the beam monitor and in-beam tests are scheduled for end of 2005.

Table 2.5: *MIMOTERA sensor main characteristics*

MIMOTERA	
Size	112 × 112 pixels
Pixel pitch	$153 \times 153\,\mu m^2$
Frame rate	10 kHz
Parallel analog output	4 channels
Technological process	$0.6\,\mu$m AMS CUA
Epitaxial (sensitive) layer before thinning	$\sim 14\,\mu$m
Epitaxial (sensitive) layer after thinning	$\sim 10.3\,\mu$m
Dynamic range (e^-)	$1 - 10^4$ (20-keV e^-)/pixel/100 μs

2.5 The SLIM dedicated Data Acquisition System

The needs for real time monitoring of hadrontherapy beam intensity and profile using Monolithic Active Pixel Sensors (MAPS) lead to the design of a dedicated, flexible and modular Data Acquisition System (DAQ SUCIMA Imager) [83]. Flexibility of the system has to be understood both in terms of compliance with the different sensors under development and with respect to the different domains of application. On-board computing power and high-throughput data transfer are the base of real-time systems and are a must for the applications envisaged within SUCIMA. In particular, for the beam monitoring application the capability of real-time identifying intensity, position and profile fluctuations is the crucial requirement that determines the DAQ performances.

The DAQ system has been developed by Institute of Nuclear Physic (Krakow) on one of the most advanced XILINX Field Programmable Gate Array chip - VIRTEX II. The system is composed of a multifunctional electronic board for the detectors analogue signals capture, their parallel digital processing and final data compression as well as transmission through the high speed USB 2.0 port. Moreover, fast decisions for the hadron beam control are possible through the logic and the data processing algorithms which can be implemented on the programmable module according to the specific detector application.

The block schematics of the SUCIMA Imager module is presented in Figure 2.14 with the Field Programmable Gate Array steering the detector logic, four parallel Analog to Digital Converter (ADC) and mastering the data transmission through the Cypress Universal Serial Bus (USB) 2.0 interface.

The main features of the SUCIMA Imager module can be summarized by few key parameters:

- 4 independent analogue input channels with 12 bit resolution ADCs for the parallel readout of different sensors or quarters. Each ADC can handle up to 65 MSPS (Mega Samples Per Second);
- 256 K of 32 bit fast static Random Access Memory (RAM) memories for each channel;

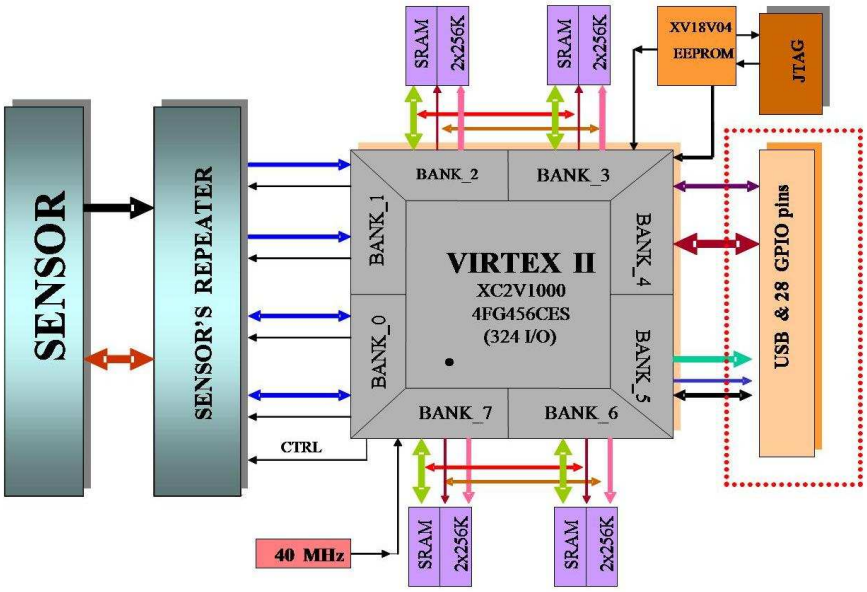

Figure 2.14: *Architecture of the SUCIMA Imager board. The core of the system consist of a DAQ Virtex 2 chip that is steering the sensor, the ADC, the access to the on board memories and data transmission to the computer via a Cypress USB 2.0 interface.*

- FIFO memory 256 K of 18 bit, can serve as the output buffer;
- high speed USB 2.0 port for communication and fast data transfer to and from a PC computer;
- 8 bit Parallel GPIO Port and I2C Port for external devices programming and communication;
- FPGA VIRTEX II chip with 1 Mega General Purpose programmable System Gates which is connected in parallel to 4 analogue input channels, 4 Static Random Access Memory (SRAM) memory banks, the FIFO and High Speed USB Port;
- 200 Hz frame readout speed from 1 Mega-pixels sensors and up to 10 kHz frame readout speed from 20 kilo-pixels sensors.

The Imager FPGA with its one million gates and with the on-board 2 MByte SRAM, allows an enormous computing power, that can be applied to on-line digital signal processing or other complicated algorithm such cluster identification and continuous pedestal tracking. This feature can become very useful when only a small fraction of the whole sensor is reached by ionizing radiations. In this case, on-line on-board sparsification algorithm would reduce the amount of data to be transferred.

A *repeater* board which distributes the analog and digital signals is part of the DAQ system to adapt to the different kind of detectors used. A picture of the DAQ board used for the in-beam tests with both pad and CMOS sensors is shown in Figure 2.15.

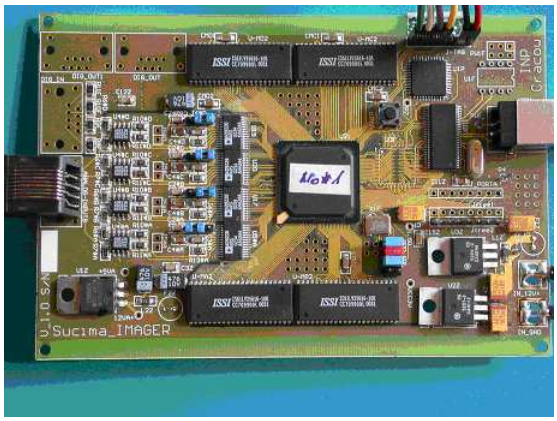

Figure 2.15: *A picture of the SUCIMA imager DAQ board with its main components: the Virtex 2, the four ADCs and the on-board SRAM. The board size is 14 x 9.5 cm^2 for 200 g weight.*

The DAQ is complemented by two National Instruments LabVIEW Graphical User Interfaces (GUI): a basic one, used especially for system debugging, from which the user can set detector parameters and save raw data to the disk; and a more advanced one in which an on-line cluster finding algorithm is implemented allowing an impressive reduction in the data volume.

Chapter 3

SLIM particle beam monitor conceptual design

The central part of the SLIM beam monitor is the focusing system and the SLIM volume and performances depend crucially on its design. The starting point for the development of the focusing system was the understanding of the secondary emission phenomenon in terms of efficiency (number of electrons per incident particle emitted from the foil) and secondary electrons distribution in energy and angle. Secondary emission is a semi-empirical phenomenon and, unluckily, experimental data at the kinetic energies for hadrontherapy with primary proton and carbon ion beams on metal targets are scarce.

The first part of the conceptual design has been, therefore, dedicated to the study of secondary emission from metal targets bombarded with high energies (exceeding 1 keV) proton or carbon ion beams. The main features of the secondary emission process and the calculations of secondary electrons yields for the SLIM beam monitor application are summarized in Section 3.1.

Several focusing systems for the stigmatic transport of the secondary electrons from the foil to the detector have been studied and are discussed in Section 3.2. The common guideline in the different prototypes design was to accelerate the secondary electrons to kinetic energies in the range 10 - 30 keV to reach the electron detector sensitive region, featuring the required spatial resolution with the minimum possible material interposed to the beam path.

According to the sensitive area of the electron detector and the pixel pitch, a proximity focusing (1:1) or a demagnification optics (< 5 to avoid distortions) for the collection of the secondary electrons have been studied. A detailed analysis of the final prototype for the CMOS detector, inspired by the optical scheme of an image intensifier tube, is discussed in Section 3.2.2. The engineering design of the focusing system is described in Chapter 4.

Section 3.3 refers to the beam-SLIM monitor interaction study and in particular to the hadron beam perturbation caused by the electrical field of the focusing system and of the aluminium foil heating at the hadron beam crossing. Due to the tight timing of the SUCIMA project, the data considered for the hadron beam emittance blow-up caused by the scattering

of the beam in the thin aluminium foils rely on a former study [84] based on a Monte Carlo programme for plural scattering. Project future developments foresee further dedicated studies and experimental validation of the model results.

3.1 The Secondary Emission study for the SLIM beam monitor

In this section are summarized the most important properties of the secondary emission process that are relevant for the SLIM beam monitor application, more details can be found in [85]. A charged particle traversing a material exchanges part of its kinetic energy with the electrons of the medium. Ionization of the target atoms by the primary beam can result in electrons receiving energy and momentum sufficiently large to escape from the foil surface. Secondary emission is a surface phenomenon: secondary electrons (SE) in metals come from a shallow region 10 - 100 Å thick. For foil targets, as in the beam monitor application, the electron emission process concerns both faces of the foil.

The interaction between the primary charged particles and the electron system of the solid (metal in the beam monitor application) leads to various excitation mechanisms:

- excitation of the conduction electrons;
- excitation of electrons by decay of plasmons generated by incident particles;
- excitation of core electrons;
- excitation by Auger mechanism.

Obviously all the excitation processes occur in parallel. A full treatment of the generation processes is an immense task and has been solved only partly so far. The models based on the solution of the Boltzmann transport equation allows to determine the density of inner excited electrons in terms of excitation functions, mean free paths and scattering functions.

However, because of the large numerical effort required for solving the differential equation in question, it is necessary to make some simplifying assumptions concerning the different excitation processes and scattering cross sections [86, 87]. Numerous Monte-Carlo simulations of secondary electron emission have been developed, but they consider primary beam energies up to 10 MeV/u [88–90].

The so-called semi-empirical theories, which do not distinguish different excitation mechanisms, constitute the most popular approach to the secondary emission process [91]. They assume a SE generation rate proportional to the ratio $1/ < E > \ (dE/dx)$ where $< E >$ is the mean energy needed to produce a free electron within the solid body. With this approach the quantity (dE/dx) takes into account all processes that contribute to the energy loss of a penetrating particle through inelastic collisions.

Among these theories, the most famous is the Theory of Sternglass [92], elaborated in 1957 and used for the beam monitor yield calculations. In literature it is pointed out that

Sternglass formulations work very well for protons, but over-estimate the yield in case of ion beams. Therefore, in the case of incident ions a revision of the Sternglass theory, called the Borovsky's modification [93] has been used.

The basic physical quantities of interest in secondary emission are the following:

- total electron yield γ_t, defined as the number of electrons emitted from the target per impinging primary particle;
- forward yield γ_f , defined as the number of electrons emitted in the forward direction (i.e., in the direction of the primary beam) per impinging primary particle;
- backward yield γ_b, defined as the number of electrons emitted in the backward direction per impinging primary particle;
- ratio between forward and backward yield R= γ_f/γ_b;
- spectrum of emitted electrons, which is defined either as the differential yield $d\gamma_t/dE$, i.e. integrated over all angles of emission or the double differential yield, with respect to both energy and angle, $d\gamma/dEd\Omega$. The quantity $d\gamma/dE$, as a function of the electron energy E, is often called the energy spectrum of emitted SE;
- angular distribution $d\gamma/d\Omega$ of electrons emitted from the solid, usually determined in respect to the polar emission angle.

The terms *thick* and *thin* targets are often used to describe the secondary emission phenomenon: *thick* targets are the foils for which forward and backward yields have reached a saturation value and do not evolve further increasing the target thickness. The term *thin* targets refers to foils for which only backward yield has reached a constant value.

3.1.1 Dependence of secondary electron yield on primary beam energy

The total, forward and backward yields vary proportionally to the inelastic stopping power of the projectile in the target (dE/dx). The constant of proportionality depends on different factors as the material, purity and surface roughness of the target and the energy, nuclear charge and incidence angle of the projectile. The general behavior of the primary energy dependence of the total yield γ_t is shown in Figure 3.1 for proton impact on different metal targets (Al, Cu, Ag, Au) at normal incidence angle [94].

The total yield increases with increasing ion energy, then goes through a maximum and decreases thereafter. Since the yield is proportional to the inelastic stopping power dE/dx, the peak shown in Figure 3.1 corresponds to the maximum value of dE/dx. This value and the magnitude of the total electron yield depend on the projectile-target combination. For protons impinging on metal, the maximum of the yield curve has values in the range 1 to 3 and it is located around 300 keV, well below the primary beam kinetic energies of interest for the SLIM beam monitor application.

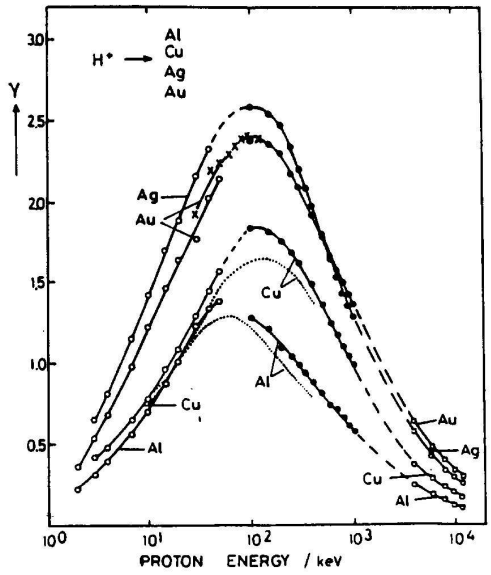

Figure 3.1: *The total electron yield γ_t as a function of the primary energy (proton impact).*

3.1.2 Dependence of secondary electron yield on primary beam angle of incidence

The angle of incidence α of the ion beam is usually measured with respect to the surface normal ($\alpha = 0$). If the angle of incidence is increased the geometrical path length of the impinging particles within the escape zone of SE is scaled by a factor $cos^{-1}\alpha$ and the total yield is predicted to vary as [95]:

$$\gamma_t(\alpha) = \gamma_t(0) \ \cos^{-1}\alpha \tag{3.1}$$

where $\gamma_t(0)$ is the total electron yield at normal incidence. While the previous relation seems to hold strictly for proton bombardment, deviations have been observed for ion impact in several experiments [96, 97]. In particular, the experimental data for ion beams for $\alpha < 70°$ degrees can be fitted by an empirical relation:

$$\gamma_t(\alpha) = \gamma_t(0) \ \cos^{-f}\alpha \tag{3.2}$$

where f is a parameter in the range $0.5 \leq f \leq 1.5$ depending on the impact energy, the projectile-target combination and also on the incidence angle itself. The parameter f is purely empirical and not related to any theoretical treatment.

In the SLIM beam monitor application the Al foil intercepts the primary hadron beam at 45° degrees. Therefore, for proton beams $\gamma_t(0)$ should be multiplied by a factor $\sqrt{2}$ to obtain $\gamma_t(45°)$. The same factor was assumed for primary carbon ion beams in the absence

of f values at hadrontherapy kinetic energies.

3.1.3 Forward and backward secondary electron yields

For foil targets secondary emission process concerns both faces of the foil. Referring to the definitions of Section 3.1, the total yield γ_t is obtained as the the sum: $\gamma_t = \gamma_b + \gamma_f$. As the total yield, backward and forward yields depend on the projectile energy, the nuclear charge of the projectile, the target material, the inelastic stopping power of the projectile in the material target and the incidence angle of the primary particles on the target. The main properties of the forward and backward yields can be summarized as follows:

- γ_f and γ_b depend on the projectile nuclear charge Z_p, at a given velocity and for a given target material both secondary emission yields increase strongly with Z_p;
- both γ_f and γ_b decrease with an increase of the projectile velocity v_p. This is true for primary energies higher than the value at which the stopping power reaches the maximum (in metal around 300 keV);
- in general $\gamma_f > \gamma_b$ for all projectile target combination. This is due to the emission in the forward direction of high-energy (>1 keV) electrons usually called *δ-electrons* that ionize other electrons of the medium producing a further secondary cascade near the surface exit;
- according to Rothard et al. [98] two simple relationships for an estimate of secondary electron yields γ_f and γ_b from metallic foils and proton impact are: $\gamma_b = 0.14$ dE/dx and $\gamma_f = 0.17$ dE/dx (dE/dx in eV/Å); in the case of ions, there are no experimental data on metal targets at the energies of interest for hadrontherapy;
- both γ_f and γ_b depend on the target thickness. A saturation value is reached increasing the thickness of the samples;
- the ratio $R = \gamma_f/\gamma_b$ increases with projectile nuclear charge Z_p;
- for a fixed target material and projectile type, the ratio $R = \gamma_f/\gamma_b$ increases with the projectile energy since the production of *δ-electrons* and thus the secondary cascade in forward direction, are favored by an increase of the projectile energy.

The scale to define a target as thick or thin depends on the projectile energy, charge and on the target material; as an order of magnitude, at 10 MeV/u a thick target is about 500 μg/cm^2 and a thin target is about 20 μg/cm^2 [99]. Experimental data on the dependence of the forward and backward yields from the thickness of the target are not available in literature for aluminium foils.

In the SLIM application the SE used for beam monitoring are those emitted in the backward direction and it is reasonable to assume that with hadrontherapy beams the 0.2 - 0.3 μm Al/Al_2O_3 foils (Section 4.3) can be considered in the region between thin and thick targets, where backward emission increases increasing the foil thickness due to backscattered δ-electrons.

3.1.4 Secondary electrons energy spectrum in metal targets

Figure 3.2 shows the typical low energy spectrum for SE from a metal foil. This spectrum is relative to an aluminium target bombarded with different projectile ions (H^+, He^+, Ar^+) at 500 keV, but the low-energy part of the spectrum (below 50 eV) is independent on the primary beam kinetic energy [100–103]. The energy distribution has a main maximum at 2.1 eV and the full width at half maximum (FWHM) is 8.2 eV. This peak contains about 85% of the secondary electron [103].

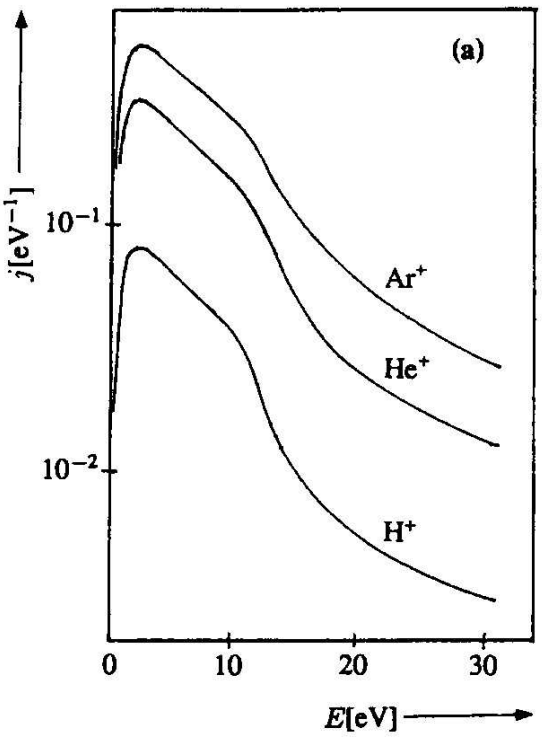

Figure 3.2: *Energy distribution of electrons emitted from Al target for 500 keV different projectiles (the curves are obtained from fit of experimental data).*

The same shape for the electron energy distribution is shown in Figure 3.3 for different target material bombarded with 500 keV protons. The low energy part of the electron spectrum (below 50 eV) depends on the target material, but for primary beams of protons and light ions (up to neon) impact is independent on the energy of the projectiles.

The energy value at which the spectra have a maximum (E_{max}) varies between 1.8 and 3.6 eV and the width of the spectrum at half maximum height ($\Delta_{1/2}$) varies between 5.4 and 11.8 eV for proton impact. At electron energies above 50 eV the shapes of the spectra become impact dependent: with increase of the impact energy the number of energetic electrons increases [104]. This behaviour indicates that the emission of low-energy electrons (up to 50 eV) is the result of a cascade process, while the high-energy part of the spectrum

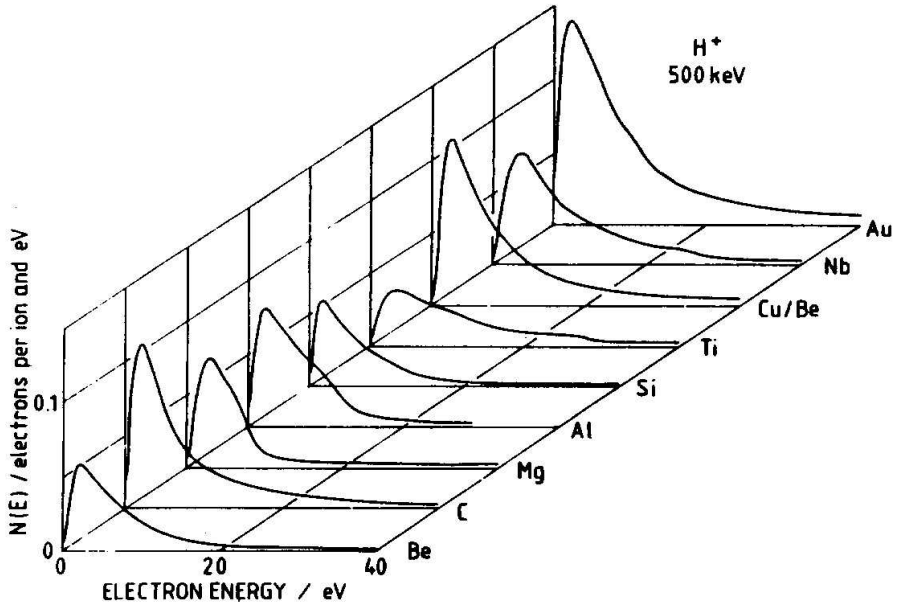

Figure 3.3: *Low energy spectra (below 50 eV) induced by 500 keV protons impinging on different targets (the curves are obtained from fit of experimental data).*

(above 50 eV) is due to direct energy transfer from the impinging ion to an electron of the solid body.

3.1.5 Secondary electrons angular distribution

A crucial parameter for the the study of the optics of the focusing system for the SE transport is the secondary electron angular distribution. The integrated angular distribution ($d\gamma_{SE}/d\Omega$) of the electrons emitted with low energies (below 50 eV) follows a cosine-law as shown in equation (3.3):

$$\frac{d\gamma_{(b,\,f)}}{d\Omega}(\theta) = \left.\frac{d\gamma_{(b,\,f)}}{d\Omega}\right|_{\theta=0} \cos\theta \tag{3.3}$$

where θ is the angle of emission with respect to the surface orthogonal. This shape was observed in various experiments [105–107] and is expected for an isotropic momentum distribution of electrons inside the solid.

3.1.6 Secondary electrons yields for the SLIM beam monitor

Sternglass theory of secondary emission is one of the most famous *empirical theories* and supplies a useful formula for calculation of the total electron yield from metal bombarded with ions or protons used for the SLIM beam monitor application [92]. Sternglass assumes that electrons can be produced in two different ways:

- by so-called *distant* (large impact parameter) collisions with a small energy transfer, which give rise to a large number of low-energy SE;

- by so-called *close* collisions with a large energy transfer and a consequent production of a small number of energetic δ-electrons that may produce further excited electrons by cascade processes.

The generation rate are set proportional to the corresponding inelastic stopping power $(dE/dx)_d$ (for distant collisions) and $(dE/dx)_c \cdot f(v_p, x)$ (for close collisions) where v_p is the incident particle velocity and x the depth below the surface at which the SE are produced.

From the Bohr-Bethe equi-partition rule of stopping powers $(dE/dx)_d = (dE/dx)_c = (1/2)(dE/dx)$, where (dE/dx) is the total inelastic stopping power defined by the Bethe-Bloch formula:

$$-\frac{dE}{dx} = 2\pi N_a r_e^2 m_e c^2 \rho \frac{Z}{A}\frac{z^2}{\beta^2}\left[\ln\left(\frac{2m_e\gamma^2 v^2 W_{\max}}{I^2}\right) - 2\beta^2\right] \tag{3.4}$$

with:

$2\pi N_a r_e^2 m_e c^2 = 0.1535\ MeV\ cm^2/g$
r_e: classical electron radius
m_e: electron mass
N_a: Avogadro's number
I: mean excitation potential
Z: nuclear charge of the target
A: atomic weight of the target atoms
ρ: density of the target
z: charge of the incident particle
β: v/c of the incident particle
γ: $1/\sqrt{1-\beta^2}$
W_{max}: maximum energy transfer in a single collision

Sternglass assumes that the δ-electrons produced in close collisions are emitted in the forward direction. Their mean free paths is exceeding those of slow electrons, so the energy transferred to the δ-electrons may be deposited and converted to slow SE. The function f(v_p, x) denotes that fraction of energy originally transferred to δ-electrons which is transformed into slow electrons within the solid. According to the model, this fraction will decrease with increasing impact energy.

Sternglass formulated his theory for high-energy proton impact (> 100 keV), but it remains valid for ions as long as:

- the energy loss is constant over the incident particle path;

- recoil of target atoms are neglected;

- the equi-partition rule is fulfilled.

At low impact energies (below 1 keV) the theory is not applicable since the slowing down of projectiles within the solid is not considered.

3.1.6.1 Secondary electrons yield for proton beams

Using Sternglass theory, the total secondary electron yield γ_t can be expressed as:

$$\gamma_t = \frac{1}{2}\,\frac{1}{E_0}\,\frac{dE}{dx}\tau\, B\, L_s\,[1 + F(v_p)] \tag{3.5}$$

with:

E_0: mean energy loss to produce one secondary electron (25 eV in Al)
$\frac{dE}{dx}$: inelastic stopping power of the incident particle evaluated with equation (3.4)
τ: surface transmission coefficient
B: constant related to the distribution of the initial velocities of the secondary electrons depending on the target material
L_s: corresponds to the mean free path for inelastic collisions (in cm) and depends on the target material only ($\mathrm{L}_s = 0.23\ \mathrm{N}\ \sigma_g)^{-1}$
N: number of atoms per unit volume
σ_g= 1.6 $\mathrm{Z}^{1/3}$ $10^{-16}\mathrm{cm}^{-2}$ (geometric area) proportional to the scattering cross section for electrons

$F(v_p)$ is related to the mean free paths of slow and δ-electrons and is represented by the relation:

$$F(v_p) = \left(1 + \frac{L_\delta}{L_s}\right)^{-1} = \left(\frac{1}{1 + \dfrac{E_p}{0.1836 \cdot A_p}}\right) \tag{3.6}$$

with $\dfrac{L_\delta}{L_s} \approx \dfrac{m_e}{M_p}\dfrac{E_p}{100}$ where M_p(MeV), E_p(MeV) and A_p are respectively the mass, the energy and the atomic number of the projectile. For Al targets:

L_s for Al $\approx$ 16.4 Å
$\tau B \approx 0.5$ (for all metals)
$\sigma_g \approx 4{\cdot}10^{-16}$ cm^{-2}
$\rho_{Al} = 2.7$ g/cm^3
$N = 6\ 10^{22}$ cm^{-3}

and equation (3.5) can be rewritten as:

$$\gamma_{Al} = 1.92 \cdot 10^{-9} \left(\frac{dE}{dx}\right)_{Al} \left(\frac{1}{1 + \dfrac{E_p}{0.1836 \cdot A_p}}\right) \tag{3.7}$$

The values of the inelastic stopping power $(\mathrm{dE/dx})_{Al}$ for proton projectiles are evaluated with equation (3.4) and compared to those found in Janni tables [108].

For aluminium oxide targets, Al_2O_3, L_s is ≈ 38.8 Å and $(dE/dx)_{Al_2O_3} \approx 0.95\ (dE/dx)_{Al}$ [109] and equation (3.5) becomes:

$$\gamma_{Al_2O_3} = 4.32 \cdot 10^{-9} \left(\frac{dE}{dx}\right)_{Al} \left(\frac{1}{1 + \dfrac{E_p}{0.1836 \cdot A_p}}\right) \approx 2.25 \cdot \gamma_{Al} \tag{3.8}$$

3.1.6.2 Secondary electrons yield for ion beams

In literature it is pointed out that Sternglass formulations work very well for primary beams of protons but over-estimate the yield in case of ions [110]. In the case of incident ions the Borovsky's modification of Sternglass formulation leads to the following expressions for ion projectiles on Al and Al_2O_3 targets respectively (with the symbols as defined for equations (3.4) and (3.6)):

$$\gamma_{t\_B\_Al} = 0.359 \frac{z^2}{E_p} A \ \ln\left(13.7\ \frac{E_p}{A}\right) \left(\frac{1}{1 + \dfrac{E_p}{0.1836 \cdot A_p}}\right) \tag{3.9}$$

and

$$\gamma_{t\_B\_Al_2O_3} = 0.807 \frac{z^2}{E_p} A \ \ln\left(13.7\ \frac{E_p}{A}\right) \left(1 + \frac{1}{\dfrac{E_p}{0.1836\ A_p}}\right) \tag{3.10}$$

3.1.6.3 SLIM yields

In the SLIM beam monitor application the primary particles are protons with energy in the range 60 - 250 MeV and carbon ions (C^{6+}) with energy 120 - 400 MeV/u (Table 2.1) impinging on aluminium foils with thickness in the range 0.2 - 0.4 μm (2000 - 4000 Å). As described in Section 4.3, the foils used consist of a support of 0.1 - 0.3 μm (1000 - 3000 Å) of Al_2O_3 coated on each side with 0.01 - 0.05 μm (100 - 500 Å) of Al for a maximum diameter of about 65 - 70 mm. As already stated, secondary emission is a surface phenomenon and concerns just the most superficial aluminium layers.

At high energies (>10 MeV/u) studies on secondary electron emission are scarce and experimental values of yields, energy spectra and angular distribution concerning protons and carbon ions on Al targets are not available up to now. Therefore Sternglass and Borovsky formulations were used to evaluate the yields. Equations (3.7), (3.8), (3.9) and (3.10) assume that the direction of the incident particles is normal to the surface target ($\alpha = 0$). Since the Al foil intercepts the hadron beam at 45° degrees, the calculated yields are multiplied by a factor $1/\cos 45°$ as explained in Section 3.1.2.

Table 3.1 contains the calculated yields for protons impinging on Al target and, as the foil Al superficial layer can be slightly oxidized, yields from Al_2O_3 are also included. The experimental values in the table were found in literature only for energies of 20 and 60 MeV

for Al targets and 5, 20, 25 MeV for Al_2O_3 targets but prove, nevertheless, that at lower energies there is a good agreement between measured and evaluated data (within 15% for Al targets).

Table 3.1: *Calculated yields using Sternglass formulation for protons impinging on Al and Al_2O_3 targets.*

Proton energy (MeV)	**Theoretical total yield (%)**	**Experimental total yield (%)**
Al target		
5	30.9	-
20	10.4	12[a]
25	8.7	
60	4.4	3.8[b]
250	1.6	
Al_2O_3 target		
5	71.5	64[a]
20	23.8	20[a]
25	19.9	15[a]
60	9.9	
250	3.7	

[a] experimental values from [98]
[b] experimental values from [110]

The forward and backward yields for protons were calculated using the relations $\gamma_b = 0.14$ dE/dx and $\gamma_f = 0.17$ dE/dx (dE/dx in eV/Å) discussed in Section 3.1.3, and are shown in Table 3.2 .

Tables 3.3 and 3.4 show the yields for carbon ions impinging on Al and Al_2O_3 calculated with Sternglass and Borovsky formulations.

As stressed in Section 3.1.3 the ratio $R = \gamma_f/\gamma_b$ for primary ion beams increases with the projectile energy and $\gamma_f > \gamma_b$ due to the emission in the forward direction of δ-electrons that ionize the target atoms producing a further secondary cascade near the surface exit. Unfortunately experimental values of R for carbon ions at the hadrontherapy energies are not available. To have an indication on the value of γ_b, it was assumed from relation $\gamma_f > \gamma_b$ that, for a fixed projectile energy, the maximum value of γ_b is half of the total yields evaluated in Table 3.4, as shown in Tables 3.5.

3.1.7 Secondary emission study conclusions

The following conclusions can be drafted for protons impinging on Al foils:

- the experimental data found in literature for primary beam energies up to 60 MeV confirm the calculated yields, as shown in Table 3.1. For higher energies it is reasonable

Table 3.2: *Calculated backward and forward yields for protons on Al and Al_2O_3 targets.*

Proton energy (MeV)	**Backward yield (%)**	**Forward yield (%)**
Al target		
5	14	17
20	5	6
25	4	5
60	2	2.4
250	0.72	0.86
Al_2O_3 target		
5	32.5	39
20	11	12.8
25	9	11
60	4.5	5.4
250	1.7	2

Table 3.3: *Calculated yields using Sternglass formulation for carbon ions impinging on Al and Al_2O_3 targets.*

Carbon ion energy (MeV)	**Theoretical total yield with Sternglass (%)**
Al target	
120	93
200	66
250	56
300	52
400	45
Al_2O_3 target	
120	209
200	148
250	230
300	117
400	100

Table 3.4: *Calculated yields using Borovsky formulation for carbon ions impinging on Al and Al_2O_3 targets.*

Carbon ion energy (MeV)	**Theoretical total yield with Borovsky (%)**
Al target	
120	78
200	50
250	41
300	35
400	27
Al_2O_3 target	
120	176
200	113
250	93
300	79
400	61

Table 3.5: *Maximum backward and minimum forward yields for carbon ions impinging on Al and Al_2O_3 targets evaluated with Borovsky formulation.*

Carbon ion energy (MeV)	**Max backward yield (%)**	**Min forward yield (%)**
Al target		
120	39	39
200	25	25
250	20	20
300	17	17
400	13	13
Al_2O_3 target		
120	88	88
200	56	56
250	46	46
300	39	39
400	30	30

to assume a scaling law;

- the low energy (below 50 eV) part of the SE spectrum, of interest for the SLIM beam monitor application, contains the majority of emitted electrons (85%). The low energy spectrum measured with 500 keV primary protons and shown in Figure 3.2 is independent from the primary energy (Section 3.1.4) and is therefore assumed to be valid at the hadrontherapy energies. The SE spectrum has a peak at $E_{max} \sim 2.1 \pm 0.3$ eV with a spread at half height of ~ 8.2 eV as shown in Figure 3.2;
- the angular distribution of the low energy electrons has a cosine-like behaviour, as pointed out in Section 3.1.5. Thus the maximum electron emission is expected in the direction perpendicular to the foil surface. While in the backward direction, as in the SLIM beam monitor application, the emitted electrons have low energy (< 50 eV) in the forward direction also high-energy electrons (δ-electrons) have to be taken into account.

The following conclusions can be drafted for carbon ions impinging on Al foils:

- experimental data are available only for carbon targets and primary energies of 10 MeV/u [99];
- in the lack of measurements at hadrontherapy energies, it is assumed that the same considerations made for proton impact are valid with Borovsky correction for the emission yield.

For both proton and ion primary beams, measurements of yields, energy and angular distribution would validate the model at energy above 60 MeV/u and confirm the above calculations. Project future developments foresee further dedicated tests.

3.2 The SLIM beam monitor focusing system

The SLIM beam monitor has been conceived to measure the beam intensity, centre of charge and profile in the extraction lines of a hadrontherapy centre during the treatment of the patient, as discussed in Section 2.3. The total beam size in a hadrontherapy centre extraction lines, varies typically from 3 to 25 mm in the vertical plane (Gaussian distribution cut at 2 σ) and from 1 mm to 36 mm in the horizontal plane (vertical and horizontal bar of charge[1] in phase space, respectively).

The beam size varies along the lines and from cycle to cycle depending on the beam parameters required at the patient. From the point of view of profile resolution, the ideal position for the monitor is where the beam cross-section is large (and the beam divergence is small). From the point of view of beam emittance blow-up (due to the interaction of the beam with the foil), the ideal position for the monitor is where the beam cross-section is small (and the beam divergence is large).

1 The phase space distribution in the horizontal plane, due to third order resonance extraction, is near-rectangular (*bar of charge)* [22].

The position for the monitor is found as a compromise between these two conflicting needs. The thin foil sensitive area is therefore fixed equal to 6 - 7 cm having considered the varying beam size (average size 10 x 10 mm^2), an orbit distortion term and that the foil intercepts the hadron beam at 45° degrees (see Figure 3.4). As the vacuum chamber radius is of the order of 3 cm, the distance between the secondary emission foil and the electron detector cannot be smaller than 7- 8 cm in the hypothesis of a 1:1 optics for the SE collection as shown in Figure 3.4. Any focusing system (FS) must consider an aperture for the primary beam crossing.

The FS should feature a stigmatic optics for the transport of the SE emitted from the foil onto a position sensitive detector (area divided in cells) preserving the information on the primary beam profile and intensity. As the diameter of the aluminium foil sensitive area is of the order of 70 mm with the primary hadron beams hitting a smaller area of about 10 x 10 mm^2, the minimum necessary number of cells of the detector to provide the required 1 mm granularity for the profile measurement is 5000, with the beam hitting only 100 cells.

The size of the cells depends on the optics used for the SE transport (see below). The number of electrons per cell per second varies in the range 10^3 e^-/(cell·s) to 10^8 e^-/(cell·s) for both proton and C-ion primary beam, having considered the beam minimum and maximum intensity detailed in Section 2.1, the secondary emission efficiencies of Tables 3.1 and 3.4, a 100% SE collection efficiency and the beam edge at 2 σ.

Different optics have been studied to suit the different SE detector size/pitch. The CMOS detector sensitive area (17 x 17 mm^2) is smaller than the Al foil surface and an optics with a demagnification factor of the order of 5 has been studied. For the PAD detectors (1 mm pitch for the final detector, 1.4 for the prototype used for the tests described in Section 6.3) a 1:1 optics is the best solution in terms of spatial resolution. The commercial system (sensitive diameter 32 mm) will be used to test both optical systems.

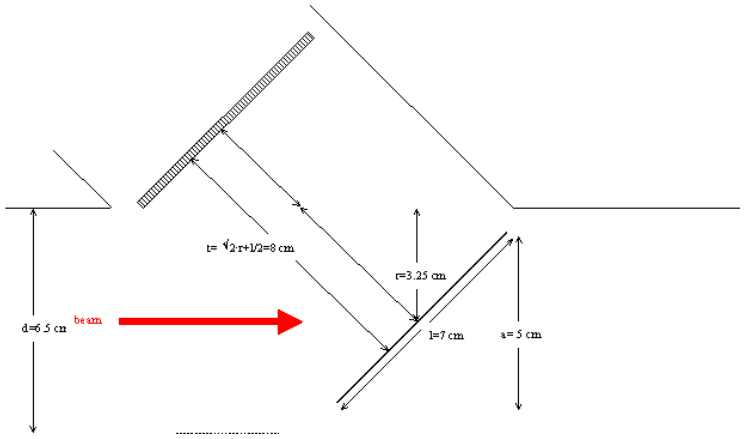

Figure 3.4: *SLIM geometry in the vacuum chamber (d: vacuum chamber diameter, r: vacuum chamber radius, l: foil diameter, a: effective foil diameter in horizontal plane, t: distance between the foil and the electron detector).*

The requirements on the FS can be summarized as follows:

- high SE collection efficiency;
- stigmatic optics to preserve the profile information;
- a spatial resolution of about 1 mm on the foil;
- no image distortions;
- final SE energies in the 10 - 30 keV range to reach the detector sensitive region;
- minimum perturbations on the primary beam due to scattering or electric fields;
- reliability, easy of maintenance and reasonable costs.

Different prototypes have been analyzed to find the solution that better suits the above requirements [111] and are described in Section 3.2.1. The guideline common to all designs was to cause the minimum disturbance, through scattering or electrical field, to the primary hadron beam. The final solution, described in Section 3.2.2.1, that fulfils the SLIM beam monitor requirements in terms of spatial resolution and collection efficiency does, nevertheless, minimally interfere with the beam through a sector of the first cylindrical electrode made by a very thin wires grid. This is the reason why alternative solutions have been analyzed before taking the final decision.

The simulations of the FS have been performed with the SIMION 3D Ion Optics Programs, version 7 [112][2]. Different source points distributed across the foil surface simulate the SE emission. The electrons are generated by a C^{++} code based on Monte Carlo algorithm according to the angular and energy distributions described in Section 3.1. Each source point has an image on the detector represented by a round spot. The diameter of the spot, as explained in Section 3.2.2, is related to the FS resolution. In all the figures that refer to the FS simulations the aluminium foil intercepts the hadron beam at 45° degrees.

3.2.1 First prototypes of the focusing system

The starting point in the design of the first FS prototypes was to avoid to interpose any material, besides the secondary emission foil, on the hadron beam path. The first solution consists of two circular ring electrodes concentric to the detector, as shown in Figure 3.5. This system was the first to be evaluated since the focusing and vacuum systems were available from a previous beam monitor. The detector considered for the simulations of the first prototype is the commercial detector described in Section 2.4 with a 32 mm active surface diameter. The central ring is a guard-ring to isolate the external ring and the detector in order to avoid eddy currents between the two.

Figure 3.6 shows the first prototype inserted in the vacuum chamber resulting from the intersection of two cylinders. The foil is polarized at -20 kV, the external ring at -22.3 kV and the internal ring and the detector are connected to the electrical ground.

2 Sincere thanks to SIMION 3D developer, David A. Dahl.

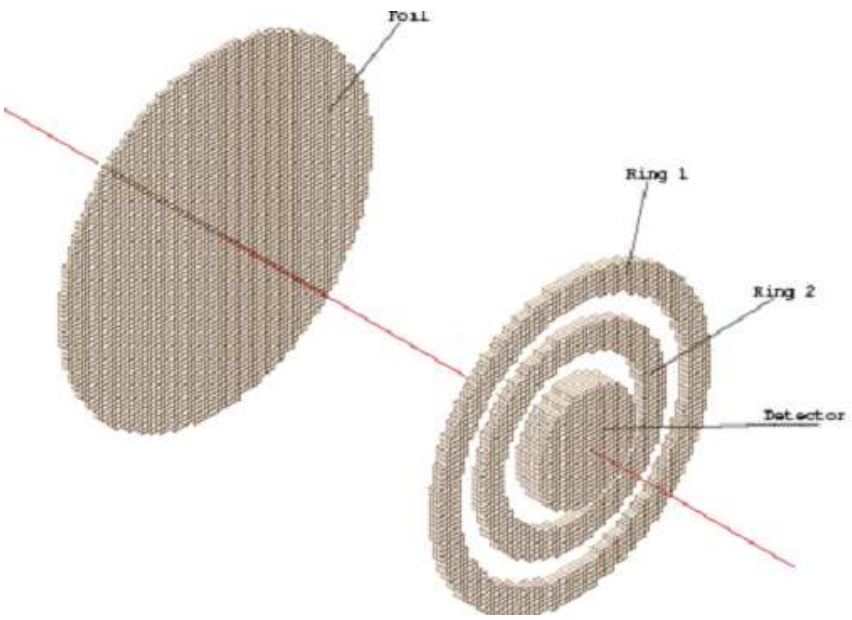

Figure 3.5: *The first FS prototype.*

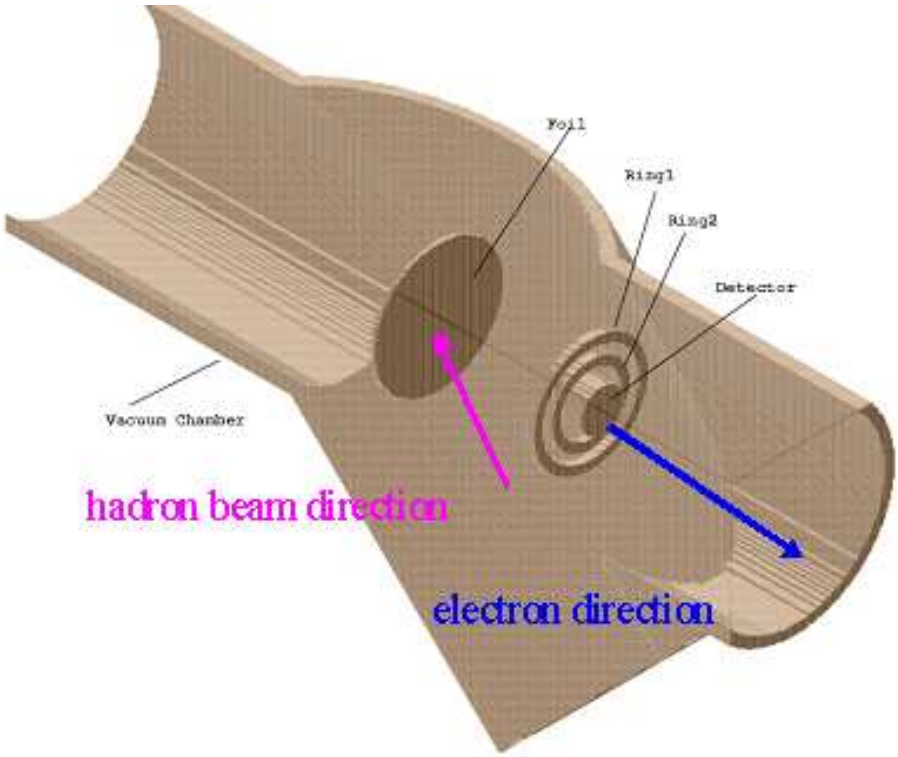

Figure 3.6: *The first FS prototype inserted in the vacuum chamber.*

The interaction between the vacuum chamber and the foil strongly disturbs the electron trajectories. As shown in Figure 3.7, electrons are attracted toward the vacuum chamber walls and it is impossible to find an acceptable optics. This results lead to the conclusion that for the SLIM beam monitor application a wider chamber not interfering with the electrostatic FS field in the region of interest is needed.

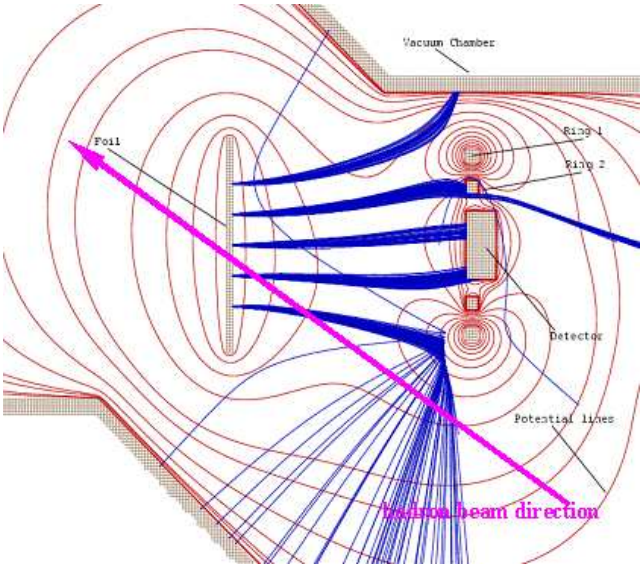

Figure 3.7: *Electron trajectories for the first prototype. The blue lines represent the electron trajectories, the red lines represent the electric field equipotential lines. The violet arrow indicates the hadron beam trajectory.*

A wider chamber obtained from the intersection of two cylinders and a cube, as shown in Figure 3.8, has been evaluated to minimize the effects of the interaction of the vacuum chamber with the FS electrodes. Focusing of the secondary electron has improved, as shown in Figure 3.9, but the electrons emitted outside the foil centre are lost and the diameter of the spot for the central point source is about 4 mm, much above the required resolution.

The situation improves with an electrostatic grid, 99% transparent to the primary beam, at 5 mm from the foil surface, as shown in Figure 3.10. The foil is polarized at - 20 kV, the external ring at - 3.6 kV, the internal ring, the grid and the detector are connected to the electrical ground. The electron collection is more efficient than in the previous version: the electrons emitted in a range of ± 22 mm from the foil centre are focused on the detector. Nevertheless this system is not acceptable since the spot diameter (2 mm) on the detector is still larger than required and all the electrons emitted outside the range of ± 22 mm are lost.

In Figure 3.11 is shown another solution with two circular rings added on the foil side and on the detector side. The voltages used in the simulation shown are -20 kV for the foil, -19 kV for the first ring and -24 kV for the second ring. The grid and the detector

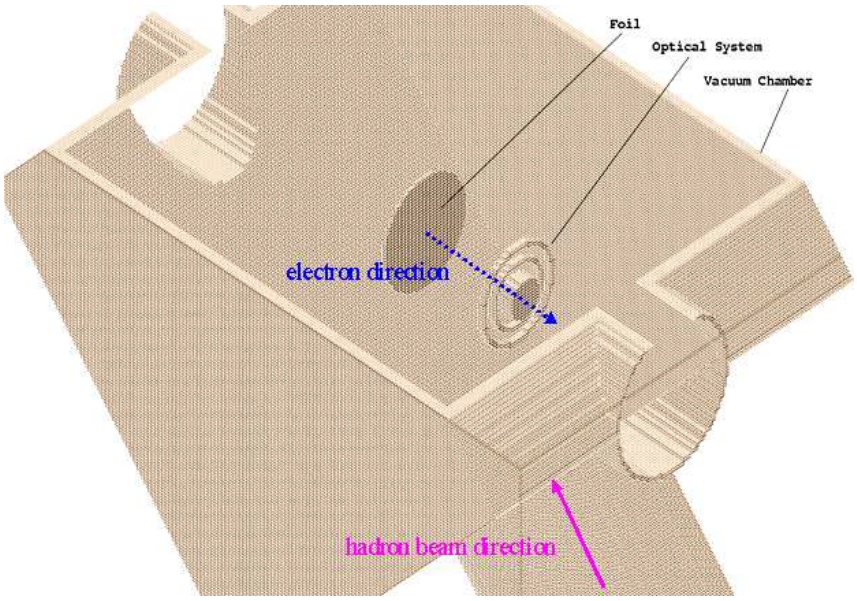

Figure 3.8: *The first prototype inserted in the second vacuum chamber.*

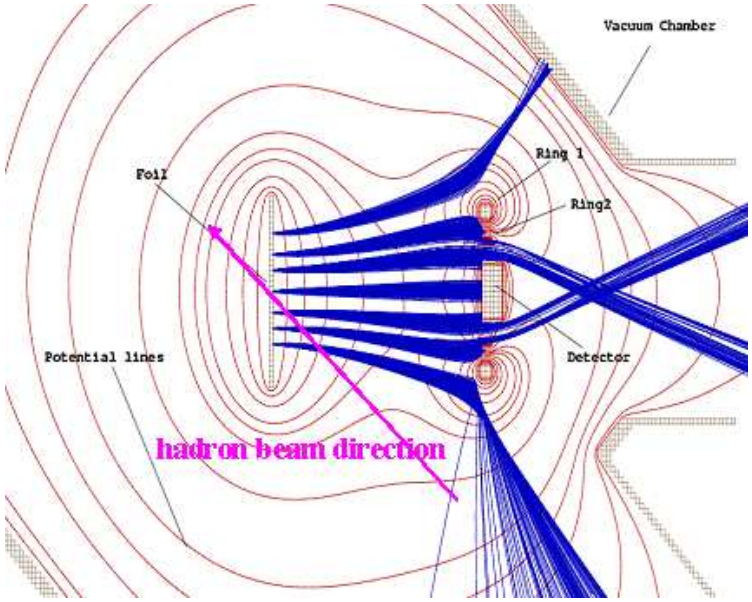

Figure 3.9: *Electron trajectories for the first prototype inserted in the second vacuum chamber. The blue lines represent the electron trajectories, the red lines represent the electrostatic field equipotential lines. The violet arrow indicates the hadron beam trajectory.*

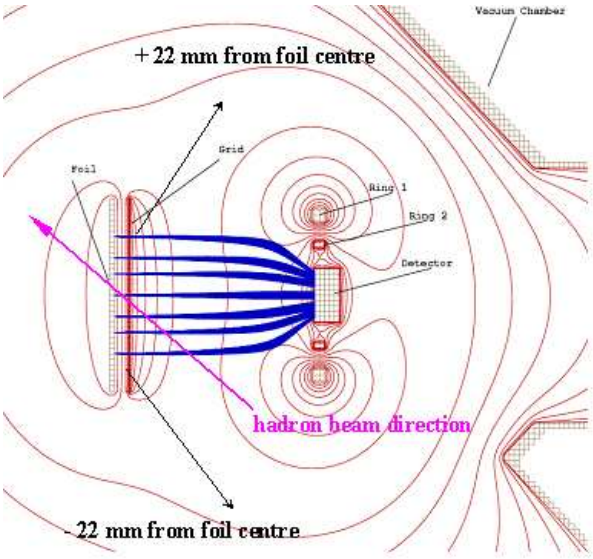

Figure 3.10: *The second prototype with an electrostatic grid at 5 mm from the foil. The blue lines represent the electron trajectories, the red lines represent the electrostatic field equipotential lines. The violet arrow indicates the hadron beam trajectory.*

are connected to the electrical ground. The electrons emitted from the whole surface are collected, but the resolution (1.8 mm) and demagnification factor (1.8) do not satisfy the requirements.

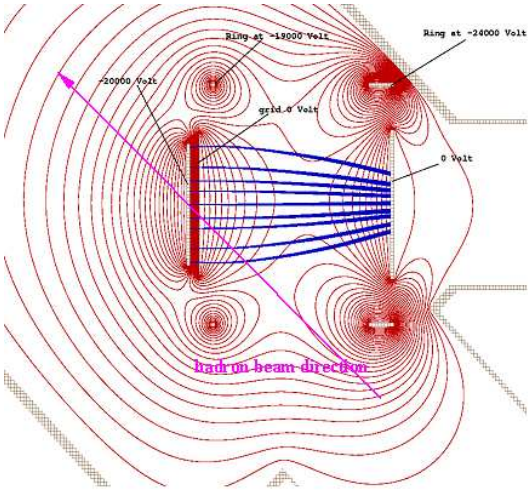

Figure 3.11: *The third prototype with an electrostatic grid at 5 mm from the foil and two circular rings. The blue lines represent the electron trajectories, the red lines represent the electrostatic field equipotential lines. The violet arrow indicates the hadron beam trajectory.*

The examples shown are a restricted sub-set of the numerous solutions examined: up to 50 different geometries have been investigated and discarded since they did not comply with all the constraints of the SLIM beam monitor. The major difficulty was to find a FS able to collect all the emitted electrons assuring at the same time the required resolution without intercepting the primary hadron beam. The key to solve the problem arose from the analysis of the electro-optics of the image intensifier tubes as discussed in Section 3.2.2.

3.2.2 Final prototypes of the focusing system

The final FS has been designed adapting to the beam monitor needs the electro-optical scheme of an image intensifier tube [113]. Image tubes are electro-optical devices used to detect, intensify optical images in the near ultraviolet, visible, near infrared, x- and γ-ray regions of the electromagnetic spectrum and for televising optical images. In general terms, an image intensifier tube consists of an image sensor, usually a photocathode, for the conversion of the incident radiant image to a low-energy electron image, an electron lens for the production of a high-energy electron image and of a phosphor screen for the conversion of the high-energy electron image to a light image.

Figure 3.12 shows the layout of an electrostatic focusing image tube that generates an inverted image. The tube has a spherical cathode, a spherical screen (the inner surface not visible in the figure) and a conical anode with the anode aperture placed near the centre of curvature of the photocathode. The curved cathode surface has the function to minimize the off-axis aberrations. The screen is positioned at a certain distance beyond the anode aperture to provide the desired image demagnification.

Since the photocathode and the screen are on curved surfaces, the input and output windows are often made of fibre optics for translation of curved images into plane images. In image tubes, variable magnification may be realized by the addition of a demagnifying lens in the area between the anode cone and the phosphor screen. This lens is usually called *zoom electrode*.

Figure 3.13 shows a possible set of electron trajectories inside the image tube with cross-focusing optics.

The FS for the beam monitor application reproduces the layout of an image tube: the cathode is represented by the aluminium foil, the focusing electrodes after the cathode are substituted by a cylindrical cage and the ring at the cage exit (see Figure 3.14). The final electrodes (cylindrically or conically shaped) play the role of the anode while the zoom electrodes is not used in our case. Unluckily it is not possible to use a spherical emitting aluminium surface because of the fragility of the foil or curved solid-state detectors; therefore the off-axis aberrations are more important than for image tubes as detailed in Section 3.2.2.1 and in Chapter 5, but still within the beam monitor specifications.

Three types of FS optimized for the three different solutions for the SE detection have been simulated. The first one, called the *conical prototype*, since the electrode at the cage exit is cone-shaped, has been optimized for the CMOS detector. The second prototype, called the *two cylinders prototype*, since the final electrode is composed of two cylinders,

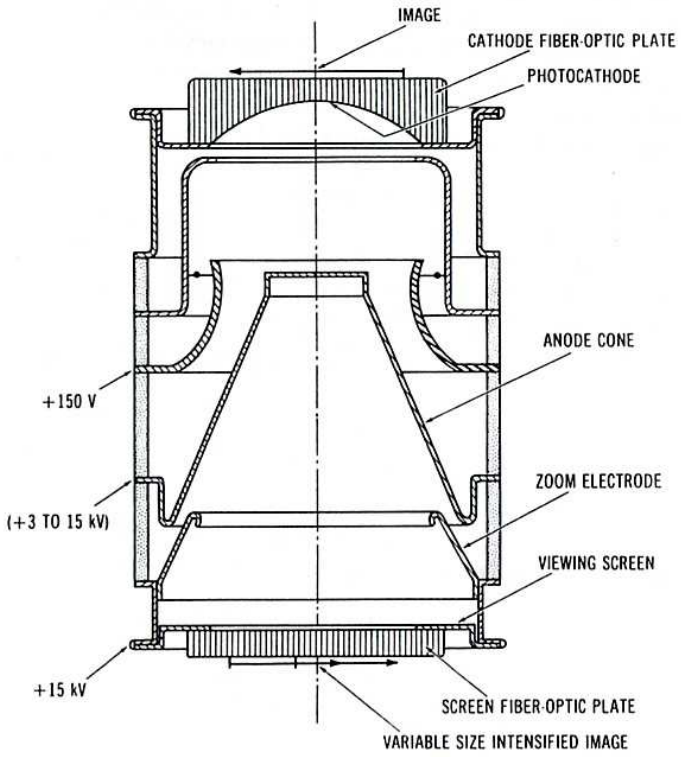

Figure 3.12: *Cross section of an electrostatic image tube. The different elements composing the tube are indicated in the figure. The inner surface of the screen, not visible in the picture, has a spherical shape.*

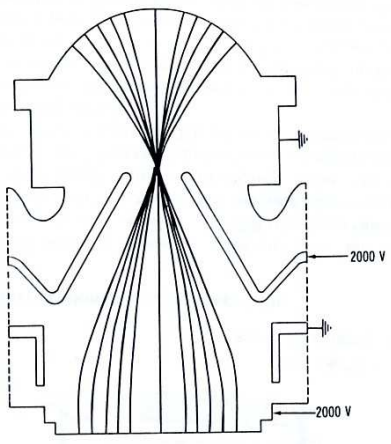

Figure 3.13: *Cross section of an electrostatic image tube with an example of electron trajectories.*

can be used for both CMOS and the first prototype pad detectors. The two systems are substantially equivalent, the conical prototype has a slightly better spatial resolution , but the choice in favour of the *two cylinders prototype* depended mainly on mechanical issues for the final electrodes construction.

As the pad sensor prototype used for the first tests has a 1.4 mm pitch, no demagnifying optics will ever fulfil the SLIM resolution requirements. Nevertheless, it has been decided to use the pad prototype for the first tests to assess the sensitivity to 20 keV electrons and to intensity variations of the primary beam. The manufacturing of the FS designed on the base of the constraints of the the final pad sensor (sensitive area diameter 50 mm, 1 mm pitch) was left for a later stage. This is the so called third solution and consists of a proximity focusing optics realized with an electrically grounded grid parallel to the foil polarized at -20 keV.

In Section 3.2.2.1 is analyzed in details only the *two cylinders solution* that has been engineered and constructed for the measurements described in this thesis. More details on the conceptual design of the chosen solution and the alternative FS can be found in [111].

3.2.2.1 The *two cylinders* prototype

Figure 3.14 represents the *two cylinders* FS. The thin aluminium foil is mounted on a cylindrical electrode, called *cage*; a circular ring electrode at the cage exit, called *ring*, allows to change the image sizes on the detector, mounted after the two final cylindrical-shaped electrodes. For an image diameter of 16 mm on the detector, the foil and the cage are supplied with -20 kV, the circular ring is polarized at -17.9 kV (nominal voltages) while the cylindrical-shaped electrodes and the detector are connected to the electrical ground.

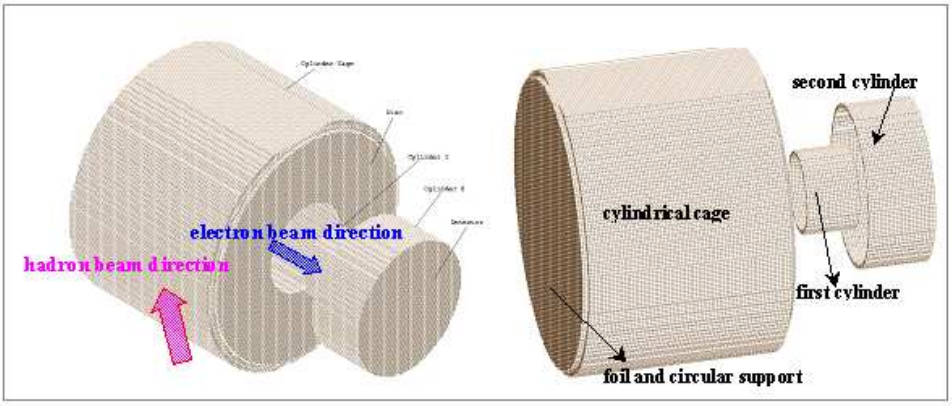

Figure 3.14: *The FS two cylinders prototype.*

A 60° degrees arc of the cylindrical cage electrode is covered with 26 wires of 40 μm diameter with 4 mm wire spacing for the primary beam crossing. Wires spacing and diameter have been chosen on the base of the following considerations:

- maximum transparency to the primary hadron beam (99%) over a region with at least 70 mm diameter;
- electrostatics field distortions due to wires spacing, also in the pessimistic hypothesis of one or two broken wires, do not perturb the SE trajectories;
- wire diameter is a compromise between transparency to the hadron beam, mechanical issues and the theoretical limit for electron field emission in high electric fields (10^7 V/cm), as detailed in Section 4.2.

A cross section of the *two cylinders* FS with in red the electrostatic field equipotential lines and in blue the electron trajectories is shown in Figure 3.15. One of the main advantages in favour of the *two cylinders* FS cylinders prototype with respect to the other solutions examined is the possibility to use only two power supplies, one for the cage and the foil polarization and the other for the ring at the cage exit.

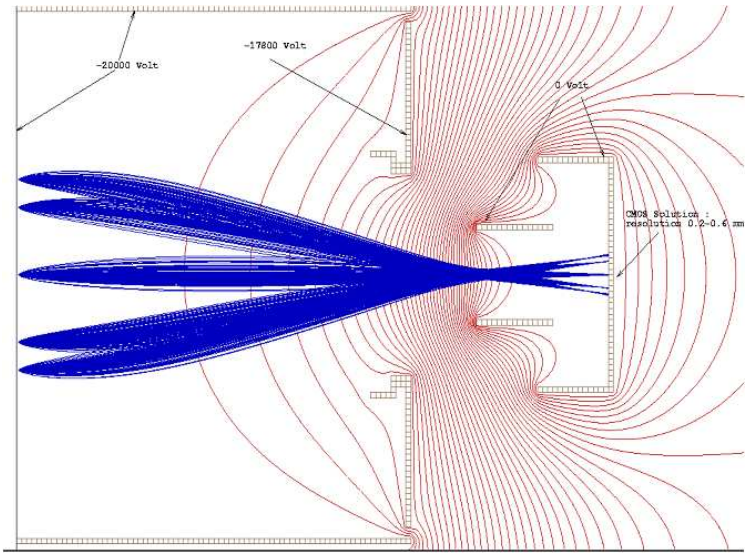

Figure 3.15: *The two cylinders prototype for the CMOS sensor with in red the electrostatic field equipotential lines and in blue the electron trajectories (grid pitch 2 mm).*

The longitudinal length of the cage is 156 mm, the diameter of the cage is 192 mm. The overall length of the system is 234 mm. The dimensions of the aluminium foil with its circular support, the cylindrical cage, the ring and the two cylindrical electrodes are illustrated in Figure 3.16.

The electrostatic focusing process is clearly represented in the potential energy view of Figure 3.17 where the red lines represents the electrostatic field equipotential lines, the blue lines the electron trajectories and the green grid the potential energy surfaces.

To evaluate the resolution of the proposed FS, the images on the detector corresponding to point sources at the Al foil were analyzed. Each source point on the aluminium foil is

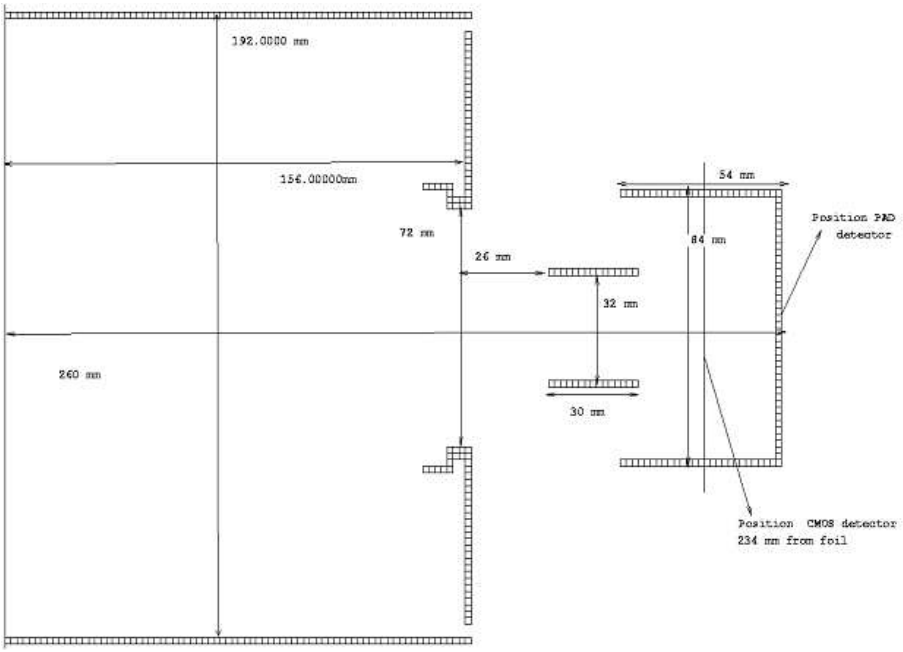

Figure 3.16: *Dimensions of the FS two cylinders prototype (grid pitch 2 mm).*

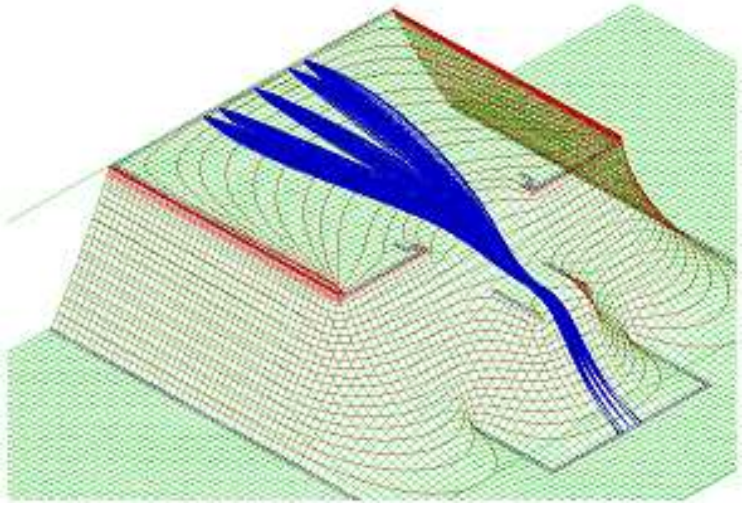

Figure 3.17: *Potential energy view for the two cylinders FS prototype.*

imaged on the detector as a round spot that, due to the aberration effects has a smaller diameter for centred emitting sources (0.2 mm) than the off-axis (± 35 mm from the foil centre) ones (0.6 mm), as shown Figure 3.18, a detail of the image in Figure 3.15.

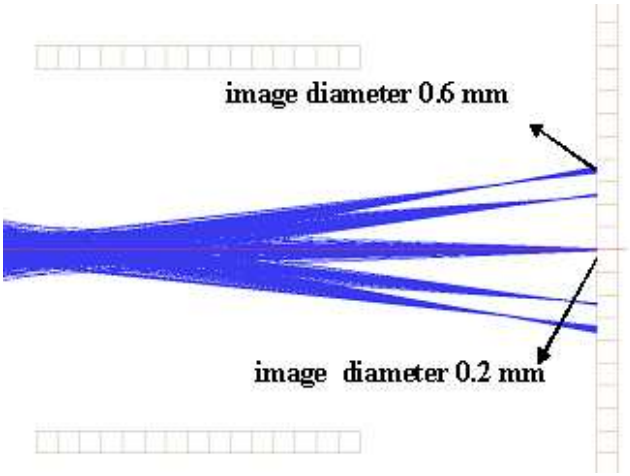

Figure 3.18: *Detail of the foil source points image on the detector (grid pitch 2 mm).*

Figure 3.19 shows the profile analysis of a gaussian primary beam (σ_{foil} = 2.5 mm) hitting the aluminium foil at different distances from the *two cylinders* FS symmetry axis. The image obtained on the detector is a gaussian profile with standard deviation sigma: $\sigma^2_{detector} = (\sigma_{foil}/F)^2 + \delta^2$, where δ represents the transmission error of the system that includes the contribution of the aberration effect and the energy and angular spread of the SE and F the demagnification factor. The demagnification factor and the δ value are evaluated for each position on the foil and reported in the figure.

The effects of aberrations increase as the beam moves toward the outer side of the foil as expected (δ varies from 22 μm to 242 μm, as shown in the figure). Nevertheless also the resolution for the outer beam (δ = 242 μm) is still close to the SLIM beam monitor requirement and acceptable for off-centred beams.

The behaviour of the demagnification factor $F(r, V_0, V_1)$ as a function of the distance from the FS symmetry axis has been evaluated, where V_0 is the cage electrode voltage and V_1 the ring electrode voltage. The results for the nominal voltages V_0 = -20 kV and V_1 = - 17.9 kV are shown in Figure 3.20. The linear fit of the values is expressed by the relation: $F = a \cdot r + b$ with b = 5.3259 ± 0.022 and a = -0.0131 ± 0.0010. The largest position incertitude from the foil centre for the source points at ± 35 mm on the detector is ∼ 8% (Figure 3.18). In a conservative way, the same value has been used as the upper limit incertitude on the demagnification factor, as shown in Figure 3.20.

To avoid the interaction of the primary hadron beam with the wire grids and the consequent secondary emission from the wires, a solution with an aperture on the cylindrical cage electrode to allow the hadron beam crossing, shown in Figure 3.21, was simulated. The

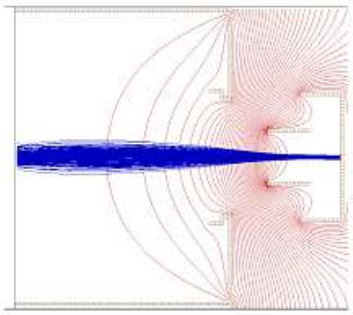

gaussian beam (σ=2.5 mm) hitting the foil center
F(0) = 5.326

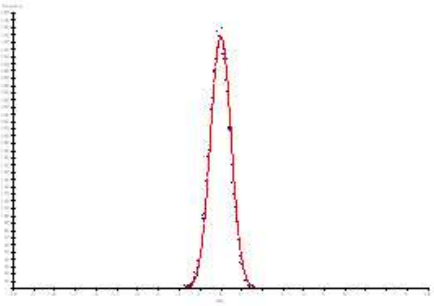

image on the detector:
σ = 0.478 mm, δ = 22 μm

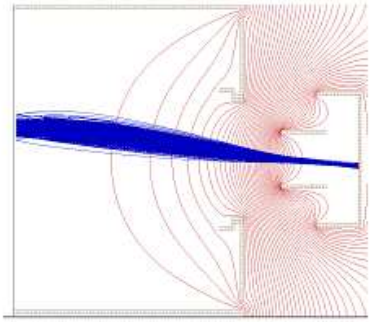

gaussian beam (σ=2.5 mm) hitting the foil at 20 mm from the center
F(20) = 5.064

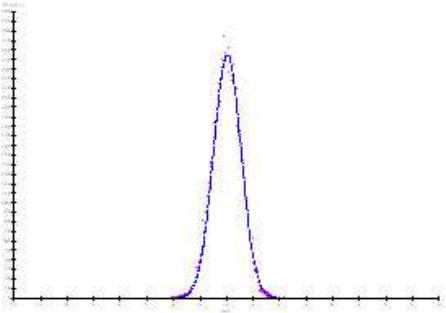

image on the detector:
σ = 0.516 mm, δ = 153 μm

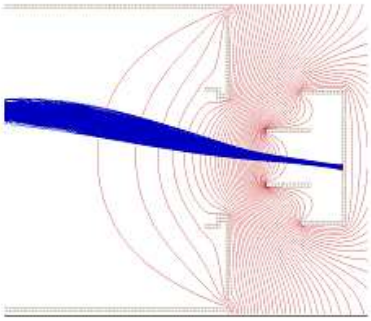

gaussian beam (σ=2.5 mm) hitting the foil at 29 mm from the center
F(29) = 4.91

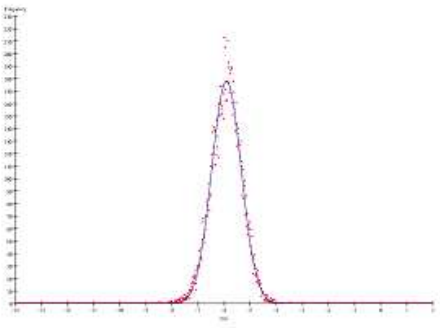

image on the detector:
σ = 0.564 mm, δ = 242 μm

Figure 3.19: *Profile analysis of a gaussian beam for different distances (r= 0, 20, 29 mm) from the FS symmetry axis.*

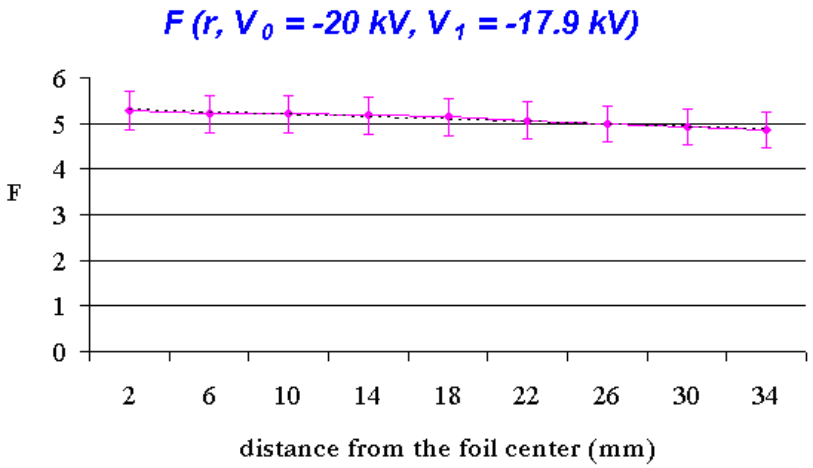

Figure 3.20: *Demagnification factor as a function of the distance from the FS symmetry axis (V_0 is the cage electrode voltage, V_1= is the ring electrode voltage).*

aperture has the same diameter of the foil (7 cm). The results of the simulations with the electron trajectories are shown in Figure 3.22. It is clear that the aperture in the cylindrical cage strongly perturbs the electric field, electrons are lost and the optical properties of the system destroyed.

The emission of SE from the cage grid hit by the the primary hadron beam was also simulated. Figure 3.23 shows a simulation of the trajectories of such electrons deflected toward the first cylinder electrode and stopped without disturbing the detector signal.

Due to out-gassing problems of the first FS prototype, a second prototype using high vacuum (10^{10} Torr) materials was designed and constructed as described in Section 4.2.2. Mechanical and material considerations lead to a slight revision of the geometry of the electric insulation between the cage and ring electrodes, as shown in Figure 3.24. The changes produced did not, anyway, modify the electrical field seen by the SE and, therefore, the optical properties of the FS described above.

The *two cylinders* FS design can be optimized for the pad sensor, lengthening the final cylindrical electrode (54 mm instead of 28 mm). This solution is represented in Figure 3.25. For an image diameter of 22 mm on the detector, the foil and the cage are supplied with -20 kV, the circular ring is polarized at -16.8 kV, while the cylindrical-shaped electrodes and the detector are connected to electrical ground. Due to time and money constraints, this device has not been constructed and the FS optimized for the CMOS sensor has been used also for the in-beam tests with the pad sensor.

In any case, in the hypothesis of a final FS prototype for the pad sensor, the solution adopted for the SE transport emitted for the Al foil polarized at - 20 kV will consist of

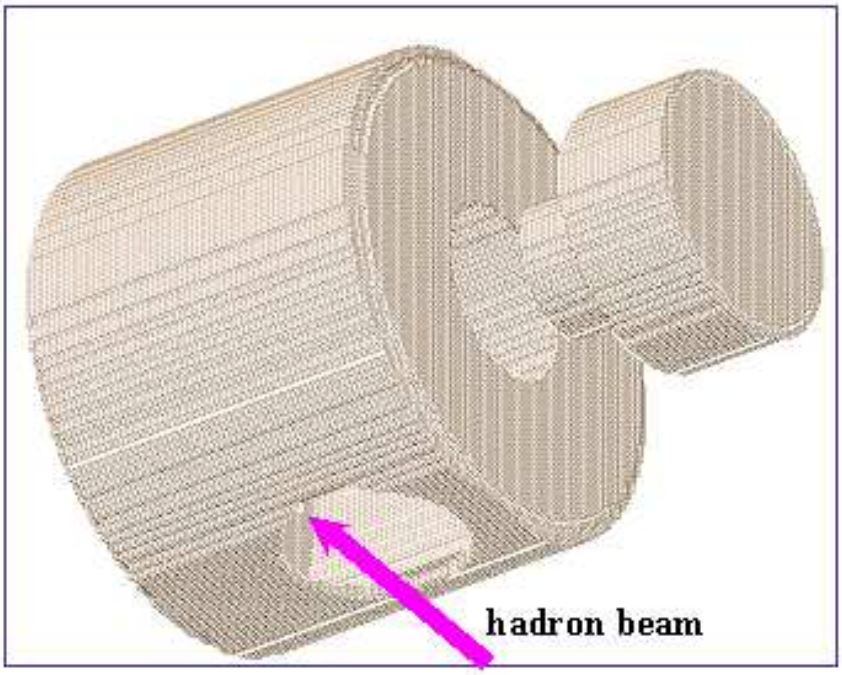

Figure 3.21: *Cylindrical cage electrode with an aperture to allow the hadron beam crossing.*

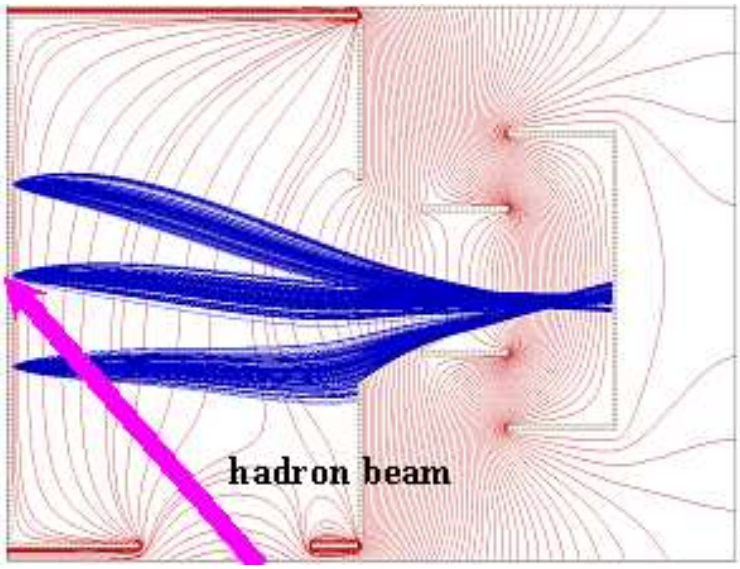

Figure 3.22: *Distortion of the equipotential lines (red) caused by the cage electrode aperture and electron beam trajectories (blue).*

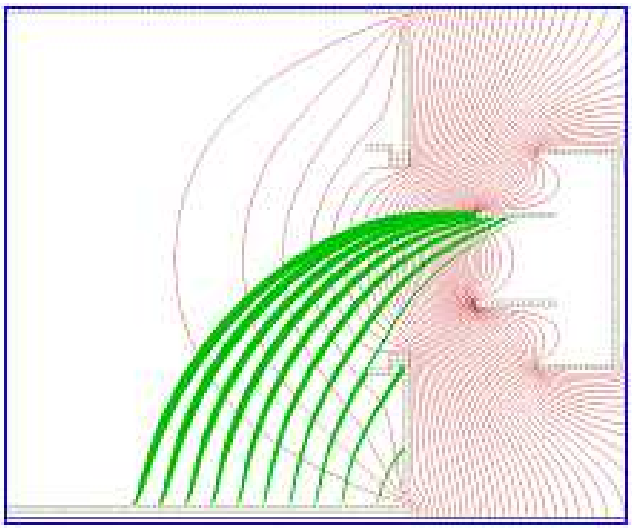

Figure 3.23: *The secondary electron emission from the cage electrode grid.*

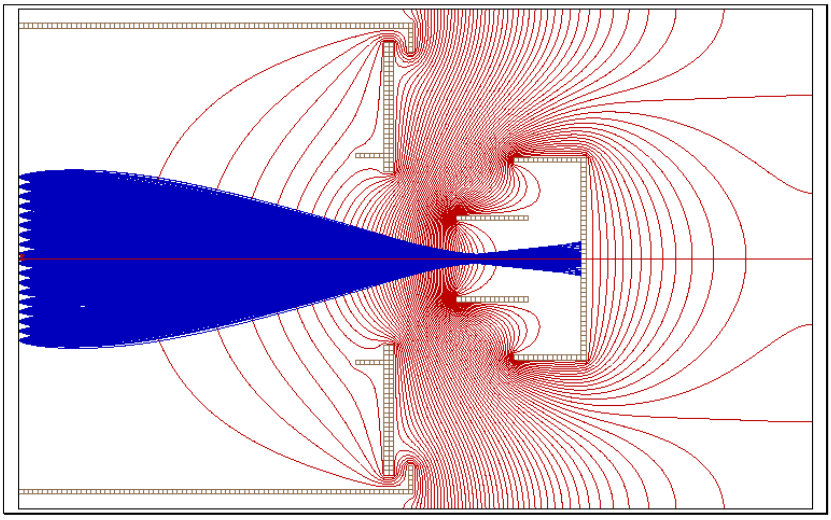

Figure 3.24: *The two cylinders final prototype for the CMOS sensor with in red the electrostatic field equipotential lines and in blue the electron trajectories.*

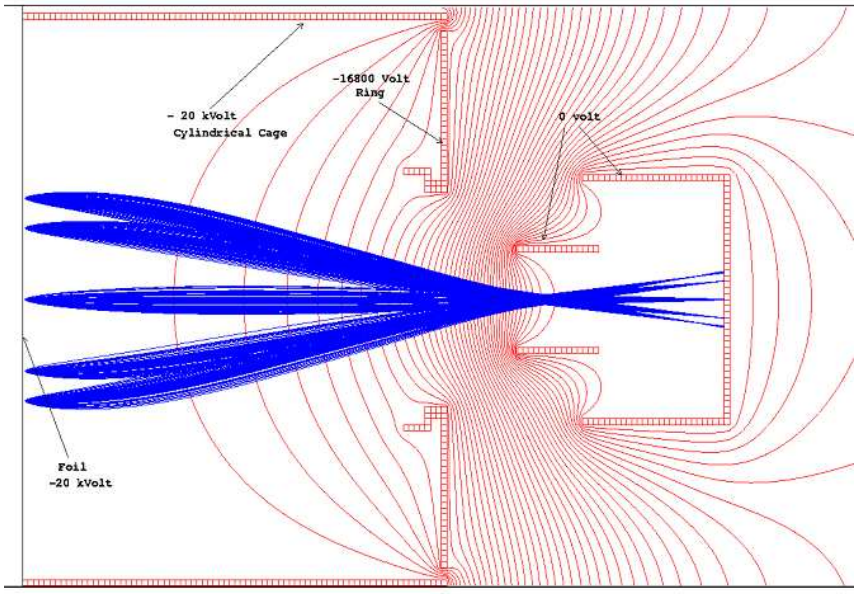

Figure 3.25: *The two cylinders prototype for the pad sensor.*

a 1:1 electro-optics solution, realized with an electrically grounded grid as illustrated in Figure 3.26. The foil is supported by a metallic disc with a diameter of 192 mm as that used for the cylindrical cage of the CMOS prototype. The grid wires have a diameter of 20 μm and the wire spacing is 2 mm to assure a transparency to the proton beam of 99%.

Analysis of the image on the sensor proved that for this configuration δ is less than 1000 μm, as required with a 1:1 optics.

3.3 Hadron beam - SLIM monitor interaction study

The beam-target interaction study consists of the following steps:

- study of the hadron beam emittance blow-up caused by the plural scattering of the beam in the thin aluminium foils;
- study of the hadron beam perturbation caused by the electrical field of the FS;
- study of the aluminium foil heating at the hadron beam crossing.

Problems with the first prototype of the FS (described in Section 4.2.1) caused delays to the project that postponed the completion of the beam-target interaction study. Simulations using the code Geant4 [114] has been scheduled for a later stage [115] when a second beam profile monitor at a convenient distance from the SLIM, taking into account the extraction line optical parameters, will be installed to measure the beam emittance blow-up.

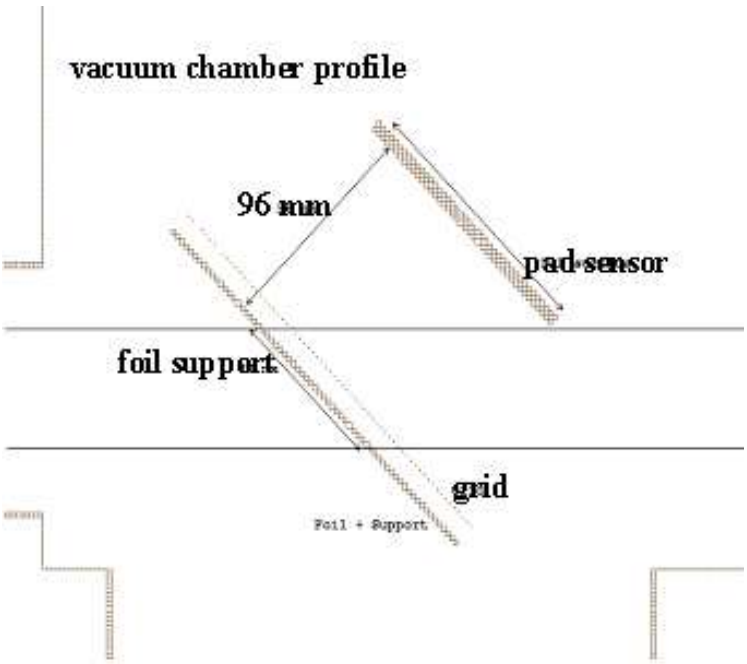

Figure 3.26: *The FS optimized for the pad sensor.*

The results of a previous study [84], that demonstrates the negligible thin foils effects on the hadron beam emittance, are summarized below. The typical aluminium foils thickness of 0.2 - 0.3 μm does not allow the use of the Highland formula for multiple scattering [116, 117] to evaluate the beam emittance blow-up. A Monte Carlo programme for plural scattering has been therefore developed. The results of the study show that with a thin aluminium foil of 0.2 μm thickness, the emittance blow-up is less than 10% for 60 MeV protons (worst case, as the effect is larger for lower beam energies). The exact value depends on the beam parameters at the monitor position in the beamline.

If the SEM foils are placed at a minimum of the β-function, the increase is of the order of 2 - 4% for 60 MeV protons. If the SEM foil is placed at a maximum of the β-function, the increase is of the order of 7 - 10%. It is evident the possibility to study an optical scheme that includes a limited number of SLIM monitors in some specific *less sensitive* position, without causing unacceptable disturbance to the therapy beam, the critical figure being determined by the extraction line acceptance.

A preliminary study [118] including 10 thin SEM foils in 60 meters of extraction lines (from the extraction section to the farthest treatment room) showed that the perturbation due to the material in the beam causes an acceptable increase in the emittance value (from 3.0 to 5.5 π mm mrad) if compared to the acceptance value for which the lines were designed (8 π mm mrad). A similar study should be repeated for a different line layout.

3.3.1 Study of the hadron beam perturbation caused by the electric field of the FS

To evaluate the effect of the FS on the primary beam, the maximum deflection angle of a 60 MeV proton beam in the FS electrostatic field has been simulated with the code SIMION 3D. The results of the simulations are shown Figure 3.27, representing a cross section of the vacuum chamber with the FS installed. The green lines represent the proton beam trajectories in the FS electrostatic field.

The maximum calculated deflection angle for a 60 MeV proton beam is 150 μrad (worst case) and it decreases with the increasing primary beam energy. It can be concluded that the primary beam deflection angle caused by the FS electrostatic field can be easily corrected using the steering magnets of the extraction line.

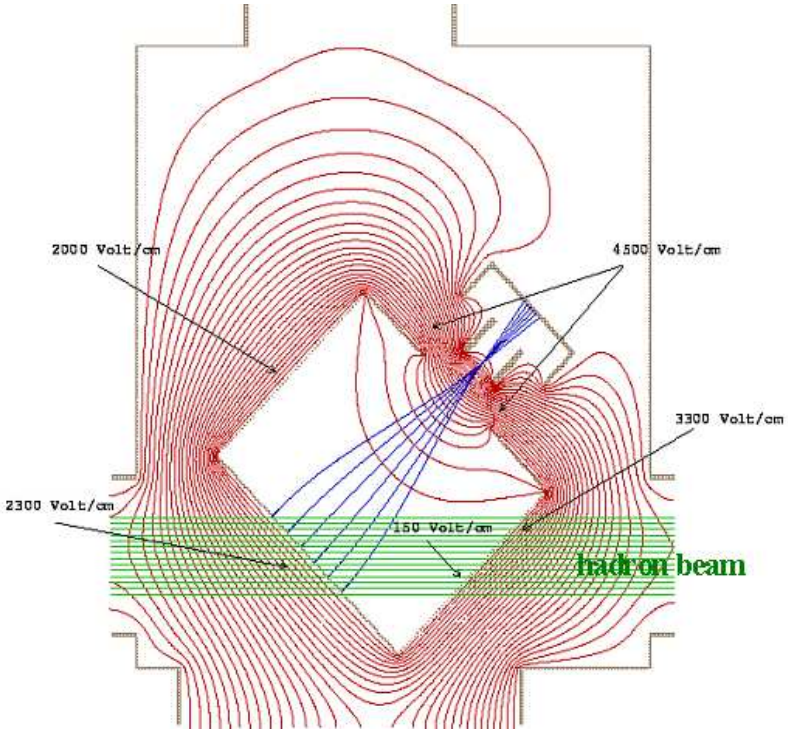

Figure 3.27: *Proton beam trajectories (green lines) in the electric field of the FS (the blue lines represent the electron trajectories, the red lines represent the electrostatic field equipotential lines).*

3.3.2 Study of the aluminium foil heating

The hadron beam traversing the Al foil exchanges part of its kinetic energy with the electrons of the medium causing heating of the target. In equilibrium conditions the absorbed heat is

equal to the emitted heat and the equilibrium temperature can be calculated by the balance condition of the black body radiation expressed by the relation (3.11):

$$Q_{absorbed} = Q_{emitted} \tag{3.11}$$

where $Q_{absorbed}$ is the heat absorbed by the target and $Q_{emitted}$ is the heat emitted from the target. The value of the equilibrium temperature determines if the heating effects could induce the target rupture.

In the following calculation, the equilibrium temperature has been evaluated for a 30 MeV proton beam for a beam current of 1 mA in the conservative hypothesis of using the SLIM beam monitor for the intensity/profile measurement of the beam for radioisotope production, a possible alternative application with a broader market (mentioned in the thesis conclusions).

Aluminium parameters:

- Density: $\rho_{\mathrm{Al}} = 2.7$ g/cm^3
- Al specific heat: $C_p = 0.897$ Joule/(deg $\cdot$ g)
- Melting point temperature: $T_m = 923$ °K

Aluminium Foil parameters:

- Foil diameter: $\Phi = 70$ mm
- Foil thickness: $h = 0.25$ μm

Proton Beam parameters:

- Energy: $E_p = 30$ MeV
- Current: $I_p = 1$ mA
- Beam cross section diameter (2σ): $d = 10$ mm
- Number of protons per second: $N_p = I_p/\mathrm{e} = 6{\cdot}10^{15}$ p/s
- Energy loss per proton at 30 MeV: $dE_p/dx = 14.5$ MeV cm^2/g (from Bethe-Bloch equation (3.4))

The absorbed heat per impinging proton can be evaluated with the relation: $Q = (dE_p/dx\ \rho_{\mathrm{Al}}\ \mathrm{h})\ e\ 10^6 = 1.63\ 10^{-16}$ Joules. The absorbed total heat is then: $Q_{absorbed} = Q\ N_p = 1.0157$ Joule/s. The equilibrium temperature T_e is evaluated with the relation for black body radiation from a body initially at room temperature $T_0 = 293$ °K (room temperature):

$$Q_{emitted} = \sigma\ 2\ S\ (T_e^4 - T_0^4) \tag{3.12}$$

where $\sigma = 5.67\ 10^{-12}$ Joule/s cm^2 deg^4 is the Stefan Boltzmann constant and S the heated foil surface: $S = 2\ \pi\ r^2 = 38$ cm^2.

With the balance condition (3.11):

$$T_e = \left(\frac{Q_{absorbed}}{2\sigma S} + T_0 \right)^{1/4} \qquad (3.13)$$
$$T_e = 314°K = 41°C$$

The equilibrium temperature T_e (314 °K) results much lower than the melting temperature T_m (923 °K). It is therefore reasonable to assume that no mechanical stresses affects the Al foil.

This evaluation does not take into account that the beam hits the foil on a limited area (beam diameter $\sim$ 10 mm to be compared with the foil diameter $\sim$ 70 mm) and the mechanical stresses that can be caused by local instantaneous rise in the temperature. A possible solution in this event consists in heating the foil at a constant temperature T, with $T \approx T_e$.

An experimental validation of the calculation above is foreseen on an aluminium and a carbon foils with a 1 mA proton beam extracted from a cyclotron for radioisotope production.

Chapter 4

SLIM particle beam monitor engineering design and construction

The SLIM beam monitor engineering design and construction is based on the results of the conceptual design described in Chapter 3. Section 4.1 refers to the engineering and construction of the beam monitor vacuum chamber. The main constraints in the tank design were to allow the rotation of the electrostatic focusing system inside and outside the beam path, keeping the vacuum tank longitudinal flange-to-flange distance minimum and avoiding discharge effects between the electrically grounded vacuum chamber and the focusing system high voltage electrodes.

Several designs with different geometries and costs have been examined. The final parallelepiped-shaped prototype has been chosen considering that the tank should be versatile enough to host different detection systems not fully designed at the time of the vacuum chamber construction and on the base of mechanical and construction costs issues detailed in Section 4.1.

A first prototype of the SLIM focusing system was developed and is described in Section 4.2.1. Vacuum problems caused by the out-gassing of the stesalite (special fibre glass trademark) and fibreglass used for the construction of the optical lenses were experienced even if the material had been previously used for high vacuum (below 10^{-6} Torr) detectors. The residual gas pressure inside the vacuum chamber decreased asymptotically towards a limit value of $4 \cdot 10^{-5}$ Torr and measurements were disturbed by the residual gas ionization caused by secondary electrons.

Vacuum tests of the optical lenses proved that the out-gassing factor of the stesalite and fibreglass components was higher than expected due to a poor material quality. To improve the performance of the focusing system, a second prototype using high vacuum materials such as stainless steel for the electrodes and Vespel (polyamide resin) for the insulating parts

was constructed and is described in Section 4.2.2. The second prototype was used for the laboratory and beam tests reported in Chapter 5 and 6, respectively.

In Section 4.3 is described the process followed to manufacture the very thin foils for the secondary electrons production. The targets consist of 65 to 70 mm diameters foils made by a support of 0.1 - 0.3 μm of Al_2O_3 coated on each side with 0.01 - 0.05 μm of Al. Secondary emission is a surface phenomenon and interests only the aluminium most superficial layer. Ten foils underwent the full process, other forty foils have been anodized and baked and should undergo the finals steps of the preparation procedure.

A dedicated control system has been developed for the control of the SLIM beam monitor equipment and is described in Section 4.4. The system is based on the National Instruments Field-Point FP2010 intelligent Ethernet controller interface and the user interface panel developed with LabVIEW Real-Time software. It guarantees that the process automation has the maximum safety for both users and instrumentation.

Section 4.5 describes the LabVIEW software for the acquisition and processing of the CCD camera image; the CCD, part of the commercial detector (Section 2.4.1), is connected to a PCI card. Besides the acquisition of the intensity matrix for the whole sensor area or for a selected region, the software developed allows background, single and multiple images acquisition and basic image processing.

4.1 Vacuum and mechanical system design and construction

The SLIM vacuum chamber (VC) has has been designed on the base of the following constraints:

- a minimum distance of 5 $\div$ 7 cm between the focusing system electrodes polarized at -20 $\div$ -30 kV and the inner surface of the vacuum chamber (connected to the electrical ground) to avoid breakdown effects. For the same reason, all the sharp metallic edges were rounded;

- the focusing system can rotate of 45° degrees around a vertical axis fixed to the metallic ring supporting the aluminium foil. The rotation allows the in-out positioning of the focusing system in respect to the hadron beam trajectory. The movement is driven by an actuator outside the vacuum chamber and connected to the focusing system by a rigid vertical axis with a bellow to guarantee the vacuum insulation;

- the transversal dimension of the vacuum chamber has been fixed taking into consideration the space needed for the rotational movement of the focusing system; extra margins are included considering that:

  - the ceramic for the solid state detectors, fixed at the final cylindrical electrode of the focusing system, was not designed at the time of the vacuum chamber design;

  - the minimum safety distances between the FS polarized electrodes and the electrically grounded vacuum chamber to avoid breakdown effects were included in the design;

- the installation of the focusing system inside the vacuum chamber is made through an aperture with a flange of 270 mm;

- besides the rotational bellow, the vacuum chamber is equipped with different kinds of flanges for the connection to the turbo pump, the insertion in the hadron beam pipeline and with medium and high voltage feedthroughs (the former for the MCP/silicon detector bias, the latter for the focusing system polarization);

- the CCD camera, used for the first laboratory and in-beam tests, was mounted on a smaller (DN35) flange and detects the light emitted in the interaction of secondary electrons with the phosphor screen through a glass view-port.

Different vacuum chambers have been designed as illustrated in Figures from 4.1 to 4.4. The first VC prototypes examined with the rotation of the focusing system around a horizontal axis were discarded to minimize the solicitations on the rotation axis itself [119] (the FS weight is $\approx$ 1 kg). The final solution chosen for the SLIM beam monitor on the base of mechanical and cost issues is described in Section 4.1.3.

4.1.1 Sphere vacuum chamber design

Figure 4.1 shows the spherical vacuum chamber solution. The sphere radius is 225 mm and the longitudinal flange-to-flange distance, L_{F-F}, is 550 mm.

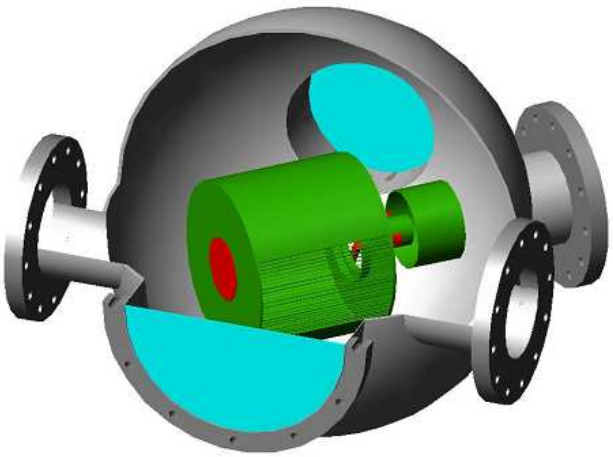

Figure 4.1: *The spherical vacuum chamber prototype: internal view with the FS.*

A second version of the spherical vacuum chamber with radius of 200 mm had also been examined. The higher manufacturing costs of the spherical solution in respect to the parallelepiped one could be contained for this solution thanks to the already available standard mould for the sphere realization of an eventual sub-contractor. Unluckily this solution does not include sufficient margins both in terms of breakdown effect and space for the not yet defined solid-state detector ceramics.

As the aim of this study was the realization of a prototype suitable for different type of secondary electrons detectors, it was decided to discard this more elegant but unpractical solution that can be, anyway, reconsidered in an engineering stage.

4.1.2 Cylinder vacuum chamber design

The first cylindrical prototypes examined foresaw a translational motion of the focusing system inside and outside the beam path with a cylindrical tank diameter of 376 mm and a total longitudinal occupancy L_{F-F} of 460 mm. The horizontal cylindrical tank solution was discarded for the axis solicitation problem mentioned above, while in the vertical cylinder solution, the port to insert and extract the focusing system and replace the most delicate part of it, the thin aluminium foil, would have been in a very uncomfortable position. Moreover the cost issues of a mechanical vacuum tight system to translate the FS of at least 125 mm are not negligible.

The drawbacks illustrated above are overcome in the hypothesis of a rotational motion around a vertical axis of the focusing system as shown in Figure 4.2.

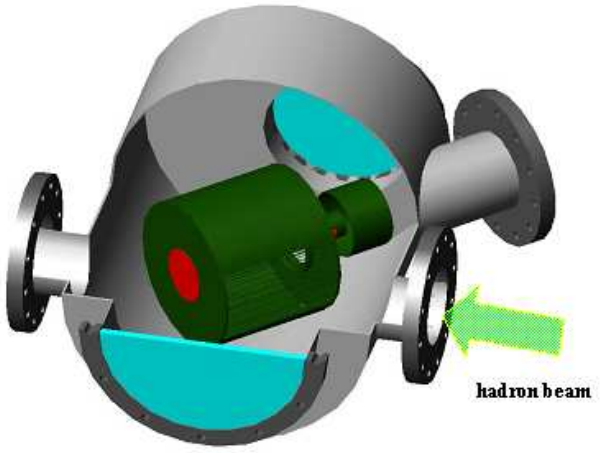

Figure 4.2: *The cylindrical vacuum chamber prototype: internal view with the FS.*

In this case the diameter of the cylindrical tank is 410 mm, for a total longitudinal occupancy L_{F-F} of 500 mm (larger than the final parallelepiped shaped vacuum chamber described in Section 4.1.3). Also a skew solution, with the cylinder axis coincident with the

focusing system axis was examined. The idea at the base of this solution is the translational motion (180 mm) along the tank axis, but it was discarded due to the largest longitudinal occupancy (in this case due to the cylinder volume, not the flange to flange distance) among all the examined solutions (650 mm for a cylinder diameter of 320 mm).

4.1.3 Final vacuum chamber prototype

Besides the pros and cons discussed above for each solution, a strong point in favour of the parallelepiped shaped vacuum chamber is the simplicity of the alignment of the focusing system in the beam path when the movement system is mounted on a flat surface. More in general, the alignment within tolerances of each port and related equipment is easier.

On the base of the mechanical and construction costs issues, besides longitudinal and transversal occupancy considerations, taking into account that the vacuum tank will host different detection systems not fully defined at time of the VC design and has, therefore, to be versatile, the choice has been in favour of the parallelepiped shaped vacuum chamber. The final design of the SLIM beam monitor vacuum chamber with the final version of the focusing system are shown in Figures 4.3 and 4.4. The longitudinal flange-to-flange occupancy L_{F-F} is 460 mm. On the upper part of Figure 4.3 is a schematic representation of the FS motion and polarization systems.

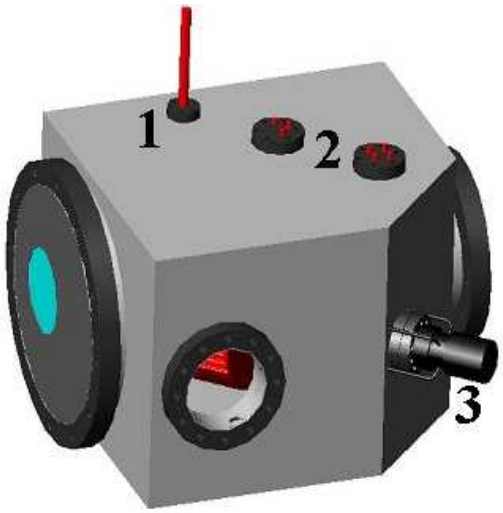

Figure 4.3: *Final version of the parallelepiped shaped vacuum chamber: external view with FS and motion (1), polarization (2) and CCD (3) systems. The larger flange with 270 mm aperture diameter (on the left) is used for the installation of the FS in the vacuum chamber*

The final prototype of the vacuum chamber in the workshop of the sub-contractor before chemical cleaning is represented in Figure 4.5. Figure 4.6 show the vacuum chamber in the CERN laboratory mounted on a variable height support, while Figure 4.7 is a detail of the upper part with the polarization and rotation flanges.

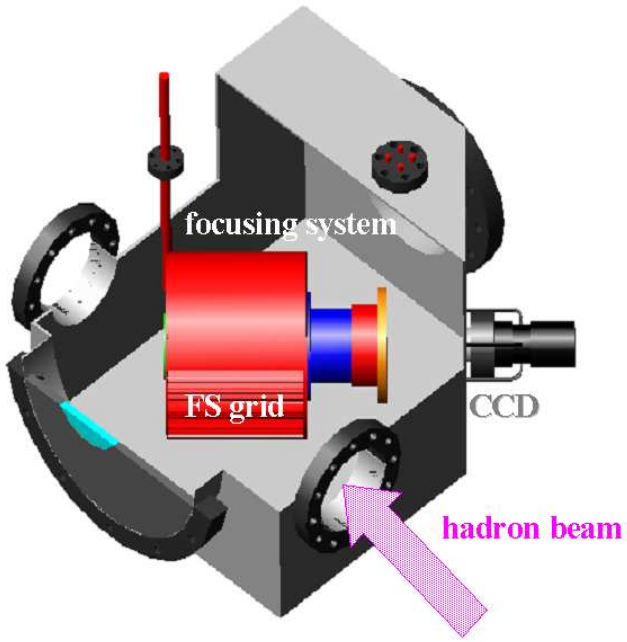

Figure 4.4: *Schematic drawing of the final version of the parallelepiped shaped vacuum chamber: inside view with the final FS (a CCD camera is mounted on the DN35 flange).*

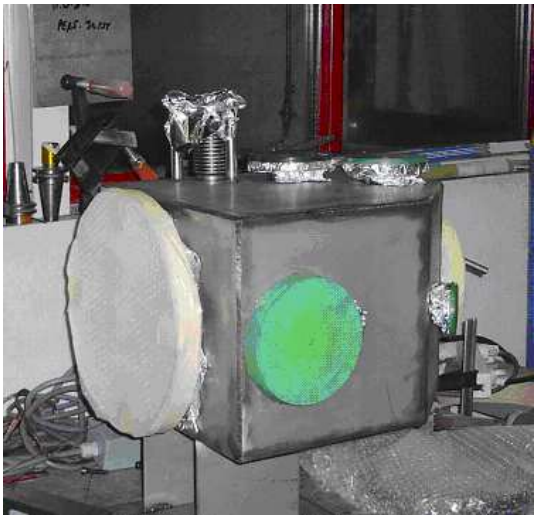

Figure 4.5: *SLIM beam monitor vacuum system in the sub-contractor workshop.*

Figure 4.6: *SLIM beam monitor vacuum system mounted on a variable height support in the CERN laboratory.*

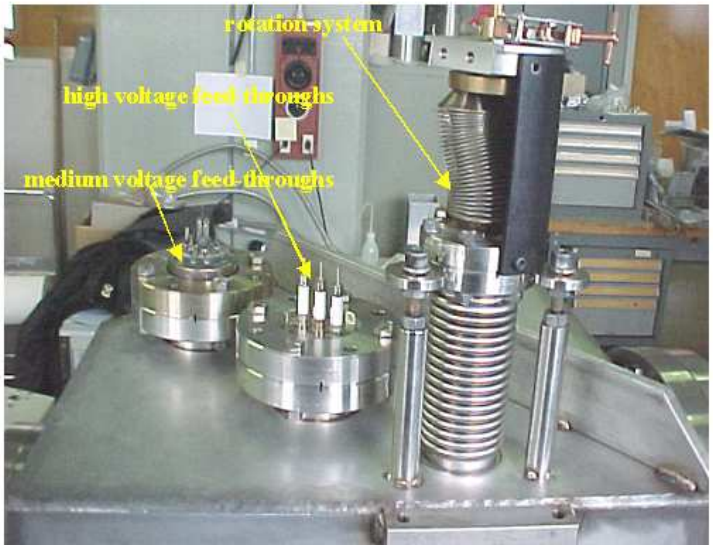

Figure 4.7: *SLIM beam monitor vacuum system, detail with the polarization feed-throughs and the rotation system.*

4.2 Secondary electrons focusing system design and construction

4.2.1 First focusing system prototype

The FS technical design consisted of the following steps:

- definition of the materials for the electrodes and the insulating parts to assure the maximum rigidity and lightness of the focusing system;
- definition of the wires of the cage electrode material, thickness ad spacing; evaluation of the wires field emission;
- rounding of the electrodes sharp edges to minimize breakdown effects;
- study of a rotation system (45° degrees) around a vertical axis for the in-out positioning of the system with respect to the hadron beam trajectory;
- design of the FS rotary axis with non-conductive connection to isolate the high voltage electrodes.

A first prototype of the SLIM focusing system was developed (Figure 4.8) and is described in details in [35].

The aluminium foil, as shown in the picture, is supported by two circular stainless steel rings 1.5 mm thick. The electrode that closes the cage on the foil side is made of 1.5 mm

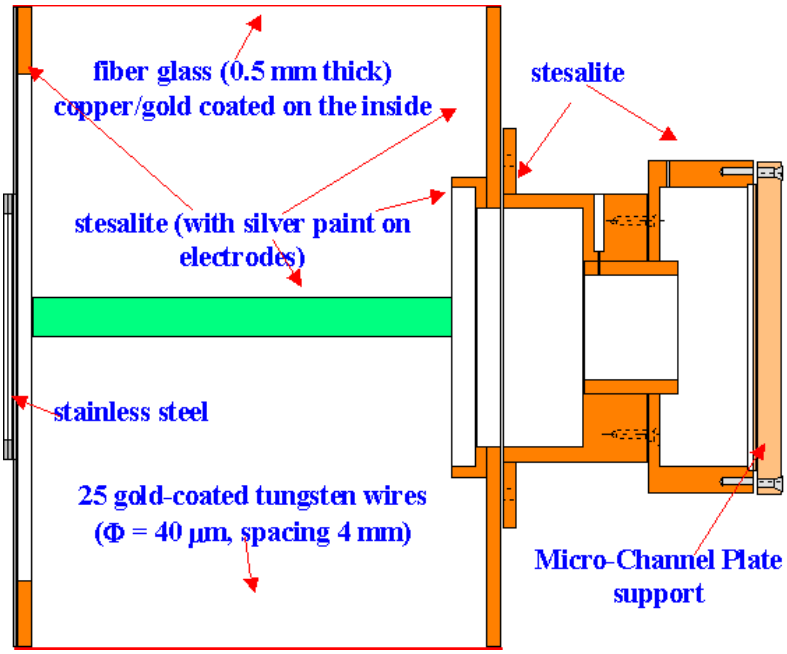

Figure 4.8: *Technical design of the first focusing system prototype with specification of the construction materials.*

thick stainless steel disk, while the cylindrical wall of the cage is made of a gold/copper coated 0.5 mm thick fibre glass foil over an arc of 300° degrees and for the remaining 60° degrees is covered with a grid of 40 μm diameter gold-coated tungsten wires spaced by 4 mm. Wire diameter and spacing has been chosen to guarantee the field uniformity in the secondary electrons trajectory region also in the hypothesis of one or two broken wires (Section 3.2.2.1), the maximum transparency to the primary hadron beam (the grid is 99% transparent to the primary hadron beam) and a negligible field emission effect.

Field emission or cold emission occurs when a high voltage difference exists between the cathode and the anode. The presence of an electric field causes a deformation and thinning of the potential barrier at the surface of a metal. The electron behaves as a wave with a finite probability to tunnel through the barrier. In the case of an exceedingly fine wire two are the relevant parameters to evaluate field emission: the wire surface smoothness and its diameter. The field limit for electron emission is E = 10^7 V/cm [120].

For the SLIM beam monitor application, V was evaluated with equation (4.1):

$$E(r) = \frac{1}{r} \frac{V_0}{ln\left(\frac{b}{a}\right)} \tag{4.1}$$

where r is the distance from the wire axis to the point at which the field E is evaluated, V_0 is the wire voltage, b the distance of the wire to the cathode (the electrically grounded vacuum chamber), a the wire radius (20 μm). At the wire surface (r = 20 μm), assuming

that the gold coated surface is smooth, V_0 = -20 kV and the cathode (vacuum tank) to anode (wire) distance b is 1 cm (conservative hypothesis), the field value is one order of magnitude below the emission limit

The cylindrical cage is closed on the side opposite to the foil by the ring electrode made in stesalite (a trade mark for a special fibre glass) with conductive paint on the electrode surface (both inside and outside the cage) except an outer ring 5 mm thick to insulate cage and ring electrodes, according to the simulations of Chapter 3, as shown in Figure 4.9.

Figure 4.9: *The cylindrical cage wall of the first prototype made of gold/copper coated fibreglass with the 60° degrees arc covered with a tungsten wire grid. The ring electrode at the cage exit is made of stesalite covered with conductive silver paint except for a 5 mm thick outer ring, visible in the picture, for the electrical insulation between cage and ring electrodes.*

In Figure 4.10 is shown a detail of the 60° degrees arc covered by the gold coated tungsten wires.

The focusing system can rotate around a vertical axis as shown in Figure 4.11 to allow the in-out positioning of the system with respect to the hadron beam trajectory. A stesalite supports allows the connection with the rotation axis and the maximum rigidity of the focusing system. The movement is generated by an actuator outside the vacuum chamber and connected to the focusing system by the rigid vertical axis. A bellow connecting the vertical axis with the vacuum chamber guarantees the vacuum insulation.

Vacuum problems caused by the out-gassing of the stesalite and fibreglass used for the construction of the optical lenses were experienced. The residual gas pressure inside the vacuum chamber decreased asymptotically towards a limit value of $4 \cdot 10^{-5}$ Torr (Chapter 5) and measurements were disturbed by the residual gas ionization caused by secondary electrons.

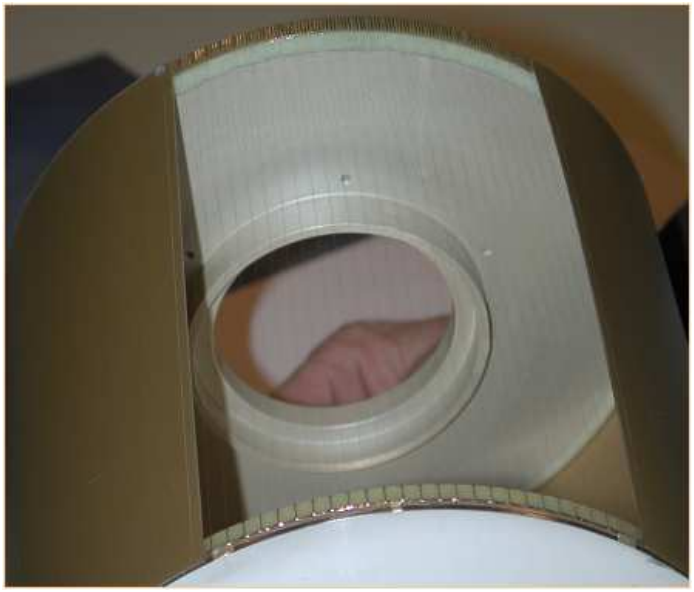

Figure 4.10: *Details of the tungsten wires grid of the first FS prototype.*

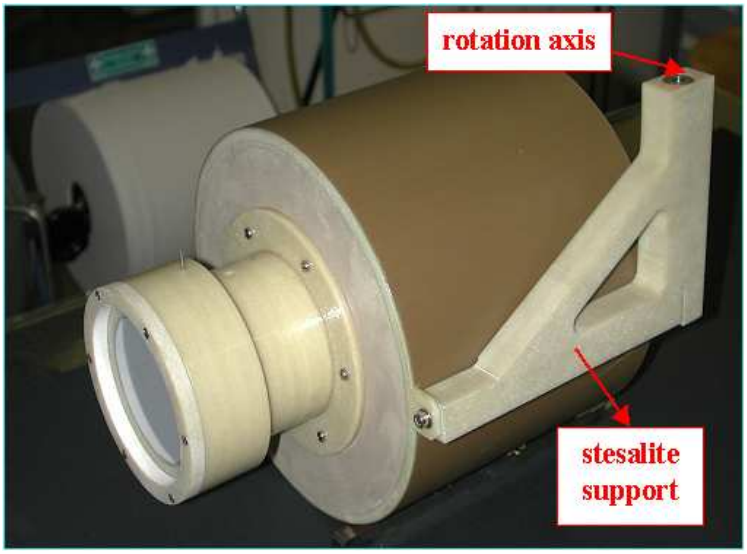

Figure 4.11: *The stesalite vertical rotation axis and support of the first FS prototype.*

4.2.2 Second focusing system prototype

A second prototype using high vacuum (10^{-10} Torr) materials such as stainless steel for the electrodes and Vespel (polyamide resin [121]) for the insulating parts was designed and constructed and is shown in Figures 4.12 and 4.13.

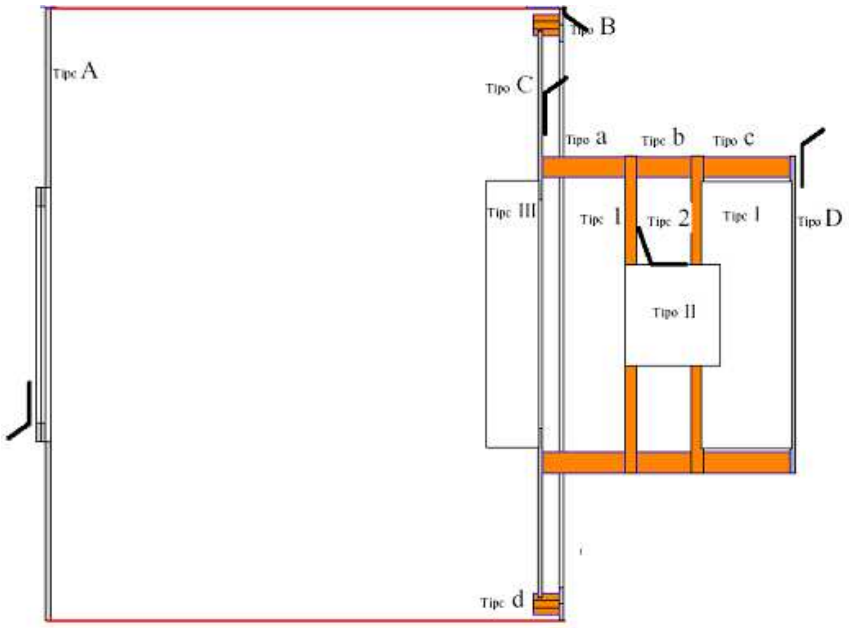

Figure 4.12: *Technical design of the final focusing system prototype (the letters and numbers refer to the design of the different components).*

The foil support, the ring at the cylindrical cage exit and the detector support are stainless steel discs 1.5 mm thick, the cylindrical cage and the two last cylinders are made of stainless steel foil 0.3 mm thick. The two final cylindrical electrodes are fixed to the cylindrical cage by Vespel supports to assure the insulation between these electrodes and the cage as shown in Figure 4.14. Figure 4.15 show a detail of the grid to allow the beam passage consisting of 26 40- μm diameter wires with 4 mm spacing to cover an arc slightly exceeding 60° degrees.

In Figure 4.16 are shown the focusing system main sizes, as total length (234 mm) and cylindrical cage height (156 mm) and diameter (192 mm). Metrology measurements by the CERN metrology laboratory (Figure 4.17) proved that electrode parallelism and coaxiality are well within the calculated tolerances (0.3 mm).

4.3 Secondary electrons production targets construction

The thin foils developed for the SLIM beam monitor consist of a support of 0.1 - 0.2 μm of Al_2O_3 coated on each side with 0.01 - 0.05 μm of Al for a maximum diameter of about 65 - 70 mm. They are produced following a technique consolidated at CERN [54] based on a

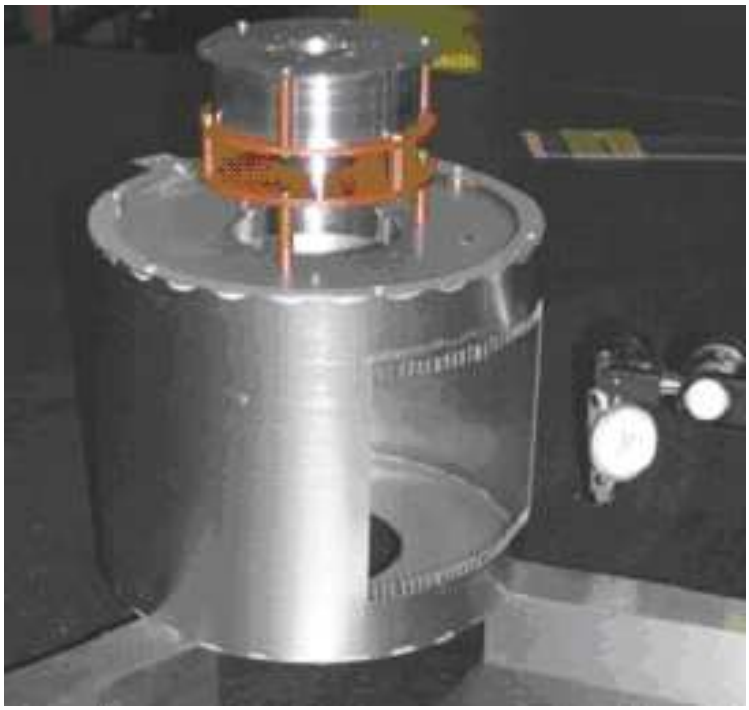

Figure 4.13: *Improved focusing system with electrodes in stainless steel, wires in gold coated tungsten and non-conductive parts in Vespel.*

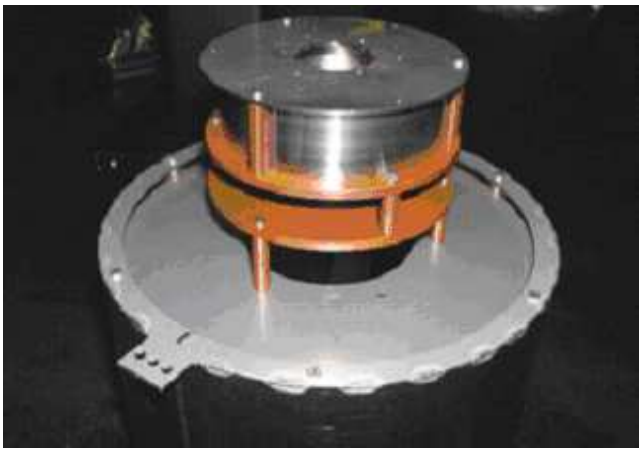

Figure 4.14: *Improved focusing system with detail of the cylindrical electrodes on the detector side.*

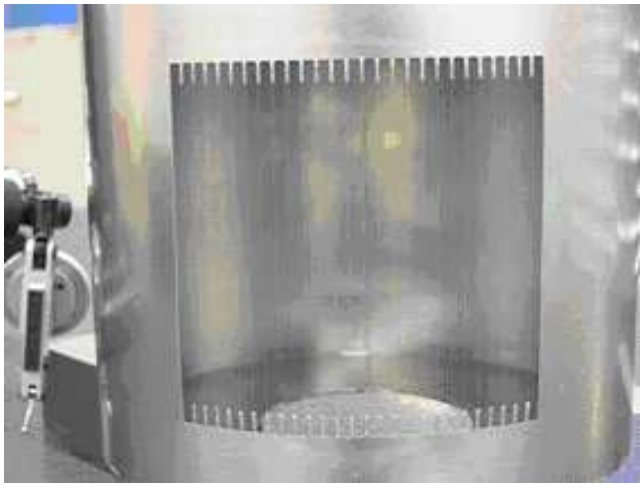

Figure 4.15: *Improved focusing system with detail of the grid for the beam passage.*

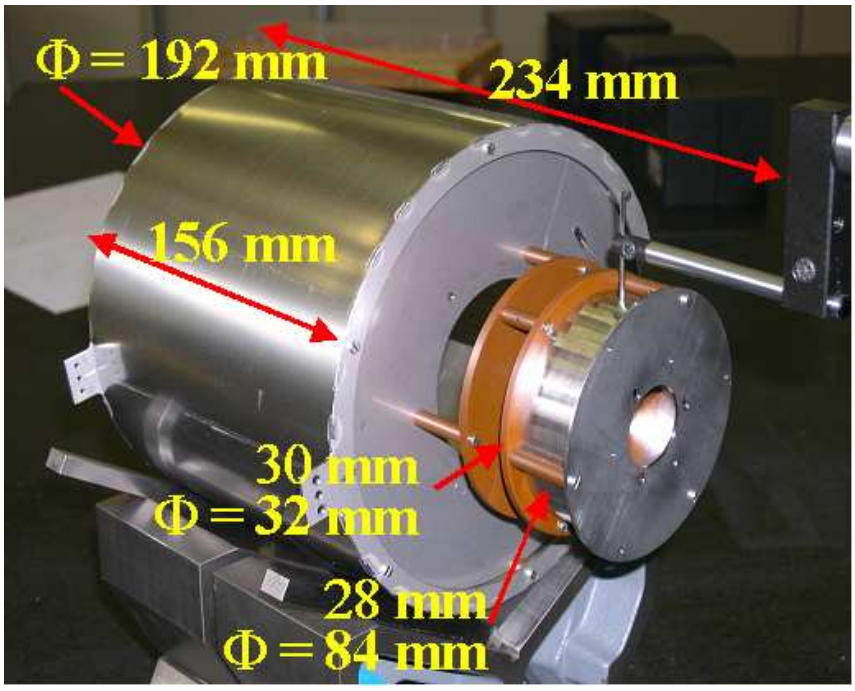

Figure 4.16: *Improved focusing system total view with main sizes.*

Figure 4.17: *Metrology measurements of the second FS improved prototype.*

electrodeposition process where an anodizing treatment causes the natural oxide present on most metals to increase in thickness.

The different steps of the foils production, schematically represented in Figure 4.18, are:

1. select a 0.1 mm thick aluminium with a purity of 99%;
2. perform metal cutting operations including de-burring (smoothing of sharp edges);
3. anneal the foil in a vacuum oven for 2 hours at 400 °C. This operation relaxes any stresses within the aluminium that would otherwise appear in the foil itself;
4. anodize at 2 mA cm^{-2} constant current in a weak electrolyte composed of 5 grams *ammonium hydrogen tetra borate* in 5 litres distilled water. With this operation a layer of Al_2O_3 is deposited on both sides of the Al foil. The mass $M_{Al_2O_3}$ of Al_2O_3 can be calculated by the following equation:

$$M_{Al_2O_3} = K\ I\ T$$

where K is the Faraday constant, I the electrolytic bath current and T the anodization time. The thickness of the Al_2O_3 layer is determined by the relation:

$$M_{Al_2O_3} = d\ S\ h$$

where d is the density of Al_2O_3, S the foil surface, h the Al_2O_3 layer thickness in Å. Under constant current conditions, the film thickness and voltage increase linearly so the voltage developed is a rough measure of the thickness; for Al_2O_3 thickness (t) is related to the cell voltage according the following relation

$$t = 13 \text{ Å Volt}^{-1}$$

Thus for 3000 Å the final voltage is 230 Volt at the constant current of 200 mA[1];

5. heat anodized foil in a vacuum oven for 2 hours at 250 °C. Without this step the resultant foil would break in vacuum;

6. clamp anodized foil between two plates: one plate with a cutout corresponding to the foil size. Scour the surface of one foil side thoroughly and then remove the plates;

7. lower the foil into a solution of methanol with 2% of bromine. With this operation only the aluminium is removed since the layer of aluminium oxide is unaffected by bromine. When the foil window appears 100% clear with the help of a rear light source, raise the foil out of the solution;

8. before foil dries out, thoroughly wash both sides with methanol then acetone by squirting weakly the foil sides. Allow foil to dry;

9. fix the foil on a metallic ring support (in the SLIM application, 1.5 mm thick) with three screws;

10. aluminize both sides of foil with 100 - 500 Å of aluminium by pure aluminium evaporation in vacuum. This discharges to the electrical ground any electrostatic build up within the oxide.

Ten foils with 3000 Å total thickness have been manufactured and are shown in Figures 4.19 (2000 Å of Al_2O_3 support + 500 Å of Al on both faces) and 4.20. Other forty foils (see Figures 4.21 and 4.22) have been treated up to the 5th step of the procedure described above for an oxide thickness of 2000 Å and 2500 Å.

4.4 Slow control system development

A dedicated control system has been developed for the control of the SLIM beam monitor equipment described in Appendix C and listed below:

- primary pump (Varian Dry Scroll);
- turbo pump (Varian Turbo-V70LP);

1 One of the two Al_2O_3 layers serves as a support for the thin foil (Figure 4.18); the oxide thickness for foils diameter of 70 mm, as for the SLIM beam monitor application, must therefore exceed 1500 Å, otherwise the foils would be too fragile and could break during manipulations

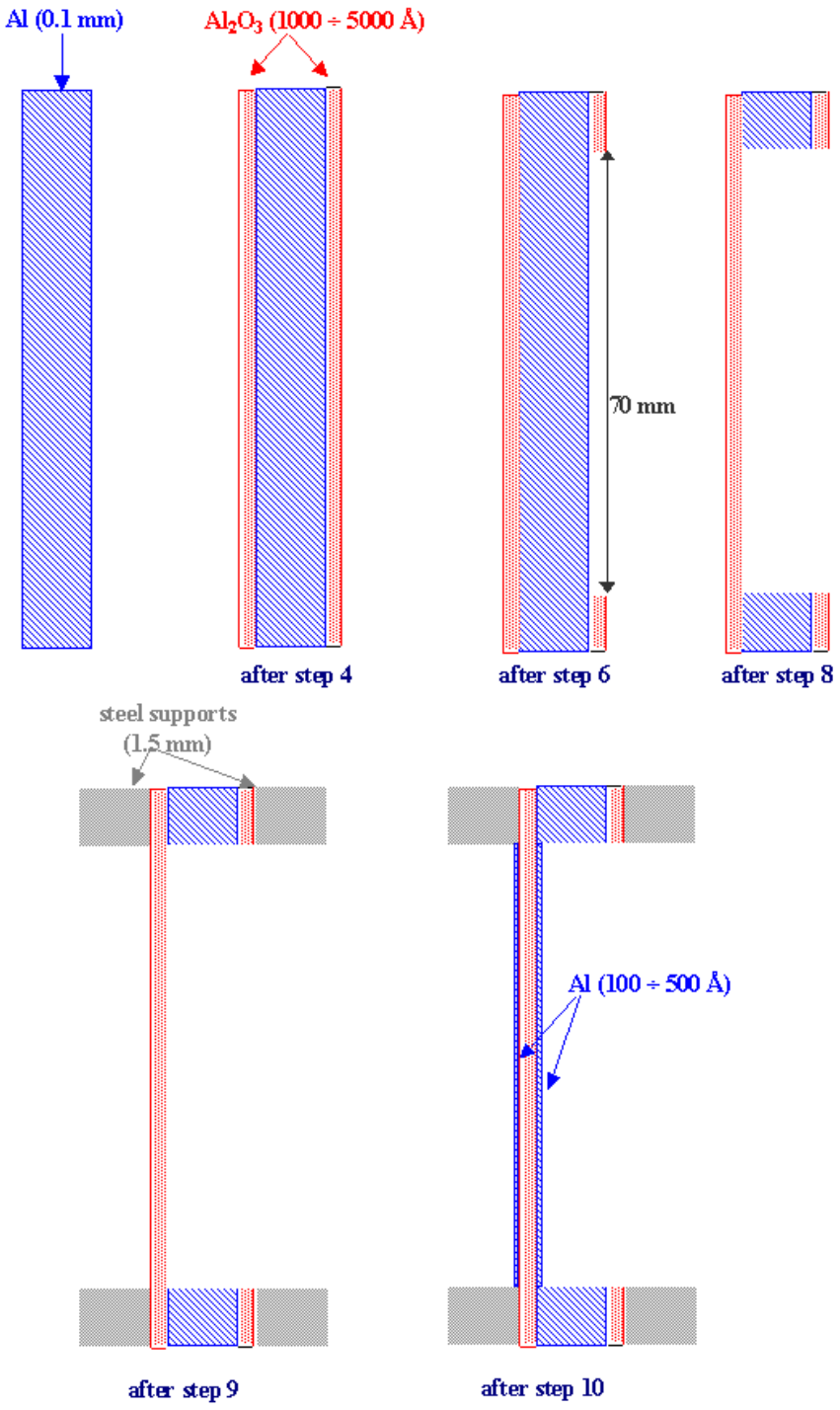

Figure 4.18: *Schematics of the foils production process (sizes not to scale).*

Figure 4.19: *The aluminium foils that underwent the full treatment mounted on a stainless steel support, ready to be mounted on the focusing system for the beam tests. The foils are conserved in a primary vacuum container.*

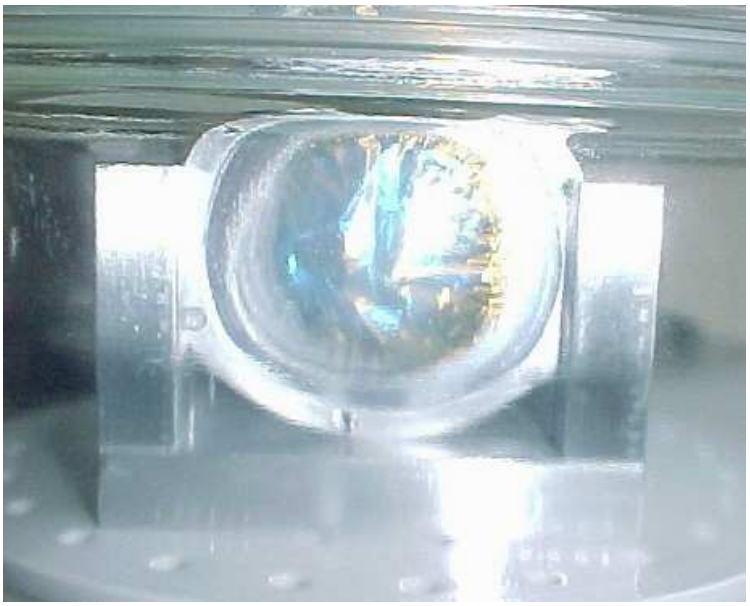

Figure 4.20: *Detail of the aluminium foil that underwent the full treatment. Foils are mounted on stainless steel supports.*

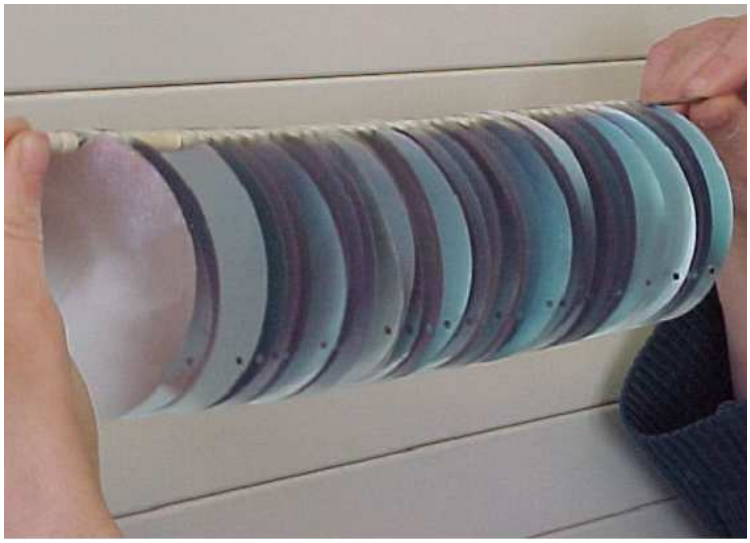

Figure 4.21: *The forty anodized and baked Al foils up to step 5 of the process. The violet reflection is due to the thickness of the Al_2O_3 layer deposited in the electrolytic process.*

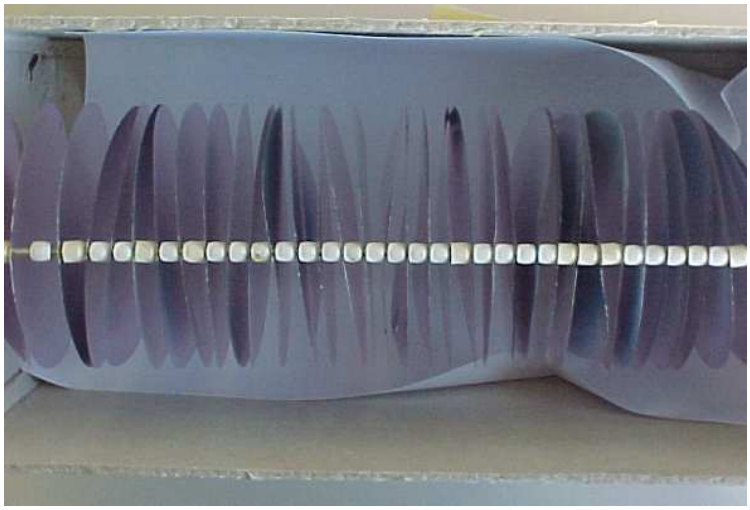

Figure 4.22: *Forty anodized and baked Al foils (view from above). The foils are conserved in a container separated by ceramic beads to avoid friction between them before undergoing the final steps of the treatment.*

- low vacuum gauge (Varian Convec-Torr);
- high vacuum gauge (Varian Mini-BA);
- actuator (Stegmann Hipedrive);
- 4 high voltage power supplies (Matsusada K7, S and U series);
- 1 vacuum valve (Varian Electromagnetic Block Valve).

The system is based on the National Instruments Field-Point FP2010 intelligent Ethernet controller interface with 32 MB DRAM Memory [122]. Field-Point is designed for measurement and industrial control applications that require systems involving diverse sensors and actuators located centrally or spread over large distances. It includes networking capabilities for distributed input/output (I/O) to perform process automation functions as well as an option to run a real-time operating system based on LabVIEW Real-Time applications.

The aim of the SLIM slow control system is to control the equipment listed above and to guarantee that the process automation has the maximum safety for both users and instrumentation. The Field-Point for the SLIM beam monitor application is composed of five components: the CPU, 16 channels for digital output, 16 channels for digital input, 8 channels for analog input and 8 channels for analog output. Each component is connected to one or more Field-Point modules according to the schematics of Figure 4.23. The CPU module has a RS232 port for the control of the actuator via a RS232/RS458 converter. FP2010 can be accessed via Ethernet network, local host, portable, remote computer or via WEB by FTP protocol.

The user interface panel represented in Figure 4.24 was developed with LabVIEW Real-Time software. On the right side of the panel there are the primary and turbo pump controls, at the center the gauge readings with the switch on/off buttons, on the left side the control for the actuator and the power supplies of the FS electrodes, the MCP and the phosphor. It is possible to vary the threshold values and power supplies ramping times through the user interface for the equipment and beam monitor protection.

Figure 4.25 shows the electrical panel with the connections to the Field-Point.

4.5 The image acquisition software development

LabVIEW software has been developed to acquire the image of the first commercial detector, consisting of a phosphor screen observed with a CCD camera connected to a PCI card (National Instruments IMAQ PCI-1407) with a BNC connector for signal transmission (Figure 4.26). LabVIEW drivers are used to interface the PCI card with the computer.

The CCD is a black & white camera with a sensor of 752 x 582 pixels and 20 ms frame rate, as described in Section 2.4.1 and in Appendix C. The acquired image is treated as a two dimensional matrix, where each element is represented by a 8-bits number that directly identifies the gray value of a particular pixel. The numbers between 0 and 255 define the different gray shading, with 0 corresponding to black and 255 to white.

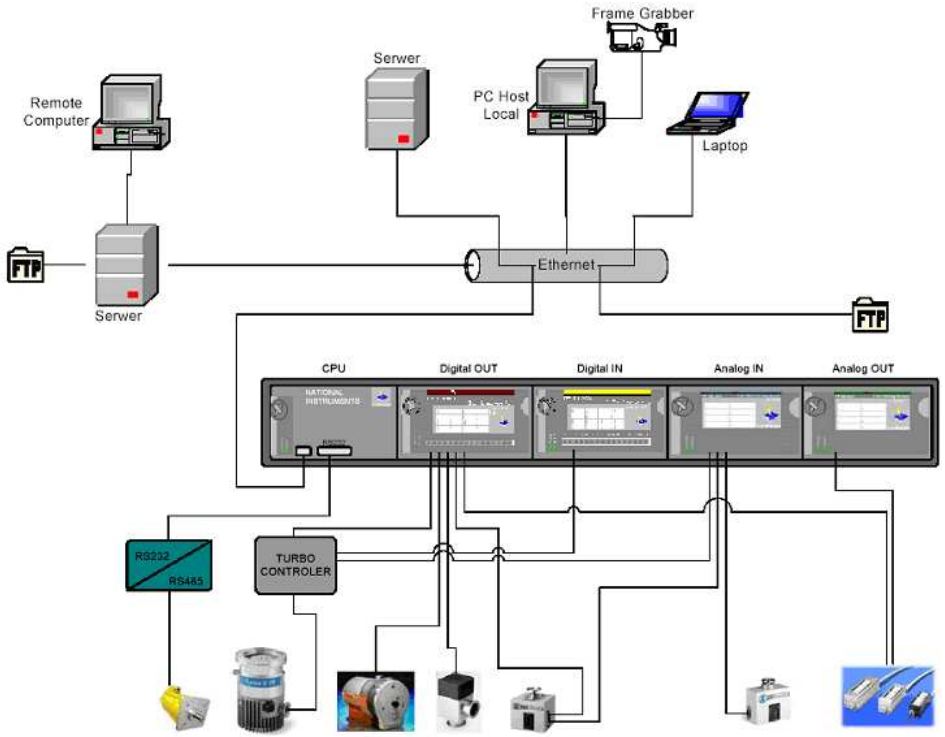

Figure 4.23: *Electrical/logical layout of the SLIM beam monitor control system based on NI field point FP2010 module. The bottom pictures represent, left to right: actuator, turbo-molecular pump, primary pump, electro-magnetic valve, Eyesys Mini-B/A gauge, Eyesys ConvecTorr gauge, high voltage power supplies.*

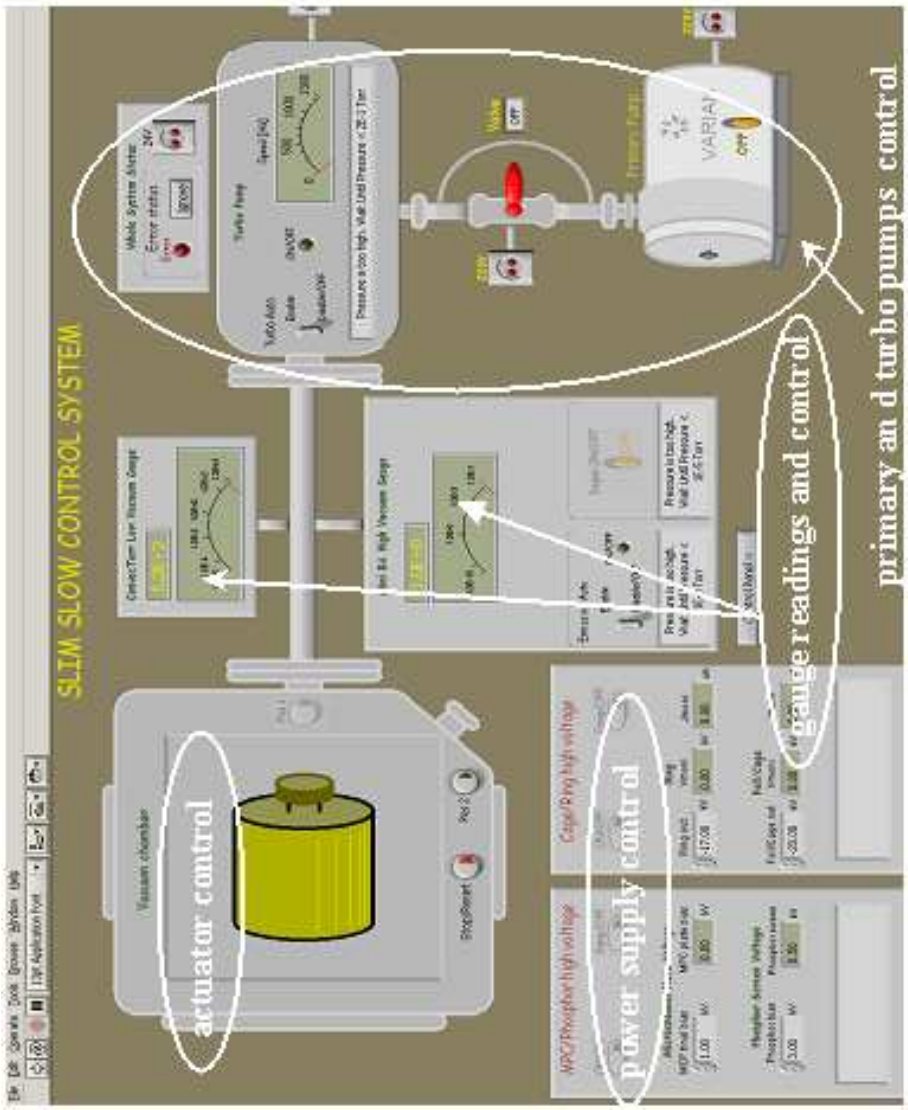

Figure 4.24: *User interface control panel.*

Figure 4.25: *Electrical panel for the SLIM beam monitor.*

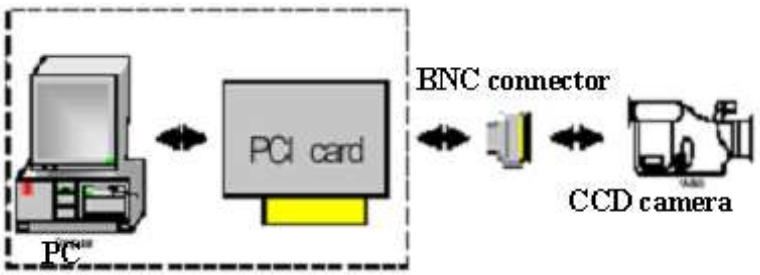

Figure 4.26: *Frame grabber connections.*

Besides the acquisition of the intensity matrix for the whole sensor area or for a selected region, the software developed features single and multiple image acquisition, movies for a detailed analysis of the measured beam behaviour and basic image processing such as beam shape and position measurements, single and multiple image projection on arbitrary axis (histograms). Separate background and signal acquisition are also possible. Figure 4.27 shows the user front panel for beam image acquisition with the histogram preview for both horizontal and vertical axes.

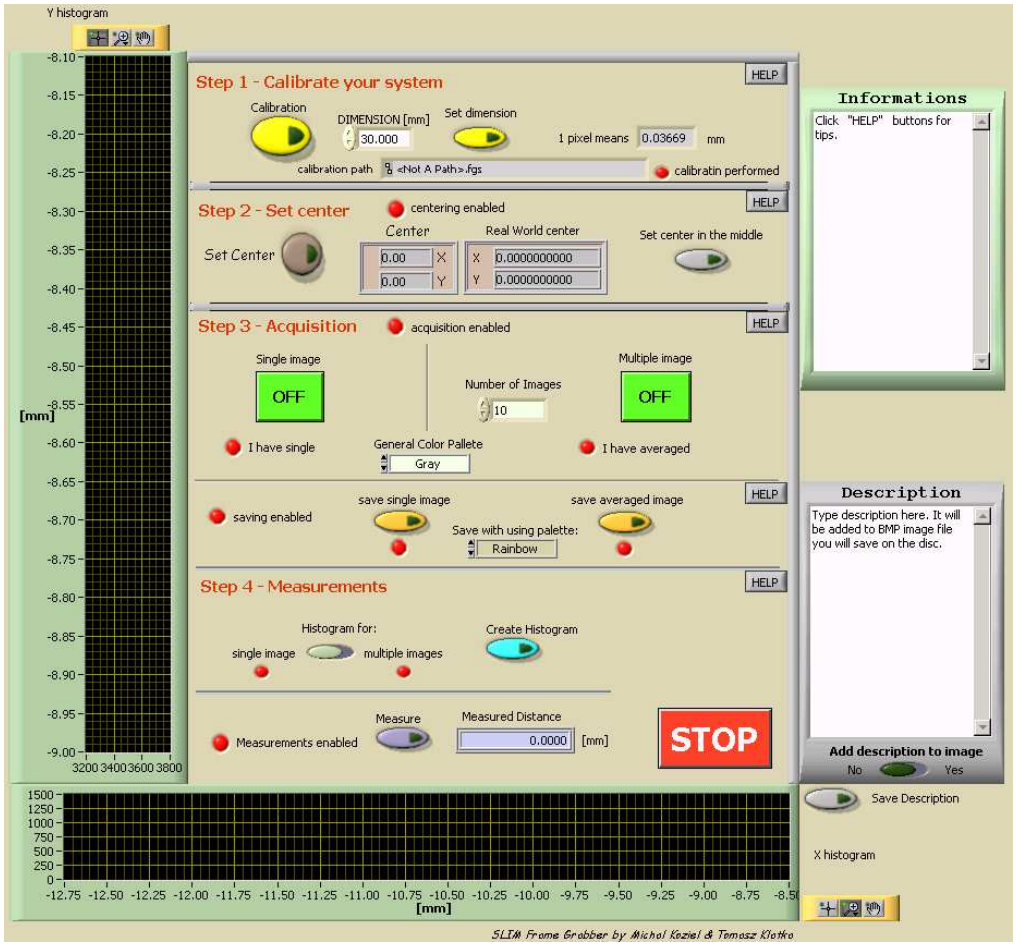

Figure 4.27: *User front panel for beam image acquisition.*

Chapter 5

SLIM particle beam monitor integration and laboratory tests

The SLIM beam monitor integration and first laboratory tests took place at the CERN, in the TERA Foundation laboratory, in the second half of 2003. After the delivery of the vacuum chamber, flanges, viewports, actuator and high voltage feedthroughs were assembled on the SLIM tank (Section 5.1). The first focusing system was installed in the tank and the beam monitor equipment was integrated with the slow control system.

Leaks and out-gassing problems were resolved. As the tank final residual gas pressure prevented the use of the commercial detector (the MCP requires better than 10^{-6} Torr), a new focusing system with high vacuum materials was designed and constructed. Major improvements on the vacuum chamber including modification of the 45° internal weldings to avoid air trapping, cleaning by vacuum firing at 900 °C, baking out with the FS installed at $\approx$ 120 °C over 3 days, were implemented (Section 5.2). After the described upgrades, the lowest pressure measured after about two weeks of pumping (and testing) was $6.5 \cdot 10^{-8}$ Torr.

Tests of the electrostatic focusing lenses optical properties have been performed using thermionic emission from a hot tungsten wire as a source of electrons and are analyzed in detail in Section 5.3. The tungsten wire is collimated so that thermionic electrons are emitted from seven holes spaced by 1 cm. The analysis of the wire image on the electron detector allowed the experimental evaluation of focusing system linearity, demagnification factor and resolution and the comparison with the SIMION 3D simulations. Aberration effects moving away from the focusing system symmetry axis were also evaluated. The experimental results confirm that the optical properties of the focusing system are in very good agreement with the computer simulations and fulfil the SLIM beam monitor requirements.

To explain the observed image shift in respect to the detector centre, the effect of an external magnetic field was investigated with the help of a permanent dipole magnet and of SIMION 3D simulations (Section 5.3.1).

Finally, the wire intensity fluctuation observed experimentally agrees well with SIMION

3D simulations of wire tilts and shifts in respect to the centres of the collimator holes as shown in Section 5.3.2.

5.1 SLIM beam monitor system integration

After the delivery of the vacuum chamber (described in Section 4.1) in March 2003, the SLIM beam monitor and the related equipment were assembled in the TERA Foundation laboratory at CERN. Flanges, view-ports, actuator and the high voltage feedthroughs were installed on the tank. The tank was mounted on a variable height support, as shown in Figure 5.1, to align it with the beam and was electrically grounded. All the equipment was integrated with the slow control system described in Section 4.4.

The vacuum system, described in Appendix C and comprising a primary pump (pumping from atmospheric residual gas pressure), a turbo-molecular pump (pumping from 10^{-1} Torr) and two gauges for the tank residual gas pressure monitoring in all the range of interest, was installed on the vacuum chamber. A vacuum bypass system controlled with an electromagnetic block valve is also part of the vacuum system (as shown on the slow control panel of Figure 4.24) to protect the thin foils from turbulences that could destroy the foil when the tank residual gas pressure is higher than 1 Torr. If pressure falls down below $8 \cdot 10^{-1}$ Torr the valve automatically turns on, allowing pumping from a normal conductance DN16 bellow. For residual gas pressure values above 1 Torr the valve automatically turns off and pumping is performed through a DN16 bellow and an interchangeable diaphragm of diameter varying in the range from 0.5 to 1.5 mm to reduce the conductance and, therefore, the turbulences in the vacuum chamber caused by the primary pump.

The Matsusada power supplies (Appendix C) were also installed on the top of the vacuum chamber mounted in two different aluminium boxes. The S- and U-series were used for the polarization of the phosphor and MCP during the laboratory tests and the first tests on beam, while the K7-series were used for the polarization of the focusing system electrodes.

All the power supplies can be switched on when the tank residual gas pressure is below a threshold pressure value that can be adjusted via the control panel and automatically switched off when the tank residual gas pressure rises above a value equal to the threshold pressure plus a 10% margin to avoid system instabilities. The final voltages set through the slow control panel are reached after a ramping time (to avoid electrical discharges in case of sudden voltages rise) set through the control panel as well.

The actuator for the FS position into and out of the beam path was fixed on the top of the vacuum chamber and connected to the FS rotation axis with two pulleys (the one on the rotation axis with twice the diameter of that on the actuator to reduce the FS rotation speed) and a $\approx$ 230 mm driving belt schematically drawn in Figure 5.2.

Through the control system it is possible to adjust the FS position, set position limits in both directions to protect the FS and the detector mounted on it, the rotation speed which is by default set to the minimum value (0.2 rotations/minute reduced by a factor two by the pulleys diameters ratio) to protect the thin foils from abrupt movements.

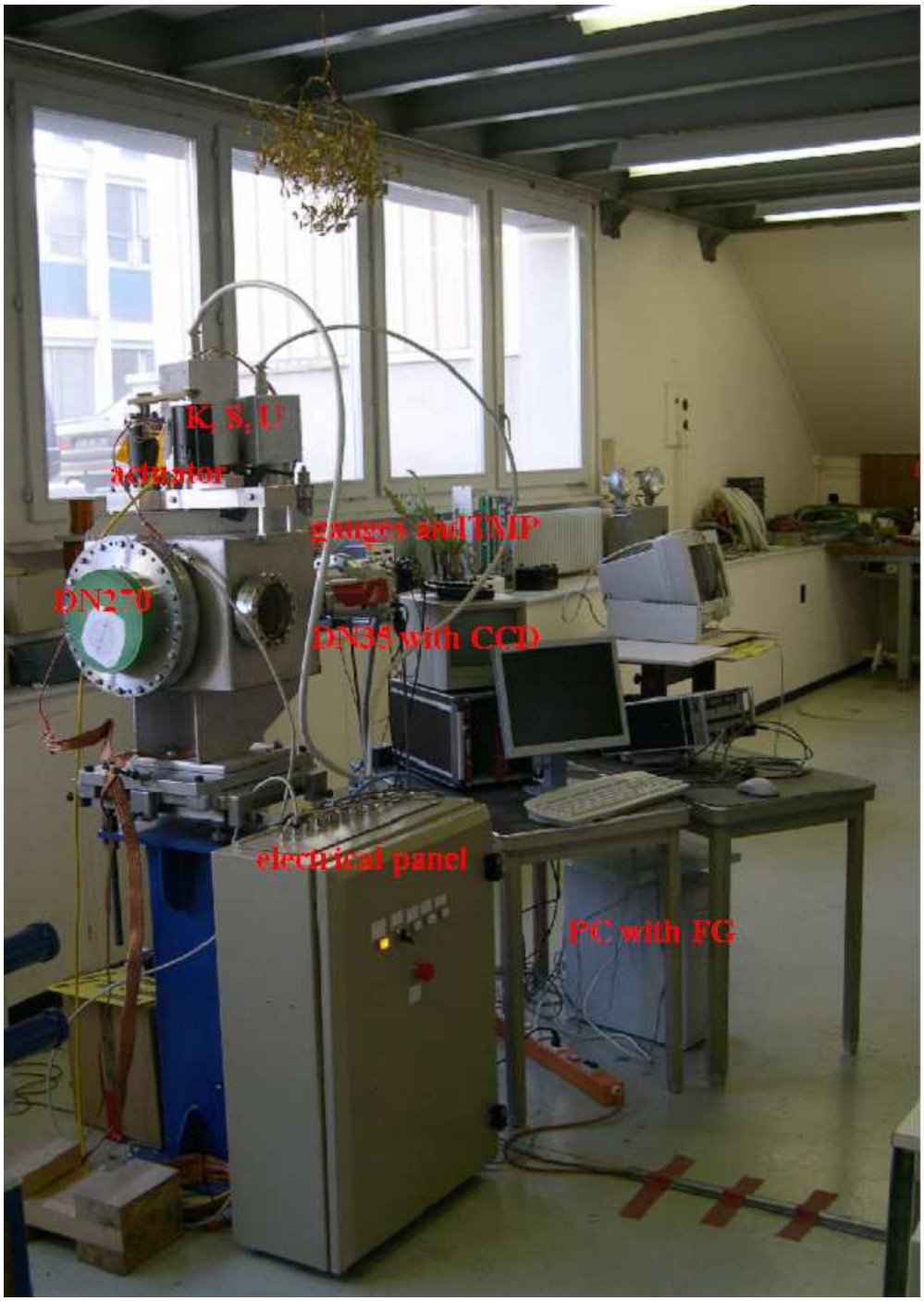

Figure 5.1: *SLIM beam monitor vacuum system mounted on a variable height support (in blue) in the CERN laboratory with the slow control electrical panel and, on the table, the frame grabber acquisition system: the frame grabber (FG) is mounted in the PC under the table. K7, S and U are the Matsusada power supplies and TMP is the turbomolecular pump; the primary pump for the forevacuum is on the floor, hidden by the electrical panel.*

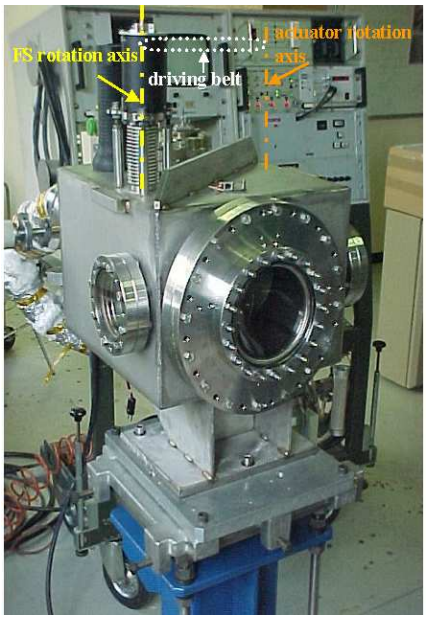

Figure 5.2: *Drawing of the FS rotation system (the actuator has been fixed on an aluminium support to have the rotation axis in the position indicated in orange).*

Figure 5.1 shows the integrated system in the CERN laboratory with the DN270 flange for the insertion of the FS, the DN35 flange with the glass viewport for the CCD camera mounted on an Al support, on the top of the tank the actuator for the FS rotation, the high voltage feedthroughs with the Al boxes where are fixed the high voltage power supplies (for both FS and MCP polarization), in front of the SLIM support the electrical panel of the slow control system, on the right the turbo-molecular pump and the gauges for the residual gas pressure measurements; under the table on the right is the PC on which the frame grabber for the CCD image acquisition is mounted and on the table the PC screen with the video monitor for the video signal display.

The CCD camera described in Section 2.4.1 was mounted on the vacuum tank with an Al support. All the measurement were taken using a lens of 25 mm focal length for a 180 mm distance from the phosphor screen plane (inside the tank) to the focal plane (outside the tank) and at the maximum lens diaphragm aperture (F = 2).

5.2 Vacuum tests

After the integration of the vacuum chamber components, equipment and slow control system, the pumping system was turned on. After the detection and fixing of a first leak on the DN270 flange for the FS system insertion and of a second leak on the CCD flange, the residual gas pressure reached after 20 hours of pumping 10^{-6} Torr and improved after heating and longer pumping times down to $6.7 \cdot 10^{-7}$ Torr as shown in Figure 5.3 (a).

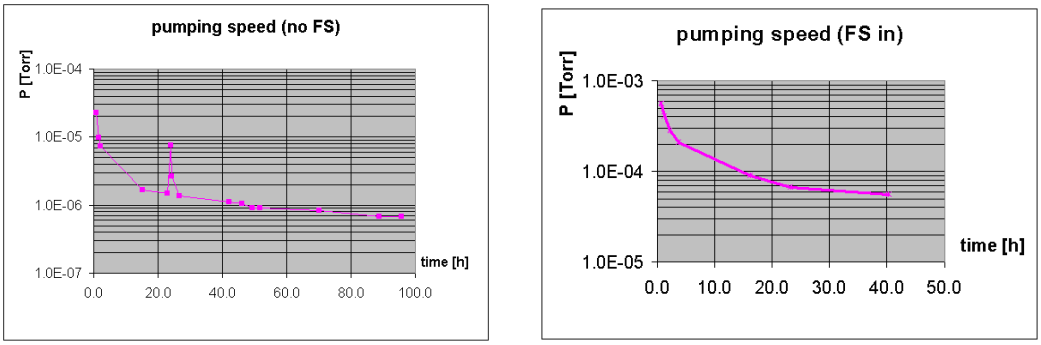

(a) (b)

Figure 5.3: *Residual gas pressure in Torr in the vacuum tank as a function of the pumping time in hours (logarithmic scale on both axis): before installation of the first FS prototype (a) and after installation of the first FS prototype (b).*

The FS materials chosen for the construction of the first FS prototype had been previously used for detectors working in high vacuum environment (residual gas pressure below 10^{-6} Torr [123]) but after the installation of the first FS prototype, the pressure went down only to $2.4 \cdot 10^{-4}$ Torr in $\approx$ 20 hours of pumping with a very slow decrease. Various actions were taken to improve the tank residual gas pressure that after two days reached a lower limit value of $5 \cdot 10^{-5}$ Torr as shown in Figure 5.3 (b).

Such poor vacuum prevented the use of the first commercial detector, as the Hamamatsu micro channel plate requires residual gas pressure better than 10^{-6} Torr to work properly without electrical discharges that could harm the system. It was therefore decided to implement some further improvement, but unluckily the residual gas pressure went down only to $2 \cdot 10^{-5}$ Torr. Material outgassing tests were performed at CERN [124] to check the percentage of degassing of each FS component.

Data analysis showed that the out-gassing factors of the stesalite and fiberglass components were higher than expected due to the use of paint and a poor material quality. To improve the vacuum performance of the focusing system, the second prototype described in Section 4.2.2 using high vacuum (10^{-10} Torr) materials was constructed.

During the construction of the final FS, major improvement on the vacuum chamber were also implemented. In particular, the 45° internal weldings were modified to avoid air trapping. The chamber was then cleaned by vacuum firing at 900° in residual gas pressure of 10^{-6} Torr for 3 hours. The measured residual gas pressure in the vacuum chamber after vacuum firing and with the new focusing system installed went down to $2 \cdot 10^{-6}$ Torr.

Spectrometric mass analysis of the residual gas pressure performed by the CERN vacuum group indicated the presence of water molecules in the residual gas and baking out of the chamber with the FS installed at $\approx$ 120° C (to avoid damages at the FS wires) over 3 days was therefore implemented. The residual gas pressure (RGP) versus time is shown in Figure 5.4. The curve in blue shows the residual gas pressure in the SLIM tank with the

FS installed during baking (initially at 110° degrees, then at 120°). The pressure behaviour compared with the slope of the magenta curve, obtained in analogue conditions before baking, clearly indicates that there was a leak in the vacuum chamber.

After tightening all the flanges bolts and the valve to bring the tank back to atmospheric atmosphere by nitrogen filling, the residual gas pressure started to decrease faster as shown by the yellow curve and, with the FS system installed, by the cyan curve. The pressure oscillations displayed are due to the out-gassing of the MCP and of the tungsten wire during the laboratory tests of the optical properties of the focusing system described in Section 5.3. The lowest pressure measured after about two weeks of pumping (and testing) reached at last $6.5 \cdot 10^{-8}$ Torr.

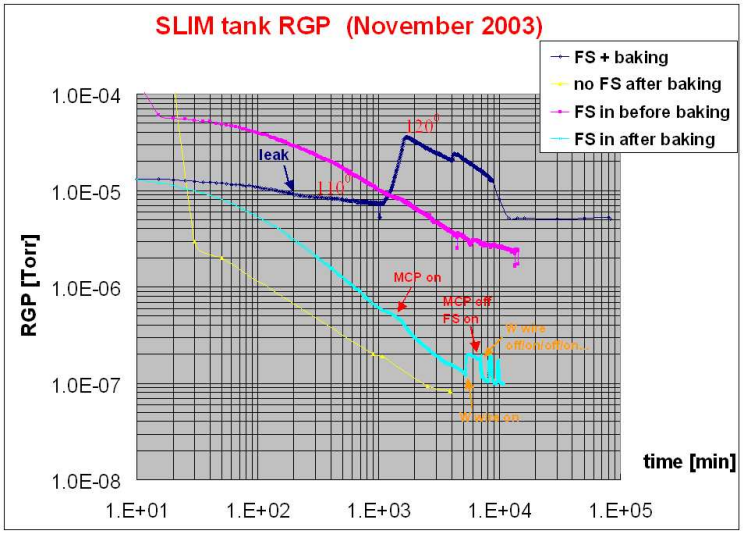

Figure 5.4: *Residual gas pressure in Torr in the vacuum tank as a function of the pumping time in hours (logarithmic scale on both axes). The blue curve represents the RGP in the tank with the FS installed during baking (baking temperatures indicated on the plot) to be compared with the magenta curve of the system in the same conditions before baking. After fixing the leak, the RGP behaviour without and with the FS installed is represented by the curves in yellow and cyan respectively. The oscillations in the cyan curves are due to the out-gassing of the MCP and of the tungsten wire that were switched on and off during the laboratory tests.*

5.3 Laboratory tests with thermionic electrons

Tests of the focusing lenses have been performed using thermionic emission from a hot tungsten wire as a source of electrons. Thermionic emission takes place over the full solid angle with a peak around a few eV. The amount of emitted electrons is dependent on the wire temperature according to the Richardson law [125]. At 2000 °K the number of emitted electrons is about 10^{14} e^-/sec for the total wire length (70 mm length, 0.125 mm diameter).

SIMION 3D simulations show, as expected, a slight deterioration of the system resolution with respect to secondary electrons, because of the flat angular distribution of thermionic electrons compared to the cosine-like secondary electrons angular distribution (Section 3.1). Nevertheless, as the optical properties (except resolution) depend mainly on the system geometry and the electric field, tests with a tungsten wire constituted the proof of principle in preparation of the tests in a hadron beam.

The wire replacing the secondary emission foil is mounted in a metallic cylindrical collimator of 6 mm diameter. The cylinder is welded to an 80 mm diameter aluminium foil on the backside of the focusing system and rotated of 60° degrees with respect to the horizontal axis, as shown in Figure 5.5, to evaluate the system optical properties in both horizontal and vertical plane.

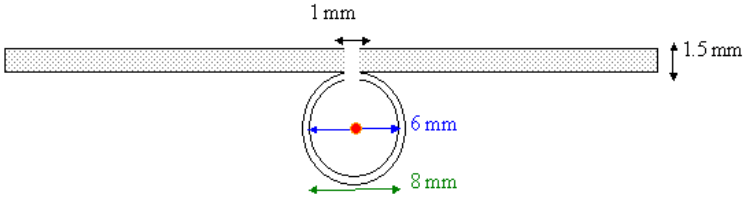

(a)

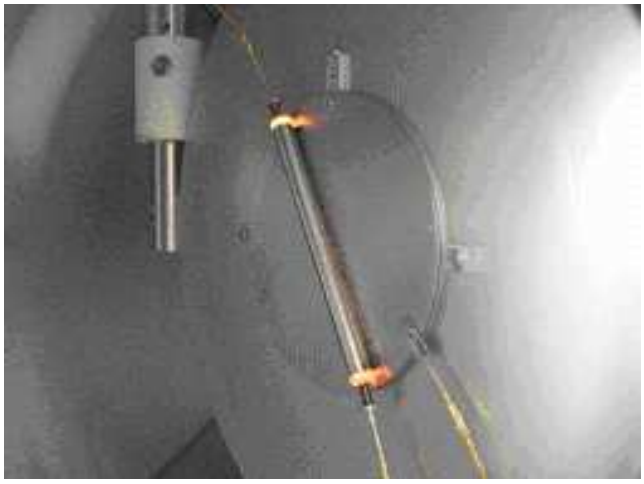

(b)

Figure 5.5: *The metallic cylinder containing the tungsten wire: cross section with sizes (wire in red) (a), welded on the backside of the focusing system (with the polarization contacts at the two extremities) (b).*

A 1 mm slit on the inner side of the cylinder allows the passage of the thermionic electrons through seven holes (0.5 to 1 mm diameter, 1 cm spacing) milled in the aluminium support as shown in Figure 5.6. The wire, at the same working high voltage of the cylindrical cage, is supplied with a floating 6 Volt dry battery through a 2 Ω resistor. The current flowing

trough the wire, that has 3 Ω resistance, is accordingly 1.2 A.

When the tungsten wire is powered on, photons are emitted as well, as clearly visible in Figures 5.5 and 5.6. The emitted electrons are accelerated outside the cylinder and focused on the detector by the electric field of the focusing system. The detector used for the first laboratory tests was the commercial system described in Section 2.4.1.

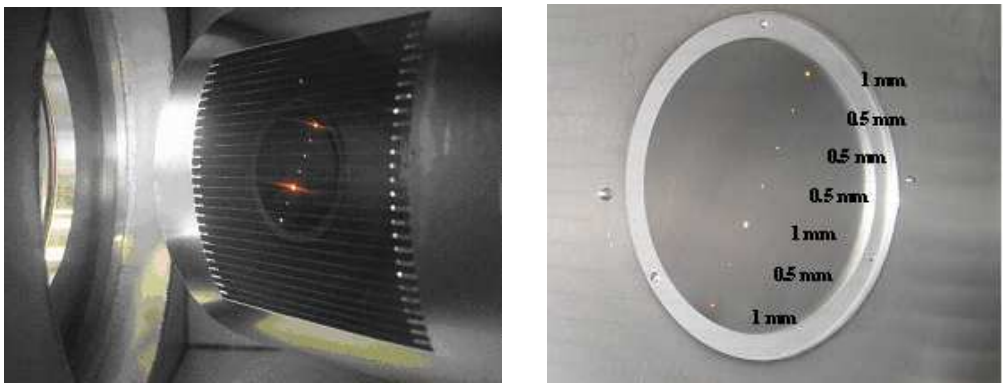

(a) (b)

Figure 5.6: *Internal view of the focusing system, where the seven holes for the electrons passage are illuminated by the hot wire(a). Detail view of the holes on the inner face of the focusing system with the hole diameter indicated on the right (b).*

The electron emission from the tungsten wire is assumed gaussian with the maximum intensity at the wire centre according to the temperature gradient. Electrons are emitted over the full solid angle with a rectangular energy distribution centred at 2 eV with a 2 eV width. The system geometry selects the thermionic electrons emitted over a $\approx 40°$ degrees cone for the 1 mm diameter holes and $\approx 20°$ degrees for the 0.5 mm diameter holes.

Computer simulations have been performed at different voltages to analyze the focusing system properties. Simulations for the nominal working voltages (- 20 kV on the cylindrical cage electrode and - 17.9 kV on the focusing ring electrode) show that 12% of the thermionic electrons arrive on the detector while 88% are lost in the cylindrical collimator. The image on the detector reproduces the image of the holes demagnified by a factor ≈ 5 and inverted due to the cross-focusing optics, as shown in Figure 5.7.

Figure 5.7 shows the simulated trajectories and the expected image on the detector for the nominal working voltages. In the computer simulations the number of emitting sources has been increased from 7 (as in the experimental set-up) to 11, leaving the outer peaks in their actual position and decreasing the spacing of the central ones, for a more meaningful comparison with the experimental data.

Moreover, it has been assumed that the number of electrons leaving the 1 mm diameter holes is four times that leaving the 0.5 mm diameter holes on the base of pure geometrical considerations. Any intensity distribution analysis, as discussed in Section 5.3.2, is anyway irrelevant for the following investigation, as the system optical properties are related to the

peaks positions and widths and completely independent of their heights.

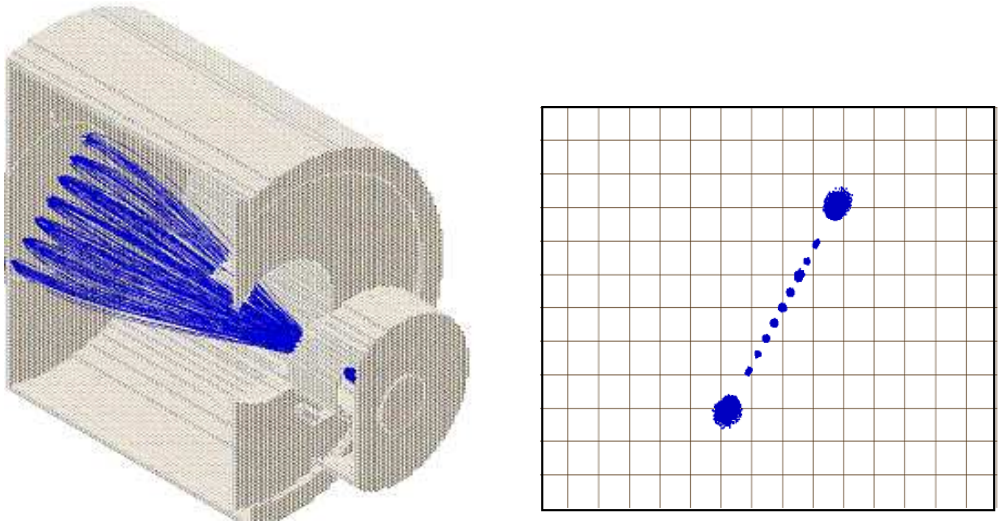

(a) (b)

Figure 5.7: *SIMION 3D simulation of the thermionic electrons trajectories inside the focusing system (a). SIMION 3D simulation of the electron image on the detector (grid pitch: 2 mm) (b).*

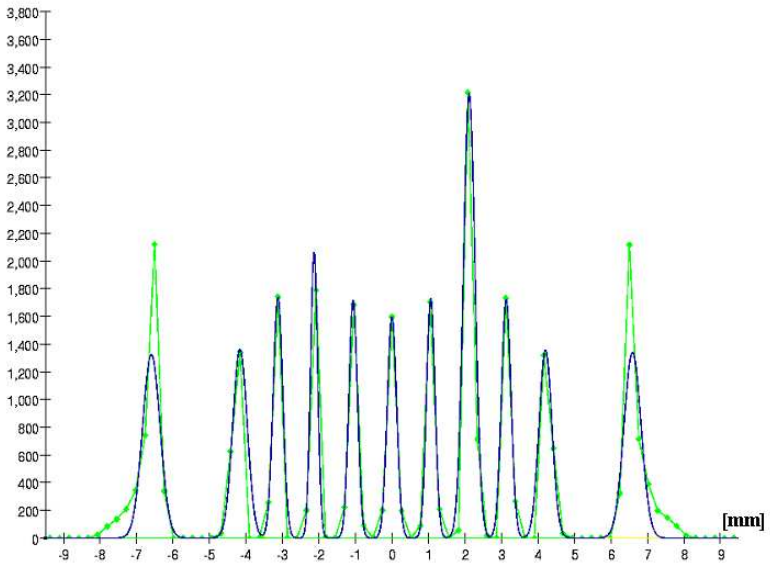

Figure 5.8: *SIMION 3D simulation of the projected profile of the collimated wire image on the detector with gaussian fit of every peak.*

Image aberration away from the focusing system symmetry axis is caused by the flatness of the aluminium foil support (emitting surface), as predicted by theory and reproduced by computer simulations. Aberration effects are clearly visible in Figure 5.8 that represents the projection of the simulated data along the wire axis overlapped with gaussian fits for every peak.

For the outer peaks (in respect to the focusing system symmetry axis) intensity falls off, the spatial resolution, defined as the standard deviation value of the gaussian fit, is larger and the most likely value of the gaussian fit, that determines the system linearity and demagnification factor, slightly shifted (4%) to the outside with respect to the internal peaks. The aberration effect are discussed in more details below, in the comparison with the experimental data.

Figure 5.9 represents the measured seven holes wire image (averaged over 16 consecutive 20 ms frames) at the nominal working voltages of the focusing system (V_0 = - 20 kV, V_1 = - 17.9 kV). To the left are the projections along the axes parallel and perpendicular to the wire; in the centre, the measured intensity distribution along the wire axis; to the right, the distribution along the wire of the holes with different diameter taking into account the image inversion due to cross focusing optics. The observed discrepancy in respect to the simulated image intensity distribution of Figure 5.8 is discussed in Section 5.3.2.

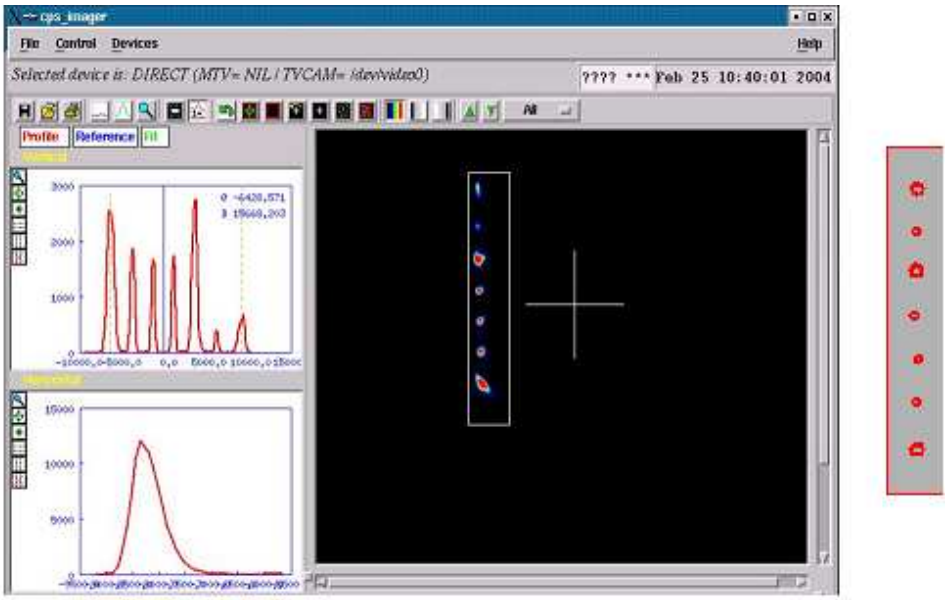

Figure 5.9: *Wire image with: left, projection along the axes parallel and perpendicular to the wire (the horizontal scale of the projections is in micrometer); centre, the measured intensity distribution along the wire axis; right, the distribution of the different diameter holes (3 holes of 1 mm and 4 holes of 0.5 mm); the image is inverted due to the cross focusing optics image inversion.*

Figure 5.10 shows the peaks position at the detector (phosphor) as a function of the holes

position at the source (collimated tungsten wire). The agreement between experimental data represented by the blue triangles (error bars are smaller than the markers) and the data obtained with the computer simulations represented by the yellow diamonds is very good. The difference is within 150 μm for every peak, except for the one at - 30 mm from the symmetry axis at the source that shows a 350 μm discrepancy.

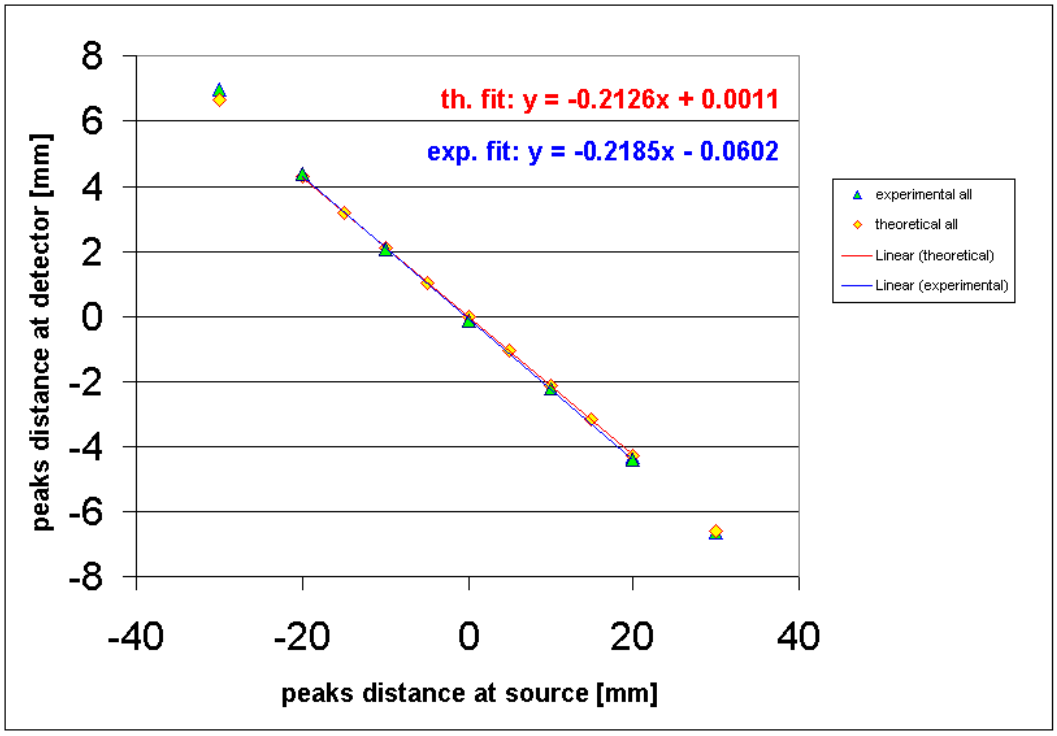

Figure 5.10: *Linearity plot of the peak positions on the detector as a function of the holes position at the source (aberration region not included in the fit). The yellow diamonds represent the simulated values, the blue triangles the experimental data.*

The two outer peaks are slightly shifted with respect to the linear fit by aberration effects (as clearly visible in Figure 5.10 both for the simulated and experimental data) and are not included in the fit. The reciprocal of the slopes of the theoretical and experimental linear fits of the central data represents the average demagnification factor, defined as the ratio between the distance of the peaks at the source (collimated wire) and at the detector (phosphor). The experimental average demagnification factor obtained in this way is 4.58 $\pm$ 0.03 and differs from the theoretical average value (4.70 $\pm$ 0.02) by less than 3%.

From the theory of electrostatic optics and SIMION simulations the demagnification factor $F(r, V_0, V_1)$, is a function of r, the distance of the electron sources (the holes in the laboratory tests) from the symmetry axis of the cylindrical lenses, V_0 the cage electrode voltage and V_1 the focusing ring electrode voltage. The simulated demagnification factors for the nominal focusing system voltages (V_0 = -20 kV, V_1 = -17.9 kV) vary from 4.8 at 0 mm

from the focusing system symmetry axis to 4.5 at -30 mm; these values are slightly smaller (less than 10%) than those obtained in Section 3.2.2.1 for secondary electrons (from 5.3 to 4.9) due to the small backward shift ($\approx$ 5.5 mm, see Figure 5.5 (a)) of the emitting wire in respect to the emitting Al foil plane of Figure 3.16. Simulations show that a longitudinal 8 mm wire backward shift accounts for a 10% image enlargement. The stretching effect caused by the external magnetic field, discussed in Section 5.3.1, should also be added to the enlargement due to the wire shift.

Besides the magnetic field effects discussed below, the lower values of the experimental data in respect to those simulated for thermionic emission can be explained considering that, due to mechanical reasons, the electron detector plane (in this case the micro channel plate input plane) was mounted shifted of about 4 mm in the electron direction causing a slight enlargement of the wire image on the phosphor with respect to the simulations.

Figure 5.11 shows the behaviour of the measured and calculated demagnification factors as a function of the distance from the symmetry axis along the wire axis at the source. The deviation between theoretical (yellow diamonds) and experimental (blue triangles) values is within 6.5%. The effect is clearly reduced (1.9 %) if a - 10 mm shift along the wire axis at the source is considered (the shifted data are represented by the green circles). This corresponds to an image shift of about 2 mm at the detector, taking into account the measured 4.58 average demagnification factor.

The image on the detector was actually measured shifted 1 mm downwards with respect to the detector centre. This effect, as discussed in Section 5.3.1, can be explained in terms of an external magnetic field. As the centre on the sensor was fixed manually to overlap with the mean position of the central hole peak image and was, anyway, not coinciding with the detector centre due to the observed image shift, it is reasonable to assume that both effects contributes to the observed discrepancy.

A possible alternative analysis is shown in Figure 5.12 where the behaviour of the measured and calculated demagnification factors is represented as a function of the distance of couples of holes symmetric with respect to the central one, for all the holes along the wire axis. In this case, all the evaluated demagnification factors are referred to the central peak and the measured maximum discrepancy between simulated and experimental data is within 3%.

The optical properties of the focusing system in terms of linearity and demagnification factor for off-centred beams are still not far from the SLIM monitor specifications and can easily be corrected using the results of the computer simulation. Slight deterioration of the optical properties would, anyway, not be significant for measurements, as actions should be taken for a better beam alignment inside the vacuum chamber.

Gaussian fits of the measured peaks shown in Figure 5.9 give a standard deviation varying in the range from 125 μm (for the central peak) up to 225 μm for the external peaks (Table 5.1). These values are compared with the sigma of the square distributions corresponding to the 1 mm or 0.5 mm diameter holes (289 μm and 144 μm, respectively), taking into account the average demagnification factor of $\approx$ 4.6.

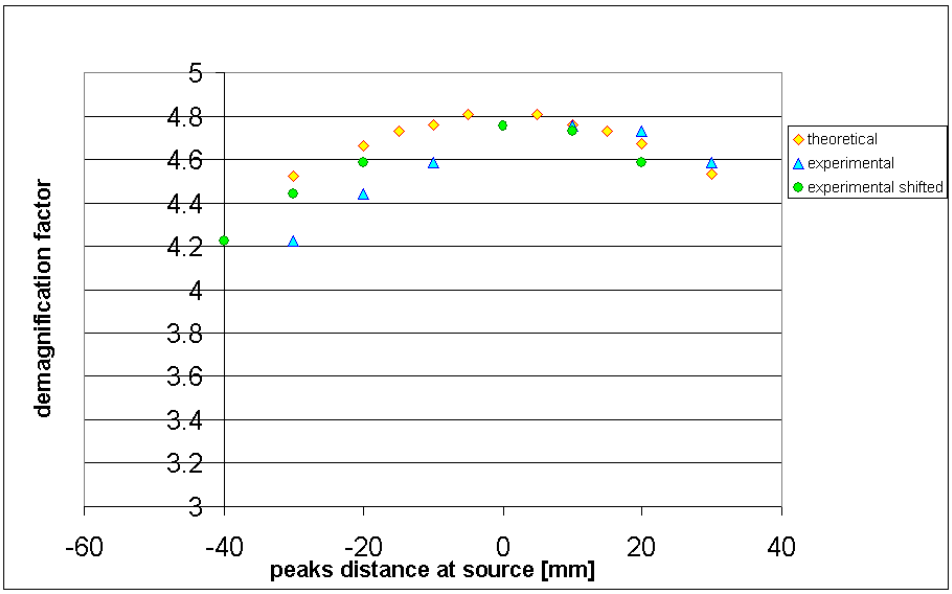

Figure 5.11: *Computer simulated (yellow diamonds) and experimental (blue triangles) demagnification factors as a function of the distance from the symmetry axis along the wire axis at the source. The green circles represent the experimental data shifted by about 2 mm at the detector.*

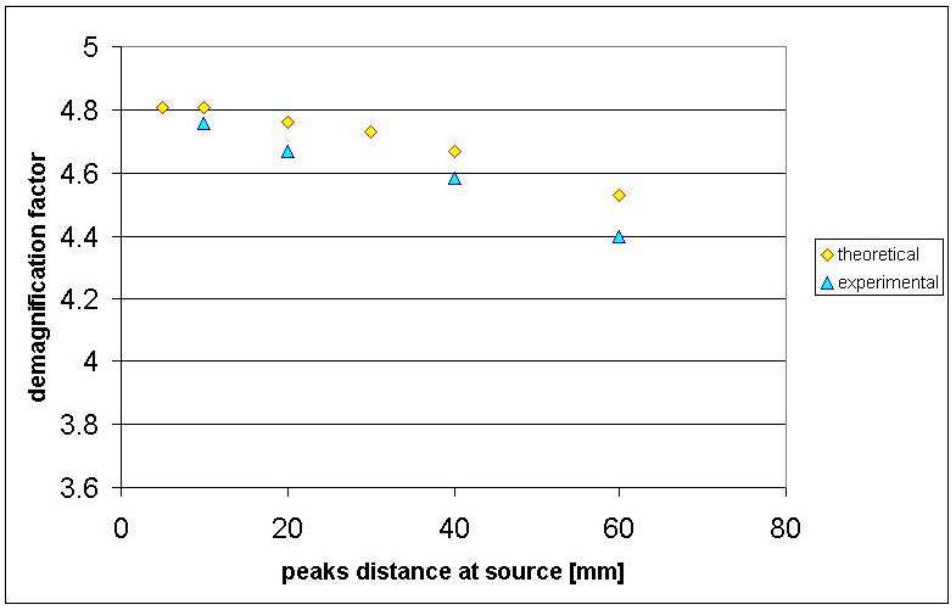

Figure 5.12: *Computer simulated (yellow diamonds) and experimental (blue triangles) demagnification factors as a function of the distance between couples of holes along the wire axis at the source.*

The transmission errors (δ) are evaluated for every hole source according to the definition of Section 3.2.2.1 ($\sigma^2_{detector} = (\sigma_{foil}/F)^2 + \delta^2$) and are reported in the last columns of Table 5.1. It is clear from the evaluated values of δ that the emitting sources can be considered as point sources. The aberration effect increases moving away from the symmetry axis of the focusing system cylindrical lenses, as expected. The average (δ) transmission error (obtained as the average of the values in Table 5.1) is 157 μm, well within the SLIM tolerances.

Table 5.1: *Focusing system transmission error evaluation for the thermionic emission tests.*

Hole diameter [**mm**]	**Measured** σ [μ**m**]	δ [μ**m**]
1	205	204
0.5	133	133
0.5	129	129
0.5	125	125
1	149	148
0.5	137	137
1	225	224

In Table 5.2 the theoretical and experimental standard deviations of the guassian fits of the simulated and experimental images on the sensor are compared. Taking into account the wire displacement discussed in Section 5.3.2 data have been simulated for a centred wire (thermionic electrons emitted over a $\approx 40^\circ$ degrees cone for the 1 mm diameter holes and $\approx 20^\circ$ degrees for the 0.5 mm diameter holes) and for a displaced wire (electrons emitted over a $\approx 180^\circ$ degrees cone for the 1 mm diameter holes and $\approx 90^\circ$ degrees for the 0.5 mm diameter holes).

Table 5.2: *Comparison of the simulated (different wire/collimator geometries) and experimental image peaks standard deviations.*

Hole diameter [**mm**]	**Simulated** σ **(40°)** [μ**m**]	**Simulated** σ **(180°)** [μ**m**]	**Measured** σ [μ**m**]
1	112	240	205
0.5	47	197	133
0.5	35	117	129
0.5	9	128	125
1	48	159	149
0.5	48	176	137
1	110	235	225

It is clear from the comparison of the experimental data with the two sets of simulated

data, that the wire was displaced from the nominal position for most of the emitting sources. Being the exact wire/collimator geometry of each emitting source unknown and considered the flat angular distribution of the thermionic electrons it is, therefore, impossible to make a more precise evaluation of the focusing system resolution. The average δ value estimated above is, nevertheless, satisfactory.

A more accurate evaluation of the focusing system resolution is left for the in-beam measurements with secondary electrons emission, as described in Section 6.4.1.

5.3.1 External magnetic field effects

The effect of an external magnetic field was simulated to investigate the measured shift of the wire image in respect to the sensor centre and the observed perturbations of the secondary electron trajectories. It was observed that the wire image could be shifted across the detector plane changing the position and orientation of a few Gauss permanent dipole magnet.

An external magnetic field with a vertical downward component of about 0.7 Gauss and an horizontal (along the focusing system symmetry axis) component of 0.3 Gauss was measured in the CERN laboratory. Simulations show that such a field, that can be ascribed to the earth's magnetic field, causes an image shift to the left side of the detector centre of about 3.5 mm and downwards of about 1 mm (Figure 5.13), as measured during the laboratory tests. This image displacement could be compensated with external permanent magnets if needed.

Simulation also show a stretching of the hole image along the wire axis reducing the measured demagnification factor by less than 3%. This result is consistent with the data shown in Figure 5.12.

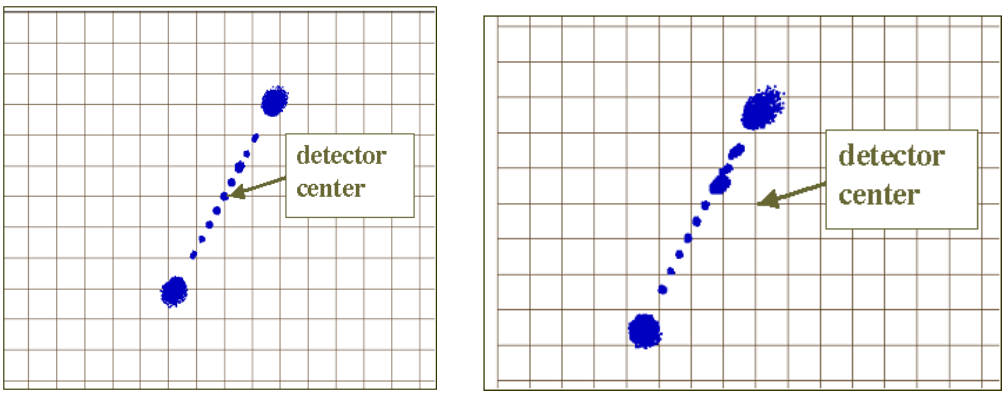

(a) (b)

Figure 5.13: *SIMION 3D simulation of the wire image with 11 holes (hole diameters is 0.5 mm, except for the two outer holes and fifth hole from above (1 mm diameter), with no magnetic field (a) and with magnetic field measured in the CERN laboratory (b) (grid pitch 2 mm).*

The experimental and simulated results indicate that compensation of the beam position offset/stretching or shielding with μmetal materials of the vacuum chamber in presence of variable magnetic field (due to any magnetic accelerator component) need to be implemented for beam measurements during therapy.

5.3.2 Measured wire intensity fluctuations

As shown by simulations and observed experimentally, wire sagging due to heat causes significant fluctuations of the number of emitted electrons and the width of their distribution on the detector. Figures 5.14 and 5.15 show the reduction in the number of electrons emitted in the hypothesis of a total shift or of a tilting of the tungsten wire, respectively.

For a shift of a couple of mm with respect to the cylindrical collimator axis, the number of electrons emitted decreases to 3%; while in the case of wire tilting, the peaks corresponding to the two outer holes disappear. Taking into account that the wire was not perfectly tight, it is reasonable to assume that according to the temperature and the mechanical conditions the wire could be locally displaced in respect to the centre of some holes of the collimator, explaining the observed hole intensity variations.

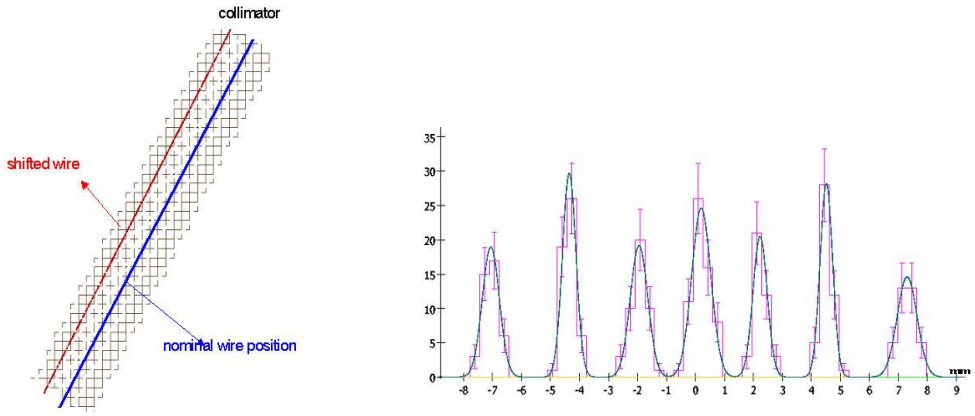

(a) (b)

Figure 5.14: *SIMION 3D simulation of the tungsten wire image with the hypothesis of a wire shift of a couple of mm with respect to the nominal position (the wire in the nominal position is represented in blue, the shifted wire in red) (a) and its image on the detector (in red the experimental data, in blue the gaussian fits) (b).*

The flat thermionic electrons angular distribution and the just discussed unpredictability of the wire/collimator geometry for each hole cause intensity and distribution variations of the collimated wire image that prevent a precise evaluation of the focusing system resolution. Nevertheless, the transmission error obtained from the experimental data is well within the SLIM tolerances. Moreover, the analysis of the system linearity and demagnifying factor results, shown in Figures 5.10, 5.12 and 5.11, confirm that the optical properties of the

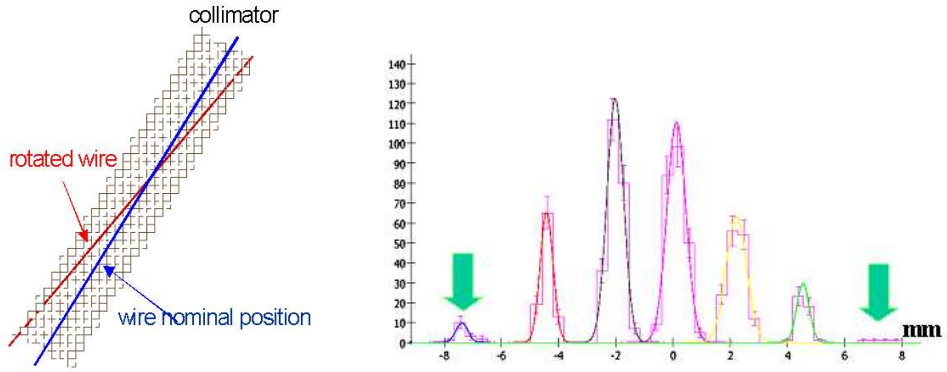

(a) (b)

Figure 5.15: *SIMION 3D simulation of the tungsten wire image with the hypothesis of a wire tilt with respect to the nominal position (the wire in the nominal position is represented in blue, the tilted wire in red) (a) and its image on the detector (in red the experimental data, in blue the gaussian fits) (b). The big arrows highlight the disappeared peaks.*

focusing system are in excellent agreement with the computer simulations and fulfil the SLIM beam monitor requirements.

The successful results of the laboratory tests paved the way for the in-beam testing carried out at the Cyclotron Laboratory of the EC Joint Research Centre, Ispra (Italy), described in Chapter 6.

Chapter 6

SLIM particle beam monitor in-beam tests

After the successful results of the laboratory tests with thermionic electrons, the SLIM beam monitor, the related equipment and control system were dismounted, packed up and shipped to the Cyclotron Laboratory of the EC Joint Research Centre (JRC) located in Ispra (Italy), where the full on-line system testing with the different sensors for the electron detection is being carried out. The Scanditronix MC40 cyclotron[1] is capable of accelerating various light ions up to an energy of 39 MeV (protons) with a maximum beam intensity of 50 μA and a minimum beam controllable intensity of $\approx$ 5 nA. The SLIM beam monitor was installed in one of the extraction lines of the cyclotron as described in Section 6.1.

As a proof of principle, in order to provide an early feedback to the dedicated sensor developer, the same commercial system used to measure the electrostatic lenses optical properties in laboratory has been integrated, despite lower than required frame rate. The results of the measurements and the related data analysis are described in Section 6.2.

The assessment of the low energy electron detection sensitivity in terms of intensity and profile measurements have been achieved with two different silicon sensors. The first tests were performed with the moderate granularity, large dynamic range, shallow back-plane pad sensor read out by low noise charge integrating front-end electronics. The results of the tests to evaluate the sensitivity to low energy electrons and to beam intensity variations to determine the system dynamic range are described in Section 6.3.

Finally, the back-thinned MIMOSA V CMOS detector has been integrated to assess the low energy electron detection proof of principle for sensors of the MIMOSA family, and the sensor profiling capability. Tests results and data analysis are discussed in Section 6.4. The new dedicated sensor, called MIMOTERA, designed to feature the required spatial granularity, dynamic range and frame rate at the hadrontherapy beam intensities, has been manufactured and is scheduled for testing.

1 Scanditronix was founded in 1965 and subsequently acquired by IBA in 1999, as a wholly-owned subsidiary (http://www.scxmedical.se/index2.htm).

6.1 SLIM monitor in-beam installation at the Ispra JRC cyclotron

After the successful results of the tests with thermionic electrons performed at the CERN laboratory and described in Chapter 5, in March 2004 the SLIM beam monitor, the related equipment and control system were dismounted, packed up and shipped to the Cyclotron Laboratory [2] of the EC Joint Research Centre (JRC).

The Scanditronix cyclotron is illustrated in Figure 6.1 (a) and the extraction beamline for the SLIM is represented in Figure 6.1 (b), while Figure 6.2 shows the SLIM installation phase and Figure 6.3 the SLIM monitor and related equipment installed and ready for the in-beam tests.

(a)

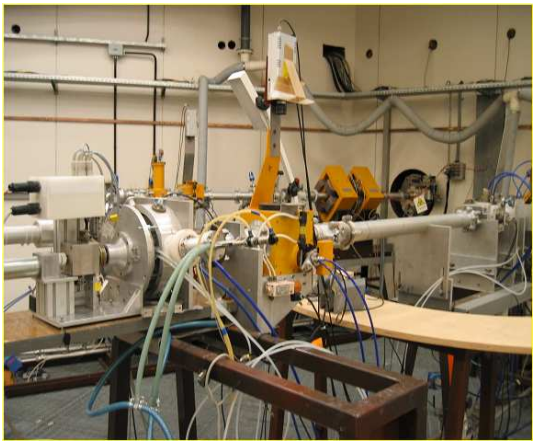

(b)

Figure 6.1: *The Scanditronix MC40 cyclotron of the EC Joint Research Centre (JRC) located in Ispra (Italy) (a). The extraction line used for the installation of the SLIM beam monitor (b).*

2 http://bms.jrc.cec.eu.int/cyc.html.

(a) (b)

Figure 6.2: *Installation of SLIM beam monitor at the end of one of the extraction lines of the JRC cyclotron: fixing of the tank support on the room floor (a) and installation of the vacuum tank on the support (b).*

Figure 6.3: *The SLIM beam monitor and related equipment installed in one of the extraction lines of the JRC cyclotron.*

With no loss of generality and considerable cost saving, initial tests were performed with

a standard Al sheet about 10 μm thick[3]. Moreover, the primary proton beam energy was chosen to equal 17 MeV for the most efficient use of beam time slots in between commercial radioisotope production without the need of readjusting the accelerator parameters. Even if 17 MeV protons are below the lower energy required for therapy (60 MeV), the only substantial difference for the tests is the increase in the secondary emission efficiency (from 4% at 60 MeV to 10% at 17 MeV).

The system was initially tested with an intensifying microchannel plate, coupled to a phosphor screen and imaged with a standard CCD camera. Following this, tests were performed with the pad silicon sensor and finally with a back-thinned MIMOSA V CMOS sensor.

The cyclotron reference profile monitor for the extracted beam is a scintillating screen observed with a TV camera and a video monitor. The screen, tilted of 45° degrees in respect to the vertical axis, consists of an aluminium block with spot deposits of aluminium oxide as shown in Figure 6.4. The distance of the Al_2O_3 deposits determines the detector granularity of 3 mm, as visible in the picture. This is the major limitation of the in-beam tests, as the screen is the only profile monitor to counter check the SLIM beam measurements that, according to the simulations of Chapter 3, claims a spatial resolution of about 100 μm for centred particle beams and of about 1 mm for off-centred beams (about 30 mm from the vacuum chamber axis), as detailed in Section 3.2.2.1.

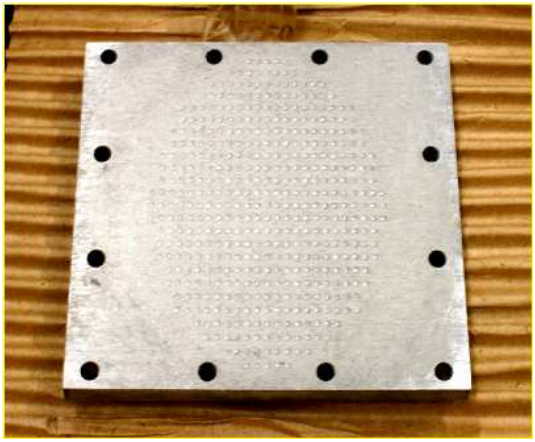

Figure 6.4: *The JRC extraction line scintillation screen for the beam profile measurement.*

The second drawback is that the video signal of the JRC reference monitor is displayed on a video monitor without the possibility of a direct digital record of the beam image for more accurate comparisons with the SLIM measurements.

3 Since the secondary emission is a surface effect, the replacement of the Al foil should not modify the backward secondary emission yield and energy and angular spectra evaluated in Chapter 3.

6.2 In-beam tests with the phosphor sensor and a CCD camera

The results of the tests with a 17 MeV proton beam, intensity in the range 90 to 140 nA, (asymmetric) cross sections from 8 to 33 mm and the phosphor sensor observed with a CCD camera for the secondary electrons detection are shown below. After the setting of the line, the beam dump was removed and the beam signal clearly detected on the SLIM beam monitor. Figure 6.5 shows the beam profile measured with the JRC reference beam monitor (the bright spot on the right is a defect of the JRC video camera). The profile of the same beam measured with the SLIM is shown in Figure 6.6, where image 6.6 (a) represents the CCD signal displayed with a video monitor and 6.6 (b) the same measurement digitized with the frame grabber.

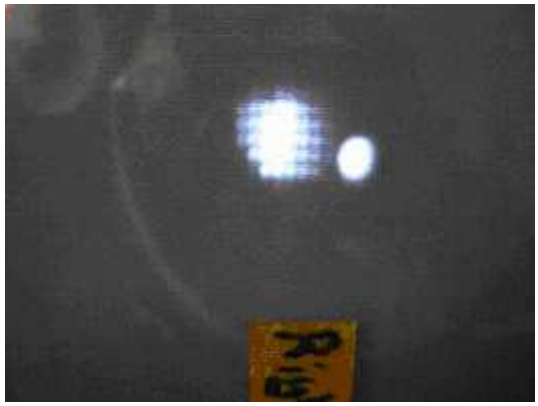

Figure 6.5: *Beam profile measured with the JRC reference beam monitor (the bright spot on the right is a defect of the JRC camera).*

The projections of the horizontal and vertical beam profiles are displayed in Figures 6.6 (c) and (d) and are in agreement with the simulations of Section 3.2.2.1. Considering that the JRC scintillation screen is tilted of 45° degrees in respect to the vertical axis and that the SLIM beam monitor is tilted of 45° degrees with respect to the horizontal axis the following relations need to be used to translate from one measured profile to the other:

$$H_{SLIM} = H_{JRC} \cdot \sqrt{2} \tag{6.1}$$

$$V_{SLIM} = \frac{V_{JRC}}{\sqrt{2}} \tag{6.2}$$

where H and V are the beam measured horizontal and vertical size respectively. The resultant demagnification factor at the nominal focusing system voltage (on the cage electrode V_0 = - 20 keV, on the ring electrode V_1 = - 17.9 keV) for a centred beam is $\approx$ 5.

It was observed that the beam changes shape and position varying the values of the

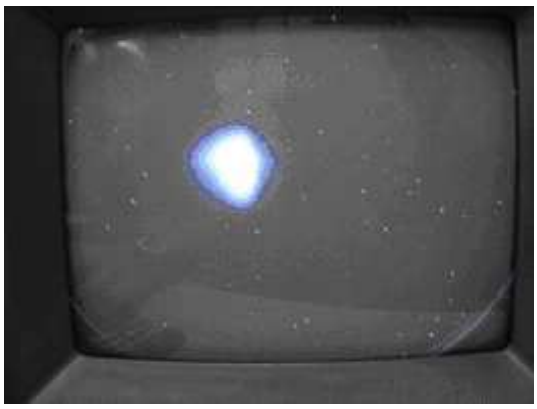

(a)

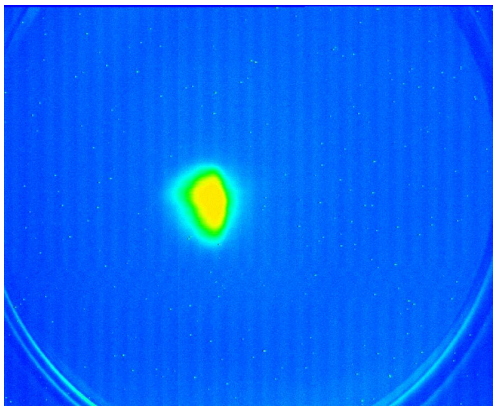

(b)

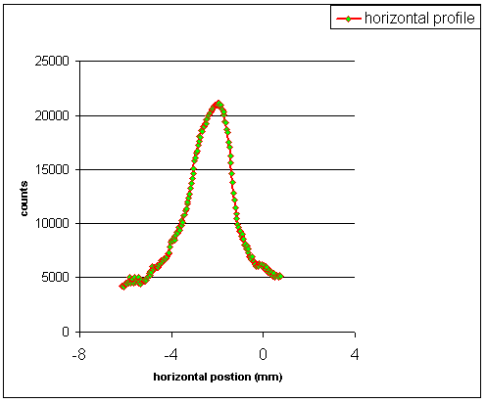

(c)

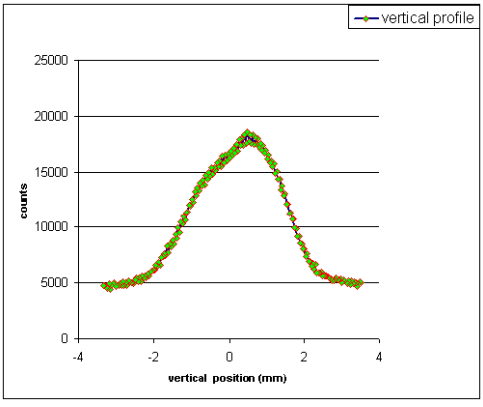

(d)

Figure 6.6: *Beam profile (≈ 10 mm x 20 mm) measured with the SLIM: CCD signal on a video monitor (a) and CCD signal digitized with the frame grabber (b). The circular edge partially visible in the picture is the phosphor screen frame (screen effective diameter is equal to 32 mm). Beam profile projection on the horizontal (c) and vertical (d) axis.*

voltages of the electrodes of the focusing system (both cage and ring), as expected. Changes in the measured beam shape induced by variations of the current in the extraction line quadrupole magnets were also measured as shown in Figure 6.7.

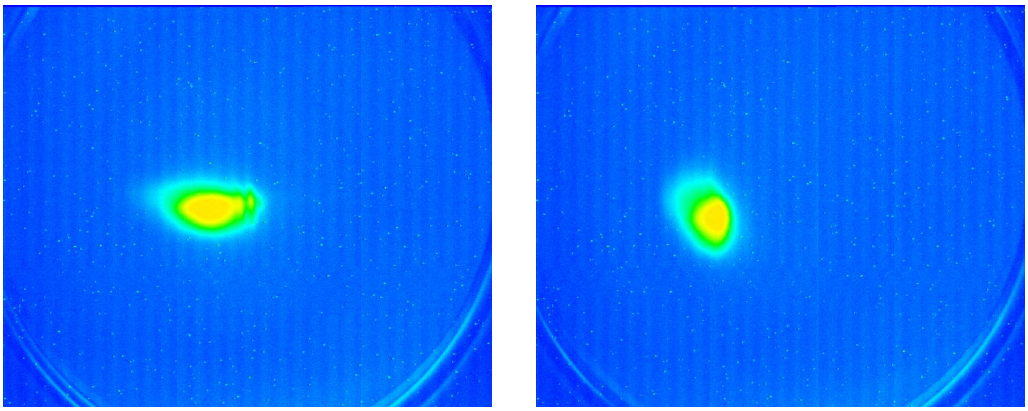

(a) (b)

Figure 6.7: *Wide (≈ 20 mm x 15 mm) (a) and focused (≈ 10 mm x 15 mm) (b) beam profile measured with the SLIM (CCD signal digitized with the frame grabber).*

The results shown should be compared with measurements with a analogous spatial resolution beam monitor but look, nevertheless very promising. As the JRC cyclotron extraction lines are not equipped with a beam monitor with granularity comparable to that of the SLIM to use as reference for the actual beam parameters, as mentioned in Section 6.1, future tests with defocusing and collimation of the extracted beam to lower the beam intensity and better define the beam shape are scheduled.

6.3 In-beam tests with the pad silicon sensor

After the encouraging results with the phosphor screen and a CCD camera for the secondary electrons detection, the position sensitive silicon detector described in Section 2.4.2, integrating 22 x 22 pads with 1.4 mm pitch, was hybridized on ceramics, mounted on the focusing system (Figure 6.8), and integrated in the beamline. The pad detector, as explained in Section 2.4.2, was expected to be sensitive to the SE emitted by the beam monitor target and accelerated to 20 keV and the front-end read-out chips to cover the required dynamic range.

Four 128-channel low noise VASCM2 ASICs chips of the VIKING family read out the sensor via the dedicated data acquisition system as described in Section 2.5, amplify and store the charge deposited on each pad over a pre-set integration time and implement four different gains (Section 2.4.2). Due to wire bonding problems, only one pad out of two could be connected to the readout chips. One of the chips was not working correctly and it was not possible to detect the signal of one sensor quarter.

During the first tests with the pad sensor, the beam was delivered to the SLIM beam

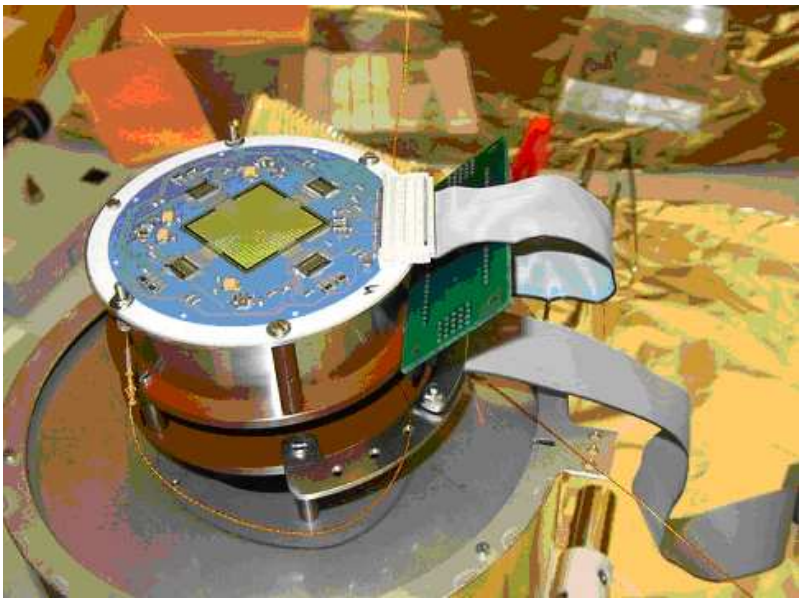

Figure 6.8: *Pad detector hybridized on ceramic and mounted at the end of the SLIM focusing system.*

monitor through a collimator with three holes, a central one (5 mm diameter) plus two smaller satellites (2 mm diameter), as shown in Figure 6.9. The collimator was installed in a support placed about 1 m upstream the SLIM beam monitor as shown in Figure 6.10.

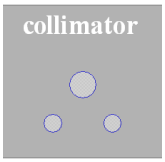

Figure 6.9: *Schematic drawing of the Al collimator with the three central holes used for the tests with the pad sensor.*

The average proton beam intensity was below 5 nA and the integration time was set to 1 ms. By changing the extraction line quadrupole settings, the beam position was swept from the larger hole to one of the secondary holes as clearly distinguishable in Figure 6.11 where the horizontal and vertical scale refers to the number of the pad. The upper left of Figure 6.11 refers to the case where the beam was illuminating the central and left holes. To the right is represented the symmetric situation while, on the bottom part, is the superposition of the two images.

After the implementation of a chips readout procedure to reduce the integration time and avoid saturation for the typical beam intensities of the Ispra cyclotron, the pad sensor was used to measure sensitivity to beam current variations and the saturation limit. The response

Figure 6.10: *Beam collimator support ∼ 1 m upstream the SLIM beam monitor.*

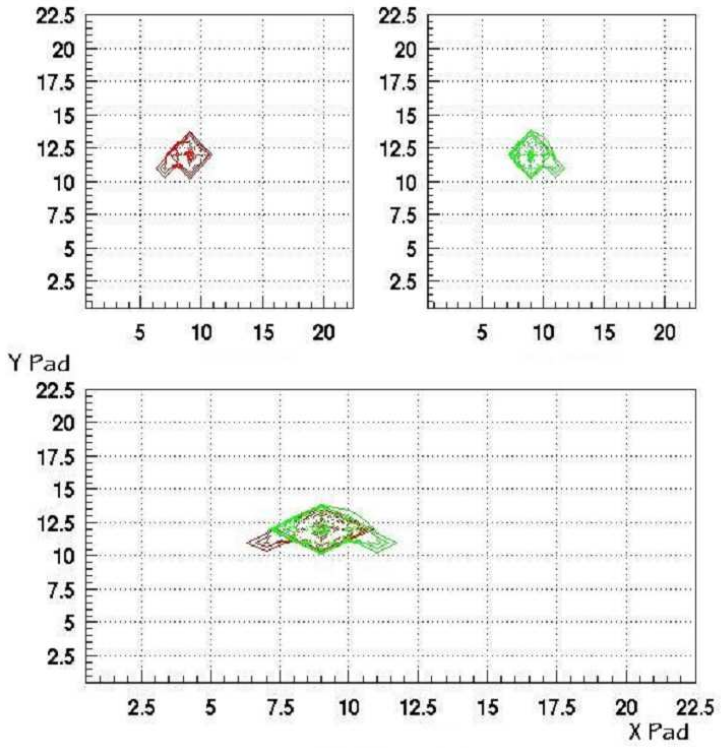

Figure 6.11: *First record of images with the pad silicon sensor of a patterned beam, produced with a collimator.*

of the system to a scan of the beam intensity (5 nA to 50 nA) is shown in Figure 6.12. Data were collected for an integration time of 20 μs and the signal may be assumed to correspond to beam intensities 5 times lower over 100 μs integration time, in the range of the maximum intensities for hadrontherapy. The measured sensitivity is $\approx$ 60 ADC/nA and the saturation limit around 30 nA, compliant with the specifications required by hadrontherapy beams.

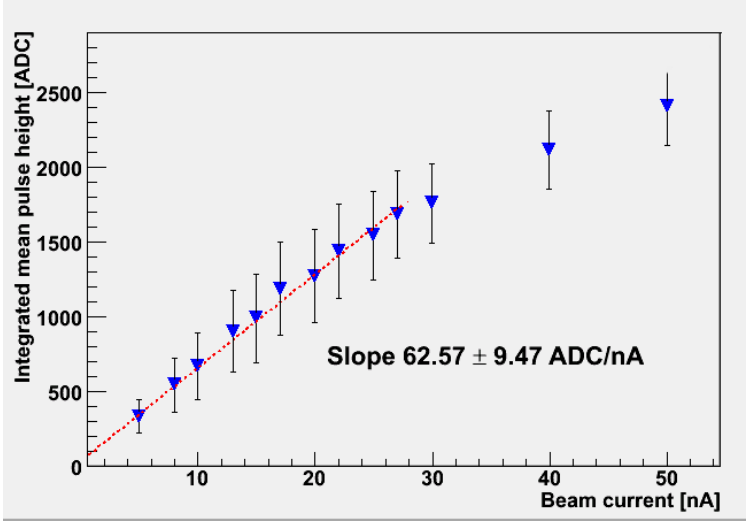

Figure 6.12: *Integrated pulse height recorded by the pad sensor with a 20 μs integration time versus the proton beam current. The slope of the best linear fit is around 60 ADC/nA. The large error bars can be ascribed to the cyclotron source instability at such low beam intensities.*

Despite the poor spatial resolution and the bonding problems, chips and sensor behaved as foreseen. The results of both sets of measurements with the first pad prototype proved that a silicon detector with shallow backplane is sensitive to 20 keV electrons, works properly with integrating electronics featuring the required dynamic range and can, therefore, be used for real-time hadrontherapy beam imaging.

6.4 In-beam tests with a CMOS monolithic active pixel sensor

As a second stage, spatial granularity and sensitivity of the system were studied integrating the back-thinned MIMOSA V CMOS sensor described in Section 2.4.3. Images of 17 MeV proton beams with 10 nA intensity were acquired and analyzed. The sensor was used in the so-called 'fast and coarse' mode meaning that only one out of nine pixels is readout (granting anyway the design granularity) and increasing the frame-rate with a corresponding integration time of 160 μs.

The data acquisition was based on the custom developed DAQ system described in Sec-

tion 2.5. The response of the system was studied inserting in the beam path, 1 m upstream the SLIM beam monitor, a 12 mm-thick Al collimator with six rows of 1 mm-diameter holes and pitches from 1.5 mm up to 6.5 mm as shown in Figure 6.13(a). The extraction line quadrupole magnets were tuned to illuminate the collimator with the wider possible beam, to cover the larger number of holes.

The measured beam image is the pixel per pixel average of 500 frames after pedestal subtraction. During the tests with the MIMOSA V sensor, the secondary electrons were accelerated only to a final kinetic energy of 10 keV with V_0 = - 10 keV (cage electrode voltage) and V_1 (ring electrode voltage) scaled down to - 8.95 kV, corresponding to a sharper image on the on-line display. The recorded image on the MIMOSA V sensor is shown in Figure 6.13(b) where the color scale is proportional to the mean signal pulse height.

Hot spots corresponding to the holes on the collimator are clearly visible and they are highlighted in Figure 6.14. The image appears tilted by about 210° degrees with respect to the collimator geometry in agreement with the mounting scheme of the sensor on the focusing system. The hole candidates are manually identified and their centre coordinates weighted on the pixel pulse height content to get an estimate of the tilting angle. The resulting points are fitted with a straight line as shown in Figure 6.14. The mean slope of the straight lines corresponds to a tilting angle of $(208.2 \pm 3)^\circ$ degrees in good agreement with the rotational degree of freedom.

To reconstruct the hole position, thin regions of interest ($\sim$ 10 pixel wide) containing a single row of holes have been selected as shown in Figure 6.15.

The contents of each strip has been projected along the rotated x axis as shown in Figure 6.16 for the first row of holes with larger pitch. Since an unexpected high level of background is present in between adjacent peaks, to determine the peak positions, a composite fit function with a quadratic background and gaussian shaped peaks was used and the results are shown in Figure 6.16.

The results of the fits of the gaussian shaped peaks are summarized in Table 6.1.

6.4.1 Optical parameters evaluation

The demagnification factor has been estimated taking into account the mean positions of each peak obtained with the fit procedure. The average measured distance between two adjacent peaks has been compared with the real one on the collimator resulting in an average demagnification factor of 3.8 to be compared to a nominal value of 5 (Section 3.2.2.1). The discrepancy can be understood in terms of a shift of the detector position with respect to the simulated focal plane due to mechanical constraints. It might be also due to aberration effect since the image is off-centered with respect to the sensor centre.

To assess the system optical properties, the point spread function (PSF), defined as the width of the image of a δ function, was evaluated. The PSF can be considered as a blurring function degrading the sharpness of the input signal and it was assumed gaussian for the present analysis. The measured peak distributions were assumed guassian (even if they result from the convolution of the PSF gaussian distribution and the circular box

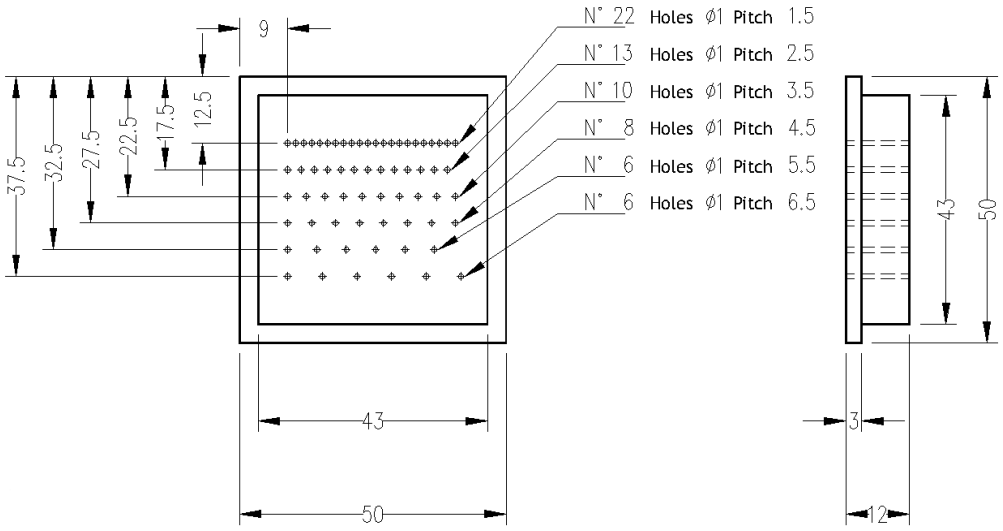

(a) Collimator

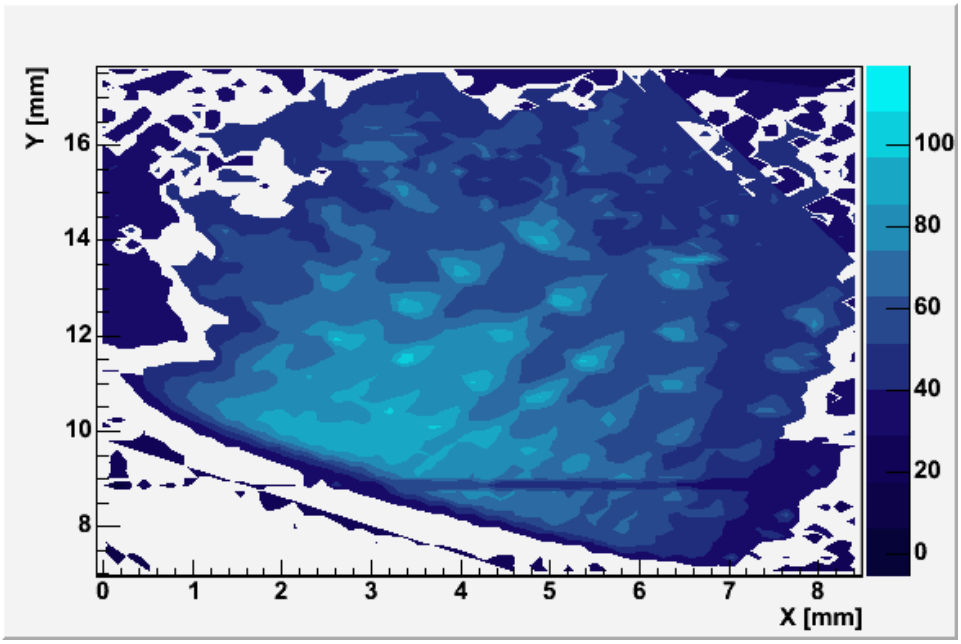

(b) Contour image

Figure 6.13: *(a) Schematic drawing of the collimator placed on the beam path, consisting of a 12 mm-thick aluminium block with 6 rows of 1 mm diameter holes. The hole pitches range from 1.5 up 6.5 mm. (b) An image of the beam profile on the SLIM monitor as detected by the CMOS sensor. According to the mounting scheme of the sensor on the focusing system the image, obtained as the average of 500 acquired frames after the pedestal subtraction, appears tilted by* 210° *degrees. The colour scale on the right represents the mean analogue signal stored in each single pixel.*

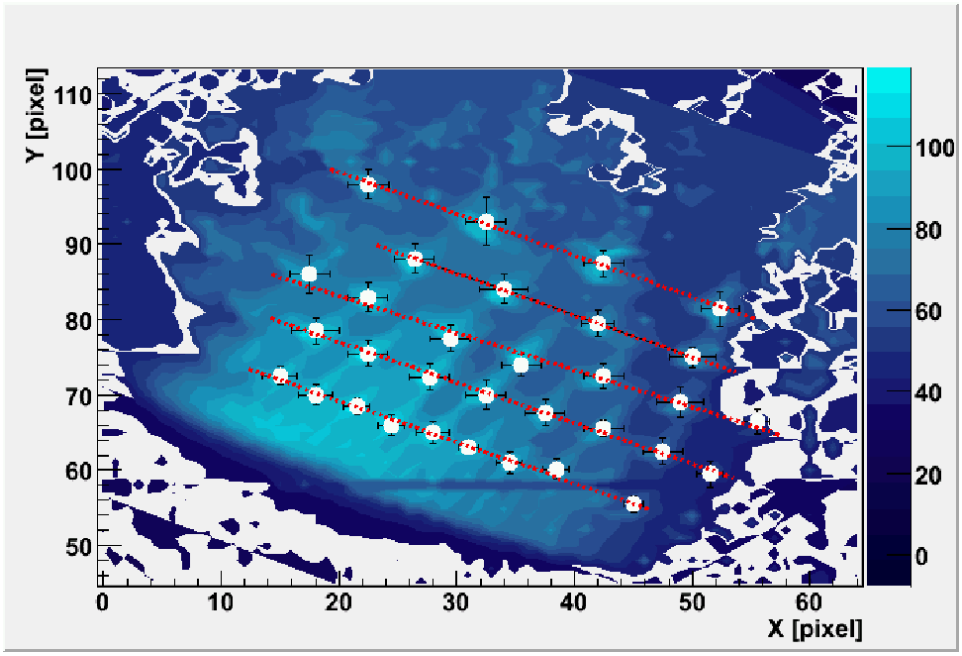

Figure 6.14: *The image on the MIMOSA sensor is tilted in respect to the collimator (Figure 6.13(a)). In the picture is shown the fit of the slope of the first five row of holes.*

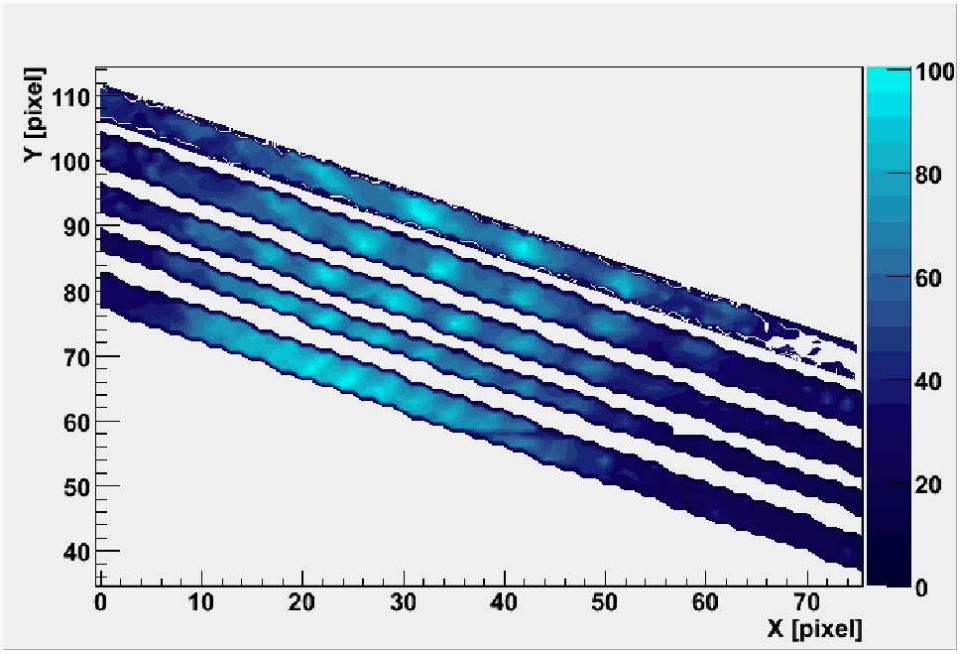

Figure 6.15: *Thin tilted regions containing one candidate row each have been selected to avoid interpolation systematic errors.*

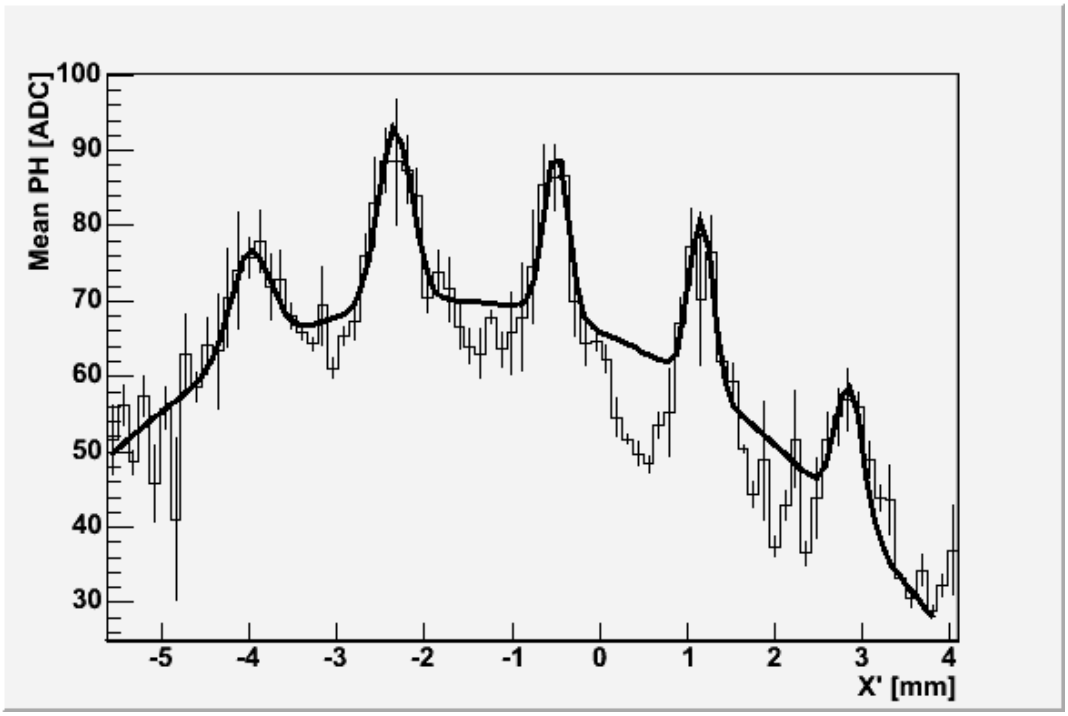

Figure 6.16: *A thin region of interest centered around the row with the larger holes pitch has been projected along the rotated x axis and the results fitted using a composite function with a quadratic background and Guassian peaks.*

Table 6.1: *Fit results of the row of holes with larger pitch. Peaks are numbered from left to right of Figure 6.16*

	parameter	**[mm]**	**[mm]**
First peak	Mean	-4.02	± 0.08
	Sigma	0.23	± 0.04
Second peak	Mean	-2.37	± 0.02
	Sigma	0.19	± 0.01
Third peak	Mean	-0.53	± 0.02
	Sigma	0.13	± 0.01
Fourth peak	Mean	1.13	± 0.02
	Sigma	0.13	± 0.01
Fifth peak	Mean	2.82	± 0.03
	Sigma	0.15	± 0.02

distribution representing the collimator hole finite size) and their sigma averaged.

The PSF was evaluated fitting the experimental data to a numerical convolution of a gaussian resolution function and a box representing the collimator holes. This procedure has been performed only for the row of holes with larger pitch, because for the other rows the high background and consequent low image contrast prevented a precise localization of the measured peaks. The PSF sigma obtained is 144 μm and is shown in Figure 6.17 together with convoluted peak shape. This result can be considered satisfactory when compared with the pixel pitch and the adverse experimental conditions.

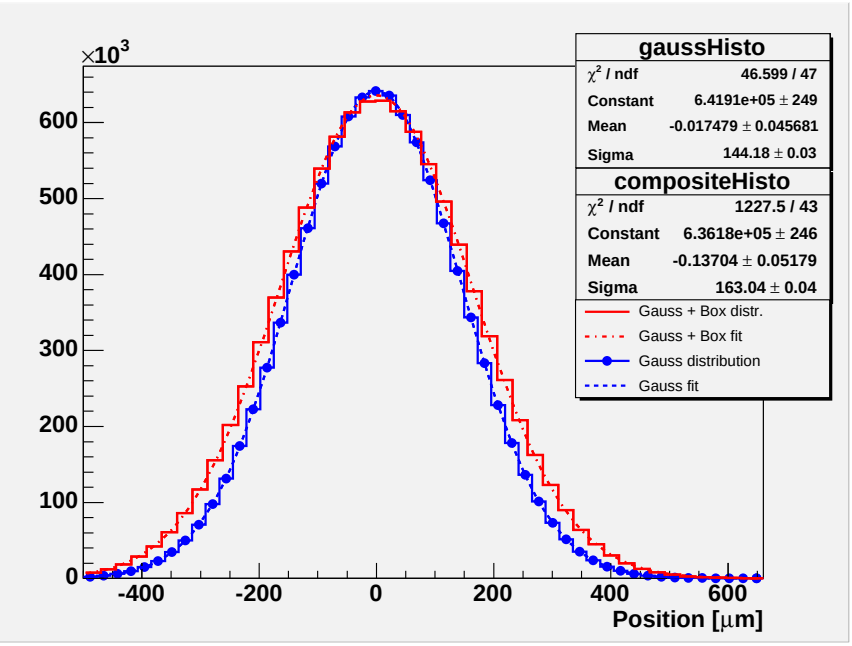

Figure 6.17: *Point spread function (in blue) obtained as the deconvolution of the measured peak (in red) and the collimator hole distributions.*

6.4.2 Image background

Four possible explanations for the high level of signal in between the adjacent hot spots have been envisaged:

1. a background ionizing radiation field in the extraction line beam pipe;
2. an electronics misbehaviour of the sensor due to a saturating secondary electron flux;
3. divergence of the proton beam after passing through the collimator, together with forward scattering of the beam from the front edges (incident beam side) of the holes in the collimating block;
4. thermionic electron emission from the Al foil caused by primary beam heating.

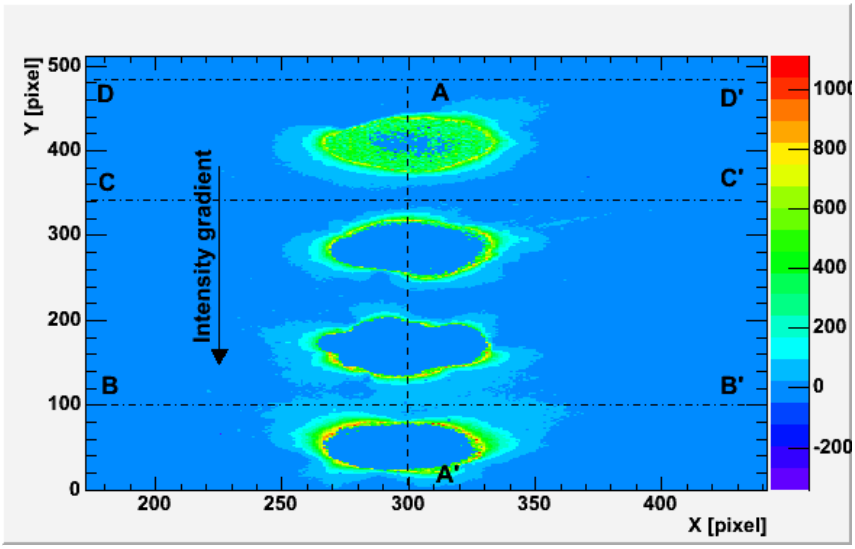

(a) Four holes collimator

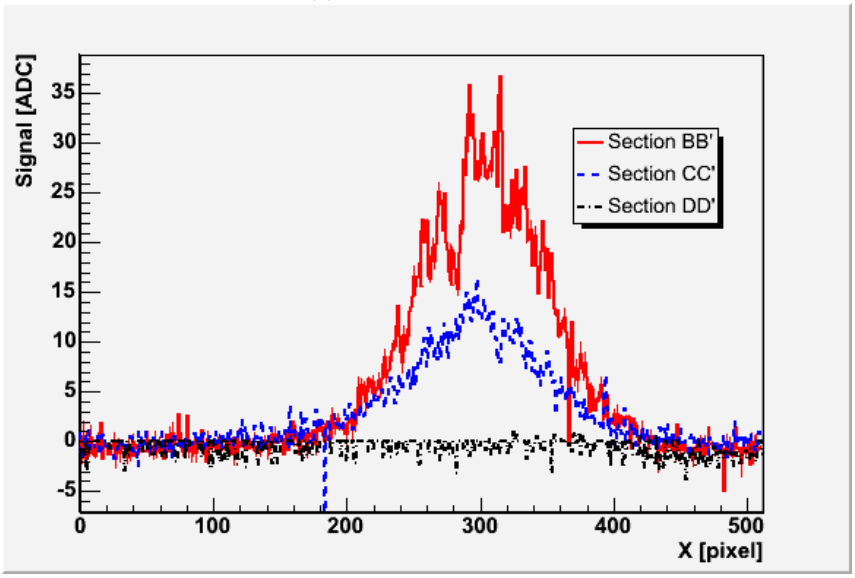

(b) Horizontal slices

Figure 6.18: *(a) The image recorded on the MIMOSA V sensor by shining a laser spot through a collimator with four 1 mm-diameter holes. As indicated in the picture, the laser was focalized to have a top to bottom intensity gradient to study the intensity dependency. Spot deformation and enlargement due to the blooming effect is clearly visible as a function of the light intensity. (b) Three horizontal slices in different positions of the sensor show the blooming effect dependency on the laser signal intensity.*

The first hypothesis was discarded by performing a run where the collimator was replaced by a solid target to completely stop the primary beam. Only in the case of very high beam intensity (in excess of 50 nA), a scattered radiation field, too small to be considered as the cause of the observed phenomenon, was measured.

The second hypothesis was studied in the laboratory by shining a very intense green laser light[4] on the sensor to characterize the MIMOSA image blooming when exposed to an over-saturating flux. The image produced by the light passing through a four hole (1 mm diameter, 2 mm pitch) collimator was recorded and indicated a non negligible blooming. Blooming is a well known effect affecting imaging devices when exposed to a saturating flux, deforming and enlarging spot sizes[5]. While in CCD cameras this is a well known problem, CMOS sensor should be naturally immune from blooming since each pixel is directly connected to the readout line. But if the injected charge density in a region of the sensor is too high, the diffusion of the charge carriers may result in an image deformation and enlargement.

Figure 6.18(a) show the image acquired using the CDS (correlated double sampling) technique[6] and zero signal is expected for all saturated pixels. In non saturating conditions the maximum and the minimum radii are around 30 pixels that, taking into account the 17 μm pitch, correspond to a reconstructed hole with a measured diameter of 1.02 mm. The contours of the four holes are not circular (laser intensity increases towards negative y values) and the overall size of the holes is bigger than the real one on the collimator.

Moreover, an horizontal slice of the profile passing in between two holes (section BB' shown in Figure 6.18(b)) indicates the presence of a not negligible background signal.

The observed background signal increased during in-beam measurements with the increase of the secondary electrons kinetic energy from 10 to 20 keV; this is another experimental evidence in support of the saturation hypothesis. The signals were acquired with the standard MIMOSAV DAQ rolling shutter mode with four frames per every cycle, where the first two frames are useless and the next two are used for the CDS. The system dynamic range, decreased in this way by a factor four, further reinforces the saturation hypothesis.

The third effect is presumably present and responsible for some of the background signal. A simple calculation of the beam divergence (0.06° degrees, $\approx$ 1 mrad) indicates that this does introduce some beam spread before the monitor foil (a 1 mm hole can spread 2 mm across at the SLIM beam monitor), but cannot account for the background signal far from the hot spots. The additional effect of the proton scattering from the non-smoothed edges of the collimating holes has to be further investigated.

4 The used laser has a wavelength of 527 nm and an intensity of 100 mW.
5 In saturation conditions the brightest part of the image tends to grow in size and in the worst case it can occupy the full sensitive surface of the sensor; the physical explanation of the image blooming in saturation condition can be related to the charge carrier diffusion.
6 When the sensor is operated in the so called Correlated Double Sampling (CDS) mode, to obtain one image two consecutive frames are required. Sampling each pixel twice and considering as a signal the difference of the two allows a significant reduction of the fixed pattern noise and of several types of temporal noise that are effectively removed from the sensors output. If one pixel is saturated already in the second last frame it will be saturated also in the last one with the same output level and the difference between the two is exactly zero or, in the case of image pedestal subtracted, it corresponds to the negative value of the pedestal.

The fourth possibility also cannot be excluded as a contributing factor, but is probably minor due to the low heating expected by the small amount of primary beam energy lost in the foil (Section 3.3), as well as the fact that upon blocking of the beam, an immediate reduction of the measured signal to zero was observed.

Thus laboratory tests and calculations demonstrate that the observed background signal is a result of various contributions. Since the blooming effect is certainly present and related to over-saturating flux, an imaging device with a higher dynamic range is needed in order not to spoil the resolution required by the beam monitor.

For this reason the MIMOTERA dedicated sensor, featuring both the dynamic range at the beam intensity of interest and the required spatial and time resolution has been designed, manufactured and is now in the post-processing phase. Beam tests with the MIMOTERA chip are scheduled as well as further studies of the background signal origin.

Conclusions

Hadrontherapy projects have been funded in Germany, Italy, France, Austria to respond to the European need of new hospital-based facilities and assure the best available techniques to a large number of patients. Optimization of the accelerator extraction scheme, of the beam delivery system and of the beam monitoring system during therapy ensure the extracted beam smoothness and delivered dose uniformity for the best treatment quality.

The aim of this doctoral thesis was the study, development and testing of an innovative beam monitoring system for real time diagnostics of charged particle beams in the extraction lines of a hadrontherapy facility, with exceptional acceptance, transparency, spatial and time resolution.

The main constraint on the novel beam monitor, **S**econdary emission monitor for **L**ow **I**nterception **M**onitoring (SLIM), is to measure beam intensity, position and profile, without significant perturbation to the extracted beam during patient treatment. The electrostatic focusing system and the secondary electron detectors of SLIM, together with the dedicated acquisition system, have been designed to produce negligible effects on the few nA clinical beam, providing the beam profile and position at 10 kHz frame rate with a granularity not exceeding 1 mm and a beam current resolution of a few percent, on the base of the clinical specifications on the beam for therapy.

The secondary electrons yields have been calculated scaling Sternglass semi-empirical theory at hadrontherapy beams energies, with Borowsky correction for ions. The agreement between the measured and the calculated yields for proton on Al target is within 15%. There are, however, no experimental data for carbon on aluminium targets. The secondary emission study angular and energy distribution and yield were the input conditions for the design of the electrostatic focusing system, based on a cross-focusing optical scheme inspired by image intensifier tubes.

The final focusing system solution, based on the CMOS sensor specifications, features a demagnification factor of ≈ 5 with the secondary electrons final kinetic energy in the 10 to 30 keV range to reach the sensor sensitive region and a spatial resolution better than 1 mm (depending on the distance from the focusing system symmetry axis) in compliance with the SLIM monitor constraints. A 60° degrees sector of the larger cylindrical electrode consists of a 40 μm diameters, 4 mm spacing wires grid. The grid ensures a 99% transparency to the hadron beam without distortion of the electrostatic field for the secondary electrons transport.

The final focusing system prototype was realized with high vacuum materials such as stainless steel for the electrodes and Vespel (polymide resin) for the insulating parts for a total length (emission foil to detector) of 234 mm, a maximum diameter of 192 mm and a total weight of $\approx$ 1 kg. The system was installed in the dedicated parallelepiped-shaped vacuum chamber (the longitudinal flange-to-flange occupancy is 460 mm) designed to host different detection systems not fully defined at the time of the vacuum chamber construction.

Ten 70 mm diameter, 0.1 to 0.2 μm thick secondary emission foils, to be mounted on the larger lens of the focusing system, were also manufactured starting from 0.1 mm thick 99% purity aluminium foils following a technique consolidated at CERN.

After the system integration, a complete qualification of the beam monitor has been performed, both in laboratory and in a hadron beam, focused on the properties of the electrostatic optics that determine the beam monitor spatial definition and on the dedicated CMOS monolithic detector sensitivity to low energy electrons, dynamic range and profiling capability. A customized slow control system for the vacuum, high voltage and motion equipment was integrated to ensure the maximum safety to both users and instrumentation.

The laboratory tests with thermionic electrons have demonstrated that the focusing system optical properties fully satisfy the SLIM beam monitor requirements. A commercial system, consisting of an image intensifier micro channel plate, coupled to a phosphor screen viewed with a standard CCD camera, was used for the electrons detection, despite lower (50 Hz) than required (10 kHz) frame rate.

The comparison of the SIMION 3D simulations with the experimental data clearly demonstrates that the electro-optical system is linear with small aberrations for distances from the symmetry axis of the focusing system larger than 20 mm, as predicted by theory. The deviation between the theoretical and the experimental average demagnification factor, obtained as the reciprocal of the linearity plot slope, is within 3%. The maximum discrepancy between simulated and experimental demagnification factors, referred to the central peak of the wire image, is within 3%.

The effect of the external magnetic field was investigated with the help of a permanent dipole magnet and simulated with SIMION 3D. The calculated effect of a 0.7 Gauss downward magnetic field, as the one measured in the CERN laboratory, is in perfect agreement with the measured shift and 3% stretching of the wire image. The magnetic measurements analysis demonstrate the need to compensate the beam position offset/stretching or to shield with μmetal materials the vacuum chamber in presence of variable magnetic field (due to any magnetic accelerator component) during therapy.

Finally, the results of the SIMION 3D simulations of tungsten wire displacements with respect to the nominal positions agree well with the measured wire intensity fluctuations.

As a proof of principle, in order to provide an early feedback to the dedicated sensor developer, the same commercial system used to measure the electrostatic lenses optical properties has been integrated in the beam line for the first in-beam tests.

With no loss of generality and considerable time saving, the primary proton beam energy during the tests was chosen to equal 17 MeV for the most efficient use of beam time slots in

between commercial radioisotope production without the need of readjusting the accelerator parameters.

After the setting of the line, as soon as the beam dump was taken away from the proton beam path, the beam signal was clearly detected on the SLIM beam monitor (10 mm x 20 mm cross section, $\approx$ 100 nA beam intensity). The horizontal and vertical projections of the beam profile were in very good agreement with the profile measured by the reference JRC scintillating screen. As expected, the beam changed shape and position, by varying the values of the voltages of the focusing system electrodes. Changes in the beam shape induced by variations of the current in the extraction line quadrupole magnets were also measured in real time.

The assessment of the low energy electron detection sensitivity in terms of intensity and profile measurements has been achieved with two different silicon sensors. The first tests were performed with the moderate granularity, large dynamic range, shallow back-plane pad sensor. The pad detector was primarily developed as low energy electron detector in a Hybrid Photodiode. It was therefore expected to be sensitive to the 20 keV SLIM electrons focused on the sensor surface.

A low noise integrating readout electronics (the VASCM2 ASIC) based on a charge sensitive amplifier followed by a double S&H circuit has been selected to read out the sensor. The current flowing into each channel is integrated during an adjustable integration time and the double S&H circuit allows a continuous signal tracking. The ASICS are characterized by a very high dynamic range going from $\pm$ 4.2 $\cdot$ 10^4 fC to $\pm$ 4.2 $\cdot$ 10^2 fC and were therefore expected to cover the dynamic range of interest.

Despite the poor spatial resolution, the experimental results clearly demonstrate that the sensor is sensitive to 20 keV electrons, works properly with integrating electronics in the intensity range of interest and can be used for real-time beam imaging. The analysis of the system response to a beam intensity scan with 20 μs integration time (5 times smaller than what required by hadrontherapy) shows that the sensitivity ($\approx$ 60 ADC/nA) and the saturation limit (30 nA) are compliant with the specification.

Finally, the back-thinned MIMOSA V sensor, featuring a high granularity but limited dynamic range, has been integrated to assess the low energy electron detection proof of principle and the profiling capability for the sensors of the MIMOSA family. The MIMOSA V was successfully back-thinned to the epitaxial layer and has been shown sensitive to short range ionizing particles. Results with a patterned proton beam, produced with a special collimator, indicate good performance and spatial resolution, albeit with a significant background signal.

Laboratory tests and calculations indicate that the measured background signal during the MIMOSA V tests is a result of various contributions. Since the blooming effect is certainly present and related to over-saturating flux, an imaging device with a higher dynamic range is needed in order not to spoil the resolution required by the beam monitor.

For this reason further beam tests with MIMOTERA, the dedicated CMOS monolithic active pixel sensor of the MIMOSA family, will be scheduled in a short time scale. The sensor

designed to provide both required dynamic range and granularity is at present (September 2005) in the post-processing phase.

The major limitations of the performed in-beam tests are the coarse spatial resolution of the JRC reference monitor (3 mm granularity) and the impossibility of a direct digital record of the beam image for more accurate comparisons with the SLIM measurements. The implemented testing activity should be completed and finalized inserting in the JRC extraction beam line a scintillation screen with comparable spatial resolution (0.1 mm) and digital record of the beam image. The device should be installed at a convenient distance downstream the SLIM, taking into account the extraction line optical parameters, to evaluate the plural scattering in the thin Al foils. Finally, the dedicated MIMOTERA sensor, based on the SLIM beam monitor specifications, will be integrated to fully assess the viability of the proposed method within compliances.

Tests with high intensity (up to 1 mA) beams to evaluate the possibility to use the SLIM beam monitor for the real time control of radioisotope production at cyclotron facilities are foreseen to respond to the growing demand of radioisotopes in nuclear medicine. A beam monitor measuring in real-time fluctuations in space and time would offer the possibility of increasing the production capability up to 50% and minimize the risk of accidental expensive target destruction, radioactive hazard and radiation dose to the personnel.

Due to the higher currents of the radioispotope production beams, thermal aspects, space charge effects and radiation hardness are expected to be critical and need to be carefully evaluated.

Appendix A

Technical Glossary

Accuracy The degree of conformity of a measured or calculated quantity to its actual, nominal, or some other reference, value. Accuracy can be expressed as the difference between the mean of the measurements and the reference value.

Active beam scanning Beam spreading technique realized bending and directing the charged particle beams with great accuracy by means of magnetic fields perpendicular to their trajectory.

Backscatter The radiation that is scattered by the atoms of a medium crossed by a ionizing beam in the direction opposite to the incident beam.

Beam diagnostics system Set of monitors along (inside or just outside) the beamline to measure the beam main parameters for the most efficient and safest operation of the accelerator complex.

Beam dosimetry system Set of interceptive monitors, as ionization chambers and multiwire proportional chambers that measure, according to international standards, the beam dose, position and profile in air, just before the patient. Their effect on the beam for therapy is well quantified and considered in the treatment plan simulations.

Benign tumour A tumour that grows locally but does not spread to other parts of the body. Benign tumors can cause problems because of their spread, as they press and displace normal tissues. They can be dangerous in confined places such as the skull.

Bolus In a passive beam spreading system a custom-made block positioned on the extracted beam path just before the patient. The contours and thickness of the block conform the beam to the shape of the far edge of the target.

Brachytherapy Radiation therapy from radioactive sources inside the body. The radiation oncologist may implant radioactive material directly into the tumour or very close to it.

Bragg peak The Bragg Peak describes the characteristic pattern of energy deposition occurring when charged hadrons move through matter. The phenomenon is exploited to con-

centrate the effect of hadron beams on the tumor being treated while minimizing the effect on the surrounding healthy tissue.

Built-in potential In a $p-n$ junction is the voltage drop across the two sides caused by the different impurities concentration and opposing any further diffusive currents. Its value depends on the doping concentration.

Calibration The way to determine, by measurement or comparison with a standard reference, the correct value of a reading on a measuring instrument.

Cancer Uncontrolled, abnormal growth of cells, which invade and destroy healthy tissues if not controlled by effective treatment.

Chemotherapy Treatment with anticancer drugs.

Conformal radiation therapy Radiation that is shaped, or *conformed*, to the tumour contour in all three dimensions. The ability to shape the beam (the more precisely the better) helps the physician to deliver most of the radiation to the tumour, not to surrounding normal tissue.

Depletion region Also known as space charge region, is a volume across a $p-n$ junction completely depleted from free charge carriers and where a positive (negative) distribution of fixed charge is present in the n side (p side). The depletion of the free carriers is due to the diffusion of majority carriers from the opposite side and their immediate recombination.

Direct charged particle detection The detection of a charged particle by the direct measurement of the effects produced during the interaction of the particle with the sensor itself.

Distal Anatomically located far from a point of reference, such as an origin or a point of attachment.

Dose The amount of energy imparted to matter by ionizing particles per unit mass of irradiated material at the place of interest.

Dynamic Range The signal amplitude interval that a measuring system can transduce linearly.

Energy gap Also known as band gap, it represents, in the band structure of solids, the energy distance between to consecutive bands within which there are no allowed energy states. It is usually referred to distance between the highest occupied and the lowest unoccupied band.

Energy Resolution The energy resolution of a detector is the spread of its response to a monochromatic signal and is usually quoted as the Full Width Half Maximum (FWHM) of the energy distribution.

Gantry In radiation therapy, a device for rotating the radiation delivery apparatus around the patient, so as to treat from different angles.

Granularity The distance between two consecutive sensitive elements of a position sensitive detector.

Gray A measure of absorbed radiation dose. One Gray (Gy) equals 1 Joule per kg and corresponds to 100 rads, in the older terminology.

Hadrons A hadron is a subatomic particle which experiences the strong nuclear force. There are over 300 different hadrons, all composed of quarks. The best known are protons and neutrons, the building blocks of the atomic nucleus.

Hybridization In the field of radiation detection is the procedure to interconnect the sensitive detecting medium to the readout electronics.

Ionizing radiation Radiation of sufficient energy to displace electrons from the atoms of cells and produce ions.

Immobilization device A device that prevents the patient from moving during radiation treatment.

Malignant tumour Cancers that spread by invading normal tissue and spreading to distant tissues (metastasis).

Metastasis The spread of a cancer from one part of the body to another. Cells in the second tumour are like those in the original tumour.

Monolithic technology Generally speaking, it refers to a technological process where all the needed components are manufactured on the same crystal. In the specific case of radiation detector, it represents the most appealing alternative to hybridization and it is obtained integrating on the same semiconductor substrate both the sensitive element and the readout electronics.

Nozzle The final element in the beam delivery system through which protons are delivered to the patient monitoring beam uniformity, alignment, and dose delivered.

Passive beam spreading Beam spreading technique consisting of scattering material placed upstream to diffuse the hadrons and of a collimator placed close to the part to be irradiated. Passive spreading systems have been employed for most of the patients treated until now with hadrons, but in the longer term they will be substituted by active systems.

Pedestal Taking into account an empty target run with some tens of frames, one may define the pedestal as the mean of the single pixel output signal distribution, while the RMS is defining the noise.

Precision The degree of mutual agreement among a series of individual measurements, values, or results. Precision is usually expressed in terms of the standard deviation of the measurements, sometimes called the measurement standard error.

Proximal The point closest to the reference point.

Quantum efficiency A figure given for a photosensitive device (CCD, for example) which

is the percentage of photons hitting the photo-reactive surface that will produce an electron-hole pair. It is an accurate measurement of the devices sensitivity. It is often measured on a range of different wavelengths, to characterize a devices efficiency at each energy.

Radiation Energy carried by waves or a stream of particles.

Radiation therapy The use of high-energy penetrating rays or subatomic particles to treat disease. Types of radiation include x-rays, electrons, protons, alpha, light ions and beta particles, and gamma rays. Radioactive substances include cobalt, radium, iridium, and cesium.

Repeatability The variation in a measurement arising when all efforts are made to keep conditions constant by using the same instrument and operator, and repeating during a short time period the procedure.

Reproducibility The variation in a measurement due to the repetition of the same investigation with different instruments and operators.

Sensitivity The minimum difference in amplitude between two signals that a measuring system can distinguish.

Spatial Resolution In a position sensitive element, the precision on the knowledge of the impact point of an incident particle.

Standard deviation The standard deviation is the most common measure of statistical dispersion or variation in a distribution, equal to the square root of the arithmetic mean of the squares of the deviations from the arithmetic mean.

Treatment volume The tissue actually treated by radiation. The treatment volume may be the diseased tissue only, but in cancer treatment it usually includes the cancer and tissues around it that may harbor microscopic extensions of cancer.

Treatment field The body region at which the radiation beam is aimed.

Treatment table The table that the patient lies on during treatment. In hadron radiation therapy, final patient alignment is performed by adjusting the motorized table with respect to the beam nozzle according to the treatment plan based on the CT scans.

Tumour An abnormal mass of tissue. Tumors are either benign or malignant.

Uncertainty Inherent variability of repeated measurements of a quantity. A prediction of the probable variability of a result, based on the inherent uncertainties in the data, found from a mathematical calculation of how the data uncertainties would, in combination, lead to an uncertainty in the result. The calculation or process by which one predicts the size of the uncertainty in results starting from the uncertainties in data is called error analysis.

X-rays High-energy, ionizing, electromagnetic radiation that can be used at low doses to diagnose disease or at high doses to treat cancer.

Appendix B

Acronims

ADC Analog to Digital Converter. An electronics device able to convert input analog signals in a digital output. It is usually characterized by the number of bits at which the conversion occurs.

APS Active Pixel Sensor. Image sensor using pixels containing an active (= power dissipating) element.

ASIC Application Specific Integrated Circuit. A chip that is custom designed for a specific application.

CCD Charge Coupled Device. A charge-coupled device is a sensor for recording images, consisting of an integrated circuit containing an array of linked, or coupled, capacitors. Under the control of an external circuit, each capacitor can transfer its electric charge to one or other of its neighbours.

CDS Correlated Double Sampling. It is a method employed to improve the signal to noise ratio SNR of integrating image sensors. By subtracting a pixels dark or reference output level from the actual induced signal, static fixed pattern noise and several types of temporal noise are effectively removed from the sensors output.

CMOS Complementary Metal Oxide Semiconductor. A process that uses both n- and p-channel devices in a complimentary fashion to achieve small geometries and low power consumption.

CT Computed Tomography. Computed tomography, also known as computed axial tomography or computer-assisted tomography (CAT) and body section roentgenography, is a medical imaging method employing tomography where digital processing is used to generate a three-dimensional image of the internals of an object from a large series of two-dimensional x-ray images taken around a single axis of rotation. The word tomography is derived from the Greek *tomos* (slice) and *graphia* (describing).

DAQ Data Acquisition System. An electronics system that takes care of transferring data from a sensor to an interfaced computer or GUI.

DNA Deoxyribonucleic acid. It is a nucleic acid that contains the genetic instructions specifying the biological development of all cellular forms of life. DNA is often referred to as the molecule of heredity, as it is responsible for the genetic propagation of most inherited traits.

EC European Commission. Branch of the governing body of the European Union (EU) invested with executive and some legislative powers. The European Commission embodies and upholds the general interest of the Union and is the driving force in the Union's institutional system. Its four main roles are to propose legislation to Parliament and the Council, to administer and implement Community policies, to enforce Community law (jointly with the Court of Justice) and to negotiate international agreements, mainly those relating to trade and cooperation.

FEE Front-End Electronics. The system electronics responsible for amplifying, digitizing, and selecting time slices from the detector signals.

FG Frame Grabber. A device that accepts standard TV signals and digitizes the current video frame into a bitmap image.

FPGA Field Programmable Gate Array. A class of integrated circuits for which the logic function is defined by the customer using development system software after the IC has been manufactured and delivered to the end user.

FIFO First In First Out. A storage method that retrieves the item stored for the longest time.

FS Focusing System. The focusing system developed for the SLIM beam monitor.

FWHM Full Width at Half Maximum. The full width at half maximum is a parameter commonly used to describe the width of a 'bump' on a curve or function. It is given by the distance between points on the curve at which the function reaches half its maximum value.

GPIO General Purpose Input/Output. GPIO devices provided a set of IO ports which can be configured for either input or output.

GUI Graphical User Interface. Computer software that allows a user friendly interface to a virtual instrument or to a DAQ.

HEP High Energy Physics. It is a branch of modern physics, in which interactions among elementary particles accelerated to very high energy are studied.

IC Integrated Circuit. A tiny complex of electronic components and their connections that is produced in or on a small slice of material (such as silicon).

LET Linear Energy Transfer. The Linear Energy Transfer is defined as the ratio between the energy ΔE deposited by a charged particle in a very short track element, and its length Δx. In formula $L_\infty = \Delta E/\Delta x$, where the index ∞ indicates that there is no limitation on the amount of energy ΔE released in any single collision of the particle with an atom or a molecule of the treated medium. Physicists call L_∞ the *unrestricted energy loss* or the *unrestricted stopping power*.

LINAC LINear ACcelerator.A linear particle accelerator is an electrical device for the acceleration of subatomic particles.

MRI Magnetic resonance imaging. A diagnostic imaging technique that uses a magnetic field and radio waves to produce highly detailed images of the body. MRI may be used in planning radiation therapy as CT and PET scans.

MAPS Monolithic Active Pixel Sensor. It is a pixel detector manufactured in a monolithic technology, with integrated active FEE.

MCP Micro Channel Plate. A micro-channel plate is a planar device which intensifies impinging radiation or particles by multiplication of electrons in small channels under the presence of a high electric field.

MIMOSA Minimum Ionizing particle MOS Active pixel sensor.

MIP Minimum Ionizing Particle. A particle having the minimum possible energy loss rate. In other words, a particle with an energy such to be in minimum of the Bethe-Bloch plot. One MIP is the amount of charge released by a particle with minimum ionizing power; when such a particle crosses a 300 μm thick Silicon detector, it produces approximately 25000 electron-hole pairs, corresponding to a charge of 3.8 fC.

MSPS Mega Sample per Second.

OER Oxygen Enhancement Ratio. The ratio of the dose required to achieve a given biological effect under hypoxic conditions to the dose required to achieve the same effect under oxygenated conditions. In formula the definition is OER = D/D_0, where D is the dose needed to produce the effect in the actual tissue and D_0 is the dose which would be needed if the tissue were fully oxygenized in an air atmosphere under normal pressure.

PET Positron Emission Tomography. A nuclear medicine imaging procedure employing radioactive isotopes that decay by emitting a positively positrons. These radioactive isotopes are bound to compounds or drugs that are injected into the body and enable physicians to study the physiology of normal and abnormal tissues. *PET scans* are used in radiation treatment planning to help identify tumor tissue by the behavior of its cells, sometimes in cases where the tumor tissue is not visible on CT scans or MRI.

PCB Printed Circuit Board. A piece of insulating material where electronics components can be mounted and interconnected using deposited metal tracks. In a multilayer PCB, several layers of conductive tracks can be stacked, separated by a dielectric material, in order to implement also very complicated routing on a reduced surface.

PIMMS Proton-Ion Medical Machine Study. The PIMMS was set up at CERN in 1996 with the aim to investigate and design a synchrotron-based hadrontherapy facility.

PPS Passive Pixel Sensor. Image sensor using pixels not containing an active (= power dissipating) element.

RAM Random Access Memory. A memory device in which information can be accessed in any order.

RBE Radio Biological Effectiveness. It is the ratio of the dose required to achieve a defined biological result using some radiation standard to the dose required to achieve the same result using test radiation, typically γ-rays.

RF Radio Frequency. Electromagnetic waves in the frequency range of 30 kHz to 300 GHz.

SE Secondary Electrons. Electrons produced in secondary emission.

SEE Secondary Electrons Emission. Emission of electrons from the surface of a substance as a result of bombardment by electrons or ions.

SEM Secondary Emission Monitor. Monitor based on secondary electrons emission.

SLIM Sem for Low Interception Monitoring. An innovative beam monitoring system for real time diagnostics of charged particle beams in the extraction lines of a hadrontherapy facility, with exceptional acceptance, transparency, spatial and time resolution. The SLIM study, development and testing was the aim of this doctoral thesis.

SNR Signal to Noise Ratio. The ratio of the amplitude of the desired signal to the amplitude of noise signals.

SRAM Static Random Access Memory. A type of memory that is faster and more reliable than the more common dynamic RAM. The term static is derived from the fact that it does not need to be refreshed like dynamic RAM.

SUCIMA Silicon Ultra fast Cameras for electrons and gamma sources In Medical Application. A project funded by the European Commission (European Commission contract: G1RD-CT2001-00561) with the primary goal of developing a novel silicon real-time, high granularity, monolithic, pixel sensor for medical applications. The SLIM beam monitor has been developed in the SUCIMA framework.

USB Universal Serial Bus. A standard data transfer protocol used to transmit information from/to an external device to/from a computer. USB version 2.0 allowing very fast transfer rate is one of the most widely used computer interface.

VC Vacuum Chamber. The vacuum chamber developed for the SLIM beam monitor.

VLSI Very Large Scale Integration. A technology that refers to semiconductor chips that are engineered to accommodate a large number of transistors.

Appendix C

Commercial equipment technical details

C.1 Commercial secondary electrons detector

The SLIM commercial detector consists of a MCP (micro channel plate) coupled to a phosphor screen viewed with a CCD camera (charged coupled device).

C.1.1 Micro channel plate and phosphor screen

The Hamamatsu[1] micro channel plate (F2224-11) technical data are summarized in Table C.1. The emission characteristics of the read-out phosphor screen (P47) and the main technical specifications are listed in Table C.2.

Table C.1: *Micro channel plate technical specifications.*

MCP F2224	
Number of stages	single-stage
Shape	circular
Read-out	phosphor screen
MCP supply voltage [V]	1000
Gain	up to a few 10^4
Effective diameter [mm]	32
Channel diameter [μm]	12
Required vacuum [Torr]	10^{-7}

The CCD is a black & white camera with a sensor of 752 x 582 pixels and 20 ms acquisition rate. The main technical parameters are listed in Table C.3.

1 http://sales.hamamatsu.com/en/home.php

Table C.2: *Read-out phosphor screen technical specifications.*

P47	
Wavelength at peak emission [nm]	410
Composition	Y Silicate : Ce
Persistence decay time to 10% [μs]	0.08
Efficiency [photons/Joule]	10^{16}
Phosphor supply voltage [V]	4000

Table C.3: *CCD camera main technical specifications.*

CCD	
Sensor	CCD 1/3”
Horizontal resolution	570 lines TV
System	standard CCIR
Sensitivity [lux]	0.2 (F 1.4)
Saturation [lux]	2
Video output	1 V_{pp} @ 75 Ω (video composite)
Supply voltage [V_{dc}]	12
Power [W]	1.05
Size [mm]	32 x 32 x 28
Weight [g]	25
Lens mount	CS

C.2 Vacuum system

C.2.1 Pumping system

C.2.1.1 Primary pump

The VARIAN[2] primary dry scroll vacuum pump SH-100 main features are illustrated in Figure C.1.

Peak pumping speed	50 Hz: 83 lpm, 5 m^3/hr, 2.9 cfm; 60 Hz: 100 lpm, 6 m^3/hr, 3.5 cfm
Media	No toxic, corrosive, explosive or particulate forming gases
Ultimate pressure	5.0 x 10^{-2} Torr (6.6 x 10^{-2} mbar)
Maximum inlet pressure	1.0 atmosphere (0 psig)
Maximum outlet pressure	1.5 atmosphere (7.5 psig)
Inlet Connection	NW25
Exhaust Connection	1/4" Female NPT (NW16 adapter provided)
Gas ballast	1/8" Female NPT (20 micron sintered plug provided)
Ambient operating temperature	5 °C to 40 °C (41 °F to 104 °F)
Storage temperature	-20 °C to 60 °C (-4 °F to 140 °F)
Motor rating (1 phase)	0.5 HP (0.37 kW)
Operating Voltages	1 phase - 50-60 Hz/100-115:200-230 VAC
Motor thermal protection	Type U automatic
Operating speed	50 Hz: 1425 RPM; 60 Hz: 1725 RPM
Cooling system	Air-cooled
Weight	Pump only: 19.1 kg (42 lbs) Shipping weight: 20 kg (44 lbs)
Leak rate (with exhaust sealed)	<1 x 10^{-7} std cc/sec Helium
Noise level (per ISO 11201)	56 dB(A)
Vibration level (per ISO 10816-1)	Class 1B, 1.5 mm/sec
Hour meter	Integral Hour Meter provided, displays running time to closest .1 hour
Certification	CE marked UL, CUL

Figure C.1: *SH-100 primary pump technical specifications.*

C.2.1.2 Turbo-molecular pump

The VARIAN turbo-molecular vacuum pump V70-LP main features are shown in Figure C.2.

C.2.2 Residual gas pressure reading system

C.2.2.1 Eyesys ConvecTorr gauge

The VARIAN Eyesys ConvecTorr gauge main features are summarized in Table C.4.

C.2.2.2 Eyesys Mini-B/A gauge

The VARIAN Eyesys Mini-B/A gauge main features are summarized in Figure C.3.

2 http://www.varianinc.com/cgi-bin/nav?/products/vacuum/

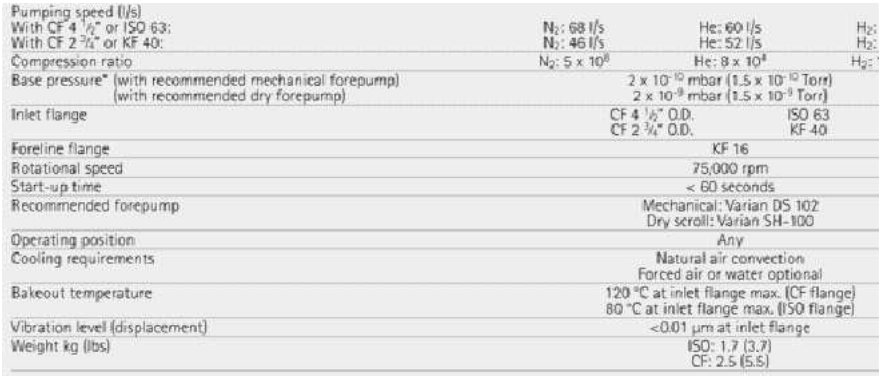

Pumping speed (l/s) With CF 4 ½" or ISO 63: With CF 2 ¾" or KF 40:	N_2: 68 l/s N_2: 46 l/s	He: 60 l/s He: 52 l/s	H_2: H_2:
Compression ratio	N_2: 5×10^8	He: 8×10^4	H_2:
Base pressure* (with recommended mechanical forepump) (with recommended dry forepump)	2×10^{-10} mbar (1.5×10^{-10} Torr) 2×10^{-9} mbar (1.5×10^{-9} Torr)		
Inlet flange	CF 4 ½" O.D. CF 2 ¾" O.D.		ISO 63 KF 40
Foreline flange	KF 16		
Rotational speed	75,000 rpm		
Start-up time	< 60 seconds		
Recommended forepump	Mechanical: Varian DS 102 Dry scroll: Varian SH-100		
Operating position	Any		
Cooling requirements	Natural air convection Forced air or water optional		
Bakeout temperature	120 °C at inlet flange max. (CF flange) 80 °C at inlet flange max. (ISO flange)		
Vibration level (displacement)	<0.01 µm at inlet flange		
Weight kg (lbs)	ISO: 1.7 (3.7) CF: 2.5 (5.5)		

Figure C.2: *V70-LP turbo-molecular pump technical specifications.*

Table C.4: *Eyesys ConvecTorr gauge main technical specifications.*

Eyesys ConvecTorr gauge	
External Power	13 to 27 V_{dc}, 150 mA maximum
Operating Temperature	0 to 50 °C
Pressure range	133 kPa (1330 mbar, 1000 Torr) to 0.13 Pa (0.1 bar, 0.1 mTorr)
Overpressure capability	200 kPa (2 bar, 1500 Torr)
Output Signal	1V/decade log linear (optional non-linear available)
Set Point Digital Potentiometer Setting	Form C relay, 100 mA at 40 V_{dc}

Units	Pascal, mbar or Torr, preset at factory
Pressure Range	1.3 Pa (1.3×10^{-2} mbar, 1×0^{-2} Torr) to 2.7×10^{-7} Pa (2.7×10^{-9} mbar, 2×10^{-9} Torr)
Input Power Supply Required	24 VDC ±10%, at 0.500A
Output Signal	1-9V, 1V/Decade, Logarithmic
Output Impedance	100 Ohms
Minimum Load Impedance	1 Ohms
Temperature Range	0-50 °C operating, –15 to 70 °C storage
Setpoint Relays	2 N.O. SPST relays, rating 40 VDC, 100mA
Degas	E-beam at 4 Watts for fifteen minutes
Size	3 3/4" H (from flange face) x 3 11/32" W x 3 11/32" D
I/O Connection	15-pin D-subminiature
Overpressure	1×10^{-2} Torr
Overpressure Limit	130k Pa/1.3 bar/1000 Torr
Cleaning	External surfaces may be cleaned with a slightly damp soft cloth
Environmental	0-50 °C, 80% RH non-condensing
Installation	Indoor use, Installation Category II, Pollution Degree 2
Altitude	2000 meters

Figure C.3: *Eyesys Mini-B/A gauge technical specifications.*

C.2.3 Electro-magnetic valve

The fore-vacuum (760 Torr down to 1 Torr) need to be very delicate to avoid turbulences that could harm the thin foils. The *by-pass system* described in Section 5.1 is realized with a direct acting electromagnetic block valve. The valve main features are summarized in Table C.5.

Table C.5: *Electromagnetic valve main technical specifications.*

Electro-magnetic valve	
Pressure range	
Plain aluminium body	atmosphere to 1 x 10^{-6} Torr
Nickel-plated body	atmosphere to 1 x 10^{-9} Torr
Leak rate	$<$ 1 x 10^{-9} std cc/sec He
Operating temperature	15 °C to 40 °C
Maximum baking temperature	125 °C when closed (coil removed)
Service life	250 000 cycles
Conductance	NW16 valve: 2.2 l/sec NW25 valve: 3.5 l/sec
Time to open or close	Open: 50 msec Close: $<$ 25 msec

C.3 High voltage power supplies

C.3.1 K7-series

The Matsusada[3] K7 series features ultra low ripple, high voltage, high stability power supplies chosen for the bias of the SLIM focusing system electrodes: for V_0 (cage electrode voltage) the K7-30 N model and for V_1 (ring electrode voltage) the K-20 N model. Remote and local programming can be implemented. The power supplies of the K7 series are fully protected against continuous short circuit. The K7-20 and K7-30 main features are summarized in Table C.6.

C.3.2 S-series

The Matsusada S series features well regulated, low ripple, high voltage power supplies chosen for the bias of the SLIM micro channel plate (S3-1.5 P). The S3-1.5 P main features are summarized in Table C.7.

3 http://www.matsusada.com/

Table C.6: *K7 series power supplies main features.*

Parameters	**K7-20 N**	**K7-30 N**
Output voltage [kV]	-20 ÷ 0	-30 ÷ 0
Output current [μA]	350	250
Ripple (p - p) [mV]	200	300
Input voltage [V]	+ 24 dc	
Stability	0.001%/5min, 0.005%/hr	
Regulation [%]	line: 0.001, load: 0.001	
Temperature coefficient	0.0025%/°C	
Operating temperature	0 ÷ 50 °C	

Table C.7: *S3-1.5 power supplies main technical specifications.*

S3-1.5	
Output voltage [kV]	0 ÷ 1.5
Output current [mA]	2
Output power [W]	3
Ripple (p - p) [%]	0.005
Regulation [%]	line: ±0.005, load: ±0.005

C.3.3 U-series

The Matsusada U series features floating output, low ripple, high voltage power supplies chosen for the bias of the SLIM phosphor screen (U6A-6PN). The U6A-6PN main features are summarized in Table C.8.

Table C.8: *U6A-6PN power supplies main technical specifications.*

U6A-6PN	
Output voltage [kV]	0.3 ÷ 6
Output current [mA]	1
Minimum load [MΩ]	6
Ripple (p - p) [%]	0.2
Isolation [V_{dc}]	7000

C.4 Actuator

The Stegmann[4] HIPER DRIVE actuator features logical and complete integration into an overall drive system of:

- gearbox;
- brushless DC motor;
- absolute encoder;
- the control and power electronics.

The actuator main features are summarized in Figure C.4.

Supply voltage		24 ± 15 %	VDC
Nominal current		4.8	A
Nominal speed		27	min^{-1}
Nominal torque		15	Nm
Nominal output power		42	W
No-load speed		38	min^{-1}
No-load current		< 1.2	A
Maximum torque		20	Nm
Repeatability		< 0.5° at the output shaft	
Maximum number of revolutions		32.000	
Interface		RS 485	
- optional		Profibus DP	
Maximal shaft loading	- axial	150	N
	- radial	200 (20 mm from flange)	N
Detent torque		> 15	Nm
Ambient temperature range (dependant on duty cycle)		0 - 60	° C
Degree of protection to DIN EN 600529		IP 65	
Insulation class to DIN EN 60034 - 1		B	

Figure C.4: *HIPER DRIVE actuator technical data.*

4 http://www.sick.com/home/en.html

List of Figures

List of Tables

Bibliography

[1] R. R. Wilson, Radiology **47**, 487 (1946).

[2] C. A. Tobias, H. O. Anger, and J. H. Lawrence, Am. J. Roentgenol. Radiat. Ther. Nucl. Med. **67**, 1 (1952).

[3] C. A. Tobias *et al.*, Am. J. Roentgenol. Radiat. Ther. Nucl. Med. **72**, 1 (1954).

[4] B. Larsson, L. Leksell, B. Rexed, and P. Sourander, Acta Radiologica **51**, 52 (1959).

[5] B. Larsson, Brit. J. Radiol. **34**, 143 (1961).

[6] B. Larsson, In Uppsala 1973, High Energy Physics and Nuclear Structure, Amsterdam 1974, 451-455.

[7] M. R. Raju, Int. J. Radiat. Biol. **67**, 237 (1995).

[8] P. L. Petti and A. J. Lennox, Annu. Rev. Nucl. Part. Sci. **44**, 155 (1994).

[9] M. R. Raju, *Heavy Particle Radiotherapy* (Academic Press, New York, 1980).

[10] J. R. Alonso, Presented at 18th Int. Seminar on Planetary Emergencies and NATO Workshop on Global Stability through Disarmament, Erice, Italy, Aug 19-23, 1993.

[11] G. Kraft, T. Haberer, D. Schardt, and M. Scholz, Presented at Int. Workshop 'Modeling in Clinical Radiobiology', Wurzburg, Germany, Apr 25-27, 1993 and in part at the 'Austron Symposium', Vienna, Austria, May 3-4, 1993.

[12] J. F. Fowler, *Nuclear Particles in Cancer Treatment* (A. Hilger ed, Bristol, 1981), 178.

[13] J. F. Fowler, *Nuclear Particles in Cancer Treatment* (A. Hilger ed, Bristol, 1981), 100.

[14] J. F. Fowler, *The Biological basis for Radiotherapy* (G.G. Steel, G. E. Adams and M. Y. Peckham, Elsevier, New York, 1983), 261-268.

[15] J. D. Chapman, E. A. Blakely, K. C. Smith, and R. C. Urtasun, In Berkeley 1976, Proceedings, Particles and Radiation Therapy, 97-102.

[16] E. A. Blakely, F. Q. H. Ngo, S. B. Curtis, and C. A. Tobias, Adv. Radiat. Biol. **11**, 295 (1984).

[17] J. T. Leith, E. J. Ainsworth, and E. L. Alpen, Adv. Radiat. Biol. **10**, 101 (1983).

[18] J. Castro, *Hadrontherapy in Oncology* (U. Amaldi and B. Larsson eds, Elsevier Science Pub. Co., Amsterdam, 1994).

[19] E. Pedroni, Status of proton therapy: results and future trends, in *Proceedings of EPAC94*, p. 407, London, 1994.

[20] E. Pedroni *et al.*, Voxel scanning for protontherapy, in *Proceedings of the NIRS International Workshop on Heavy Charged Particle Therapy and Related Subjects*, pp. 94–109, Chiba, 1991.

[21] T. Haberer, W. Becher, D. Schardt, and G. Kraft, Nucl. Instrum. Meth. **A330**, 296 (1993).

[22] L. Badano *et al.*, Nucl. Instrum. Meth. **A430**, 512 (1999).

[23] C. M. Washington and D. Leaver, *Principles and Practice of Radiation Therapy* (C. V. Mosby ed, St. Louis, 2003).

[24] G. W. Swan, *Optimisation of human cancer radiotherapy* (Springer-Verlag, Berlin, 1981).

[25] PTCOG, *Particles: a newsletter for those interested in proton, light ion and heavy charged particle radiotherapy* (J. Sisterson. ed, Cambridge, UK, 2005).

[26] G. Gademan, *Hadrontherapy in Oncology* (U. Amaldi and B. Larsson eds, Elsevier Science Pub. Co., Amsterdam, 1994).

[27] R. Orecchia, European Journal of Cancer **34**, 459 (1998).

[28] R. Orecchia and M. Krengli, Tumori **84**, 205 (1998).

[29] A. J. M. V. ed and F. A. T. M. S. co ed, *Towards Coordination of Cancer Research in Europe* (IOS PRESS, 1994).

[30] K. D. Grass and M. P. eds, *Proposal for a dedicated ion beam facility for cancer therapy* (GSI, Darmstadt, 1998).

[31] U. Amaldi and G. Tosi, TERA Note 1-1 (1991).

[32] M. Pullia, Proceedings of the MT19 - 19^{th} International Conference on Magnet Technology (2005).

[33] P. Mandrillon *et al.*, In Berkeley 1986, Proceedings, Biomedical Accelerators, 93- 115.

[34] J. F. Fowler, In Berkeley 1986, Proceedings, Biomedical Accelerators, 5- 17.

[35] L. Badano *et al.*, SLIM (SEM for Low Interception Monitoring) an innovative non-destructive beam monitor for the extraction lines of a hadrotherapy center, in *Proceedings of DIPAC2003, Mainz, Germany*, pp. 77–79, 2003.

[36] L. Badano *et al.*, IEEE Trans. Nucl. Sci. **51**, 133 (2004).

[37] L. Badano *et al.*, IEEE Trans. Nucl. Sci. **52**, 830 (2005).

[38] K. Abbas *et al.*, submitted to NIM for publication in August 2005 .

[39] M. Caccia *et al.*, Nucl. Phys. B (Proc. Suppl.) **125**, 133 (2003).

[40] L. Badano and S. Rossi, CERN-PS-97-019-DI.

[41] S. Vatnitskya, Radiotherapy and Oncology **41**, 169 (1996).

[42] L. Badano, *Injection and extraction lines instrumentation for PIMMS* (CERN PS/DR/Note 2000-011 (Tech), Geneva, 2000).

[43] J. Camas *et al.*, *Screens versus SEM Grids for Single Pass Measurements in SPS* (CERN SL/95-62 (BI), Geneva, 1995).

[44] J. Bosser *et al.*, *Profile Measurement in LEAR Transfer Line* (87-04 CERN, Geneva, 1987).

[45] G. Ferioli, private communication.

[46] C. D. Johnson, *The development and Use of Alumina Ceramic Fluorescent Screens* (PS/90-42 (AR) CERN, Geneva, 1977).

[47] F. Sauli, *Principles of Operation of Multiwire Proportional and Drift Chambers* (CERN 77-09 report, Geneva, 1997).

[48] G. Coutrakon *et al.*, Med Phys. **21**, 1691 (1994).

[49] Y. Hirao *et al.*, Nucl. Phys. A **538**, 541 (1992).

[50] Y. Hirao *et al.*, *Heavy Ion Medical Accelerator in Chiba. A design Summary and Update* (Division of Accelerator Research NIRS-M-89 HIMAC-001, 1992).

[51] E. Urakabe *et al.*, Performance of parallel plate ionization chambers for medical irradiation, in *Proceedings of the Particle Accelerator Conference*, pp. 3819–3820, 1997.

[52] P. Strehl, Beam instrumentation and diagnostics, in *Joint Universities Accelerator School, Archamps*, 1998.

[53] P. Forck *et al.*, Prepared for 3rd European Particle Accelerator Conference (EPAC 92), Berlin, Germany, 24-28 Mar 1992.

[54] G. Molinari, private communication.

[55] C. Fernandez-Figueroa and G. Molinari, Prepared for 3rd European Particle Accelerator Conference (EPAC 92), Berlin, Germany, 24-28 Mar 1992.

[56] C. Chianelli *et al.*, Nucl. Instr. Meth. **A273**, 245 (1988).

[57] E. P. Marsh, M. D. Strathman, D. A. Reed, and R. W. Odom, In *Batavia 1990, Proceedings, Accelerator instrumentation* 213-217.

[58] J. Bosser *et al.*, *Profile measurement in the LEAR transfer line* (CERN SPS/ABM/Note 1987-06 (Tech), Geneva, 1987).

[59] M. Pelliccioni, *Fondamenti fisici della radioprotezione* (Pitagora, Bologna, 1989).

[60] B. Bhargava and P. Tripuraneni, The Lancet **359**, 543 (2002).

[61] W. Patrick *et al.*, *Coronary Lesions: a pragmatic approach* (T&F STM, 2001).

[62] D. Antoniucci, *Primary Angioplasty* (Taylor & Francis Group, 2004).

[63] A. Airoldi *et al.*, Nucl. Instrum. Meth. **A540**, 259 (2005).

[64] M. Caccia, Nuclear Instruments and Methods in Physics Research A **465**, 195 (2000), hep-ex/0101011.

[65] SUCIMA Collaboration, M. Caccia *et al.*, Monolithic Active Pixel Dosimeter, United States Patent Application no. PCT/IT2002/000700, 2005.

[66] G. Deptuch *et al.*, Nucl. Instrum. Meth. **A465**, 92 (2000).

[67] R. Turchetta *et al.*, Nucl. Instr. and Meth. A **458**, 677 (2001).

[68] G. Deptuch *et al.*, IEEE Trans. Nucl. Sci. **49**, 601 (2002).

[69] P. Weilhammer *et al.*, Nucl. Instrum. Meth. **A383**, 89 (1996).

[70] W. Dulinski, S. Gadomski, E. Nygard, S. Roe, and P. Weilhammer, Nucl. Instrum. Meth. **A395**, 410 (1997).

[71] VASCM2 data sheet **V 0.9** (downloadable at: http://www.ideas.no).

[72] J. Millman and A. Grabel, *Microelectronics* (McGraw-Hill, 1987).

[73] E. R. Fossum, IEEE Trans. on Electron Devices **44**, 1689 (1997).

[74] A. Fish and O. Yadid Pecht, *CMOS Imagers: From Photo-transduction to Image Processing* (Yadid-Pecht and Etienne-Cummings, Kluwer, 2004).

[75] G. Deptuch *et al.*, Nucl. Instr. and Meth. A **512**, 299 (2003).

[76] W. Kucewicz *et al.*, Nucl. Instr. and Meth. A **518**, 411 (2004).

[77] G. Deptuch, *New generation of monolithic active pixel sensors for charged particle detection*, PhD thesis, Strasbourg, 2002.

[78] M. Caccia *et al.*, (1999), hep-ex/9910019.

[79] G. Claus *et al.*, Nuclear Instruments and Methods in Physics Research A **465**, 120 (2000).

[80] W. Dulinski *et al.*, Nuclear Instruments and Methods in Physics Research A **546**, 274 (2005).

[81] G. Deptuch, W. Dulinski, M. Caccia, and M. Winter, IEEE Transaction on Nuclear Science **52**, 1745 (2005).

[82] G. Deptuch, Nuclear Instruments and Methods in Physics Research A **543**, 537 (2005).

[83] A. Czermak *et al.*, Data Acquisition system for Silicon Ultra fast Cameras for electron and *gamma* In Medical Applications (SUCIMA imager, in *Astroparticle, particle and space physics, detectors and medical physics applications*, edited by E. Barone, M.and Borchi, C. Leroy, P. G. Rancoita, P. L. Riboni, and R. Ruchti, pp. 360 – 365, World Scientific, 2004.

[84] M. Pullia, private communication.

[85] L. Badano and O. Ferrando, SUCIMA Internal Note 01, April 2002.

[86] J. Devooght, A. Dubus, and J. Dehaes, Nucl. Instrum. Meth. **B 13**, 623 (1986).

[87] J. Devooght, A. Dubus, and J. Dehaes, Phys Rev. **B 36**, 5110 (1987).

[88] H. Fitting and J. Reinhardt, Phys. Status Solidi **A 88**, 245 (1985).

[89] J. Ganachaud and M. Cailler, Surf. Sci. **83**, 519 (1979).

[90] T. Koshikawa and R. Shimizu, J. Phys. **D7**, 1303 (1974).

[91] D. Hasselkamp *et al.*, *Particle Induced Electron Emission II* (Springer-Verlag, Berlin, 1992), 20.

[92] E. Sternglass, Phys. Rev. **108**, 1 (1957).

[93] J. E. Borovsky *et al.*, Nucl. Instrum. Meth. **B 30**, 191 (1988).

[94] D. Hasselkamp *et al.*, *Particle Induced Electron Emission II* (Springer-Verlag, Berlin, 1992), 43.

[95] D. Hasselkamp *et al.*, *Particle Induced Electron Emission II* (Springer-Verlag, Berlin, 1992), 56.

[96] N. Benazeth, J. Microsc. Spectrosc. Electron. **12**, 235 (1987).

[97] P. Thieberger *et al.*, Phys. Rev. **A 61**, 42901 (2000).

[98] H. Rothard *et al.*, Phys. Rev. **A 41**, 2521 (1990).

[99] H. Rothard *et al.*, Phys. Rev. **A 57**, 3660 (1998).

[100] D. Hasselkamp and A. Scharmann, Surface Sci **119**, L388 (1982).

[101] D. Hasselkamp and A. Scharmann, Vak. Tech. **31**, 242 (1982).

[102] A. Koyama *et al.*, Nucl.Instr. and Methods **B 13**, 637 (1986).

[103] D. Hasselkamp *et al.*, *Particle Induced Electron Emission II* (Springer-Verlag, Berlin, 1992), 60 - 62.

[104] D. Hasselkamp, private communication.

[105] R. Abbot, J. Appl. Phys. **30**, 871 (1959).

[106] J. Mischler *et al.*, Surface Science **136**, 532 (1984).

[107] J. Mischler *et al.*, Rad. Effects **97**, 1 (1986).

[108] J. Janni, p. 348 (1982), Atomic Data and Nuclear Data tables 27.

[109] J. Janni, p. 218 (1982), Atomic Data and Nuclear Data tables 27.

[110] C. M. Castaneda *et al.*, Nucl. Instrum. Meth. **B129**, 199 (1987).

[111] O. Ferrando, SUCIMA Internal Note 07, April 2003.

[112] A. Dahl, SIMION 3D - Version 7.0 - Idaho National Engineering and Environmental Laboratory.

[113] I. P. Csorba, *Image Tubes* (Howard W. Sams & Co., Inc., USA, 1985).

[114] S. Agostinelli *et al.*, Nuclear Instruments and Methods in Physics Research A **506**, 250 (2003).

[115] F. Bohuraleb, private communication.

[116] V. L. Highland, Nucl. Instr. Meth. **129**, 497 (1975).

[117] G. R. Lynch and O. I. Dahl, Nucl. Instrum. Meth. **B58**, 6 (1991).

[118] B. Zanderighi, Degree thesis in Physics (University of Milano, Italy, Academic Year 1994/1995).

[119] L. Badano and O. Ferrando, SUCIMA Internal Note DEL 20, April 2003.

[120] G. N. Fursey, *Field Emission in Vacuum Microelectronics* (Plenum US, 2005).

[121] Dupont Inc. product.

[122] FP 2000/2010 User Manual - National Instruments - July 2001 Edition.

[123] A. Placci, private communication.

[124] S. Meunier, Vacuum tests performed by Sophie Meunier CERN (AT/VAC).

[125] A. C. Melissinos, *Experiments in Modern Physics* (Academic Press, New York, 1966).

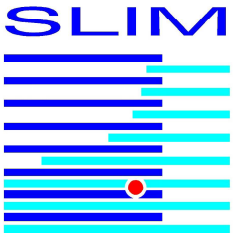

SLIM Publications

Revues Spécialisées

1. M. Caccia, A. Airoldi, M. Alemi, M. Amati, L. Badano, V. Bartsch et al., *Silicon Ultra fast Cameras for electrons and gamma sources In Medical Applications*, Nucl. Phys., vol. B125, pp. 133-138, 2003.
2. W. Kucewicz, M. Alemi, M. Amati, L. Badano, V. Bartsch et al., *Position sensitive silicon detectors for real time dosimetry in medical applications*, Nucl. Instr. Methods, vol. A518, pp. 411-414, 2002.
3. L. Badano, O. Ferrando, T. Klatka, M. Koziel, G. Molinari and M. Pezzetta, *Secondary Emission Monitor for Low-Interception Monitoring (SLIM): An Innovative Non-destructive Beam Monitor for the Extraction Lines of a Hadrontherapy Center*, IEEE Trans. Nucl. Sci., vol. 51, issue 6, pp. 2990 – 2998, 2004.
4. A. Bulgheroni, M. Alemi, L. Badano, D. Berst, C. Bianchi, J. Bol et al., *Silicon Ultra fast Cameras for electron and γ sources In Medical Applications: a progress report*, Nucl. Phys. B, Proceedings Supplements, vol.125, 133 - 138, 2003.
5. L. Badano, O. Ferrando, G. Molinari, T. Klatka, M. Koziel et al., *SLIM (Sem for low interception Monitoring): An innovative Non-destructive Beam Monitor for the Extraction Lines of a Hadrontherapy Center*, IEEE Trans. Nucl. Sci., vol. 52, issue 4, pp. 830 – 833, 2005.
6. K. Abbas, L. Badano, S. Braccini, A. Bulgheroni, M. Caccia, C. Cappellini, A. Czermak, G. Deptuch, W. Dulinski, B. Dulny, O. Ferrando, P. N. Gibson, U. Holzwarth, M. Jastrzab, T. Klatka, M. Koziel, G. Molinari and B. Sowicki, *Tests with a back-thinned monolithic pixel sensor for a real-time hadrontherapy beam monitor*, to be submitted to Nucl. Instr. Methods.

Conférences

1. L. Badano, O. Ferrando, G. Molinari, M. Pezzetta*, SLIM (Sem for low interception Monitoring): An innovative Non-destructive Beam Monitor for the Extraction Lines of a Hadrontherapy Center,* Proceedings of the 6th European Workshop on Beam Diagnostics and Instrumentation for Particle Accelerators, DIPAC 2003, Mainz 2003, pp. 77-79.
2. M. Alemi, L. Badano, D. Berst, C. Bianchi, J. Bol et al., *Silicon Ultra fast Cameras for electrons and gamma sources In Medical Applications*, 2003 IEEE NSS Conference Record, vol. 3, pp. 1574-1578, 2004.
3. L. Badano, O. Ferrando, T. Klatka, M. Koziel, G. Molinari and M. Pezzetta, *Secondary Emission Monitor for Low-Interception Monitoring (SLIM): An Innovative Non-destructive Beam Monitor for the Extraction Lines of a Hadrontherapy Center*,

2004 IEEE NSS Conference Record (IEEE Cat. No.03CH37515), vol. 3, pp. 1574 – 1578, 2004.

4. L. Badano, O. Ferrando, G. Molinari, T. Klatka, M. Koziel et al., *SLIM (Sem for low interception Monitoring): An innovative Non-destructive Beam Monitor for the Extraction Lines of a Hadrontherapy Center*, 2004 IEEE NSS Conference Record (IEEE Cat. No. 04CH37604), vol. 4, pp. 2244 – 2247, 2004.
5. L. Badano, O. Ferrando, T. Klatka, M. Koziel, G. Molinari et al., *SLIM (Sem for low interception Monitoring): An innovative Non-destructive Beam Monitor for the Extraction Lines of a Hadrontherapy Center*, accepted for publication in the Proceedings of the Cyclotrons 2004 Conference, Tokyo 2004.

Notes Internes SUCIMA

1. L. Badano, O. Ferrando, *Secondary Emission Study for the SLIM Beam Monitor*, SUCIMA Internal Note 01, 2002.
2. L. Badano, O. Ferrando, M. Pezzetta, *Engineering Design Study for the SLIM Beam Monitor*, SUCIMA Internal Note DEL 11, 2003.
3. L. Badano, O. Ferrando, *Production of Thin Aluminium Foils for the SLIM Beam Monitor*, SUCIMA Internal Note SUCIMA Internal Note DEL 16, 2003.
4. L. Badano, O. Ferrando, *The Vacuum Chamber System for the SLIM Beam Monitor*, SUCIMA Internal Note DEL 20, 2003.

Brevets

1. L. Badano, O. Ferrando, M. Caccia, L. Conte, M. Alemi, C. Cappellini, A. Airoldi, C. Bianchi, R. Novario, W. De Boer, E. Grigoriev, H. Niemiec, W. Kucewicz, F. Cannillo, G. Clauss, C. Colledani, G. Deptuch, W. Dulinski, P. Grabiec, J. Marczewski, K. Domanski, B. Jaroszewicz, K. Kucharski, G. Popowski, A. Zalewska, A. Czermak, *Monolithic Active Pixel Dosimeter,* Brevet d'invention soumis le 5 novembre 2002, n^0. PCT/IT02/00700.

Résumé

La mesure en continu de l'intensité et du profil des faisceaux de particules utilisés en thérapie par hadrons (ou hadronthérapie) est critique pour l'optimisation de la sécurité du patient, du dépôt optimal de dose ainsi que du fonctionnement de l'accélérateur. A cette fin un moniteur innovant, **S**em for **L**ow **I**nterception **M**onitoring (SLIM), permettant de mesurer l'intensité et le profil des faisceaux de hadrons pendant tout le traitement, a été développé et testé dans le cadre du projet **S**ilicon **U**ltra Fast **C**ameras for electrons and gamma sources **I**n **M**edical **A**pplication (SUCIMA). Le moniteur de faisceau est basé sur l'émission secondaire des électrons par une feuille d'Al/Al_2O_3 d'épaisseur submicronique placée a 45^o sur le parcours du faisceau extrait. Les électrons secondaires, émis avec un flux proportionnel à l'intensité du faisceau de particules, sont accélérés, jusqu'à 20 keV, par un système de focalisation électrostatique et dirigés sur un capteur silicium monolithique à pixels actifs, en technologie CMOS. L'optique électrostatique et ce système de détection donnent l'intensité du faisceau et sa position avec une précision de 1 mm, à un taux de répétition de 10 kHz. Une qualification exhaustive du moniteur de faisceau a été réalisée en laboratoire et sur faisceaux de hadron de basse intensité au cyclotron du Joint Research Centre à Ispra. Les tests en laboratoire du système de focalisation, utilisant l'émission thermoïonique d'un fil de tungstène chaud comme source d'électrons, confirment que les propriétés optiques répondent pleinement aux contraintes imposées en termes de linéarités, facteur de réduction, effets d'aberration et résolution spatiale. Les mesures de l'intensité d'un faisceau de hadrons effectuées avec un détecteur à pad en silicium, avec une fenêtre d'entrée mince, une granularité modérée et une grande gamme dynamique, ont prouvées que la sensibilité du système et la limite de saturation sont conformes aux spécificités requises. Les derniers résultats ont été obtenus avec un capteur monolithique à pixels actifs (MIMOSA V) développé en technologie CMOS et aminci avec succès jusqu'à la couche épitaxiale. Ce capteur a une excellente granularité mais une gamme dynamique très limitée. Ces résultats mettent en évidence la bonne sensibilité du capteur aux particules ionisantes de faible parcours et sa bonne résolution spatiale, malgré un bruit de fond significatif. Les essais en laboratoire et les calculs indiquent que le bruit de fond observé est du a la saturation de détecteur. La qualification finale du moniteur de faisceau SLIM, à l'aide d'un capteur monolithique à pixels actifs fabriqué en technologie CMOS (MIMOTERA) et conçu pour fournir la résolution spatiale et la gamme dynamique requis, est programmée à court terme. La viabilité de la méthode proposée ouvre aussi de nouvelles perspectives dans le domaine de la production de radio-isotopes.

Mots-clés: accélérateurs médicaux, hadronthérapie, instrumentation en temps réel de faisceau, diagnostic de faisceau, capteurs CMOS monolithiques a pixels actifs

Abstract

Real-time monitoring of hadrontherapy beam intensity and profile is critical for the optimisation of dose delivery to carcinogenic tissue, patient safety and the operation of the accelerator complex in general. A novel non-disruptive beam profile monitor, **S**em for **L**ow **I**nterception **M**onitoring (SLIM), has been developed and tested in the framework of the SUCIMA (**S**ilicon **U**ltra-fast **C**ameras for electrons and gamma sources **I**n **M**edical **A**pplication) project. The beam monitor is based on the detection of secondary electrons emitted from a sub-micron thick Al/Al_2O_3 foil intercepting the extracted beam path at 45^o. The SLIM electrostatic focusing system and secondary electron detectors, together with the dedicated acquisition system, have been designed to produce negligible effects on the few nA clinical beam, providing the beam profile and position at 10 kHz frame rate with a granularity not exceeding 1 mm and a beam current resolution of a few percent, on the base of the clinical specifications on the beam for therapy. The final focusing system design, based on the CMOS monolithic silicon sensor specifications, features a demagnification factor of ~5 with the secondary electrons final kinetic energy in the 10 to 30 keV range to reach the sensor sensitive region. A comprehensive qualification of the beam monitor has been performed, both in laboratory and with a low intensity hadron beam at the Cyclotron Laboratory of the Joint Research Centre in Ispra. Laboratory tests with thermionic electrons emitted from a hot tungsten wire have clearly demonstrated that the focusing system fully satisfies the SLIM beam monitor requirements in terms of linearity, demagnification factor, aberration effects and spatial resolution. A scan of the hadron beam intensity measured with a moderate granularity, large dynamic range, shallow back-plane pad silicon sensor showed that system sensitivity and saturation limit are compliant with the specification required by hadrontherapy. The latest results achieved with a back-thinned monolithic active pixel CMOS silicon sensor (MIMOSA V), featuring a high granularity but limited dynamic range, indicate excellent performance and spatial resolution, albeit with a significant background signal. The source of this background, as the laboratory tests and calculations verify, originates from blooming associated to detector saturation. Further beam tests with MIMOTERA, the dedicated monolithic sensor of the MIMOSA family, designed to feature both required dynamic range and granularity, are scheduled in the near future to fully qualify the SLIM beam monitor. The viability of the proposed method opens up new perspectives in the field of radioisotope production as well as hadrontherapy.

Keywords: medical accelerators, hadrontherapy, novel real-time non-disruptive beam instrumentation, beam diagnostics, CMOS monolithic active pixel sensors